Development of fast-actuation piezo systems for high-performance Fluid Power technologies

Department of Mechanics, Mathematics and Management
MECHANICAL AND MANAGEMENT ENGINEERING
Ph.D. Program
SSD: ING-IND/08–Fluid Automation

Final Dissertation

Development of fast-actuation piezo systems for high-performance Fluid Power technologies

by
Francesco Sciatti

Supervisors:

Prof. Riccardo Amirante

Prof. Paolo Tamburrano

Coordinator of Ph.D Program:
Prof. Giuseppe Casalino

Course n°37, 01/11/2021 – 31/10/2024

Department of Mechanics, Mathematics and Management
MECHANICAL AND MANAGEMENT ENGINEERING
Ph.D. Program
SSD: ING-IND/08–FLUID AUTOMATION

Final Dissertation

Development of fast-actuation piezo systems for high-performance Fluid Power technologies

by
Francesco Sciatti

Referees:

Prof. Massimo Rundo

Prof. Andrew R. Plummer

Supervisors:

Prof. Riccardo Amirante

Prof. Paolo Tamburrano

Coordinator of Ph.D Program:
Prof. Giuseppe Casalino

Course n°37, 01/11/2021 - 31/10/2024

Politecnico di Bari

LIBERATORIA PER L'ARCHIVIAZIONE DELLA TESI DI DOTTORATO

Al Magnifico Rettore
del Politecnico di Bari

Il sottoscritto Francesco Sciatti nato a Fasano (BR) il 25/08/1992

residente a Fasano (BR) in via Stella Maris 9-11 e-mail: francesco.sciatti10@gmail.com

iscritto al 3° anno di Corso di Dottorato di Ricerca in INGEGNERIA MECCANICA ciclo XXXVII

ed essendo stato ammesso a sostenere l'esame finale con la prevista discussione della tesi dal titolo:

Development of fast-actuation piezo systems for high-performance Fluid Power technologies

DICHIARA

1) di essere consapevole che, ai sensi del D.P.R. n. 445 del 28.12.2000, le dichiarazioni mendaci, la falsità negli atti e l'uso di atti falsi sono puniti ai sensi del codice penale e delle Leggi speciali in materia, e che nel caso ricorressero dette ipotesi, decade fin dall'inizio e senza necessità di nessuna formalità dai benefici conseguenti al provvedimento emanato sulla base di tali dichiarazioni;
2) di essere iscritto al Corso di Dottorato di ricerca in INGEGNERIA MECCANICA ciclo XXXVII, corso attivato ai sensi del "*Regolamento dei Corsi di Dottorato di ricerca del Politecnico di Bari"*, emanato con D.R. n.286 del 01.07.2013;
3) di essere pienamente a conoscenza delle disposizioni contenute nel predetto Regolamento in merito alla procedura di deposito, pubblicazione e autoarchiviazione della tesi di dottorato nell'Archivio Istituzionale ad accesso aperto alla letteratura scientifica;
4) di essere consapevole che attraverso l'autoarchiviazione delle tesi nell'Archivio Istituzionale ad accesso aperto alla letteratura scientifica del Politecnico di Bari (IRIS-POLIBA), l'Ateneo archivierà e renderà consultabile in rete (nel rispetto della Policy di Ateneo di cui al D.R. 642 del 13.11.2015) il testo completo della tesi di dottorato, fatta salva la possibilità di sottoscrizione di apposite licenze per le relative condizioni di utilizzo (di cui al sito http://www.creativecommons.it/Licenze), e fatte salve, altresì, le eventuali esigenze di "embargo", legate a strette considerazioni sulla tutelabilità e sfruttamento industriale/commerciale dei contenuti della tesi, da rappresentarsi mediante compilazione e sottoscrizione del modulo in calce (Richiesta di embargo);
5) che la tesi da depositare in IRIS-POLIBA, in formato digitale (PDF/A) sarà del tutto identica a quelle **consegnate**/inviate/da inviarsi ai componenti della commissione per l'esame finale e a qualsiasi altra copia depositata presso gli Uffici del Politecnico di Bari in forma cartacea o digitale, ovvero a quella da discutere in sede di esame finale, a quella da depositare, a cura dell'Ateneo, presso le Biblioteche Nazionali Centrali di Roma e Firenze e presso tutti gli Uffici competenti per legge al momento del deposito stesso, e che di conseguenza va esclusa qualsiasi responsabilità del Politecnico di Bari per quanto riguarda eventuali errori, imprecisioni o omissioni nei contenuti della tesi;
6) che il contenuto e l'organizzazione della tesi è opera originale realizzata dal sottoscritto e non compromette in alcun modo i diritti di terzi, ivi compresi quelli relativi alla sicurezza dei dati personali; che pertanto il Politecnico di Bari ed i suoi funzionari sono in ogni caso esenti da responsabilità di qualsivoglia natura: civile, amministrativa e penale e saranno dal sottoscritto tenuti indenni da qualsiasi richiesta o rivendicazione da parte di terzi;
7) che il contenuto della tesi non infrange in alcun modo il diritto d'Autore né gli obblighi connessi alla salvaguardia di diritti morali od economici di altri autori o di altri aventi diritto, sia per testi, immagini, foto, tabelle, o altre parti di cui la tesi è composta.

Luogo e data: Bari, 09/01/2025 Firma _____

Firmato digitalmente da: Sciatti Francesco
Firmato il 2025/01/09 12:49
Seriale Certificato: 3721402
Valido dal 11/07/2024 al 11/07/2027
InfoCamere Qualified Electronic Signature CA

Il sottoscritto, con l'autoarchiviazione della propria tesi di dottorato nell'Archivio Istituzionale ad accesso aperto del Politecnico di Bari (POLIBA-IRIS), pur mantenendo su di essa tutti i diritti d'autore, morali ed economici, ai sensi della normativa vigente (Legge 633/1941 e ss.mm.ii.),

CONCEDE

- al Politecnico di Bari il permesso di trasferire l'opera su qualsiasi supporto e di convertirla in qualsiasi formato al fine di una corretta conservazione nel tempo. Il Politecnico di Bari garantisce che non verrà effettuata alcuna modifica al contenuto e alla struttura dell'opera.
- al Politecnico di Bari la possibilità di riprodurre l'opera in più di una copia per fini di sicurezza, back-up e conservazione.

Luogo e data: Bari, 09/01/2025 Firma _____

Firmato digitalmente da: Sciatti Francesco
Firmato il 2025/01/09 12:50
Seriale Certificato: 3721402
Valido dal 11/07/2024 al 11/07/2027
InfoCamere Qualified Electronic Signature CA

…To my mum and my fiancé…

I love you

Abstract

This PhD research project investigates the transformative potential of piezoelectric actuators in addressing the inherent limitations and problems of conventional hydraulic components, particularly focusing on valves and pumps.

Despite the great advantages it offers, such as high-power density, precise control and large force output, conventional hydraulic technology suffers from low energy efficiency due to substantial energy losses that occur as the pressurized oil flows through the hydraulic circuit and its components, particularly the control-ones. Conventional hydraulic technology typically utilizes analogue spool valves, such as proportional and servovalves, as control components in various industrial and aeronautical applications where high precision and fast response are required. However, the spool design of these valves leads to high power dissipation, caused by the significant pressure drop across the small narrow passages uncovered during valve control. Moreover, the actuation system's architecture introduces additional drawbacks, such as increased complexity and higher manufacturing costs, which remain still unresolved.

To explore these challenges, the research begins by developing comprehensive simulation models of aircraft fuel systems, specifically focusing on quantifying energy inefficiencies in servovalves within fuel metering units. Building on these insights, the first goal of the project is to design and model innovative spool valve architectures powered by piezoelectric actuators, replacing traditional electromagnetic actuators. By leveraging the fast response times and simplicity of piezoelectric materials, this approach aims to improve energy efficiency, reduce costs, and simplify the design of conventional spool valves.

The project also explores the potential of digital hydraulics, which aims to replace conventional proportional and servovalves in industrial and aeronautical applications with low-cost, robust on/off valves in order to minimize power dissipation. However, the practical implementation of digital hydraulics is currently limited by challenges in manufacturing on/off valves that meet strict requirements, such as high switching frequencies and speeds (below 5 ms), minimal pressure losses, and the ability to handle large flow rates in a compact form. Once again, piezoelectric actuators could provide a crucial solution to these challenges. Thus, the second goal of this research is to design and model innovative high-frequency switching on/off valve architectures, marking digital hydraulics as a promising technology for improving energy efficiency in various fluid power applications.

Lastly, this research addresses, as third goal, the growing demand for pumps in industries such as chemistry, biomedicine, aerospace, robotics, and liquid cooling. These fields require pumps that are compact, reliable, quiet, and capable of precise flow control—qualities that conventional hydraulic pumps often struggle to meet due to inherent structural limitations. Specifically, the research project explores the use over again of piezoelectric actuators to design, develop and testing innovative precision fluid pumps that can meet these stringent requirements, aiming to expand the power capabilities of this innovative technology.

Acknowledgments

First and foremost, I would like to express my heartfelt thanks to my supervisors, Prof. Riccardo Amirante and Prof. Paolo Tamburrano, for their invaluable guidance and support throughout this PhD journey. Your constant encouragement has been essential in helping me grow and expand my knowledge every step of the way.

A special thank you to my mum, Giulia, for her unwavering support and dedication, not only to my work but also for shaping me into the person I am today. To my brother Vittorio, I'm grateful for your constant motivation and for always being there whenever I needed you.

To my amazing girlfriend, thank you for your love, patience, and encouragement throughout this entire process, from the intense research phases to the final writing of this thesis. I am equally grateful to her family, who have embraced me as one of their own and made me feel like a son.

I would also like to thank Marsel, a true friend who has been a constant presence and source of support throughout these years, even from afar.

A special thanks to Lazzaro, Vincenzo, and Dr. Dan—one of the best colleagues I have had the privilege of working with during this incredible PhD journey.

Thanks to Roberto, Vincenzo and Dario, my friends from padel, who made stressful days easier with their silly but uplifting messages.

Finally, I want to remember my grandfather and grandmother, who taught me the true values of life and have always inspired me.

This achievement wouldn't have been possible without all of you. Thank you!

Table of Contents

List of Figures – Page

Chapter 1

Chapter 2

Chapter 3

Chapter 4

Chapter 5

List of Tables – Page

Chapter 1

Chapter 2

Chapter 3

Chapter 4

Chapter 5

Chapter 6

Chapter 7

Nomenclature

Chapter 1

$Q_{1,L}$	Internal Leakage Main Stage
$Q_{2,L}$	Internal Leakage Pilot Stage
x	Sliding Spool Displacement
Δp	Pressure Drop Main Stage

Chapter 2

$(\%DC)$	DCS Duty Cycle
f	DCS Frequency
F_{act}	PEA Actuation Force
F_b	PEA Blocking Force
F_b	PEA Max. Blocking Force
h_{apa}	APA Deformation Short Axis
k_p	PEA Stiffness
K_{VF}	Conversion Coefficient
l_p	APA Deformation Main Axis
Q_M	HFSV Average Flow Rate
t_{OFF}	DCS Pause Time
t_{ON}	DCS Pulse Duration
V_{amp}	Amplified Voltage
x	PEA displacement
x_{max}	PEA Free Stroke
τ	DCS Overall Period

Chapter 3

A_A	Piston Lateral Area IGV Actuator
A_b	Spool Area Bypass Valve
A_{pr}	Piston Area Pressurizing Valve
$A_{r,fn}$	Restriction Area Fuel Nozzles
$A_{l,s_{IGV/FM}}$	Spool Leakage Area (IGV – FM Servovalve)
$A_{r,s_{IGV/FM}}$	Metering Chamber Restriction Area (IGV – FM Servovalve)
$A_{r,sh}$	Restriction Area Engine Shut-off Valve
$A_{s,IGV/FM}$	Spool Lateral Area (IGV – FM Servovalve)
$b_{IGV/FM}$	Overall Slot Width (IGV – FM Servovalve)
c_{IGV}	Spool Radial Clearance (IGV Servovalve)
C_A	Piston Damping Factor IGV Actuator
C_r	Damping Factor IGVs Actuation Mechanism

C_{pr}	Spool Damping Factor Pressurizing Valve
$C_{D,b}$	Discharge Coefficient Bypass Valve
$C_{IGV/FM}$	Spool Damping Factor (IGV – FM Servovalve)
$C_{D_{fn}}$	Discharge Coefficient Fuel Nozzles
$C_{D_{IGV/FM}}$	Discharge Coefficient (IGV – FM Servovalve)
$C_{D_{pr}}$	Discharge Coefficient Pressurizing Valve
$C_{D_{sh}}$	Discharge Coefficient Engine Shut-off Valve
$d_{n,IGV/FM}$	Nozzle Diameter (IGV – FM Servovalve)
$d_{o,IGV/FM}$	Fixed Orifice Diameter (IGV – FM Servovalve)
D_e	Cylinder Diameter IGV Actuator
D_i	Piston Rod Diameter IGV Actuator
$D_{IGV/FM}$	Spool Diameter (IGV – FM Servovalve)
e_{IGVFM}	PI Controller Error (IGV – FM Servovalve)
$F_{f,IGV/FM}$	Flow Force (IGV – FM Servovalve)
$G(s)_{IGV/FM}$	Pilot Stage Second Order Transfer Function (IGV – FM Servovalve)
k_b	Spring Stiffness Bypass Valve
k_{pr}	Spring Stiffness Pressurizing Valve
$K_{1,IGV/FM}$	Moog Conversion Factor (IGV – FM Servovalve)
$K_{f,IGV/FM}$	Flapper Stiffness (IGV – FM Servovalve)
$K_{I,IGV/FM}$	PI Controller Integral Gain (IGV – FM Servovalve)
$K_{p,IGV/FM}$	PI Controller Proportional Gain (IGV – FM Servovalve)
$i_{IGV/FM}$	Pilot Stage Input Current (IGV – FM Servovavle)
$l_{IGV/FM}$	Spool Length (IGV - FM Servovalve)
m_A	Piston Mass IGV Actuator
m_r	IGVs Actuation Mechanism Mass
m_{pr}	Spool Mass Pressurizing Valve
$M_{IGV/FM}$	Spool Mass (IGV – FM Servovalve)
$p_1 - p_2$	Piston Delta Pressure IGV Actuator
p_{cc}	Combustion Chamber Pressure
p_d	Boost Pressure (Pressure at the inlet of Main Fuel Pump)
p_{fn}	Pressure at the Outlet Fuel Nozzles
$p_{l,IGV/FM}$	Left Spool Pressure (IGV – FM Servovalve)
p_{max}	System Maximum Pressure
p_p	Pressure at the outlet of Main Fuel Pump
p_{pr}	Metered Pressure (Pressure at the outlet Pressurizing Valve)
$p_{r,IGV/FM}$	Right Spool Pressure (IGV – FM Servovalve)
p_{se}	Main Metered Fuel Pressure (Pressure at the outlet of FM Servovalve)
$p_{se,crack}$	Cracking Pressure Pressurizing Valve

$p_{se,lin}$	Linear Trend Pressure Pressurizing Valve
p_{sh}	Pressure at the Outlet Engine Shut-off Valve
P_a	Power Absorbed Main Fuel Pump
$P_{d,b}$	Power Dissipated Bypass Valve
$P_{d,IGV/FM}$	Power Dissipated (IGV – FM Servovalve)
$P_{d,pr}$	Power Dissipated Pressurizing Valve
$q_{n,l\ IGV/FM}$	Left Nozzle Flow Rate (IGV – FM Servovalve)
$q_{n,r\ IGV/FM}$	Right Nozzle Flow Rate (IGV – FM Servovalve)
$q_{o,l\ IGV/FM}$	Left Fixed Orifice Flow Rate (IGV – FM Servovalve)
$q_{o,r\ IGV/FM}$	Right Fixed Orifice Flow Rate (IGV – FM Servovalve)
$q_{s,l_{IGV/FM}}$	Left Spool Flow (IGV – FM Servovalve)
$q_{r,l_{IGV/FM}}$	Right Spool Flow (IGV – FM Servovalve)
Q_b	Flow Rate Bypass Valve
Q_{fn}	Flow Rate Fuel Nozzles
$Q_{IGV/FM}$	Flow Rate (IGV – FM Servovalve)
Q_p	Flow Rate Main Fuel Pump
Q_{pr}	Flow Rate Pressurizing Valve
Q_{sh}	Flow Rate Engine Shut-off Valve
$T_{q\ IGV/FM}$	Pilot Stage Torque (IGV – FM Servovalve)
w_b	Slot Width Bypass Valve
w_p	Piston Velocity IGV Actuator
w_{pr}	Slot Width Pressurizing Valve
$x_{IGV/FM}$	Flapper – Nozzles Clearance (IGV – FM Servovalve)
$x_{0,b}$	Spring Preload Bypass Valve
$x_{0,pr}$	Spring Preload Pressurizing Valve
x_b	Spring Deformation Bypass Valve
x_{pr}	Spring Deformation Pressurizing Valve
$x_{f\ IGV/FM}$	Flapper Displacement (IGV – FM Servovalve)
$X_{IGV/FM}$	Spool Displacement (IGV – FM Servovalve)
X_A	Piston Position IGV Actuator
$\varepsilon_{IGV/FM}$	Spool Radial Eccentricity (IGV – FM Servovalve)
η_p	Main Fuel Pump Efficiency
Δp	Pressure Drop IGV Servovalve
ρ	Jet Fuel Density
μ	Jet Fuel Viscosity
$\theta_{IGV/FM}$	Flow Angle (IGV – FM Servovalve)
$\xi_{IGV/FM}$	Pilot Stage Damping Ratio (IGV – FM Servovalve)
$\omega_{n,IGV/FM}$	Pilot Stage Natural Frequency (IGV – FM Servovalve)

A_r	Metering Chamber Restriction Area
c	Poppets' Radial Clearance
C_{ap}	Ring Stack Actuator Capacitance
C	Poppet Damping Factor
C_D	Discharge Coefficient
C_{stop}	Stop Damping Coefficient
d	Ring Stack Actuator Inner Diameter
D	Ring Stack Actuator Outer Diameter
D_p	Poppets' Diameter
DC	Command Signal Duty Cycle
$e(t)$	PI Controller Error
E	Actual Bulk Modulus
E_0	Pure Liquid Bulk Modulus
f	Command Signal Switching Frequency
F_{act}	Ring Stack Actuator Actuation Force
F_b	Ring Stack Actuator Blocking Force
$F_{b,max}$	Ring Stack Actuator Max. Blocking Force
F_c	Viscous Force
F_{flow}	Flow Forces
F_i	Inertia Force
F_s	Additional Spring Force
F_{stop}	Stop Poppets' Force
$G(s)$	Amplifier Second Order Transfer Function
H	Ring Stack Actuator Height
i	Current provided to Ring Stack Actuator
i_M	Average Current provided to Ring Stack Actuator
k_a	Amplifier Gain
k_p	Ring Stack Actuator Stiffness
k_s	Additional Spring Stiffness
K_b	Hysteresis Correction Factor
K_I	PI Controller Integral Gain
K_P	PI Controller Proportional Gain
K_{stop}	Stop Spring Stiffness
K_{VF}	Conversion Factor
I_{max}	Amplifier Maximum Current
l_p	Poppets' Length
L_0	Chamber Internal Length
m	Moving Parts Mass

n	Hysteresis non-linear term
p	Chamber Pressure
p_a	Atmospheric Pressure
p_p	Supply Pressure
p_t	Discharge Pressure
$P_{d,v}$	Ideal Power Average Loss
q_c	Chamber Flow Rate
Q	Valve Flow Rate
Q_M	Valve Average Flow Rate
T	Oil Temperature
V_0	Chamber Geometrical Volume
V_{amp}	Amplified Voltage
V_c	Control Voltage
V_{cham}	Chamber Volume Variation
V_{max}	Ring Stack Actuator Max. Operating Voltage
x_{max}	Ring Stack Actuator Max. Free Stroke
x	Ring Stack Actuator Displacement – Poppets' Position
α	Hysteresis Parameter
β	Hysteresis Parameter
δ	Hysteresis Parameter
δ_0	Additional Spring Pre-compression
Δp	Pressure Drop across the Valve
ε	Poppets' Radial Eccentricity
ω_n	Amplifier Natural Frequency
ξ	Amplifier Damping Ratio
ρ	Oil Density
ϑ	Velocity Angle
τ	Command Signal Overall Period
μ	Oil viscosity
σ	Relative Gas Content at Atmospheric Pressure
γ	Gas-Specific Heat Ratio

Chapter 5

$A_{r,s}$	Spool Metering Chamber Restriction Area
$A_{l,s}$	Spool Leakage Area
b	Overall Slot Width
c	Spool Radial Clearance
C_{ap}	APA Capacitance
C_p	APA Damping Factor

C_s	Spool Damping Factor
C_D	Discharge Coefficient
D_s	Spool Diameter
$e(t)$	PI Controller Error
F_{act}	APA Actuation Force
$F_{act,max}$	APA Max. Actuation Force
F_b	APA Blocking Force
$F_{b,max}$	APA Max. Blocking Force
F_f	Flow Forces
$G(s)$	Amplifier Second Order Transfer Function
h_{APA}	APA Height
H	Ring Stack Actuator Height
K_a	Amplifier Gain
k_p	APA Stiffness
K_b	Hysteresis Correction Factor
K_I	PI Controller Integral Gain
K_P	PI Controller Proportional Gain
K_{VF}	Conversion Factor
I_{max}	Amplifier Maximum Current
l_{APA}	APA Length
l_s	Spool Length
m_p	APA Moving Mass
$2m_p$	APA Overall Mass
m_s	Spool Mass
n	Hysteresis non-linear term
p_p	Supply Pressure
p_t	Discharge Pressure
Q	Valve Flow Rate
T	Oil Temperature
V_0	Chamber Geometrical Volume
V_{amp}	Amplified Voltage
V_c	Control Voltage
w_{APA}	APA Width
x_{max}	APA Max. Free Stroke
x_{in}	Sine Wave Input Amplitude (Set Point)
x_{out}	Sine Wave Output Amplitude (Spool Position)
x	APA Displacement – Spool Position
α	Hysteresis Parameter
β	Hysteresis Parameter
δ	Hysteresis Parameter

Δp	Pressure Drop across the Valve
ε	Spool Radial Eccentricity
$\omega_{n,a}$	Amplifier Natural Frequency
ξ_a	Amplifier Damping Ratio
ρ	Oil Density
ϑ	Velocity Angle
μ	Oil viscosity

Chapter 6

Single Cylinder Piezohydraulic Pump

A_{ch}	Pumping Chamber Area
A_p	Piston Area
A_{Valve}	Valve Face Area
a_{valve}	Valve Opening Area
B	Bulk Modulus
c_{free}	Valve Damping
c_{end}	End Stop Damping
C_f	Valve Force Coefficient
C_d	Valve Discharge Coefficient
D_{ch}	Pumping Chamber Diameter
$d_{in,BW}$	Belleville Washers Inner Diameter
$d_{in,Valve}$	Valve Inner Diameter
d_p	Piston Diameter
$d_{out,BW}$	Belleville Washers Outer Diameter
$d_{out,Valve}$	Valve Outer Diameter
d_{Valve}	Geometric Valve Diameter
E	Pumping Chamber Young Modulus
E_{Valve}	Valve Young Modulus
F	Ring StackActuation Force
f	Pump Driving Frequency
F_{pre}	Valve Preload Force
$F_{b,max}$	Ring Stack Max. Blocking Force
$F_{pressure}$	Pumping Chamber Force
F_{Valve}	Valve Force
k_{BW}	Belleville Washers Stiffness
k_{end}	End Stop Stiffness
k_{piezo}	Ring Stack Stiffness
k_{spring}	Valve Stiffness
$k(T)$	Heat Transfer Coefficient

k_1	Timoshenko Coefficient
K_{fluid}	Fluid Stiffness
$K_{p,ax}$	Pump Axial Stiffness
$K_{p,ra}$	Pump Radial Stiffness
K_{pump}	Overall Pump Stiffness
K_{VF}	Conversion Factor
L	Pumping Chamber Height
l_{fluid}	Fluid Characteristic Length
M	Total Moving Mass
m_{fluid}	Fluid "Added Mass"
m_{Valve}	Valve Mass
n	Hysteresis non-linear term
p_{bias}	Upstream Inlet Reed Valve Pressure
p_{ch}	Pumping Chamber Pressure
P_{Do}	Valve Downstream Pressure
p_{Target}	Pump Pressure Target
P_{Target}	Pump Power Target
P_{Up}	Valve Upstream Pressure
Q	Valve Flow Rate
Q_0	Orifice Flow Rate
Q_{in}	Inlet Flow Pumping Chamber
Q_{out}	Out Flow Pumping Chamber
Q_{Target}	Pump Flow Rate Target
t_{BW}	Belleville Washers Thickness
t_{Valve}	Valve Thickness
t_{Wall}	Pumping Chamber Wall Thickness
T_0	Ring Stack Initial Temperature
T_{st}	Ring Stack Temperature
V_0	Chamber Geometrical Volume
V_{eff}	Effective Driving Voltage
V_{st}	Ring Stack Volume
W_T	Heat Power
x_{max}	Ring Stack Free Stroke
x_{Valve}	Valve Position
x_{Valve}^T	Valve Tip Displacement
x	Ring Stack Displacement
x_V	Input Voltage
z_V	Output Voltage Loss
α	Hysteresis Parameter

β	Hysteresis Parameter
δ	Hysteresis Parameter
ΔT	Maximum Temperature Increase
ΔV_{ch}	Pumping Chamber Volume Variation
ξ	Valve Damping Ratio
ρ_{st}	Ring Stack Density
ρ_{fluid}	Fluid Density
ρ_{Valve}	Valve Density
τ	Pump Time Operation Limit

Multi-Cylinder Piezohydraulic Pump

A_p	Piston Area
F	Ring StackActuation Force
i	Specific Cylinder
k	Proportionality Factor
k_{piezo}	Ring Stack Stiffness
p_{cy}	Cylinder Pressure
p_{OUT}	Outlet Pressure
Q_i	Flow Rate from a Specific Cylinder
Q_{TOT}	Total Flow Rate Multi-Cylinder Piezohydraulic Pump
x_{max}	Ring Stack Free Stoke
x	Ring Stack Displacement
X_f	Peak Free Displacement
z	Number of Cylinder
ω	Sinusoidal Command Signal Angular Frequency

Chapter 7

p_{cham}	Pumping Chamber Pressure
p_{in}	Fixed Inlet Pressure (Upstream Inlet Reed Valve)
v_{opn}	Inlet Reed Valve Opening Degree

Abbreviations

ABS	Antilock Braking Systems
APA	Amplified Piezo Stack Actuator
CFD	Computational Fluid Dynamics
DCS	Digital Command Signal
DCV	Discrete Control Voltage
DFCU	Digital Flow Control Unit
DFM	Duty Cycle Frequency Method
DHBC	Digital Hydraulic Buck Converter
DHHA	Digital Hydraulic Hybrid Actuator
DHPMS	Digital Hydraulic Power Management System
DMFC	Direct Methanol Fuel Cell
ECS	Engine Control System
FADEC	Full Authority Digital Electronic Control
FFA	Federal Aviation Administration
FM	Fuel Metering
FMU	Fuel Metering Unit
FN	Fibonacci Number
HFSV	High Frequency Switching Digital Hydraulic Valve
IGV	Inlet Guide Vane
invPFM	Inverted Pulse Frequency Modulation
ISA	Induced Strain Actuator
ISO	International Organization for Standardization
LFM	Linear Force Motor
LP	Low Pressure
HP	High Pressure
LVDT	Linear Variable Differential Transformer
MEMS	Micro-Electro-Mechanical System
PCM	Pulse Code Modulation
PEA	Piezoelectric Actuator
PEMFC	Proton Exchange Membrane Fuel Cell
PFM	Pulse Frequency Modulation
PI	Proportional Integral
PNM	Pulse Number Modulation
PWM	Pulse Width Modulation

COPYRIGHT

1. INTRODUCTION

This chapter provides an overview of the research project, beginning with the significant role of aviation and its environmental challenges in contemporary society. It then introduces conventional hydraulic technology and fluid precision pumps. The chapter outlines the motivation behind the research, defines its aims and objectives, emphasizes the original contributions made, and concludes with an overview of the thesis structure.

The state-of-the-art review of conventional hydraulic technology formed a significant part of this research project and was published in two high-impact review papers in well-regarded journals [1], [2].

1.1 Aviation Environmental Challenges

Aviation plays a crucial role in modern life, connecting people, businesses, and families worldwide while boosting economic growth. In 2016 alone, the aviation sector generated $2.7 trillion in economic activity and supported 65.5 million jobs, representing 3.6% of global gross domestic product (GDP) [3]. Despite these benefits, conventional aircraft propulsion systems, which depend on fossil kerosene-based fuels (jet fuels), significantly contribute to global warming [4]. The combustion of these fuels releases large amounts of carbon emissions into the atmosphere daily. This problem has been exacerbated by the rapid growth of air travel in recent years, leading to annual carbon dioxide (CO_2) emissions exceeding 900 million tons [5]. In addition to CO_2, the aviation industry is also responsible for non-CO_2 emissions, including nitrogen oxides (NO_x), sulphur oxides (SO_x), hydrocarbons (HC), black carbon (soot), and water vapor (H_2O) [6]. These pollutants have severe consequences for the environment, contributing to the formation of contrails and cirrus clouds [7], [8], and for human health, leading to both physical and mental issues, particularly in children [9].

To preserve the benefits of aviation while addressing these environmental challenges, it is crucial to consider alternative energy sources, such as electric energy, hydrogen, and fuel cells or reduce fuel consumption [10]. Therefore, improving the performance of key components that regulate fuel flow to the combustion chamber of conventional gas turbine engines offers a potential and promising solution.

In a conventional aircraft fuel system, several components work together, including fuel tanks, fuel lines, centrifugal boost pumps, filters, main fuel pumps, fuel metering units (FMUs), and fuel injector nozzles. Among these, the FMU plays a crucial role by managing the fuel flow to the combustion chamber through conventional servovalves. However, the architecture of these control systems has remained largely unchanged for the past 50 years, presenting several unresolved drawbacks.

1.2 Conventional hydraulic technology

Fluid power is a technology based on the use of pressurized fluids, including liquids (hydraulics) or gases (pneumatics) to generate, control, and transmit power. The basics of modern fluid power

systems date back approximately 350 years ago to the discoveries of Blaise Pascal (Pascal's Law) and Daniel Bernoulli (Bernoulli's Principle) [11]. These studies enabled Joseph Bramah, an English inventor and locksmith who is considered the grandfather of modern hydraulic technology, to patent the first hydraulically operated machine, "The Hydraulic Press," in 1795 [12]. With the advent of the Industrial Revolution, hydraulic technology experienced a strong growth thanks to the development of several hydraulic components, which led to modern hydraulic technology [13]. Fig. 1 shows the hydraulic schematic of a conventional hydraulic system with valve control, where the hydraulic components needed to realize an exemplary hydraulic circuit are represented using ISO (International Organization for Standardization) symbols [2].

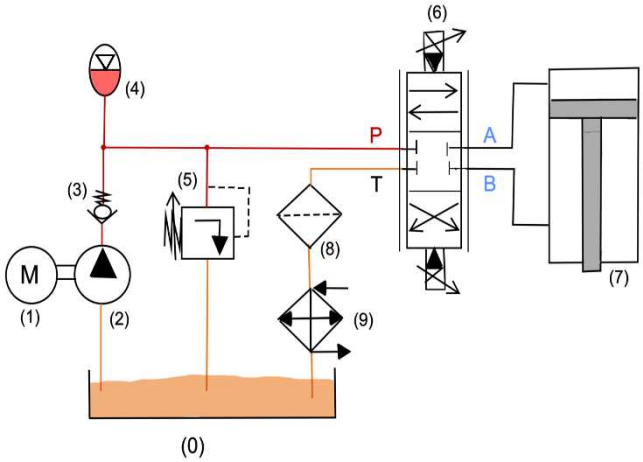

Fig. 1. Conventional hydraulic circuit: (**1**) Prime Mover; (**2**) Hydrostatic Pump; (**3**) Check Valve; (**4**) Accumulator; (**5**) Pressure Relief Valve; (**6**) Electrohydraulic Servovalve; (**7**) Linear Actuator; (**8**) Filter; (**9**) Heat Exchanger.

Over the past few decades, engineers and researchers worldwide have faced the main challenge of realizing progressively efficient hydraulic components. Of all the hydraulic components, the control-ones are the most critical since they have a great impact on the overall energy efficiency of hydraulic systems. Control valves play an important role in hydraulic systems as they manage hydraulic power by regulating the mechanical power transmitted to an actuator. This control can be obtained by managing pressure (using pressure control valves), controlling flow rate (with flow control valves), or directing flow (via directional control valves) [14]. The latter are available with different performance and characteristics depending on the application. In most cases, the higher the performance, the higher the cost of the valves.

Conventional hydraulic systems typically use analogue spool valves, such as proportional and servovalves (both direct drive and two-stage types), as directional control valves in a variety of industrial and aeronautical applications that require high precision and fast response [15]. These valves, indeed, unlike on/off valves, allow for precise control of an actuator position and/or velocity without causing rapid acceleration or deceleration. Therefore, the flow of pressurized fluid delivered to an actuator, and consequently its position and velocity, can be easily controlled based on the input electrical signal to the valve [16].

Proportional valves are generally a single-stage configuration, in which a sliding spool is centered by means of two springs within the valve body and is directly moved by two proportional solenoids positioned on opposite sides of the valve [17]. The sliding spool is designed with notches and grooves to control the flow rate based on its position [18]. These valves typically have a "dead band," caused by spool overlap, which can account for 10% or more of the spool's total stroke [17].

Fig. 2 shows the typical architecture of one of the most commonly used valve types, a four-way three-position (4/3) proportional valve, as produced by Atos [17], along with its ISO symbol.

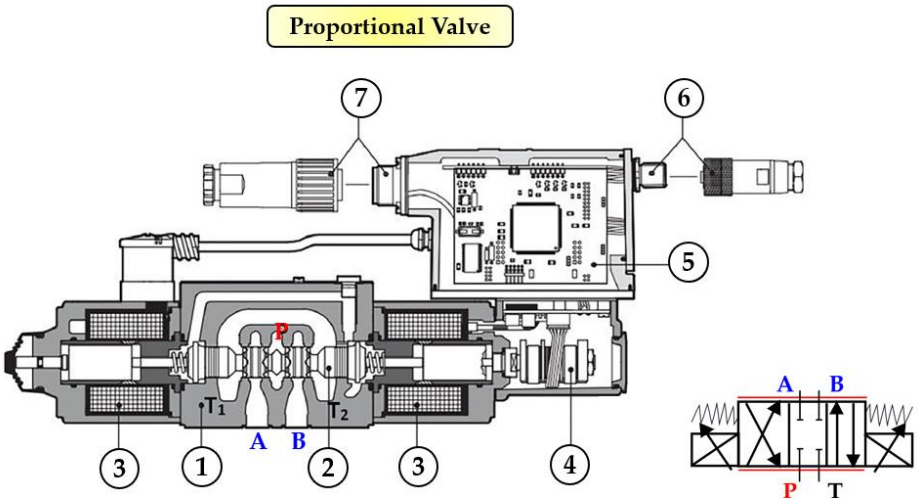

Fig. 2. ATOS-DKZOR-T four-way three-position (4/3) Proportional Valve: (**1)** Valve Body; (**2)** Sliding Spool; (**3**) Solenoid; (**4**) Linear Variable Differential Transformer (LVDT); (**5**) Electronic Control; (**6**) and (**7**) Connectors.

In this configuration, the sliding spool is moved directly by either the right or left solenoid, depending on the desired hydraulic flow paths (P-A and B-T, or P-B and A-T). Oil enters the valve through the high-pressure port (P) and flows through the metering section (P-A or P-B), where the flow rate is regulated by the spool's notches and the degree of opening, before exiting toward the actuator. Afterward, the oil discharged from the actuator flows back into the valve through the metering sections (A-T_1 or B-T_2). Ports T_1 and T_2 are internally connected so as to form a single discharge port T.

Proportional valves can operate in either an open-loop or a closed-loop configuration. In closed-loop systems, a position sensor (typically a Linear Variable Differential Transformer (LVDT)) is used for more precise control of the sliding spool position [19]. In both configurations, standard commercial electronic cards provide the solenoids with a Pulse Width Modulation (PWM) signal, with a frequency usually ranging from 200 to 20,000 Hz. By adjusting the duty cycle of the PWM signal, the current flowing through the solenoids can be varied, which in turn changes the electromagnetic force generated, the valve's opening degree, and the flow rate provided. Additionally, a dither signal, which can be a square or sinusoidal wave with a frequency lower than that of the PWM signal, is often employed to keep the spool vibrating. This vibration helps overcome any stiction between the spool and the valve body bore [20].

One key limitation of proportional valves is due to the direct actuation by solenoids, which are relatively heavy and often operate in only one direction [17]. Additionally, at high pressures or flow rates, the actuation force from solenoids may not be strong enough to counterbalance flow and spring forces, limiting the valve's maximum flow rate. Most proportional valves achieve a maximum flow rate of around 100 L/min, though some can exceed 150 L/min at low pressure drops [17]. For example, the ATOS DKZOR-AES proportional valve can handle up to 160 L/min, but only with a pressure drop limited to 70 bar. As the pressure increases, the maximum flow rate decreases, and at 210 bar, it is reduced to about 90 L/min. This limitation occurs because the solenoids' power is insufficient to fully open the valve at high pressure, restricting the sliding spool stroke [17].

In terms of dynamic characteristics, proportional valves are only minimally affected by operating pressure. This kind of analogue spool valves typically exhibit a −90° phase lag frequency ranging from 10 Hz to 70 Hz [17], [21]. The higher frequency values are usually achieved with smaller valves or those incorporating closed-loop control systems.

As a result, proportional valves are mostly used in industrial and transportation applications rather than aerospace, where faster response times and greater actuation forces are required.

Electrohydraulic servovalves, instead, are mainly classified in two main types. The direct drive type, in which the sliding spool is directly controlled by integrated electronics using a Linear Force Motor (LFM), and the two-stage type, in which the sliding spool is housed in the main stage and is controlled indirectly by the electronics through the pilot stage [21]. Concerning the latter, there are three main types depending on the architecture of the pilot stage: the double nozzle-flapper, the deflector jet, and the jet pipe.

Fig. 3 illustrates the architecture of a four-way three-position (4/3) double nozzle-flapper servovalve, showing the sliding spool both in the neutral position (x=0) and in motion (x>0), along with its ISO symbol. It is important to note that in Fig. 3 "x" represents the sliding spool displacement. The pilot stage is equipped with a torque motor consisting of permanent magnets, pole pieces, and an armature. A flexure tube is used to support the flapper while separating the torque motor from the hydraulic fluid. A feedback spring connects the sliding spool with the flapper to achieve mechanical feedback (electrical feedback in two-stage servovalves is also possible using a position transducer (LVDT)). It is important to note that, electrical feedback is better suited for aerospace applications, where weight and reliability are crucial, while mechanical feedback is preferred in industrial settings, where valves need to be more cost-effective and require low maintenance [1].

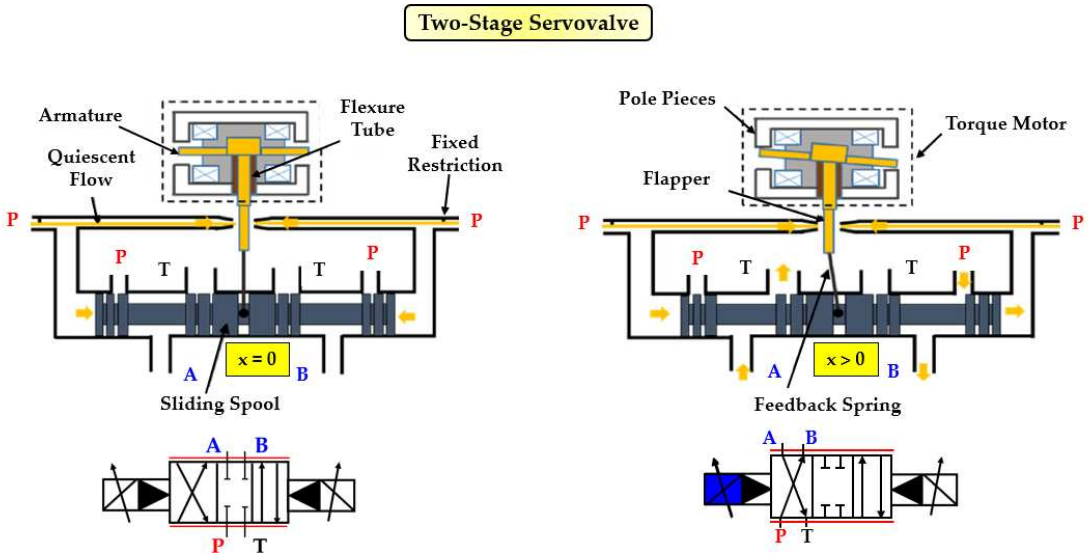

Fig. 3. Four-way three position (4/3) two-stage servovalve (double nozzle-flapper).

When the coil is energized, a proportional torque is generated on the flapper, which is deflected according to the direction and intensity of the applied current (usually less than 0.05 A [22]). The deflection of the flapper partially restricts the pilot oil flowing out of one of the nozzles, creating a pressure difference on the lateral faces of the spool, which is forced to move, bending the feedback spring. The sliding spool stops in a final position determined by the equilibrium of the forces acting on the spool (actuation force = flow force + feedback spring force) [21]. The electrical input power has an order of magnitude of 0.1 W, which is amplified to at least 10 W of hydraulic power in the pilot stage and is then converted by the sliding spool to control around 10 kW of hydraulic output power. Therefore, the valve power amplification factor is 10^5 [22].

This hydraulic amplification enables two-stage servovalves to generate large actuation forces, improving response speed. This large actuation force, known as chip shear force, is crucial in preventing the spool from jamming due to particle contamination. If a particle gets stuck between the metering edges, the high actuation force can shear it off, making these servovalves ideal for aerospace applications where valve failure must be avoided [22]. Specifically, two-stage servovalves are essential components in FMUs of conventional aircraft fuel systems, as they control the fuel flow to the combustor and adjust the angle position of Inlet Guide Vanes (IGVs) to regulate airflow into the compressor, optimizing engine performance [23], [24], [25].

Table 1 summarizes key characteristics of a commercially available two-stage double nozzle-flapper servovalve with mechanical feedback from Moog [21]. This type of valve is divided into 5 series based on size, with weight increasing alongside size; the maximum weight remains around 1 kg, making these valves compact and lightweight compared to proportional valves. The actuation force also increases with size due to larger sliding spool diameters, reaching up to an actuation force of 700 N. Internal leakage, caused by the quiescent flow needed in the pilot stage even when the sliding spool is in the neutral position, ranges from (0.35 to 0.75) L/min depending on the valve size. Response times also vary, taking between 2.5 ms and 12 ms to reach 90% of the valve opening.

Table 1. Characteristics of Moog type 30 double nozzle-flapper valve [21].

	Valve Weight [kg]	Max Flow at 210 bar [L/min]	Actuation Force at 210 bar [N]	Response Time at 210 bar [ms] (to reach 90% of the Opening)	Internal Leakage at 210 bar [L/min]
Series 30	0.19	12	245	2.5	< 0.35
Series 31	0.37	26	245	2.5	< 0.45
Series 32	0.37	54	490	4.5	< 0.50
Series 34	0.50	73	620	7	< 0.60
Series 35	0.97	170	710	12	< 0.75

With regard to the dynamic characteristics, Fig. 4 presents the frequency response Bode plots of the same two-stage servovalves, measured at a supply pressure of 210 bar and 50% of the maximum input current amplitude. The graphs show that under these operating conditions, the −90° phase lag frequency ranges from approximately 90 Hz to 250 Hz, with the highest values observed in the smaller valve sizes [21].

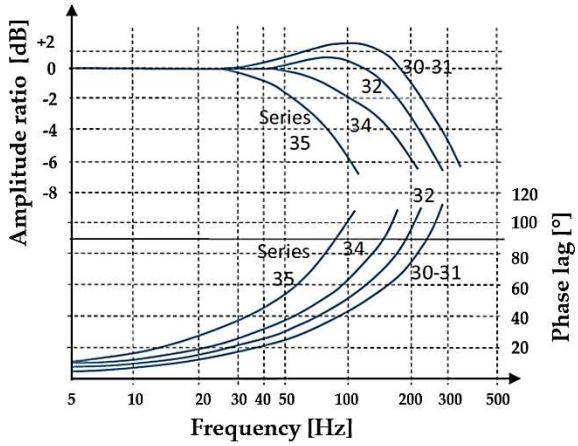

Fig. 4. Bode plot for type 30 Moog double nozzle-flapper servovalves for supply pressure of 210 bar and 50% of the maximum input amplitude [21].

In addition to two-stage servovalves, manufacturers also produce direct drive servovalves, which are actuated using LFMs. In these systems, direct current flows through a coil, interacting with a magnetic field created by rare earth magnets. Compared to proportional solenoids, LFMs offer several advantages, such as reduced moving mass, greater driving force, and improved linearity. These features lead to better performance, particularly in terms of response speed and chip shear force. The maximum force generated by a LFM can reach around 200 N [21].

Fig. 5 shows a direct drive servovalve, specifically the Moog D633 model, along with its ISO symbol [21]. This valve delivers a maximum flow rate of approximately 70 L/min at 350 bar. It achieves full stroke (0 to 100%) in around 15 ms. The valve's maximum power consumption is about 28.8 W, operating at 1.2 A and 24 V (DC), and it weighs 2.5 kg [21].

A direct drive architecture has the disadvantage of having lower actuation forces than two-stage servovalves; hence, it has lower chip shear capability and a lower response speed. Consequently, it is less convenient for some applications, such as aircraft, where the actuation forces and weight are important factors. Instead, for those industrial applications where these

factors are less important, a direct drive servovalve is an interesting architecture, especially in terms of simplicity of construction, in contrast to the complexity of pilot stages, which have many finely toleranced parts, some of them needing to be assembled manually [21].

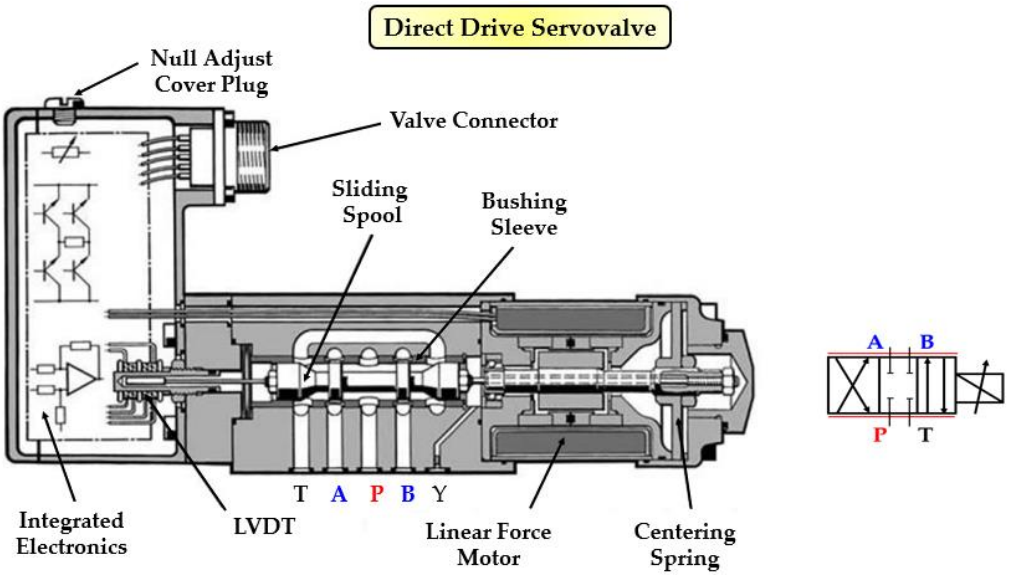

Fig. 5. Moog D633 four-way three-position (4/3) direct drive servovalve.

Servovalves, both direct drive and two-stage types, respond faster than proportional valves due to their small spool overlaps, high actuation forces, and the absence of heavy moving parts [17], [21]. Servovalve sliding spools are precision-made and paired with bushing sleeves to achieve minimal overlaps (often 1% of the spool stroke or less [26]). Unlike proportional valves, where the spool typically slides directly inside a cast iron valve housing, servovalve sliding spools are matched individually to their bushing sleeves (as shown in Fig. 6 [21]). Additionally, servovalve sliding spools usually lack grooves or notches; instead, rectangular slots or annular grooves are cut directly into the bushing sleeves to control the flow [21].

Fig. 6. Example of sliding spool and bushing sleeve for servovalves [21].

A detailed performance comparison of the conventional four-way three-position (4/3) spool valves discussed earlier can be found in Table 2 [22]. It is evident that two-stage servovalves stand

out for their exceptional performance characteristics, which include high-actuation forces [21], excellent accuracy [27], precise controllability [28], rapid response times [29], high-bandwidth and low weight [21]. However, it is important to note that a faster valve is not always a benefit, it depends on the hydraulic circuit and its use cases.

Table 2. Typical performance of conventional analogue (4/3) spool valves, operating at 40 L/min with 70 bar pressure drop [22].

	Open-Loop Proportional Valve	**Position Controlled Proportional Valve**	**Direct Drive Servovalve**	**Two-Stage Servovalve (Mechanical Feedback)**	**Two-Stage Servovalve (Electrical Feedback)**
Actuation Force	< 50 [N]	~ 50 [N]	~ 200 [N]	~ 500 [N]	~ 500 [N]
Step Response (100%)	100 [ms]	50 [ms]	15 [ms]	10 [ms]	3 [ms]
– 90° phase lag frequency	5 [Hz]	10 [Hz]	50 [Hz]	100 [Hz]	200 [Hz]
Cost	very low	low	medium	high	very high
Size	large	very large	very large	small	medium

1.3 Precision Fluid Pumps

Conventional hydraulic pumps, both dynamic pumps and positive displacement pumps, are machines designed to boost the energy of liquid as it flows through them. Specifically, these devices convert the mechanical energy from a prime mover, such as an electric motor, into hydraulic fluid power [30]. The most commonly used types are centrifugal pumps for their high flow rates and gear pumps for their ability to generate high pressure (large head) [31]. While the design and manufacturing processes for conventional hydraulic pumps are well-established, advancements in fields like chemistry, biomedicine, aerospace, robotics, and liquid cooling have increased the demand for pumps that are more reliable, compact, simple in design, capable of precise flow control, and operate quietly. Conventional hydraulic pumps struggle to meet these demands due to inherent structural limitations [32], [33], [34], [35].

In particular, in fields like chemistry and biomedicine, including applications such as micro-injection, disease detection, and analysis, pumps are required to have excellent controllability, biocompatibility, and precise regulation of flow rate and pressure, while remaining unaffected by external environmental factors. The typical flow rate range for these pumps is 10 μL/min to 10 mL/min, with pressure ranges from 0.02 bar to 0.1 bar, and a resolution in the μL range [36].

On the other hands, in applications, such as fuel supply systems for aerospace vehicles and automobile engines, large-load electronic chip cooling systems, and precision driving systems, the required flow rate is generally 10 mL/min to 1000 mL/min, with pressure ranges from 0.1 bar to 10 bar, and resolution in the mL range [36].

As a result, precision fluid pumps have become a fundamental and critical technology that requires further research to meet the growing demands in these fields.

1.4 Motivation

The architectures of conventional analogue spool valves have not substantially changed for many years, therefore there are a few drawbacks that are still unsolved. Two-stage servovalves, for example, are often criticized for their susceptibility to contamination in the pilot stage, which can lead to premature wear. Additionally, the torque motor, a key component that includes delicate mechanical and electrical parts, such as the flexure tube, requires precise manufacturing to ensure the necessary stiffness, adding to its complexity and cost. Research has also shown that the pilot stages of two-stage servovalves are prone to severe cavitation [21].

Direct drive servovalves face different challenges, mainly due to their high weight and large size, which result from the use of large LFMs needed to directly move the sliding spool.

In addition to these issues, conventional analogue spool valves, both proportional and servovalves, are associated with significant energy losses, primarily caused by two factors:

1. The internal leakage ($Q_{1,L}$) that occurs in the main stage due to necessary geometrical tolerances for spool movement, such as the radial clearance between the sliding spool and the valve body or the bushing sleeve (in the case of proportional or servovalves, respectively) [37], [38];
2. The high pressure drops (Δp) that occur when pressurized oil flows through the small passages uncovered by the sliding spool during valve control [21].

Moreover, another cause of power consumption occurs for two-stage servovalves:

3. The continuous and constant quiescent oil flow ($Q_{2,L}$) required in the pilot stage even when the sliding spool is in the neutral position [21].

In order to provide a better explanation of the energy losses that occur within conventional spool valves, Fig. 7 depicts a sliding spool in motion (x > 0) and in the neutral position (x = 0) within the bushing sleeve of a generic four-way three-position (4/3) servovalve, where "x" represents the sliding spool displacement [2].

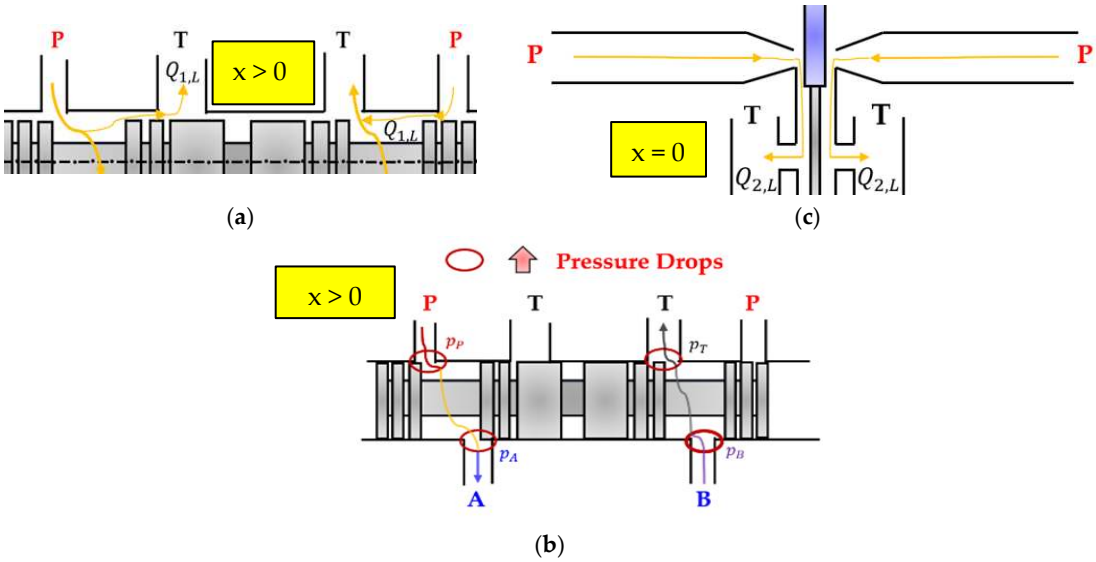

Fig. 7. Main power losses in a conventional two-stage servovalve: (**a**) Internal leakage of the main stage; (**b**) High pressure drops due to the small passages of the main stage; (**c**) Internal leakage of the pilot stage [2].

One potential solution to solve these problems could be to replace electromagnetic actuators with piezoelectric actuators (PEAs) to develop innovative piezoelectric valves. PEAs offer excellent characteristics like simple designs, fewer moving parts, high reliability, and fast response, making them ideal for this purpose. A piezo valve, namely a valve actuated by a PEA, could eliminate the need for both the torque motor and flexure tube in two-stage servovalves, reducing complexity and manufacturing costs. Moreover, using PEAs for the direct actuation of direct drive servovalves could provide faster dynamic responses and lower weight compared to LFMs. These piezovalves can replace conventional servovalves in the FMUs of conventional aircraft fuel systems, enhancing engine performance while lowering aviation's environmental impact.

To address the energy consumption issues associated with conventional analogue spool valves, the emerging field of digital hydraulics offers a promising solution. This innovative technology aims to replace conventional analogue spool valves, both proportional and servovalves, with low-cost and robust digital on/off valves, known as digital hydraulic valves, for industrial and aeronautical applications. These valves, similar in design to poppet valves, offer larger flow areas and lower pressure drops, which can significantly minimize energy losses and enhance the overall efficiency of hydraulic systems [39], [40], [41].

However, the practical application of this novel technology is currently limited due to the challenges in manufacturing these digital on/off valves. These valves, indeed, must meet specific criteria, including high switching frequencies and speeds of less than 5 ms, minimal pressure losses, and the ability to maintain a large flow rate while remaining compact. Once again, the use of PEAs could be the ideal solution for developing these digital on/off valves.

Finally, PEAs could also be the key for driving precision fluid pumps (known as piezopumps), that are compact, simple in design, capable of precise flow control, and quiet, making them suitable for innovative fluid power applications.

1.5 Aim and Objectives

The aims and objectives of this PhD research project can be summarised as follows:

1. The first objective is to develop a comprehensive model of conventional aircraft fuel systems for gas turbine engines (both turboprop and turbofan). This model will enable manufacturers and researchers to assess FMU performance across various operating conditions and analyze the power and energy demands of conventional servovalves, critical components in regulating fuel flow to the combustion chamber;
2. After evaluating the high-power consumption of servovalves in aerospace applications, the second objective is to design and simulate innovative digital hydraulic valves and servovalves actuated by smart materials, specifically PEAs. Concerning the novel digital hydraulic valve architectures, the aim is to replace conventional servovalves in both aerospace and industrial contexts by achieving high switching speeds, minimal pressure losses, high flow rates in a compact form, and reduced power consumption. Instead, the novel piezovalve designs aim to address the typical drawbacks of conventional servovalves, making them lightweight, reliable, robust, and highly efficient with rapid response times;

3. The third final objective addresses the limitations of innovative fluid precision pumps, particularly their low power (typically a few watts or less) and flow rate constraints. This goal involves designing, simulating and testing novel piezopump architectures to expand their power capabilities. This research is motivated by potential aerospace applications, especially for accessory actuators within landing gear systems.

This research project will be carried out in collaboration with GeAvio srl and the University of Bath research group.

1.6 Research Contribution

The original contributions of this PhD research include:

- Development of Simulation Models for Aircraft Fuel Systems: Creation of a detailed numerical code for simulating the entire architecture of an aircraft fuel system, intended to evaluate the power consumption problem of conventional servovalves;
- Design of Novel Piezovalve and Digital Hydraulic Valve Architectures: Design and development of innovative servovalve and digital hydraulic valve architectures driven by PEAs, intended to improve efficiency and reduce power consumption in aerospace and industrial applications;
- Numerical Simulation Codes for Innovative Valves: Creation of numerical codes specifically for simulating the performance of the proposed valve architectures;
- Development of Piezopump Architectures: Design of new piezopump architectures, aimed at expanding the power capabilities of this novel technology;
- Simulation Models for Piezopumps: Development of numerical codes for simulating the performance of the proposed piezopump architectures;
- Prototype Testing of Novel Pump Designs: Implementation of a testing setup to evaluate the performance of the novel developed piezopump prototypes.

1.7 Structure of Thesis

The thesis is divided into eight chapters:

- Chapter 1: Provides an overview of the research project, outlining the motivation and objectives behind this work.
- Chapter 2: Examines the critical role of two-stage servovalves, particularly within FMUs in conventional aircraft fuel systems. In addition, it reviews the literature on innovative servovalve architectures and precision fluid pumps using PEAs, along with the current state-of-the-art in digital hydraulic technology and recent advances in digital hydraulic valves.
- Chapter 3: Describes the layout and simulation model of the aircraft fuel system developed for gas turbine engines (both turboprop and turbofan), focusing on evaluating FMU performance and analyzing the energy consumption of servovalves, which are key in controlling fuel flow to the combustion chamber.

- Chapter 4: Presents a feasibility study on two digital hydraulic valve architectures directly actuated by a commercially available multilayer ring stack PEA, capable of delivering the high actuation forces required for this application.
- Chapter 5: Addresses the challenges of direct-drive servovalves by exploring the feasibility of using commercially available amplified piezo stack actuators as alternatives for LFMs.
- Chapter 6: Details the design, simulation, and testing of single and multi-cylinder piezoelectric pumps, aimed at expanding the power capabilities of this advanced technology.
- Chapter 7: Provides a numerical investigation using Computational Fluid Dynamics (CFD) software (Ansys Fluent) to assess the cavitation potential in the developed single cylinder piezoelectric pump.
- Chapter 8: Concludes with a discussion of potential future developments for this PhD research project.

1.8 List of Publication

This section lists the publications authored and co-authored by the thesis author. The publications where the thesis author has contributed as the primary author are highlighted below:

1. Sciatti, F., Tamburrano, P., De Palma, P., Distaso, E., & Amirante, R. (2022, December). Detailed simulations of an aircraft fuel system by means of Simulink. In *Journal of Physics: Conference Series* (Vol. 2385, No. 1, p. 012033). IOP Publishing [42].
2. Sciatti, F., Tamburrano, P., Distaso, E., & Amirante, R. (2023, October). Modelling of the entire aircraft fuel system through simulink for accurate performance evaluation. In *Fluid Power Systems Technology* (Vol. 87431, p. V001T01A050). American Society of Mechanical Engineers [43].

These papers aim to deliver a comprehensive simulation model of an entire fuel system for gas turbine engines, including turboprop and turbofan configurations. This model can assist manufacturers and researchers in assessing conventional aircraft fuel system performance across various operating conditions. The research particularly examines the critical role of the FMU and its key components, namely two-stage servovalves, which control both the fuel flow rate to the combustion chamber and the angle of the IGVs. This work was carried out in collaboration with GeAvio srl.

3. Sciatti, F., Tamburrano, P., Distaso, E., & Amirante, R. (2023, December). Digital hydraulic technology: applications, challenges, and future direction. In *Journal of Physics: Conference Series* (Vol. 2648, No. 1, p. 012053). IOP Publishing [44].

The aim of this paper is to provide a brief overview of the recent advancements in digital hydraulic technology, focusing on the various applications and their benefits.

4. Sciatti, F., Tamburrano, P., Distaso, E., & Amirante, R. (2024). Digital hydraulic valves: Advancements in research. *Heliyon* [2].

This paper presents a thorough review of the research advancements in digital hydraulic technology, with a specific focus on valve control.

5. Sciatti, F., Tamburrano, P., Plummer, A. R., Distaso, E., De Palma, P., & Amirante, R. Numerical Simulations of a High Frequency Switching 4/2 ON/OFF Valve for Pulse Modulation Switching Digital Circuits. *GFPS 2022 Conference* [45].

The aim of this paper is to evaluate the performance of a novel high frequency switching four way-two position (4/2) ON/OFF valve actuated directly by a commercially available multilayer piezoelectric actuator.

6. Sciatti, F., Di Domenico, V., Tamburrano, P., Sell, N., Plummer, A. R., Distaso, E., Caramia, G., & Amirante, R. Numerical Analysis of a High-Power Piezoelectric Pump using Computational Fluid Dynamics (CFD) Simulations. *GFPS 2024 Conference*. Forthcoming [46].
7. Sciatti, F., Di Domenico, V., Tamburrano, P., Sell, N., Plummer, A. R., Distaso, E., Caramia, G., & Amirante, R. Investigation of Cavitation Phenomena in a "High-Power" Piezohydraulic Pump: A Computational Fluid Dynamics (CFD) Approach. *ATI 2024 Conference*. Forthcoming [47].

These papers initiate a numerical investigation using CFD software to assess the potential for cavitation initiation in a specific piezohydraulic pump developed at the University of Bath. These studies were realized in collaboration with the University of Bath research group.

Publications where the thesis author has contributed as a co-author:

1. Tamburrano, P., Sciatti, F., Plummer, A. R., Distaso, E., De Palma, P., & Amirante, R. (2021). A review of novel architectures of servovalves driven by piezoelectric actuators. *Energies*, *14*(16), 4858 [1].

This paper offers a thorough review of innovative architectures of electro-hydraulic servovalves that exploit actuation systems based on piezoelectric materials.

2. Tamburrano, P., Distaso, E., Plummer, A. R., Sciatti, F., De Palma, P., & Amirante, R. (2021, July). Direct drive servovalves actuated by amplified piezo-stacks: Assessment through a detailed numerical analysis. In *Actuators* (Vol. 10, No. 7, p. 156). MDPI [48].

This paper addresses the key challenges of direct drive servovalves by presenting a feasibility study that explores the use of commercially available amplified piezo stacks as substitutes for LFMs. These PEAs are evaluated for their potential to directly actuate a new four-way three-position (4/3) direct drive servovalve design.

3. Tamburrano, P., De Palma, P., Plummer, A. R., Distaso, E., Sciatti, F., & Amirante, R. (2021). Simulation of a high frequency on/off valve actuated by a piezo-ring stack for digital hydraulics. In *E3S Web of Conferences* (Vol. 312, p. 05008). EDP Sciences [49].

This paper conducts a feasibility study on replacing commercially available servovalves in industrial and aeronautical applications with an innovative high-frequency switching two-way two-position (2/2) on/off valve. The valve is directly actuated by a commercially available ring stack—a multilayer piezo-actuator capable of delivering the high actuation forces required for these demanding applications.

4. Tamburrano, P., Sciatti, F., Distaso, E., & Amirante, R. (2023). Comprehensive numerical analysis of a four-way two-position (4/2) high-frequency switching digital hydraulic valve driven by a ring stack actuator. *Energies*, *16*(21), 7355 [50].

This study aims to enhance the energy efficiency of hydraulic systems by examining an innovative high-frequency switching four-way two-position (4/2) on/off valve architecture, which utilizes a ring stack actuator.

5. Sell, N., Sciatti, F., Plummer, A., & Love, T. (2024). Design and Testing of a Multi-Cylinder Piezopump for Hydraulic Actuation. *Energies*, *17*(19), 4876 [51].

This paper presents the design, simulation, and testing of a multi-cylinder piezohydraulic pump aimed at overcoming current limitations in power output and flow rate in piezoelectric pump technology.

2. LITERATURE REVIEW

This chapter reviews the literature on innovative servovalve architectures and precision fluid pumps that utilize piezoelectric actuation systems. It also provides a comprehensive overview of the current state-of-the-art of digital hydraulic technology, focusing on the research progress of digital hydraulic valves.

The chapter begins by exploring one of the most important applications of two-stage servovalves, specifically their role in FMUs within conventional aircraft fuel systems.

Next, the chapter explores PEAs, emphasizing their use in driving servovalves. The characteristics of these actuators are discussed in detail, followed by a comprehensive comparison of novel piezo valve architectures found in the literature with commercial servovalves. Key performance parameters of these piezo valves are evaluated to assess their potential as innovative design solutions for industrial and aeronautical applications.

The following section delves into digital hydraulic technology, examining different architectures of digital hydraulic valves. It provides an in-depth analysis of designs developed by researchers and companies over the years, emphasizing their potential to improve control precision, efficiency, and reliability in fluid power applications.

The final section focuses on precision fluid pumps driven by PEAs, examining their working principles, advantages, and performance.

These literature review studies were published in leading journals [1], [2] and presented at important national and international conferences [42], [43], [44].

2.1 Conventional Aircraft Fuel Systems – FMU

According to the Federal Aviation Administration (FAA) [52], the fuel system in gas turbine-powered aircraft stands as one of the most important components. Its main functions include delivering clean fuel to the engine in the right quantity, at a pressure and a temperature suitable for satisfactory combustion [53], [54], [55], in addition to regulating the fuel flow rate injected into the combustion chamber to match the required thrust throughout all phases of flight [42], [43]. Due to the critical nature of these tasks, the fuel system must consistently operate at optimal efficiency to ensure the safety and reliability of the aircraft.

The conventional fuel system for gas turbine engines that run on kerosene-based fuels is made up of various components, including fuel tanks, fuel lines, centrifugal boost pumps, check valves, filters, main fuel pumps, FMUs, and fuel injector nozzles [56]. The FMU, is the core of the fuel system. It controls the fuel flow delivered to the combustor chamber and adjusts the angle position of the IGVs, which in turn regulate the airflow entering the compressor [23], [24]. To fulfil these requirements, the FMU contains several hydraulic components, such as bypass valves, two-stage electrohydraulic servovalves (i.e. Fuel Metering (FM) servovalve and IGV servovalve), IGV actuators, pressurizing valves, and shut-off valves. Among these components, the bypass valve, the FM servovalve, and the IGV servovalve are essential [57], [58]. By maintaining an almost-constant pressure difference across the FM servovalve, the bypass valve guarantees a

proportional correlation between the fuel flow rate and the opening degree of the FM servovalve, regardless of whether the aircraft is in steady-state or dynamic operation [59], [60]. Consequently, efficient fuel control within the combustion chamber becomes achievable through the FM servovalve. Simultaneously, the IGV servovalve regulates the fuel flow rate directed to the IGV actuator, effectively controlling the angle position of the IGVs to optimize engine efficiency across various operating conditions [23]. Therefore, the performance of the entire Engine Control System (ECS) is strongly impacted by the reliability of the FMU [61], [62].

Traditional hydraulic-mechanical ECS face challenges in meeting the control requirements of modern engines due to their narrow control range, low precision, and complex structure [63], [64]. To address this issue, the Full Authority Digital Electronic Control (FADEC) has become the main trend as the control system for aeroengines since the 1980s [65], [66]. With FADEC, the pilot in the cockpit can easily adjust the thrust level by using a throttle lever, as shown in Fig. 8 [42], [43]. The established control law enables the Electronic Control Unit (ECU) to calculate the required fuel flow rate, and determines a signal to the FMU electrohydraulic servovalves, which are used to transmit fuel to the combustor chamber and/or to the IGV actuators [25], [67].

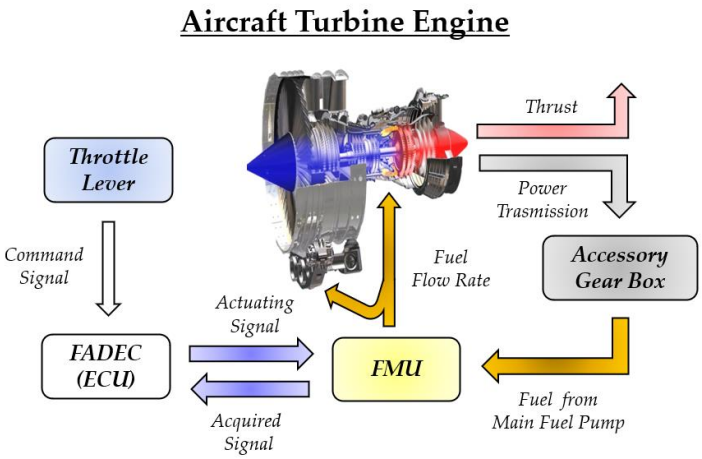

Fig. 8. Gas turbine engine control system [42], [43].

A typical example of an aircraft fuel system layout operating on kerosene-based fuels is the General Electric CJ610 fuel system, which is shown in Fig. 9 [23]. Generally, the components of an aircraft fuel system can be divided into two independent groups: airframe components and engine components [56]. The airframe components can be summarized as follows:

- The fuel tanks, which are usually located in the wings, fuselage, or tail. Regardless of how many individual storage units an aircraft fuel system may contain, fuel is essentially fed to each engine from one main fuel tank;
- The boost pumps, which are electrically operated and are usually centrifugal. These pumps are located in the fuel tanks and maintain a constant fuel pressure in the line between the tank and the engine-driven main fuel pump. To align the flow rates of the centrifugal boost pumps and the main fuel pump, some of the centrifugal boost pump flow rate is recirculated back into the fuel tank;
- The airframe shut-off valves, designed to disconnect the fuel lines from the engine without any danger of fuel spillage;

- The low-pressure filters, needed to remove solid particles from the fuel that could cause damage to the engine-driven main fuel pump.

An interface point is designated at the fuel inlet of the engine components, and various parameters such as fuel pressure and temperature are defined at the interface point. In modern gas turbine engines, the temperature at the main fuel pump inlet can be as high as 90°C, while the fuel pressure is approximately 3 bar [68]. The engine components consist of:

- The main fuel pump, which is typically a positive displacement pump driven by the engine via the accessory gear box. Its primary function is to provide high-pressure fuel to the FMU for combustion and to act as hydraulic fluid for the compressor variable-geometry systems. As a result, it delivers a flow rate that exceeds the engine requirements;
- The pressure relief valve, which is crucial to safeguard the system against potential over-pressure situations;
- The bypass valve, which guarantees a linear relationship between the fuel flow rate and the opening degree of the FM servovalve;
- The IGV servovalve, which is typically a four-way three-position (4/3) two-stage servovalve. It regulates the fuel flow rate delivered to the IGV actuator;
- The IGV actuator, which changes the position of the inlet guide vanes/compressor vanes;
- The FM servovalve, which is typically a two-way two-position (2/2) two-stage servovalve. It controls the fuel flow rate delivered to combustion chamber;
- The pressurizing valve, which ensures sufficient fuel pressure within the FMU to maintain correct system operation;
- The engine shut off valve, designed to separate the FMU from the combustion chamber;
- The fuel injector nozzles, which inject the fuel into the combustion chamber in the form of atomized or vaporized spray.

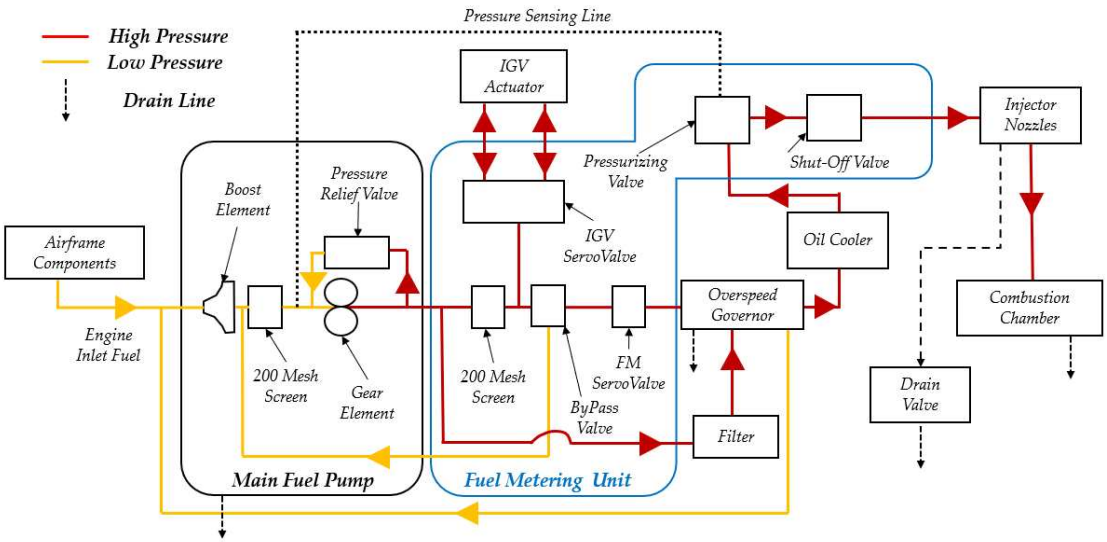

Fig. 9. Typical layout of a conventional aircraft fuel system, adapted from [23].

2.2 Smart Materials – Piezoelectric Actuators

The growing demand for next-generation industrial, military, commercial, medical, automotive, and aerospace technologies has driven extensive research and development into advanced smart materials. These materials represent a novel class of substances that can respond to external stimuli in a controlled and predictable manner. Actuators that utilize the strain induced in these materials to produce motion are referred to as Induced Strain Actuators (ISAs) [69]. Commonly employed smart materials in ISA applications include piezoelectric, electrostatic, electromagnetic, photostrictive, electrostrictive, magnetostrictive and shape memory alloys.

As shown in Table 3, PEAs demonstrate exceptional performance in terms of nanometer-scale resolution, rapid response times, and immunity to magnetic interference. These characteristics give them a distinct advantage over other technologies, such as shape-memory alloys and magnetostrictive actuators, particularly in precision manufacturing, displacement output, medical treatment, and microfluidic control applications [70]. Furthermore, Fig. 10 shows how the structural scalability and high power-to-weight ratio of PEAs make them an especially promising solution for applications in robotics, automation, industrial systems, and aerospace [70], [71].

Table 3. Comparison of different types of smart materials actuators and their driving principles, accuracy, advantages and disadvantages [70].

Actuator type	Driving principle	Accuracy	Advantages	Disadvantages
Electrostatic	Coulomb force	Below the micron	High efficiency, small size, temperature-insensitive	Small output force, harsh environment
Electromagnetic	Electromagnetic induction	Micron	High frequency, reliable, low cost, temperature-insensitive	Large volume, heat, noise
Shape-memory alloys	Shape-memory effect	Micron	Flexible, small, large deformation, high energy	Temperature-sensitive, slow response
Magnetostrictive	Magnetostrictive effect	Below the micron	High force, no fatigue or heat loss	Sensitive to magnetic fields, hysteresis
Electrostrictive	Electrostrictive effect	Below the nanoscale	Low creep, good reproducibility	Temperature-sensitive, average energy density
Photostrictive	Photostrictive effect	Micron	Anti-Electromagnetic interference, lightweight, fast	Temperature-sensitive, low efficiency
Piezoelectric	Inverse piezoelectric effect	Sub-nanometer	Antimagnetic interference, high efficiency, high response frequency	Hysteresis, creep, temperature-sensitive

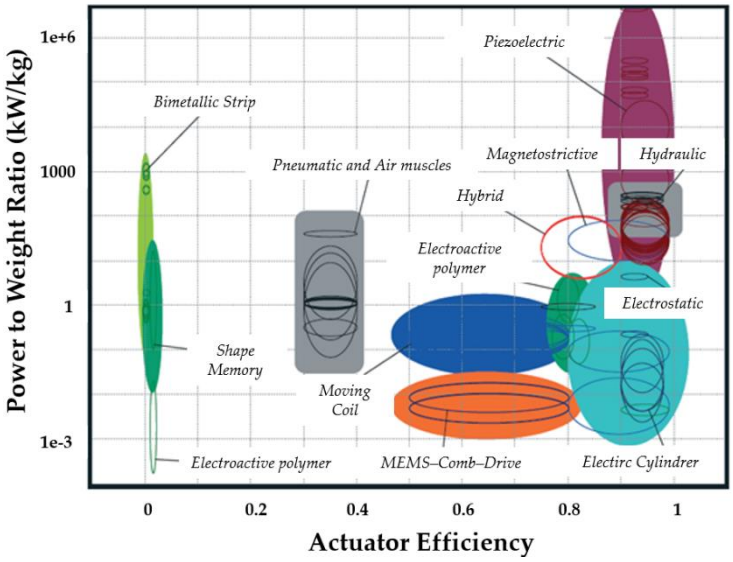

Fig. 10. Power to weight ratio versus actuator efficiency [71].

PEAs use the piezoelectric inverse effect to convert electrical energy into mechanical energy. The most used material for these actuators is lead zirconate titanate. As explained in Chapter 1, the use of PEAs instead of electromagnetic actuators in servovalves, both direct drive and two stage types, could help to solve the typical problems associated with these spool valves. In addition, the piezoelectric actuation could be capable of extending the bandwidth of current servovalves (up to 150–300 Hz) into a kiloHertz range [72]. It has also been proven that PEAs can be employed for several working cycles without being damaged [73]. PEAs are susceptible to temperature variation, have a low Curie temperature, and their actuation force decreases with temperature [74]. However, these weaknesses should not be an issue for the typical operating range of the hydraulic oil used in servovalves (30–60°C). The main problems of PEAs to be managed in servovalves are hysteresis (which can be as high as 20%) and creep, which could affect the accuracy of control [75]. Therefore, closed-loop control is mandatory to tackle this problem, and techniques to deal with these problems have been shown in the literature [76], [77], [78].

Commercially available PEAs are produced by a few manufacturers such as Thorlabs, Noliac, Piezodirect, Piceramic, etc [1]. In order to produce displacement, an amplified voltage (V_{amp}), usually up to 100 V or 200 V, must be applied to a PEA. The PEA in turn exerts an actuation force linearly decreasing with its displacement. Fig. 11 qualitatively shows the relationship between the actuation force (F_{act}) and the displacement (x). For a given voltage applied to the PEA, the relation is a straight line with a certain slope, which translates along the horizontal axis when the voltage is changed. Therefore, the maximum actuation force, called the blocking force (F_b), is obtained when an actuator is blocked from moving. When the maximum voltage is applied, the maximum blocking force is obtained ($F_{b,max}$). The blocking force can be put in relation to the voltage using a force/voltage coefficient (K_{VF}), thus obtaining:

$$F_{act} = F_b - k_p x = K_{VF} V_{amp} - k_p x \tag{1}$$

where k_p is the actuator stiffness. The maximum displacement (x_{max}), called the free stroke, is obtained for a null actuation force, namely, when a free actuator experiences no resistance to movement, and when the maximum voltage is applied.

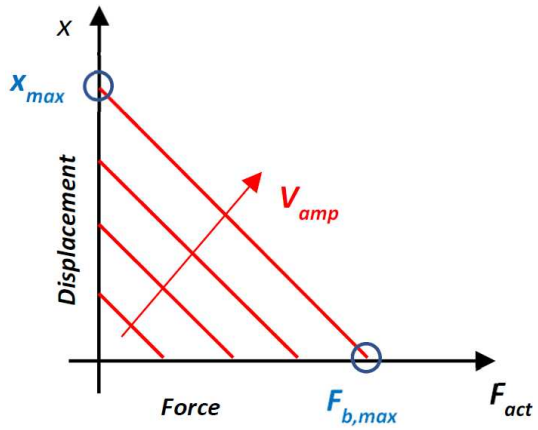

Fig. 11. Displacement–force–voltage relationship for a PEA.

The main types of commercially available PEAs include piezo stacks (Fig. 12a), amplified piezo stacks (Fig. 12b), bimorph (rectangular) benders (Fig. 12c), and ring benders (Fig. 12d) [1].

(**a**) (**b**) (**c**) (**d**)

Fig. 12. Main types of commercially available PEAs: (**a**) Piezo Stack; (**b**) Amplified Piezo Stack; (**c**) Bimorph (rectangular) Bender; (**d**) Ring Bender [1].

Piezo stacks are very large and can generate very high actuation forces but low displacement; amplified piezo stacks use amplification systems to reach higher displacement but at the expense of the actuation force, which is lower than that of piezo stacks. Bimorph (rectangular) benders and ring benders are much smaller than piezo stacks and amplified piezo stacks but generate lower actuation forces. A ring bender generates a higher actuation force than a rectangular bender, but the latter achieves higher displacement. A comparison among these actuators is provided in Table 4 and in Fig. 13 [1]. As shown in Table 4, the different actuator designs have different characteristics. Blocking force and free displacement are plotted in Fig. 13 for these actuators.

Table 4. Comparison of different types of PEAs [1].

Type of Piezoelectric Actuator	Actuation force	Displacement	Size
Piezo stacks	very high	very low	very large
Amplified piezo stacks	high	medium	large
Bimorph benders	low	high	small
Ring benders	medium	low	very small

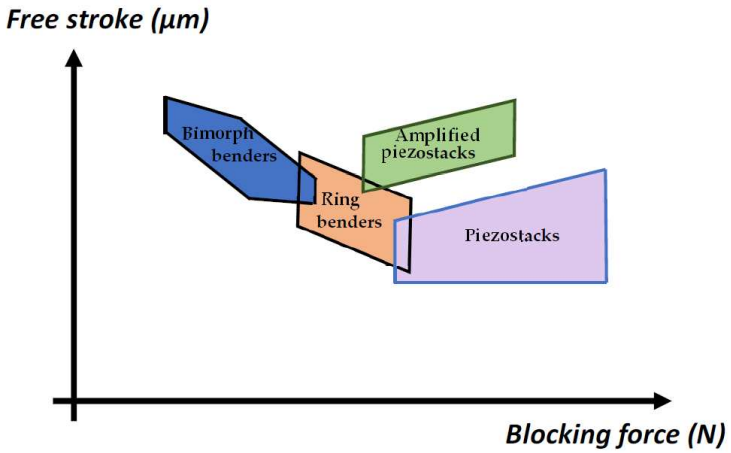

Fig. 13. Comparison among different types of PEAs in terms of free stroke and blocking force [1].

2.2.1 Servovalves driven by Piezo Stack Actuators

A piezo stack actuator, shown in Fig. 12a, consists of a series of piezoelectric elements stacked one on top of the other and enclosed between two electrodes. The thickness of the layers is on the order of 25-100 μm. The voltage to be applied depends on the material and the thickness of each element. The longer the stack, the higher the displacement achieved by the stack. As an example, a commercially available piezo stack actuator, model NAC2023 produced by Noliac, is 15 cm long and can produce a blocking force of 9450 N with a free stroke of 244.2 μm [1]. Without preload, piezo stacks are sensitive to pulling forces; therefore, it is recommended to apply a pre-load in order to optimize the performance of the actuators [1]. It has been proven that selecting a correct value for the preload allows a longer lifetime to be achieved for this type of PEA. The values for the optimum preload range from 20 to 50 percent of the maximum blocking force [79]. The force must be applied to the full surface of the actuator in order to ensure good load distribution. Fig. 14 shows the wrong and correct operation of a piezo stack.

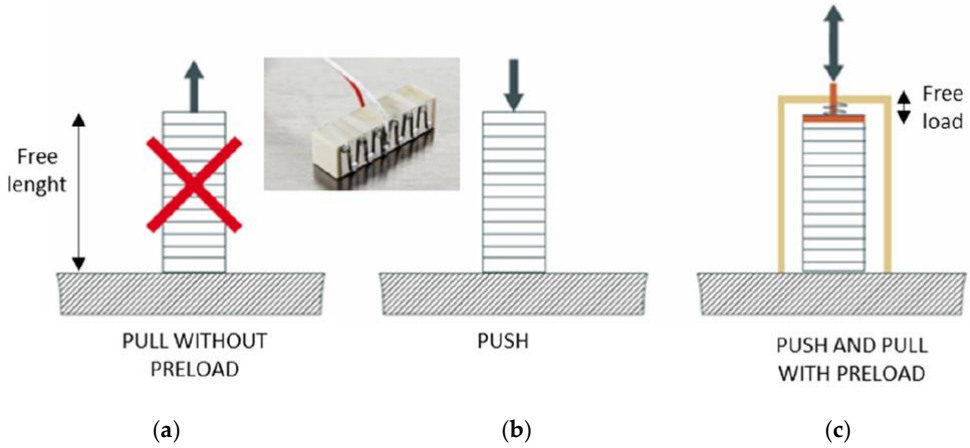

Fig. 14. Piezo stack actuator: wrong pull-mode operation (**a**) and correct operation (**b**-**c**).

Back in the 1990s, a research study was conducted on the application of piezo stacks to servovalves [80]. There were two piezo stack actuators that were connected to both sides of a spool through steel balls to directly actuate the sliding spool of the servovalve, as shown in Fig. 15. The piezoelectric multilayer actuators were pre-compressed by about 20 μm. The displacement of the sliding spool was measured by a non-contact reluctance-type position sensor. Feed forward control was employed in order to obtain high speed response. The authors stated that this servovalve had a bandwidth of over 5 kHz and could pass a flow of 5.4 L/min for a pressure drop of 100 bar. The application of this valve architecture to higher flow rate values is not documented in the paper. This research study can be regarded as the precursor for more recent studies.

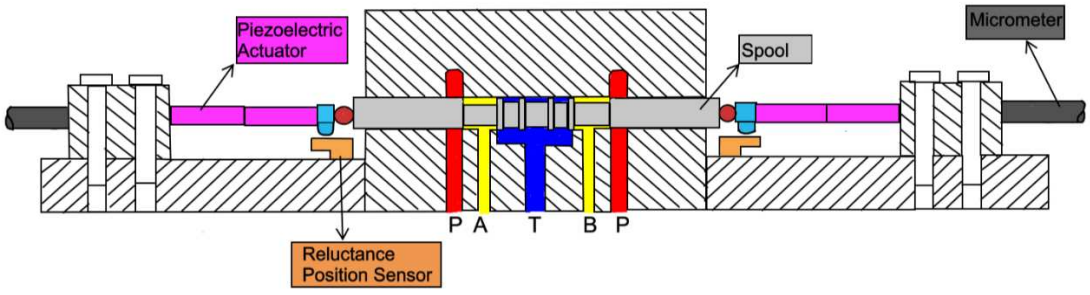

Fig. 15. Redrawn schematic representation of the piezo valve realized in [80].

The main problems of that architecture are the high cost of using two piezo stack actuators. To cope with this problem, in [81], a spring mechanism and only one piezo stack were used to obtain bidirectional spool control, as shown in Fig. 16. A leaf spring allowed the spool to be kept in the neutral position when no voltage was applied to the piezo stack. Nonlinear effects such as hysteresis and creep were managed using a Fuzzy Logic control algorithm with a Preisach hysteresis nonlinear model in a feedforward loop. The valve was tested at a very low flow rate (up to 4 L/min for a supply pressure of 7 MPa). In these conditions, the results illustrated that the piezo valve had a frequency response bandwidth of 470 Hz, and the system could reach the steady state in 4.77 ms.

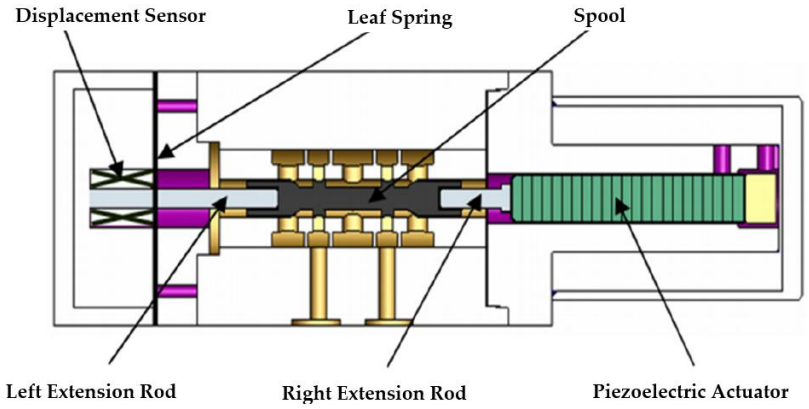

Fig. 16. Structure of the piezo valve realized in [81].

Again, the application of this valve architecture to higher values of flow rate and pressure was not addressed in the paper.

In [82], a similar servovalve was developed but using four components: a piezoelectric stack coupled with a rod, a spool, a disc spring rod, and a driving disc spring, as shown in Fig. 17. The four components were not fixed together but were in contact with each other to drive the sliding spool. An internal preload was applied to the piezo stack to cope with the pulling forces generated by the inertia and the friction of the spool. With a supply pressure of 21 MPa, the flow rate was measured to be 4.45 L/min at a maximum input voltage of 5 V. The –3 dB frequency was 710 Hz, and the step response time of the spool displacement was 0.52 ms.

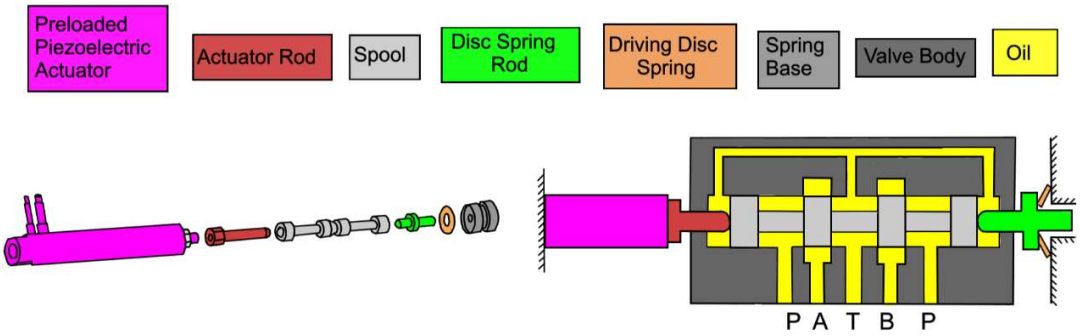

Fig. 17. Redrawn schematic representation of the direct drive piezo valve proposed in [82].

In [83], [84], piezo stack actuators were used in place of the torque motor for the actuation of the flapper in a double nozzle-flapper servovalve. There were two flapper moving mechanisms that were proposed to compensate for the hysteresis and the thermal expansion of the piezo stacks, and these systems were experimentally assessed. A simplified valve was used in the experimental test; there were no actuator ports, and a spring was used to simulate the flow force, as shown in Fig. 18. The experimental results showed that with a supply pressure of 210 bar, a high dynamic response could be obtained: concerning the first moving mechanism, the phase lag was −90° for a frequency of 200 Hz, and the amplitude ratio was –3 dB for a frequency of 150 Hz. The results were further improved by using the second mechanism, the phase shift being –90 ° for a frequency of 300 Hz.

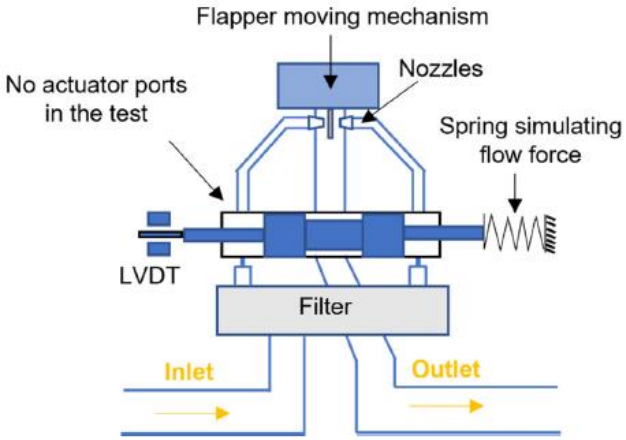

Fig. 18. Redrawn schematic of the double nozzle-flapper test valve actuated by piezo stacks used in [83], [84].

In [85], four two-way two position (2/2) poppet valves, each driven by a piezo stack actuator, were used as flow variable resistors in place of the torque motor to actuate the main stage of a conventional two-stage servovalve, as shown in Fig. 19. Each piezo actuator had a nominal full stroke of 40 μm and a driving force of 2000 N at an operating voltage of 160 V. A LVDT was used to measure the sliding spool position and to achieve closed-loop control.

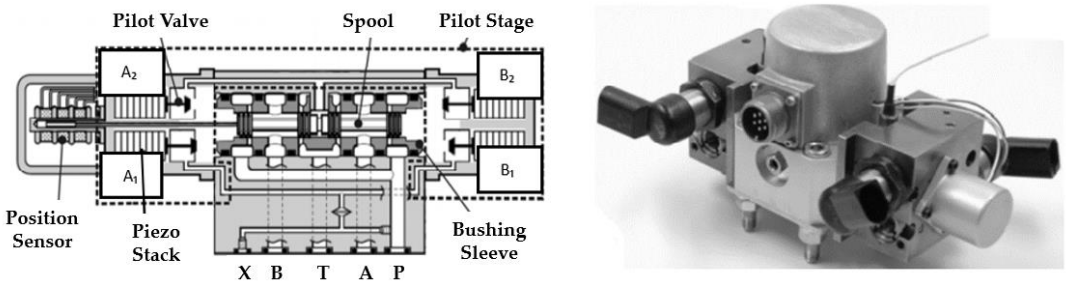

Fig. 19. Pilot operated piezo valve actuated by four piezo stacks proposed in [85].

The operation principle of this valve configuration can be described in the following way: while valves A2 and B1 are closed, valves B2 and A1 are open, and vice-versa. By changing the stroke of each pilot valve and the phase lag between them, flow modulation can be achieved. The valve was capable of controlling 32 L/min at a pressure drop of 70 bar. This architecture provided better dynamics than a conventional servovalve. Indeed, tests performed at 210 bar showed that the rise time was only 1.07 ms to reach an opening of 0.52 mm. The frequency values corresponding to an amplitude decrease of −3 dB and a phase lag of −90° were 340 Hz and 300 Hz, respectively, with reference to the maximum opening.

In [85], a new design for a direct drive servovalve was also proposed, called a hybrid valve, in which the bushing sleeve was actuated by a piezo stack with a stroke of ±50 μm, and the spool was driven by a LFM with a stroke of ±0.5 mm, as shown in Fig. 20. A closed-loop control system was used to simultaneously control the position of the spool and the position of the sleeve while compensating for hysteresis. The experimental results, performed with a pressure drop of 35 bar across each metering chamber, showed that the hybrid valve had a nominal flow rate of 40.5

L/min. The frequency values corresponding to an amplitude decrease of −3 dB and a phase lag of −90 ° were 620 Hz and 850 Hz, respectively. Due to the additional leakage between the moving sleeve and the valve housing, the overall internal leakage of the hybrid valve was about 1 L/min, thus being greater than that of commercially available direct drive valves.

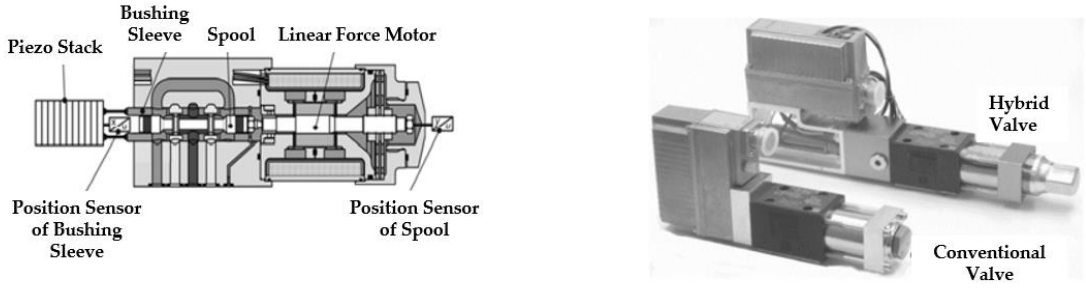

(**a**) (**b**)

Fig. 20. Hybrid valve design proposed in [85] (**a**); comparison with a conventional direct drive servovalve (**b**).

In [72], a piezo stack actuator was used to move an upper moving plate coupled with a stationary plate, as shown in Fig. 21. Annular grooves were built in the two opposing plates to form multiple metering edges (Fig. 21b). The working principle was to control the flow rate by adjusting the axial distance between the two plates, x_s. This piezo valve provided several advantages, such as the reduction of internal leakage, very good valve response, an increase in the flow area, and high flow rates for a given pressure drop.

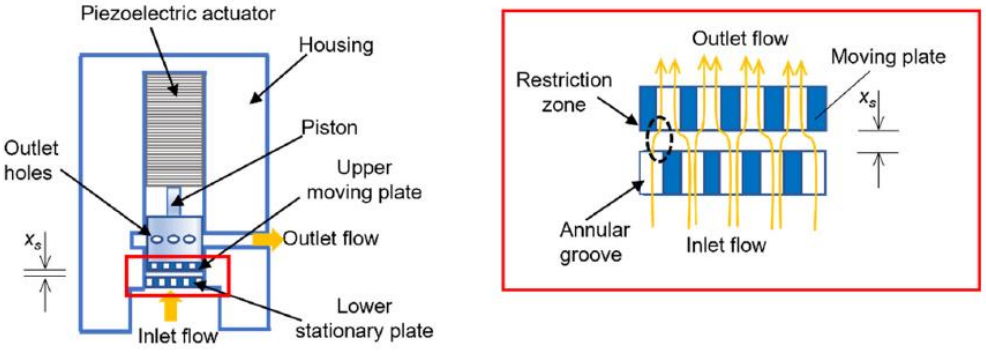

(**a**) (**b**)

Fig. 21. Redrawn schematic cross section of the piezo valve actuated by a piezo stack as proposed in [72] (**a**); redrawn schematic of the flow path through the annular grooves (**b**).

The piezo valve prototype used a PEA which had a free stroke of 68 μm and could produce a blocking force of up to 12 kN. The valve was capable of opening or closing fully in less than 1.5 ms and could pass a flow of 65 L/min at a pressure drop of 20 bar. The bandwidth performance of the valve was also investigated experimentally: it was up to 425 Hz for input voltage amplitudes up to 85 per cent of the maximum [72].

2.2.2 Servovalves driven by Amplified Piezo Stack Actuators

The main weakness concerning the use of a piezo stack actuator is its low stroke, which is very small compared to its length. Indeed, these PEAs generate values of displacement that are usually

less than 100 μm. Therefore, the main issue associated with piezo stacks is the large dimensions of the valve; in the case of direct actuation, the low stroke of the spool causes low flow rate through the valve. In addition, asymmetrical piezo stack designs, e.g., [72], [81], [82], will suffer from the offset and hence reduced amplitude because of thermal expansion as they heat up (stack heating is significant when operating at high voltage and high frequency due to the high peak current that is generated).

To increase the displacement (hence, the flow rate) and to reduce thermal problems, amplification systems can be adopted. Fig. 22 shows an example of an Amplified Piezo Stack Actuator (APA) based on an elliptical shell used to transform the deformation occurring along the main axis (l_p) into deformation along the short axis (h_{apa}), which is amplified [86]. This amplification mechanism allows the PEA to achieve large deformation (up to 1000 μm) but at the expense of the actuation force, which is much lower than a piezo stack [87]. This APA design can give a significant advantage over other piezo stack designs in terms of temperature independence since the thermal expansion coefficient of the shell is designed to match the stack, so there will be no thermal effect.

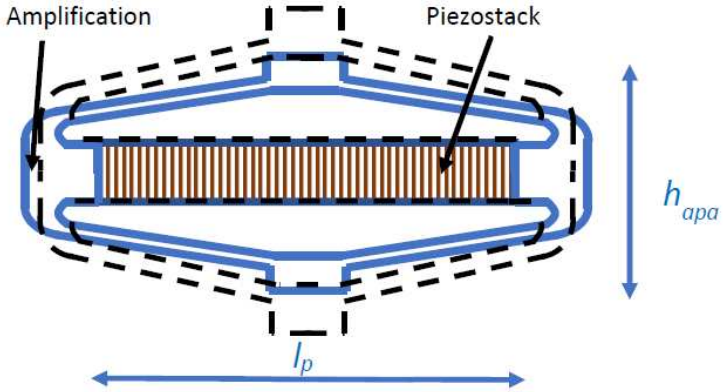

Fig. 22. Redrawn schematic of the amplified piezo stack actuator with elliptical shell [86].

In [88], an APA was adopted to directly actuate the spool, as shown in Fig. 23. A prototype was constructed. The amplification system was a lever mechanism connecting the spool to a preloaded piezo stack. The lever was able to amplify the displacement of the piezo stack from 0.06 mm to 0.3 mm. The maximum voltage applied to the PEA was 800 V. The valve was constructed to obtain 7.5 L/min for an inlet pressure of about 100 bar. A very lightly damped mode at about 340 Hz was noticed.

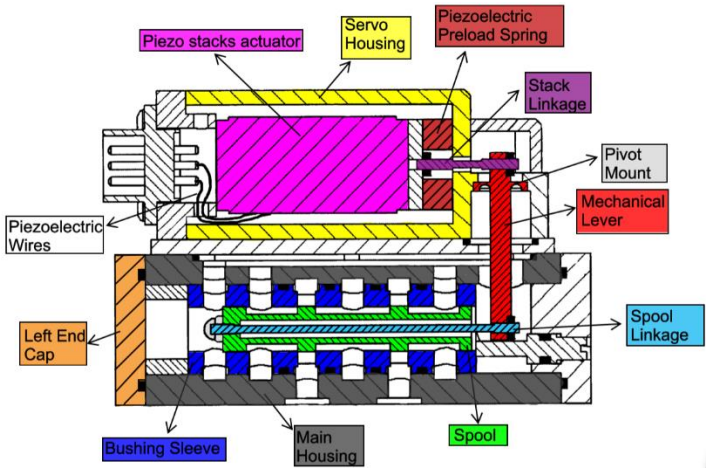

Fig. 23. Redrawn cross section view of the direct drive piezo valve proposed in [88].

Similar valve architectures were developed in [89], [90], [91], in which a piezo stack actuator with a lever amplification mechanism was used to directly actuate the main stage valve, as shown in Fig. 24. To control the position of the spool, closed-loop control was used.

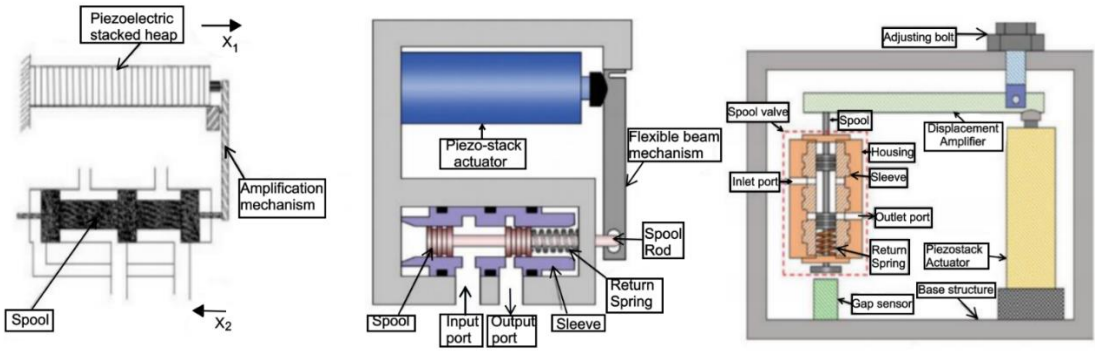

(**a**) (**b**) (**c**)

Fig. 24. Schematic configurations of the direct drive piezo valves proposed in [89] (**a**), [90] (**b**),and [91] (**c**).

The direct drive piezo valve developed in [89] was a pneumatic valve, which proved to be much faster than a normal solenoid valve. The architecture proposed in [90] was very similar but used with oil. With the maximum input voltage, the spool displacement reached 0.56 mm, and the maximum flow rate was 22.8 L/min for a pressure drop of 30 bar. The −3 dB frequency was 181 Hz.

A similar piezo valve, developed in [91], was tested at various operating temperatures by the use of a heat chamber. It was shown that good control was achieved even at very high temperatures. The experimental results showed that at 30 °C, the input voltage necessary to reach a maximum spool position of 0.3 mm was 80 V, and the valve was capable of passing 9 L/min (the pressure drop through the valve was not reported in the paper).

The problem associated with these designs is that the lever mechanism does not provide temperature compensation; therefore, changes in performance can be expected because of thermal expansion when the stack heats up during operation.

In [92], a commercially available piezo stack actuator with a mechanical flexure amplification system similar to that shown in Fig. 22 was used in place of a conventional torque motor to move the flapper in a double nozzle-flapper pilot stage, as shown in Fig. 25.

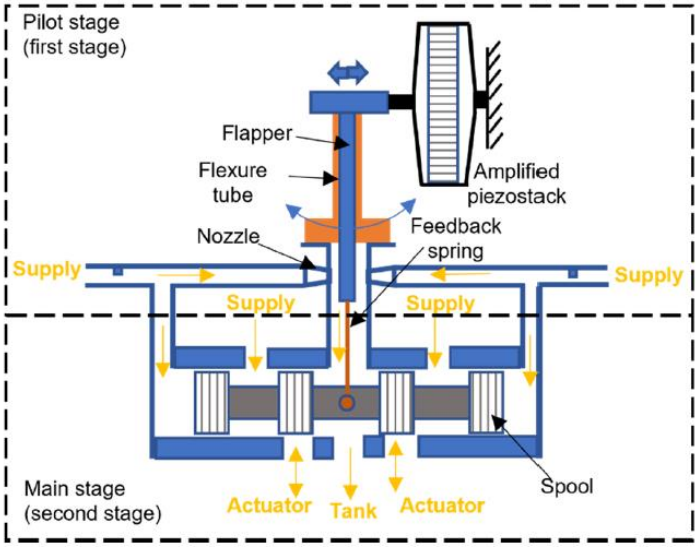

Fig. 25. Redrawn representation of the two-stage servovalve with PEA developed in [92].

The working principle was very similar to that of a conventional two-stage servovalve. Indeed, the force generated by the voltage applied to the piezo stack actuator moved the flapper, which in turn created a differential pressure at the sliding spool ends and allowed the spool to move. The negative values of the operating voltage moved spool to the left, while the positive values moved to the right. For a supply pressure of 210 bar, a flow rate of 10.5 L/min was obtained at the maximum input voltage of 35 V from null. In these conditions, the −90° phase lag was obtained for a frequency of 284 Hz; the response time was 0.8 ms.

In this design, the use of an APA in place of the torque motor can lead to an increase in the size and weight of the pilot stage, thus affecting the main characteristics of a two-stage servovalve, which are the low weight and small size.

2.2.3 Servovalves driven by Bimorph Bender Actuators

To increase the displacement to volume ratio, bimorph (rectangular) benders have been developed by a few manufacturers.

A bimorph bender actuator (also called plate actuator) consists of two or three layers sandwiched between electrodes, as shown in Fig. 26. The piezo layers are operated in opposite mode (contraction/expansion) by being polarized in opposite directions. A layer of a metal alloy can be positioned between the ceramic elements.

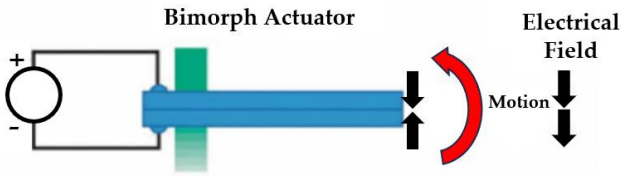

Fig. 26. Bimorph bender actuator [1].

Because of their characteristics (low weight, high displacement and cost-effectiveness), bimorph bender actuators have the potential to replace the torque motor in the pilot stages of servovalves, according to the scheme of Fig. 27 [93].

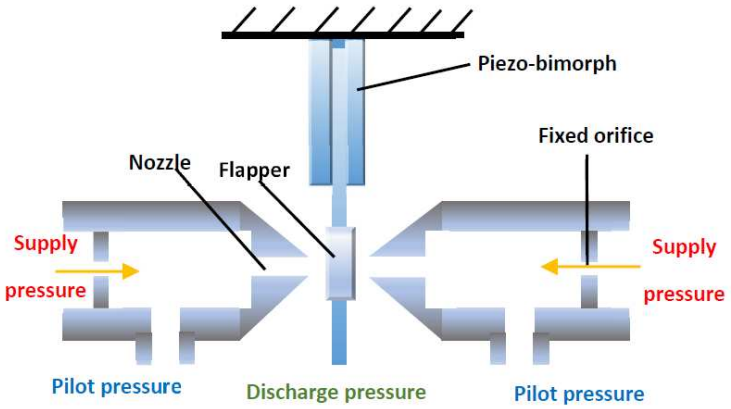

Fig. 27. Redrawn schematic of a bimorph actuator used for the control of a double nozzle-flapper valve, proposed in [93].

The main problem is the very low actuation force generated by these actuators, being of the order of a few Newtons. For example, model CMBP09 produced by Noliac has a length of 5 cm, a width of 7.8 mm, and a height of 1.8 mm, providing a maximum free stroke of ±635 μm and a maximum blocking force of 2.9 N [1].

To evaluate the effects of the hydraulic oil upon the piezoelectric bimorph actuator, a Simulink model was used in [93] to investigate the architecture of Fig. 27. The simulation results showed that at a frequency of 200 Hz, the maximum displacement of the flapper without oil (32.5 μm) was significantly higher than the maximum displacement obtained when the flapper was immersed in oil (5 μm). This is due to the additional mass that the fluid provided to the actuator.

In [94], [95], [96], [97], bimorph bender actuators were used to actuate the flapper in a complete double nozzle-flapper servovalve (pilot stage + main stage), as shown in Fig. 28a. LVDTs were used to measure the sliding spool position, thus achieving closed-loop control to cope with the hysteresis of the bimorph benders.

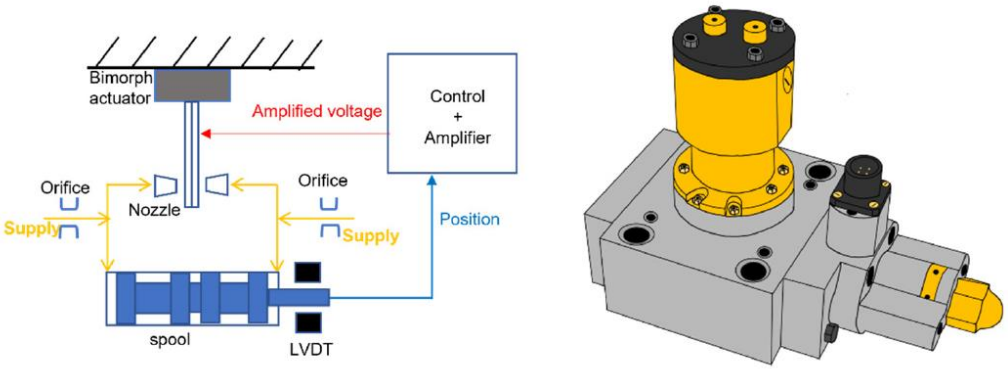

(**a**) (**b**)

Fig. 28. Redrawn schematic of a bimorph actuator controlling a double nozzle-flapper valve (**a**) and redrawn representation of the piezo valve prototype constructed in [94] (**b**).

The piezo valve constructed in [94] is shown in Fig. 28b. It employed a parallel bimorph bender actuator, which provided a free stroke of ±1 mm and a blocking force of 0.35 N for a maximum operating voltage of ±60 V. The test results showed that this piezo valve had a bandwidth of 140 Hz and could pass 7 L/min at a pressure drop of 14 bar. Similar results were also obtained in [95], [96].

In [98], [99], a multilayer bimorph actuator was used in place of the torque motor to move the deflector in a prototype of deflector jet piezo valve, as shown in Fig. 29. An existing design of main stage valve body was used (Moog 26 series), fitted with an integrated LVDT to measure the spool position. When a voltage was applied to it, the PEA bent and moved the deflector, which, in turn, directed the jet of fluid to one of the two control ports. This created a pressure difference on the spool ends, thus allowing the spool to move in the opposite direction to the movement of the deflector. A feedback wire attached to the rectangular piezoelectric bimorph bender was used to achieve mechanical feedback and generate a restoring force that could center the deflector and stop the spool at a fixed position. The valve showed effectiveness and reliability during operation and good performance levels. The simulation results, predicted using Simulink, were compared to the experimental results. At a supply pressure of 140 bar, the −3 dB bandwidth of the experiment results (≈38 Hz) was 13.6% slower compared to the predictions (≈40 Hz). The −90° phase frequency was approximately 50 Hz in both cases.

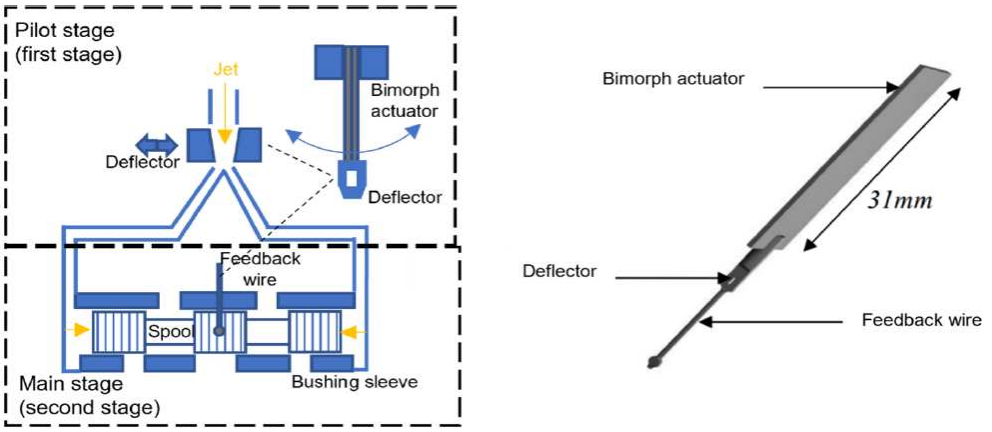

(**a**) (**b**)

Fig. 29. Deflector jet valve actuated by a bimorph rectangular actuator [98], [99]; redrawn schematic of the operating principle (**a**) and redrawn representation of the actuator-deflector assembly (**b**).

2.2.4 Servovalves driven by Ring Bender Actuators

The designs in which a bimorph (rectangular) bender is used to actuate the pilot stage of a two-stage servovalve might have an issue concerning the very low actuation force generated by these piezo actuators. For example, the bimorph bender employed in [98], [99] had a maximum blocking force of only 1 N. To increase the actuation force, ring benders, which are constructed by a few manufacturers, can be used. The ring bender has recently become available and is composed of several thin layers of piezoceramic with internal silver palladium electrodes, which, in turn, are connected to external electrodes, as shown in Fig. 30. By applying voltage to the external electrodes, which usually ranges from -100 V to +100 V, the ring bender can deform concavely or convexly [100], [101]. A ring bender has higher stiffness and higher blocking force

than a bimorph actuator of similar size but lower displacement. For example, model CMBR07, produced by Noliac, exhibits a free displacement of +185 um and a maximum blocking force of 13 N at a maximum operating voltage of 100 V [1].

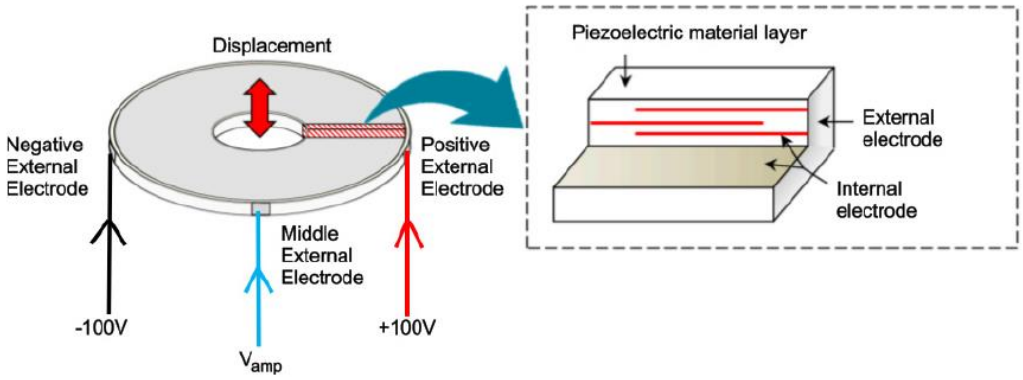

Fig. 30. Shape and components of a ring bender [100].

In [101], a prototype of double nozzle-flapper pilot stage was developed in which two ring benders were mounted with O-rings inside a housing to actuate the flapper, as shown in Fig. 31a. A total of two ring benders were used for redundancy, which is needed in aircraft applications. Experimental tests were performed on the prototype. The flapper stroke was ±50 um. The maximum flow rate was 0.61 L/min.

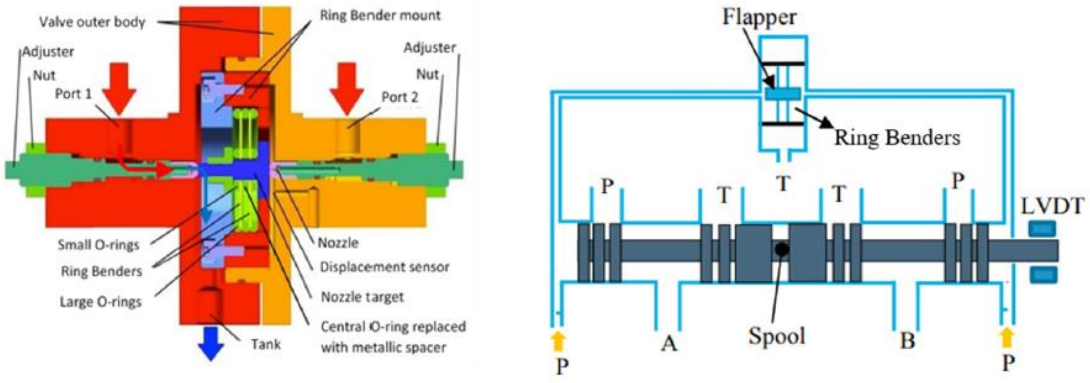

(**a**) (**b**)

Fig. 31. Nozzle-flapper pilot stage controlled by piezoelectric ring benders developed in [101] (**a**) and application to an entire 4/3 valve [102] (**b**).

In [102], the application of this novel pilot stage to a typical 4/3 valve was assessed using a detailed Simulink model, which reproduced all of the real phenomena present in such a complex hydraulic system. Step and sinusoidal tests were simulated for a supply pressure of 210 bar, thus predicting the valve potential. It was shown that the interval time necessary to reach 90% of the set point was about 3 ms for a spool position of 0.1 mm, 4 ms for a spool position of 0.6 mm, and 6 ms for a spool position of 1 mm. With regard to the frequency response, at a 100 Hz and ±1 mm amplitude, the phase shift was around −90°.

In [103], [104], [105], a two-stage piezo valve was developed using additive manufacturing. The pilot stage employed a four-way three-position small spool directly driven by a ring bender, as shown in Fig. 32.

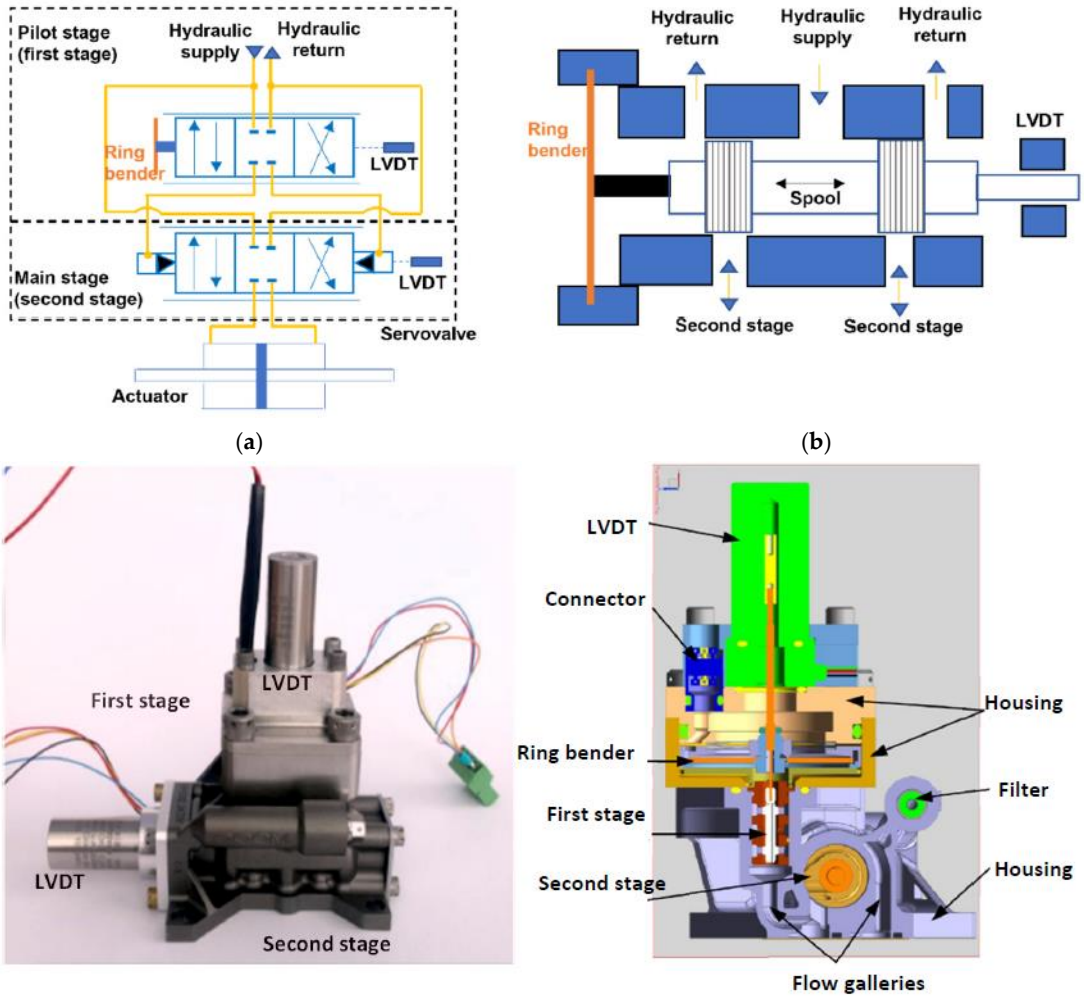

Fig. 32. Piezo valve developed in [103], [104], [105]: redrawn hydraulic scheme (**a**); redrawn first stage schematic (**b**); new valve prototype photo (**c**); redrawn valve representation (**d**).

To minimize the internal leakage, a significant overlap was used between the bushing sleeve and the spool lands in the first stage. A conventional main stage was hydraulically connected to the pilot stage, and the sliding spool was controlled by the flow, which passed through the small spool. A total of two LVDTs were used to measure the ring bender position and the sliding spool position, respectively. The ring bender was characterized by a maximum displacement equal to ±115 μm and a maximum blocking force equal to ±39 N for a maximum operating voltage of 100 V. A Simulink model, simulating the amplifier, the pilot stage and the main stage, was developed and validated against experimental data. The valve worked very well at different operating conditions; at a supply pressure of 210 bar, the −90° phase frequency was around 100 Hz.

In [106], [107], [108], a novel pilot stage configuration composed of two normally closed two-way two-position (2/2) valves actuated by two piezoelectric ring benders was developed, as shown in Fig. 33. Again, an LVDT was used to achieve closed-loop control. The differential pressure, which allows the spool to move from its neutral position, was generated by opening and closing the piezo valves. To assess the validity of this design, an experimental prototype of the 2/2 piezo valve was constructed and was experimentally tested in a hydraulic test rig. The

step tests performed on the test rig show that the piezo valve had high potential in terms of response speed since the time required for the displacement and for the pilot pressure to change from 10% to 90% of their final values was less than 5 ms. After the experimental validation, a Simulink model was developed to simulate the entire valve. The results of the simulated step tests showed that the response time was very fast, with about 6 ms predicted to reach 90% of the full opening. Concerning the sinusoidal tests, the predicted phase shift was 40.8° for an input sine signal with an amplitude of 1 mm and a frequency of 50 Hz, and 117.7° for an input sine signal with an amplitude of 1 mm and a frequency of 100 Hz.

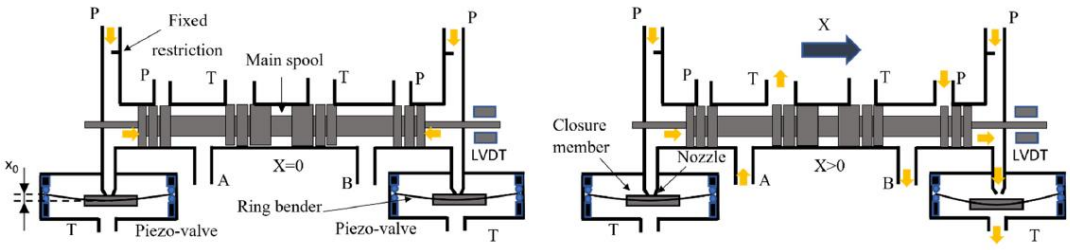

(**a**) (**b**)

Fig. 33. Operating principle of the piezo valve developed in [106], [107]: spool not modulating flow (**a**) and flow modulation (**b**).

The main advantage of this architecture compared to a conventional servovalve is in terms of power consumption. Indeed, common architectures of two-stage servovalves have high internal leakage in the pilot stage. As an example, for an inlet pressure of 210 bar, the quiescent flow in a Moog double nozzle-flapper valve (series 30) is around 0.73 L/min [21], whilst the leakage flow predicted through each piezo valve, when the spool was in the neutral position (null), was negligible and was equal to 0.029 L/min. This allowed the piezo valve to avoid a power consumption of about 0.4 kW in the neutral position, for a supply pressure of 210 bar. In addition, this novel configuration has the potential to reduce the complexity of the pilot stage because the torque motor is removed.

2.2.5 Discussion and Comparison

A comparison among the main types of PEAs (piezo stack, amplified piezo stack, bimorph bender, ring bender) is now provided, highlighting advantages and disadvantages of each type. A piezo stack actuator is fragile with respect to tensile stress; to manage this and to improve its dynamic performance, a correct value of preload must be applied to it. Piezo stacks can be employed to directly drive the sliding spool in direct drive servovalves [80], [81], [82] or to replace the torque motor in two-stage servovalves [83], [84], [85]; they can also be used to actuate a moving bushing sleeve in a hybrid direct drive servovalve [85] or to actuate a moving plate with annular grooves in a novel direct drive valve design [72]. It was shown that the direct actuation of servovalves using piezo stacks can provide some advantages, such as simplicity, fast response speed, high bandwidth, and high actuation forces (hence, high chip shear force capability). However, the main disadvantages resulting from the use of a piezo stack actuator are the low stroke and high dimensions. This means that a very large stack is needed to achieve high values of flow rate; therefore, a very large valve must be designed. It must also be taken into account

that the performance of a piezo stack actuator can be affected by changes in the operating temperature.

To overcome these issues, novel designs of servovalves actuated by piezo stacks with amplification mechanisms have been proposed in the scientific literature. The mechanical amplification, which is obtained through a lever allows higher displacement to be reached but at the expense of the actuation force, which is lower than that provided by a piezo stack. APAs can replace the torque motor to actuate the pilot stage of servovalves [92], but this causes an increase in the size of the pilot stage. Alternatively, they can replace heavier LFMs for the actuation of direct drive servovalves [88], [89], [90], [91].

Bimorph (rectangular) benders and ring benders have been suggested by a few authors as substitutes for the torque motor in two-stage servovalves in order to reduce the high complexity of the torque motor assembly. These PEAs are smaller than piezo stacks and APAs; therefore, their use will not affect an important characteristic of two-stage servovalves, which is the small size. The application of direct drive servovalves is not possible with these PEAs given their low actuation force. Rectangular benders have been proposed to actuate either the flapper of double nozzle-flapper servovalves [93], [94], [95], [96], [97] or the deflector of deflector jet servovalves [98], [99]. However, a ring bender might be preferred over a rectangular bender for the actuation of a pilot stage because of the higher actuation force of the former. Some prototypes have been developed using ring benders to actuate either the flapper of the pilot stage [101], [102] or a small spool serving as pilot spool [103], [104], [105]. The results are very satisfactory in terms of performance levels. A novel configuration has also been studied: making use of both two-ring benders and a different configuration for the hydraulic bridge, this novel valve can eliminate internal leakage in the pilot stage while obtaining a good step response and bandwidth [106], [107], [108].

All PEAs suffer from high hysteresis; therefore, closed-loop control systems are mandatory in all configurations to cope with hysteresis. Most of the proposed piezo valves need a position sensor to obtain closed-loop control; only very few configurations make use of mechanical feedback, thus not needing a position sensor [92], [98], [99].

The characteristics of the piezo valve typologies analysed in this paper are listed in Table 5 in order to summarize the advantages and disadvantages of these configurations.

Table 5. Comparison among the piezo valve typologies analysed.

Actuator	Valve Type	Description	Advantages	Disadvantages
Piezo stack	Direct drive servovalve [80], [81], [82]	A piezo stack or two piezo stacks directly move the spool	• Very fast response • No leakage of the pilot stage • Simplicity of construction (no pilot stage) • High chip shear force capability	• Large size • Low ratio of actuator displacement to actuator volume • Temperature dependent actuator • A position sensor is needed • High hysteresis
Piezo stack	Two-stage servovalve (double nozzle-flapper) [83], [84]	A piezo stack moves the flapper of the pilot stage in place of the torque motor	• Very fast response • Simplicity of construction (the torque motor is removed) • High chip shear force capability.	• Large pilot stage size • High leakage in the pilot stage • Temperature dependent actuator • A position sensor is needed • High hysteresis
Piezo stack	Two-stage servovalve (four pilot valves) [85]	Four piezo stacks control the main stage spool	• Very fast response • Simplicity of construction (the torque motor is removed) • High chip shear force capability	• Large pilot stage size • Temperature dependent actuators • Complexity of control • A position sensor is needed • High hysteresis
Piezo stack	Hybrid direct drive servovalve [85]	The bushing sleeve is actuated by a piezo stack, the spool by a LFM	• Very fast response • High flow • High chip shear force capability	• High leakage through the moving sleeve • Complexity of control • High hysteresis • Completely new design
Piezo stack	Direct drive valve with a moving plate [72]	A piezo stack actuates a moving plate with annular grooves	• Very fast response • Low internal leakage • Very high flow	• Temperature dependent actuator • A position sensor is needed • High hysteresis
Amplified Piezo Stack	Direct-drive servovalve [88], [89], [90], [91]	A piezo stack with mechanical amplification directly moves the spool	• Very fast response • No leakage of the pilot stage • Simplicity (no pilot stage) • Lower weight than LFMs	• Large size • Temperature dependence • Low chip shear force capability • A position sensor is needed • High hysteresis

Table 5. Cont.

Actuator	Valve Type	Description	Advantages	Disadvantages
Amplified Piezo Stack	Two-stage servovalve (double nozzle-flapper) [92]	A piezo stack or two piezo stacks directly move the spool	• Very fast response • Simplicity of construction (the torque motor is removed) • No need for a position sensor (mechanical feedback)	• Large pilot stage size • High leakage in the pilot stage • High hysteresis
Bimorph (Rectangular) Bender	Two-stage servovalve (double nozzle-flapper) [93], [94], [95], [96], [97]	A rectangular bender is used to actuate the flapper of the pilot stage	• Very fast response • Simplicity of construction (the torque motor is removed) • Low weight and small size	• Low force of the rectangular bender • High leakage in the pilot stage • A position sensor is needed • High hysteresis
Bimorph (Rectangular) Bender	Two-stage servovalve (deflector jet) [98], [99]	A rectangular bender is used to actuate the deflector of the pilot stage	• Very fast response • Simplicity of construction (the torque motor is removed) • No need for a position sensor (mechanical feedback) • Low weight and small size	• Low force of the rectangular bender • High leakage in the pilot stage • High hysteresis
Ring Bender	Two-stage servovalve (double nozzle-flapper) [101], [102]	Two ring benders actuate the flapper of the pilot stage	• Very fast response • Simplicity of construction (the torque motor is removed) • High chip shear force capability • Low weight and small size	• High leakage in the pilot stage • A position sensor is needed • High hysteresis
Ring Bender	Two-stage servovalve (pilot spool) [103], [104], [105]	A ring bender moves a pilot spool controlling the main stage spool	• Very fast response • High chip shear force capability • Low internal leakage • Very high flow	• A position sensor is needed • High complexity due to the small pilot spool • High hysteresis
Ring Bender	Two-stage servovalve (two pilot valves actuated by ring benders) [106], [107], [108]	Two ring benders control the main stage spool with no leakage in the pilot stage at null	• Very fast response • High chip shear force capability • Very low internal leakage • Very high flow	• A position sensor is needed • Need for two piezo actuators • High hysteresis

2.3 Digital Hydraulic Technology

As computer and microelectronic technology are increasingly used in industrial and aeronautical applications, the trend towards digitalization has become inevitable in the progress of hydraulic technology [2]. The outstanding results achieved in information, communication, and power electronics, coupled with the similarities between electrical and hydraulic systems, demonstrate that use of digital concepts into hydraulic technology could be instrumental to address the energy issues faced by conventional hydraulic systems [39], [41]. The term "digital hydraulic technology" was first introduced more than a decade ago by Matti Linjama [40]. Over the last years, this novel technology has gradually gained recognition as a distinct branch of fluid power, particularly in research fields. Alongside the traditional institutes in Tampere (TUT/IHA) [109], and Linz (JKU/IMH/LCM) [110], several other European research institutions, such as Bath University (PTMC) [111], RWTH Aachen (IFAS) [112], and Aalborg University (AAU/ET) [113], have focused their attention on various research related to digital fluid power.

Although digital pneumatic systems have been reported in literature [114], [115], [116], the majority of digital fluid power systems that have been studied so far are hydraulic. This is mainly because digital hydraulic technology offers significant advantages compared to conventional hydraulic technology, including higher reliability, lower energy consumption, greater precision in machine movements, fewer shutdowns, less production loss, higher component standardization, and lower original investment and maintenance costs [117], [118], [119], [120]. Fig. 34 illustrates the advantages of digital hydraulic technology over conventional hydraulic technology.

The standard definition of digital hydraulic technology, namely “a system which controls a discrete fluid with a modulated, discrete, digital signal directly to realize active and intelligent control of the system output”, was provided only four years ago in [121]. The authors noted that the previous definitions by M. Linjama [122] and H. Yang [123] only partially captured the characteristics of digital hydraulic technology. Based on the new definition, hydraulic components with the ability to discretize fluid flow or control signals are referred to as digital hydraulic components, while hydraulic systems composed of such components are known as digital hydraulic systems. Interestingly, the idea that discrete control could offer advantages over continuous control was already discussed in the 19th century [124], [125], [126].

The large variety of the digital hydraulic systems can be classified into two main categories [122]:

1. High frequency switching digital hydraulic systems;
2. Parallel digital hydraulic systems;

High-frequency switching digital hydraulic technology employs components that switch rapidly and continuously over time, allowing active and intelligent control of the system’s output [121]. These systems can be classified as temporal output discrete systems [127], [128]. To control the opening and closing of the components and achieve high-frequency switching, PWM techniques are employed, allowing the system to attain different discrete output values [121]. Theoretically, these systems can achieve any value within a specific range, although the output remains discrete due to

the switching frequency of the components [121]. The latter significantly impacts the system's performance, as lower switching frequencies provide better control but lead to increased pressure pulsations [122]. This technology finds practical use in Digital Hydraulic Buck Converters (DHBCs) [129], Antilock Braking Systems (ABSs) [130], and fuel injectors [131].

On the other hand, parallel digital hydraulic technology involves connecting digital hydraulic components in parallel to actively and intelligently regulate the system's output [121]. These systems can be classified as spatial output discrete systems [127], [132]. By employing digital coded signals, such as binary scheme, they can manage the opening and closing states of the parallel-connected components, allowing for different state combinations and enabling the system to achieve various discrete output values [121]. Furthermore, since these systems can attain a specific number of discrete output values, determined by the number of parallel-connected components, the need for frequent "on/off" switching of the components becomes unnecessary [122]. In comparison to high-frequency switching digital hydraulic systems, parallel digital hydraulic systems, used in applications such as Digital Flow Control Units (DFCUs) [133], Digital Hydraulic Power Management Systems (DHPMSs) [134], and Digital Hydraulic Hybrid Actuators (DHHAs) [135], offer enhanced scalability, programmability, and reliability [136].

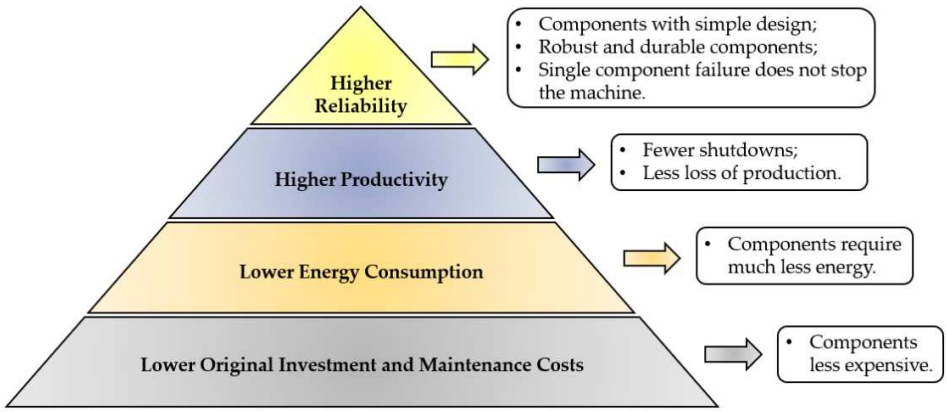

Fig. 34. Advantages of digital hydraulic technology compared to conventional hydraulic technology, adapted from [117].

2.3.1 Digital hydraulic valves

Digital hydraulic valves are the core components in digital hydraulic technology, and their characteristics have a great impact on the performance of the entire digital hydraulic system. These valves, being on/off, may not require a spool for flow adjustment and can have the same architecture as that of poppet or ball valves. The latter are capable of performing several working cycles with lower pressure drops than analogue and fragile spool valves because the flow area can be designed larger [49]. The main difference between a ball valve and a poppet valve is that the former may experience leakage due to the gap between the ball and the valve seat, while the latter ensures no leakage. A cross-section view and the relative ISO symbols of a two-way two-position (2/2) digital hydraulic valve with a poppet-type design are shown in Fig.35.

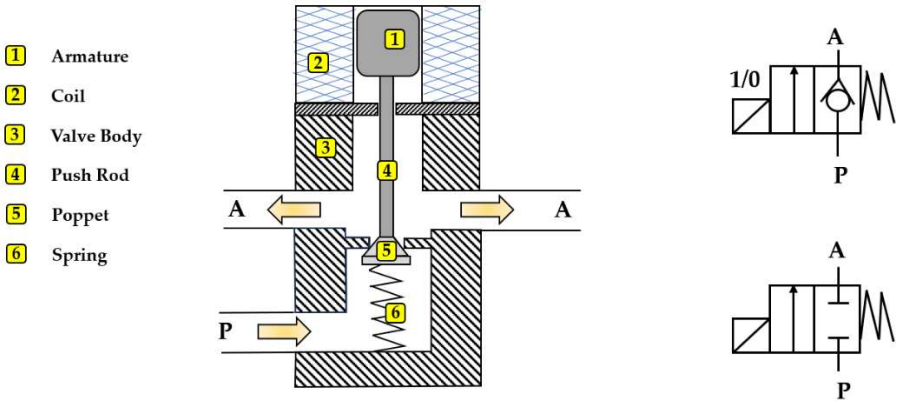

Fig. 35. A two-way two-position (2/2) digital hydraulic valve (poppet-type design) and its ISO symbols.

As shown in Fig. 35, the digital hydraulic valve is composed of an armature (1), a coil (2), a valve body (3), a push rod (4), a poppet (5) and a spring (6). Regarding its operation, when the coil is not energized, the absence of electromagnetic force causes the poppet to remain in close contact with the valve seat, thanks to the combined action of the spring force and hydraulic force. Conversely, upon energizing the coil, the progressively rising of the electromagnetic force overcomes the cumulative spring force and hydraulic force, initiating the gradual opening of the valve.

The use of digital on/off valves rather than conventional analogue spool valves, including proportional and servovalves, results in many advantages for digital hydraulic technology [40], [122]:

- Simpler and less expensive valves;
- Simpler control electronics;
- Higher robustness;
- Lower energy consumption;
- Longer lifetime;
- Higher flexibility;
- Easy connection with computers and PLCs;
- Higher safety and reliability;
- Less sensitive for contamination;
- No need for spool position feedback;
- No leak if poppet type valves are used.

In terms of this last point, proportional valves are designed with appreciable overlap (greater than 5% of the sliding spool stroke), leading to minimal leakage [17], [21]. In contrast, the sliding spool overlap in servovalves is usually very small (often 1% of the sliding spool stroke or less [26]), resulting in high leakage [17], [21].

Digital hydraulic valves can be controlled using digital control methods, which involve generating a Digital Command Signal (DCS) from a computer or controller to activate or deactivate the valve. The DCS is then amplified through an electronic power supply and used to drive the digital hydraulic valve, as shown in Fig. 36. Digital approaches are commonly used for controlling digital

hydraulic valves because the latter, being on/off, have only two steady states that can be compared with the "one" and "zero" of digital control methods. According on the different control approach, digital hydraulic valves can be further classified into [121]:

1. High Frequency Switching Digital Hydraulic Valves;
2. Parallel Digital Hydraulic Valves.

The digital control approach employed depends on both the specific application requirements and the characteristics of the valve being used. To illustrate this, Fig. 37 presents a classification of digital hydraulic valves based on the different digital control approaches involved.

Fig. 36. A scheme representing the control of digital hydraulic valves.

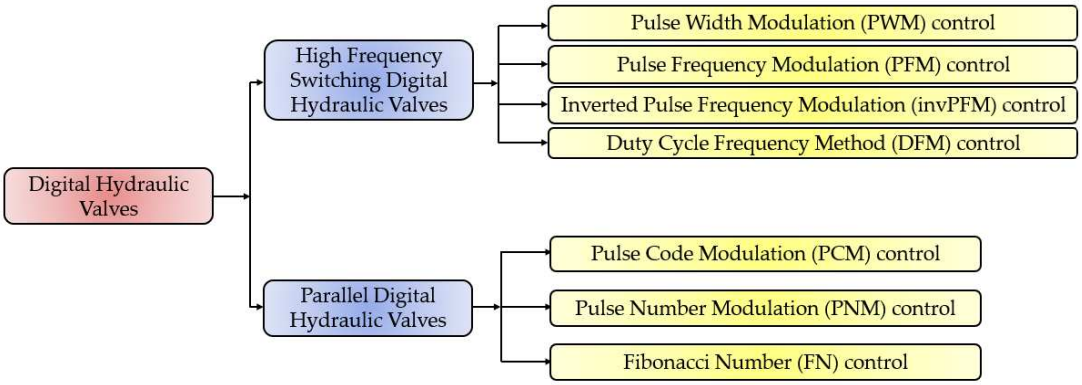

Fig. 37. Classification of digital hydraulic valves based on the different control approaches involved.

2.3.1.1 High Frequency Switching Digital Hydraulic Valves

Switching technologies are a type of digital hydraulic systems that involve the use of high frequency switching On/Off valves (HFSVs). These valves are commonly known as pulse modulation switching digital hydraulic valves since they use pulse modulation techniques to control the flow of hydraulic fluid. Among the pulse digital control approaches, the PWM, the Pulse Frequency Modulation (PFM), the inverted Pulse Frequency Modulation (invPFM) and the Duty Cycle Frequency Method (DFM) are the most common employed to adjust the valve's output [137]. To differentiate between the various pulse digital control methods, it is necessary to examine the DCS used for controlling the poppet position of the HFSV. In pulse control signals, the DCS is an alternating signal that switches between "logical one" and "logical zero" states, which are represented

by the pulse duration (t_{ON}) and the pause time (t_{OFF}), respectively [137]. The sum of the pulse duration (t_{ON}) and the pause time (t_{OFF}) gives the overall period (τ) of the DCS:

$$\tau = t_{ON} + t_{OFF} \tag{2}$$

To describe the amount of the pulse duration (t_{ON}), the concept of duty cycle is introduced. The duty cycle, denoted by (*%DC)*, is the ratio of the pulse duration (t_{ON}) to the overall period (τ) of the DCS, as evaluated in the following equation:

$$(\%DC) = \frac{t_{ON}}{\tau} \tag{3}$$

Since the previous control approaches are limited to a single control variable, specifically the pulse duration (t_{ON}) or the pause time (t_{OFF}), a third equation is necessary to differentiate the DCS among the main pulse digital control approaches, as shown in Table 6 [137], [138], [139].

Table 6. Pulse digital control approaches used to control HFSVs [137], [138], [139].

Pulse Digital Control Approach	Control Variable	Third Equation	Variables Calculated
PWM	t_{ON}	$\tau = \frac{1}{f} = \text{const.}$	$t_{OFF} - (\%DC)$
PFM	t_{OFF}	$t_{ON} = \text{const.}$	f
invPFM	t_{ON}	$t_{OFF} = \text{const.}$	f
DFM	t_{ON}	$(\%DC) = \text{const.}$	$t_{OFF} - f$

The PWM method controls the pulse duration (t_{ON}), while keeping the period (τ) or the switching frequency (f = 1/ τ) constant, in order to modify the duty cycle (%DC) of the DCS. In contrast, the other three digital control approaches, namely the PFM, the invPFM and the DFM, can be used to manage the frequency (f) of the DCS.

An illustration of the DCS used to control HFSVs with these four pulse digital control approaches is shown in Fig. 38.

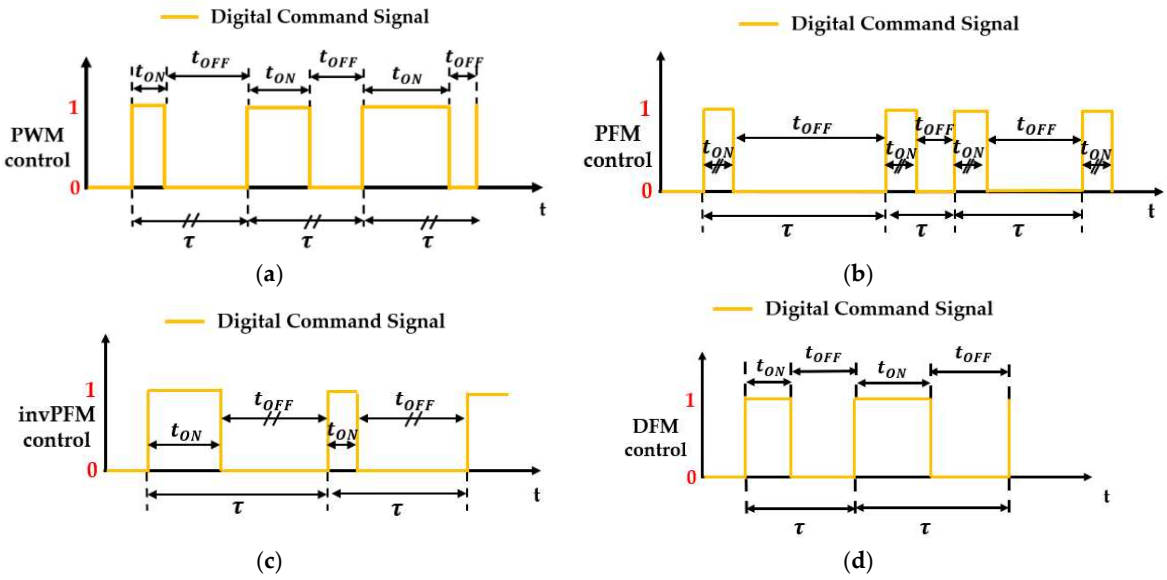

Fig. 38. Differences between the digital command signal used to control HFSVs: (**a**) PWM; (**b**) PFM; (**c**) invPFM; (**d**) DFM, adapted from [137], [138], [139].

The use of different pulse modulation techniques allows for the description of the working principle of a two-way two-position (2/2) HFSV. As shown in Fig. 39, a pulse control signal (from 0 to 1) is delivered to the HFSV and flow modulation is obtained by adjusting the frequency (through PFM, invPFM or DFM controls) or the duty cycle (through PWM control) of the DCS. The controllability of the valve is influenced by the switching frequency. A lower switching frequency results in higher controllability, but it also leads to an increase in pressure pulsation and a decrease in the average flow rate obtained. To suppress noise and achieve a smoother flow rate, accumulators and inertance tubes are commonly employed [140]. In the graph, the average flow rate provided by the 2/2 HFSV is represented by the symbol (Q_M) on the right y-axis.

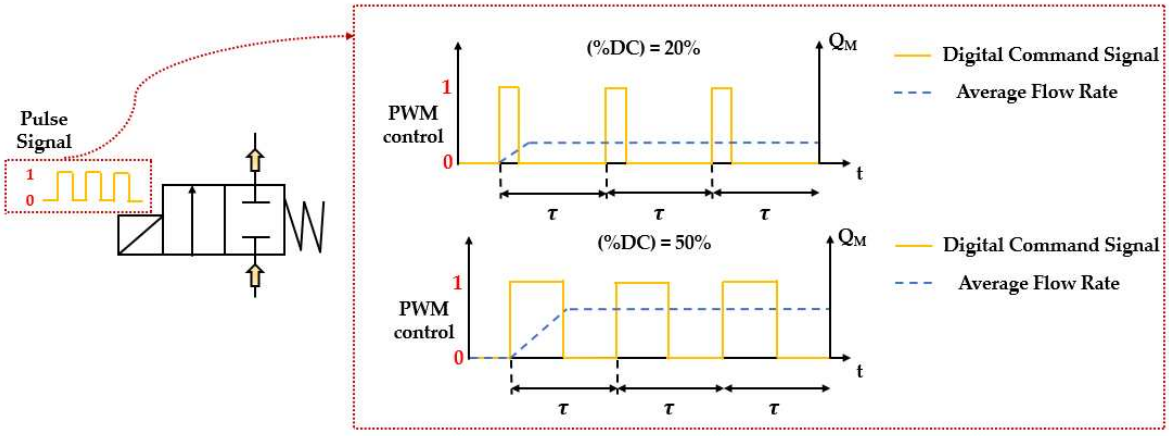

Fig. 39. Two way two-position (2/2) HFSV controlled with the PWM control approach.

The behaviour of an HFSV (poppet-type design) changes depending on how the control variable of the DCS is modulated. There are five distinct operation modes [137], [139]:

1) Deactivated Mode: the pulse duration (t_{ON}) is so short that the poppet does not move;
2) Ballistic Mode: increasing the pulse duration (t_{ON}) the poppet starts to move, but it does not reach the upper end stop and is pushed back to the lower end stop;
3) Normal Mode: the pulse duration (t_{ON}) is long enough to fully open the valve;
4) Inverse Ballistic Mode: the pause time (t_{OFF}) is so short that the poppet cannot reach the lower end stop;
5) Activated Mode**:** the pause time (t_{OFF}) is so short that the valve remains always open.

Fig. 40 depicts the five operation modes of an HFSV controlled by the PWM technique [137]. In the graph, the poppet position of the HFSV is represented by the symbol (x) on the right y-axis.

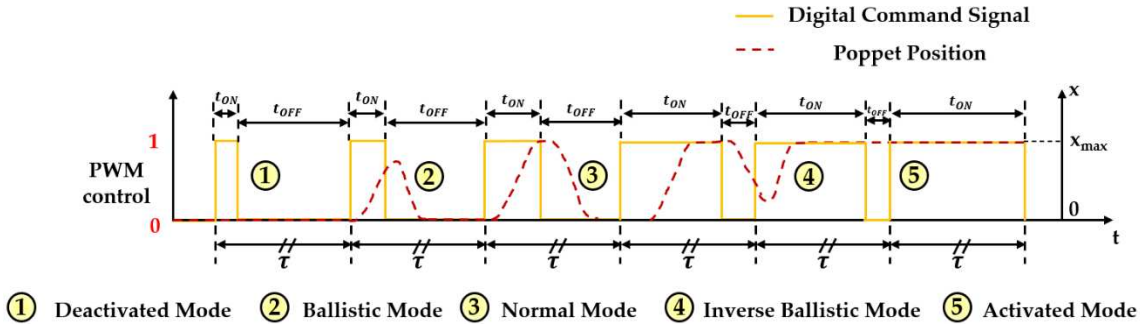

Fig. 40. Different behavior of an HFSV controlled by PWM technique, adapted from [137].

A thorough examination of Fig. 39 and Fig. 40 clearly reveals that the crucial performance indicators of an HFSV encompass its static flow characteristics, dynamic characteristics, power consumption and noise and vibrations [141]. The dynamic characteristic of an HFSV represents its behaviour during opening and closing, while the static flow characteristic depicts the relationship between the average output flow rate and the duty cycle of the pulse control signal, measuring the level of linearity between them [142]. To gain a better understanding of these two performance indicators of HFSVs, Fig. 41 presents the schematic dynamic diagram and the static flow curve of an HFSV (poppet-type design) controlled using the PWM approach.

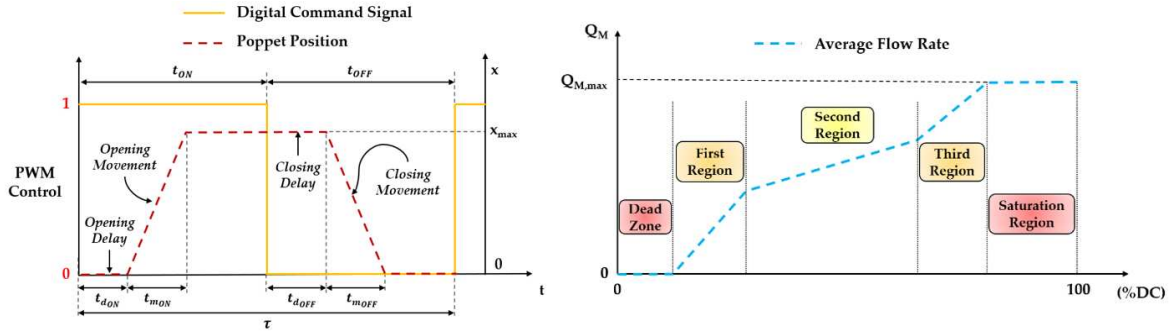

Fig. 41. Performance Indicators of an HFSV: (**a**) Schematic Dynamic Movement; (**b**) Static Flow Curve, adapted from [142].

Fig. 41(a) illustrates the dynamic performance of the HFSV during its operation. This performance is quantified using four key parameters, i.e. the delay before it starts to open (opening delay time, $t_{d_{ON}}$), the duration it takes to fully open (opening moving time, $t_{m_{ON}}$), the delay before it starts to close (closing delay time, $t_{d_{OFF}}$), and the duration it takes to fully close (closing moving time, $t_{m_{OFF}}$). The combined total of the opening delay time and opening moving time defines the opening switching time of the valve, while the combined total of the closing delay time and closing moving time defines the closing switching time of the valve. An important detail to note is the presence of hysteresis in the movement of the HFSV's poppet. The latter is caused by two factors, namely the electrical hysteresis due to the inductance of the coil, and the inherent mechanical hysteresis [143]. These factors result in a delay in the opening switching time when the coil is energized, and a delay in the closing switching time when the coil is de-energized. In contrast, Fig. 41(b) presents the five distinct regions of the static flow curve of the HFSV [144], each corresponding to the operational modes seen earlier in Fig. 40. Examining Fig. 41 closely suggests that longer opening and closing delay times increase the dead zone and saturation region, which in turn decreases the linearity of the flow rate [142]. Additionally, extended opening and closing movement times expand the first and third regions, further reducing linearity [142]. This brief analysis suggests that improving the dynamic performance of the HFSV is crucial for enhancing the linearity of its output flow rate. This improvement can be achieved by reducing the interval time associated with the opening delay, opening movement, closing delay, and closing movement.

To meet the requirements of improved dynamic performance and flow linearity, and reduced power consumption, noise and vibration for a single HFSV, scholars have explored different Discrete Control Voltage (DCV) strategies or various PWM strategies [142]. Regarding the former, the controller adjusts the DCS based on the DCV strategy employed, combining multiple DCV signals with different amplitudes according to a specific logic. Specifically, four DCV signals have been explored over the years. The working principle of each DCV signal is detailed in Table 7, while Fig. 42 provides an illustration for a better understanding [142]. Specifically, Fig.42 shows how the controller modifies the DCS waveform based on the employed DCV strategy in order to obtain the desired DCV signal.

Table 7. Working Principle of four different DCV Strategies [142].

DCV Strategy	Controller Action at a Specific Instant in Time				
	System Start	**Rising Edge of DCS**	**HFSV Critical Max Opening Current**	**HFSV Maximum Opening**	**Falling Edge of DCS**
Single-Voltage Control	—	DCV with fixed amplitude for valve opening	—	—	The DCV drops to zero for valve closing
Double-Voltage Control	—	High voltage for accelerating valve opening	—	The controller switches to low voltage	The voltage drops to zero, initiating the valve closing
Three-Voltage Control	—	High voltage for improving the opening speed	—	The controller switches to low voltage	Reverse voltage for increasing closing speed
Four-Voltage Control	Preload voltage at system start	High voltage for accelerating valve opening	The controller switches to holding voltage	—	Reverse voltage for increasing closing speed

In single-voltage control, recent research highlights its shortcomings in meeting HFSV requirements for dynamic performance, power efficiency, vibration reduction, and noise control [145]. Double-voltage control, in comparison, enhances both the dynamic performance (in terms of the opening and closing speed) and power consumption, even though it suffers in terms of robustness due to the significant variation in the dynamic characteristics of the HFSV at different oil supply pressures [146]. Three-voltage control innovatively employs reverse voltage during valve closing, rapidly reducing electromagnetic force and improving closing speed, while also improving energy conversion efficiency and robustness by adjusting the DCV signal amplitude [147], [148], [149], [150]. Four-voltage control introduces a preload-voltage excitation before valve opening, significantly enhancing dynamic performance (in terms of the opening speed) compared to single-voltage, double-voltage, and three-voltage control strategies [151], [152].

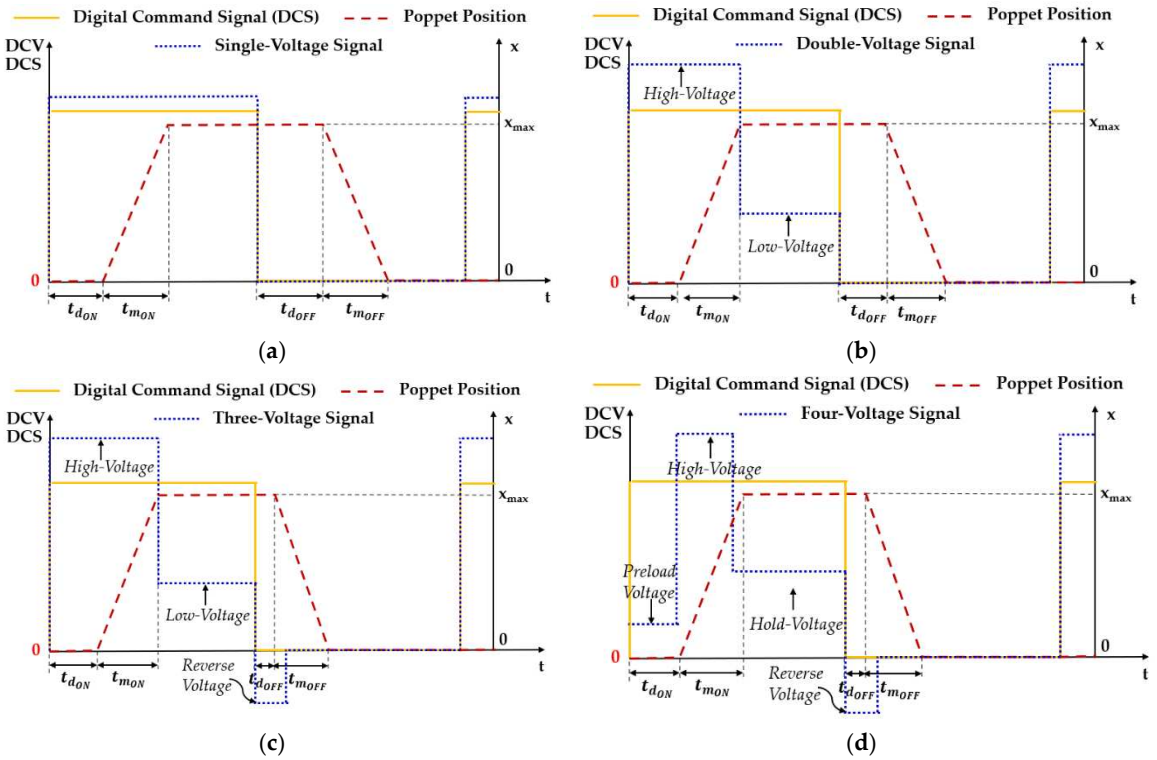

Fig. 42. Four different DCV signals used to control a single HFSV: (**a**) Single-Voltage control; (**b**) Double-Voltage control; (**c**) Three-Voltage control; (**d**) Four-Voltage control, adapted from [142].

On the other hand, in the realm of pulse control strategies, researchers have explored several PWM subcategories, including the compound PWM control, the adaptive PWM control, the intelligent PWM control, and the soft-landing PWM control. The compound PWM control involves multiple pulse control signals with varying carrier frequencies, enhancing the dynamic performance and energy efficiency of HFSVs [153]. The adaptive PWM control adjusts duty cycles of pulse control signals based on oil supply pressure, ensuring optimal dynamic performance under different operating conditions [154]. The intelligent PWM control allows the dynamic characteristics of a single HFSV to be self-adjusted and improved by controlling opening and closing initial currents through intelligent pulse control signals [155], [156]. The soft-landing PWM control minimizes noise and vibration during rapid HFSV operations, though it comes with a slight decline in dynamic performance compared to conventional PWM control [157].

To summarize, Table 8 offers a comparison of different control strategies explored for a single HFSV, encompassing both DCV and PWM approaches. The assessment considers aspects such as opening and closing dynamics, energy efficiency, vibration and noise reduction, and robustness. Performance indicators in the table are rated on a scale from 1 to 5, with higher values indicating better performance in the respective category [142].

Table 8. PWM and DCV strategies performance comparison for a single HFSV [142].

	Digital Control Approach	Opening Dynamic Performance	Closing Dynamic Performance	Energy Efficient	Noise and Vibration Reduction	Robustness
DCV Strategies	Single-Voltage Control	4	1	1	1	1
	Double-Voltage Control	4	2	4	1	2
	Three-Voltage Control	4	4	3	2	3
	Four-Voltage Control	5	4	2	3	3
PWM Strategies	Compound PWM	4	4	3	1	3
	Adaptive PWM	4	5	4	3	4
	Intelligent PWM	5	5	4	3	4
	Soft-Landing PWM	3	4	3	5	3

Optimal opening dynamics are achieved with the four-voltage control and intelligent PWM control. Regarding closing dynamics, effectiveness is observed in the adaptive PWM control and intelligent PWM control, utilizing a dynamically applied reverse voltage signal. In terms of power consumption, the double-voltage control, adaptive PWM control and Intelligent PWM control are the most efficient, while the single-voltage control is the least efficient. The soft-landing PWM control excels in vibration reduction, and the robustness is highest in the adaptive PWM control and intelligent PWM control, showing minimal sensitivity to variations.

Independently on the control strategy, HFSVs can be effectively used in a digital hydraulic circuit to replicate the functionality of a conventional four-way three-position (4/3) spool valve. This is achieved by using four 2/2 HFSVs, each responsible for establishing one of the fluid pathways: P → A, A → T, P → B, and B → T This setup enables the realization of the digital hydraulic circuit of a four-way three-position (4/3) HFSV. The working principle of the 4/3 HFSV, composed of four 2/2 HFSVs, is illustrated in Fig. 43.

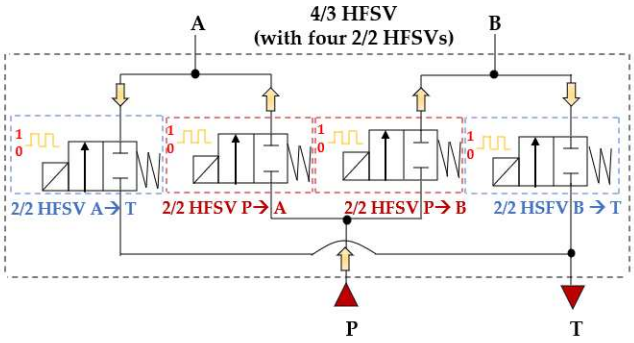

Fig. 43. Four-way three-position (4/3) HFSV made up of four 2/2, adapted from [122].

Interestingly, the system can be simplified by reducing the number of components from four 2/2 HFSVs to just two 4/2 HFSVs. This is achievable if the digital hydraulic circuit of the 4/3 HFSV is configured as shown in Fig. 44 [50].

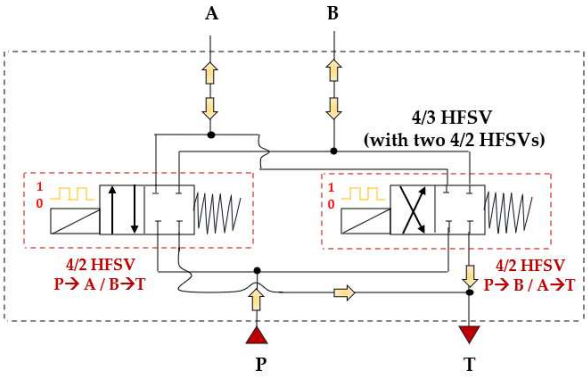

Fig. 44. Four-way three-position (4/3) HSFV composed of two 4/2 HFSVs [50].

2.3.1.2 Parallel Digital Hydraulic Valves

The Parallel Digital Hydraulic Valve, also known as the Digital Flow Control Unit (DFCU), is made up of multiple robust on/off valves connected in parallel, enabling precise flow control [133]. Each individual on/off valve in the system possesses key parameter characteristics, including the switching time, reliability, repeatability, and flow capacity [40]. Concerning the latter, there are three conventional control approaches for determining the flow capacity of each on/off valve within a DFCU [40]:

1. Pulse Number Modulation (PNM): With this approach, the On/Off valves have the same size and, thus, the same flow capacity (1:1:1:1…);
2. Pulse Code Modulation (PCM): This method is based on the use of the orifices positioned after the valves, which enable the flow capacities of the different valves to be set according to a binary series (1:2:4:8:16…);
3. Fibonacci Numbers (FN): With this scheme, the orifices positioned after the valves allow the flow capacities of the different valves to be set according to a Fibonacci series (1:1:2:3:5:8:13…).

Independently on the coding, a DFCU has 2^N possible combinations (where N represents the number of parallel connected switching valves), which are called states of the DFCU. By activating and deactivating these valves, the flows from each valve are combined, obtaining different state of the DFCU. This control strategy was already proposed by Flugge-Lotz and Taylor in the past century, where multiple, parallel-operated actuators with different gains could be switched in different logic combinations [158].

Another fundamental property of the DFCU is that it does not require the switching of any individual valve between “on” and “off” to achieve continuous system output. Valve switching is only needed when the state of the DFCU changes [159].

Fig. 45 depicts a picture of a DFCU composed of three two-way two-position (2/2) on/off valves, along with its simplified symbol and the corresponding working principle using the PCM coding. The two broken lines in the simplified symbol indicate almost proportional flow control of the unit, while the number of valves in the unit is determined by the variable N.

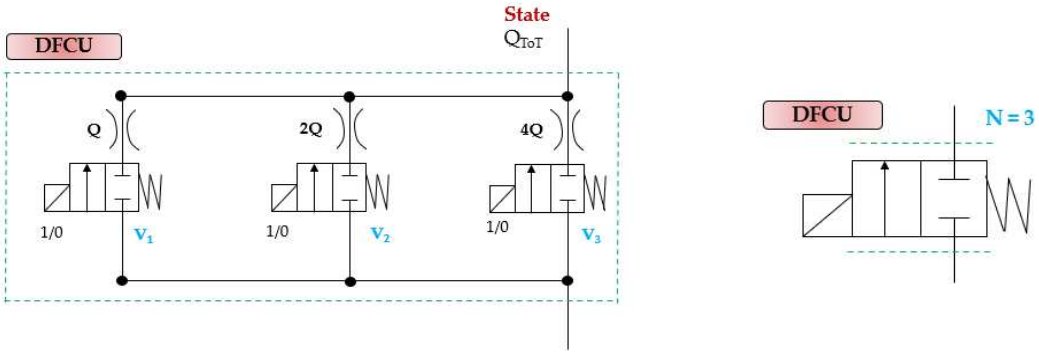

(**a**) (**b**)

V_1	V_2	V_3	DFCU state Q_{ToT}
0	0	0	0
1	0	0	Q
0	1	0	2Q
1	1	0	3Q
0	0	1	4Q
1	0	1	5Q
0	1	1	6Q
1	1	1	7Q

(**c**)

Fig. 45. A Digital Flow Control Unit (DFCU) made up of three two-way two-position (2/2) on/off valves: (**a**) Complete representation; (**b**) Simplified symbol (N represents the number of parallel connected switching valves); (**c**) Binary state table, adapted from [117].

Similarly to the 4/3 HFSV, four independent DFCUs can be used in a digital hydraulic circuit to replace the pathways of a conventional four-way three-position (4/3) spool valve, specifically (P → A, A →T, P → B, B → T), and replicate its function. The working principle of the four-way three-position (4/3) DFCU Valve is shown in Fig. 46, where each of the four DFCUs is composed of five 2/2 on/off valves [160], [161].

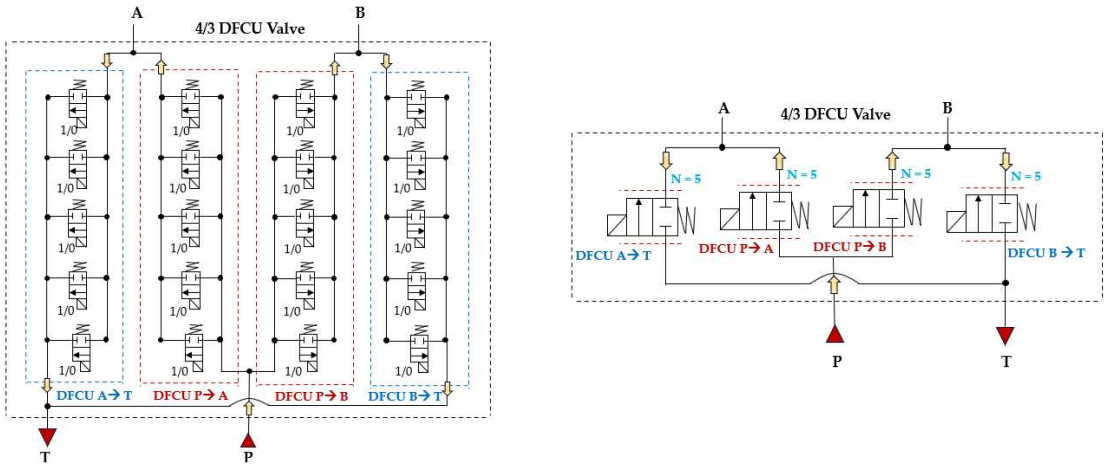

Fig. 46. Four-way three-position (4/3) DFCU Valve: (**a**) Complete representation; (**b**) Simplified representation, adapted from [160], [161].

As shown in Fig.46(a), the on/off valve that makes up each DFCU is a normally closed two-way two-position (2/2) On/Off valve, which blocks flow when it is in the unactuated position (0) and allows the passage of flow when actuated (1). Clearly, the more precise flow rate is required, the more on/off valves need to be used in each DFCU [117]. In particular, the same controllability of a conventional spool valve can be achieved if the maximum discrete flow rate provided by each DFCU is approximately 200Q, where Q represents the flow rate provided by the minimum valve of each DFCU, as previously shown in Fig. 45(a). This can be obtained if each DFCU is equipped with 200 equally sized on/off valves (using PNM coding), 11 on/off valves (with FN coding) or 8 on/off valves (via PCM coding) [40]. Fig. 47 illustrates a performance comparison between a 4/3 proportional valve, which uses machined notches and grooves on the sliding spool to achieve the desired flow rate trend based on spool position [17], and a 4/3 DFCU Valve consisting of four DFCUs, each incorporating 8 on/off valves and controlled through PCM coding [117]. In the graphs of Fig. 47, x/x_{Max} represents the ratio between the spool stroke and the maximum spool stroke; whereas Q/Q_{ToT} is the normalized flow rate, namely the ratio between the flow rate and the maximum flow rate provided by the valve.

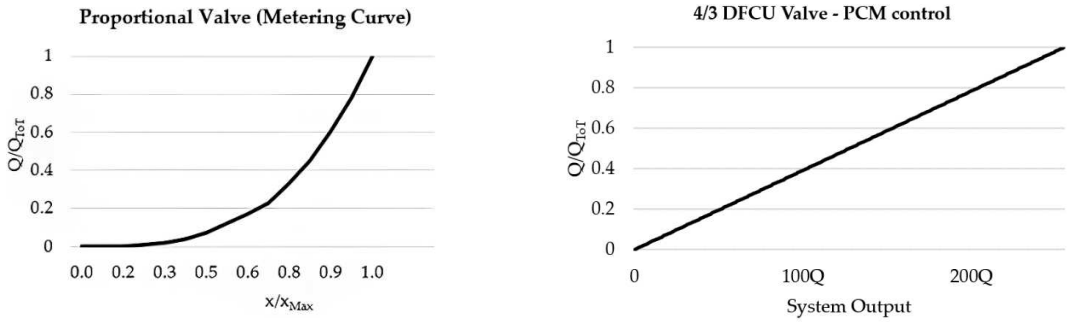

Fig. 47. Comparison between analogue and digital hydraulic valves: (**a**) Proportional Valve; (**b**) 4/3 DFCU Valve, adapted from [117].

Regarding the coding schemes, the PCM is the most used for controlling DFCUs. [162]. Its main advantage is the high resolution, namely the ratio between the maximum flowrate and the largest step between two consecutive flow-steps [163]. However, the PCM scheme has an important drawback, namely the high probability of pressure peaks caused by non-uniform on/off valve switching times [164]. During DFCU state changes, some valves may close before others open, resulting in brief periods of undesired flow rates, which led to pressure peaks [165]. Conventional solutions such as accumulators, pressure relief valves, and orifices are often expensive and can negatively affect system dynamics [166]. In response, scientific researchers have proposed other solutions, such as altering the holding time of the valves [167], or synchronizing their switching time [168], [169]. Additionally, modifying the coding scheme is another option for mitigating the pressure peaks [168], [170].

The PNM is the simplest control approach that uses on/off valves with the same size and, thus, with equal flow capacities. The PNM scheme is considered theoretically superior to the PCM coding due to its faster speed, lower power consumption, and excellent fault-tolerance performance [171], [172]. Furthermore, it is also considered the most effective strategy for addressing pressure peak issues. This is because, when the DFCU state changes, the valves, being of the same size, open and close simultaneously [165]. Fig. 48 shows a comparison of the fault-tolerance performance between the PNM and the PCM approaches used to control a DFCU [122].

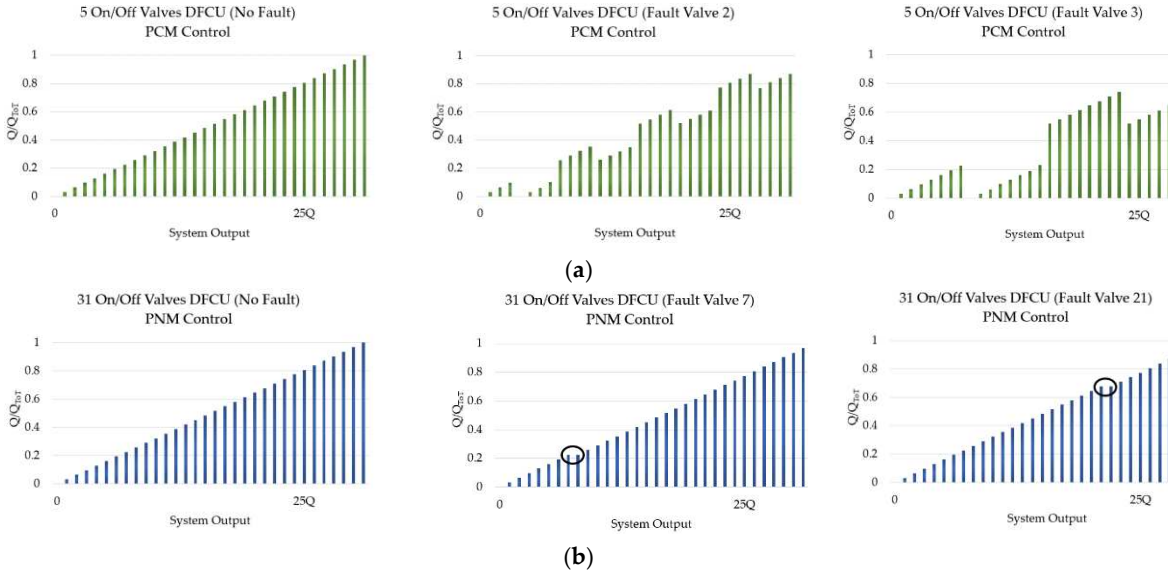

Fig. 48. Fault-tolerance performance: (**a**) PCM coding; (**b**) PNM coding, adapted from [122].

The main weakness of the PNM coding scheme is due to the fact that a large number of on/off valves is needed in order to obtain a good resolution. Unfortunately, considering the size problem of a DFCU, the PNM control approach cannot be used in most situations [122]. Fig. 49 shows the poor resolution of the PNM control approach compared to the PCM coding scheme.

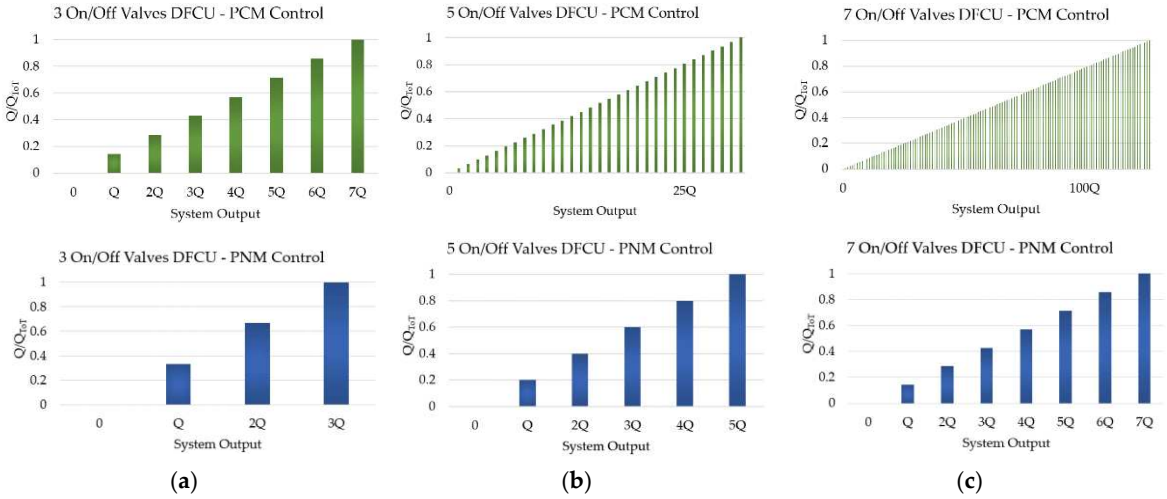

Fig. 49. Comparison between the PCM and the PNM control approaches: (**a**) DFCU made up of 3 On/Off Valves; (**b**) DFCU made up of 5 On/Off Valves; (**c**) DCU made up of 7 On/Off Valves, adapted from [122].

As shown in Fig. 49(c), a DFCU with 7 on/off valves achieves a maximum flow rate of 128Q, when the PCM coding is involved. In contrast, the DFCU offers a maximum flow rate of only 7Q, when the PNM is used.

The FN control approach is a compromise between the PCM and the PNM coding. It has the advantage of limiting pressure peaks more effectively than binary coding while requiring fewer valves than the PNM approach [165]. Additionally, it enhances redundancy and enables optimization of valve operations [40].

The strengths and weaknesses identified in conventional DFCU coding schemes underscore the persistent challenge in formulating an effective control strategy that shows high-performance in various aspects, encompassing control accuracy, valve lifespan, and pressure peak management. Consequently, researchers have recently shifted their focus towards investigating the potential application of PWM approaches for DFCU control [142]. This technique uses PWM signals with different duty cycles to individually control each on/off valve that is connected in parallel within a DFCU, enabling accurate flow rate adjustments [173]. However, this method presents several challenges, such as pressure peaks, a shorter lifespan, and the production of vibration noise [142].

In an effort to address these challenges, a combination of different coding control strategies, such as PWM and PCM has been explored [120]. This combined strategy, compared to the PCM coding scheme, not only provides superior control performance but also helps to mitigate the impact on the flow rate during valve switching [142]. As a result, it presents a promising solution for improving both the efficiency and longevity of DFCUs.

In summary, Table 9 offers a comparison of the performance of control strategies for DFCUs. The performance indicators in the table are represented by values ranging from 1 to 5, where a higher value signifies better performance in the corresponding category [142].

Table 9. Control strategies performance comparison for DFCUs [142].

Digital Control Approach	Control Accuracy	Lifespan	Pressure Peaks
PCM	3	3	3
PNM	1	5	1
FN	2	4	2
PWM	5	1	5
PWM + PCM	4	2	4

Table 9 indicates that the PWM approach stands out in terms of control accuracy. However, it does not perform as well when considering DFCUs' lifespan and pressure peaks problem. In these aspects, the PNM scheme is shown to be the most effective among all coding schemes. Table 9 also highlights that PCM coding is the most commonly used strategy due to its balanced performance across all categories.

2.3.2 Research Advancements in Digital Hydraulic Valves

Digital hydraulic valves are the key components of digital hydraulic technology. Considering their benefits over conventional analogue spool valves, this section focuses on exploring the research progress and performance of digital hydraulic valves developed over the years.

2.3.2.1 Research Progress in High Frequency Switching Digital Hydraulic Valves

HFSVs are designed to meet specific criteria. These include the ability to achieve high switching frequencies and high switching speeds, specifically less than 5 ms. Additionally, HFSVs aim to minimize pressure losses and deliver a large flow rate while maintaining a compact size [122]. Currently, the fastest valves can achieve switching frequencies ranging from 50 to 150 Hz, with the potential to reach up to 1000 Hz for short-term operation in very small valves [174].

In literature, the various high frequency switching digital hydraulic valves can be classified into two main categories based on their actuation system:

- HFSVs with electromagnetic actuators;
- HFSVs with smart materials.

2.3.2.1.1 HFSVs with electromagnetic actuators

Research publications on the development of HFSVs with electromagnetic actuators can be found regularly from 1970s [175], [176], [177], [178]. All these valves presented very fast response times, but their flow rates were limited to very low flow applications. A valve capable of producing higher flow rates was realized in [179]. However, it presented a complex design and high energy consumption.

In 1991, to increase the flow rate, minimize the power consumption, and at the same time, maintain simplicity of design, Cui et al. designed a novel rotary 2/2 HFSV (poppet type) [180]. It presented a single stage structure but could perform as a double-stage valve. Fig. 50 provides an illustration of the operational principle. Referring to Fig. 50(a), the pressurized fluid initially entered chamber (A) which was sealed, causing no movement of the poppet. A DCS was then delivered to the torque motor, allowing the poppet to rotate by a small angle in the position shown in Fig. 50(b).

This action aligned the machined ports on the poppet with the ports on the valve body, thereby allowing the pressurized fluid to flow through the path (B) and reach chamber (C). The pressure imbalance between the supply and load pressure caused the poppet to move to the right, opening the valve. To close the valve, the torque motor rotated the poppet counterclockwise, as illustrated in Fig. 50(c). In this way, the chamber (C) was connected with the tank, and the pressure difference between the supply and tank pressures caused the poppet to return to its original position, closing the valve.

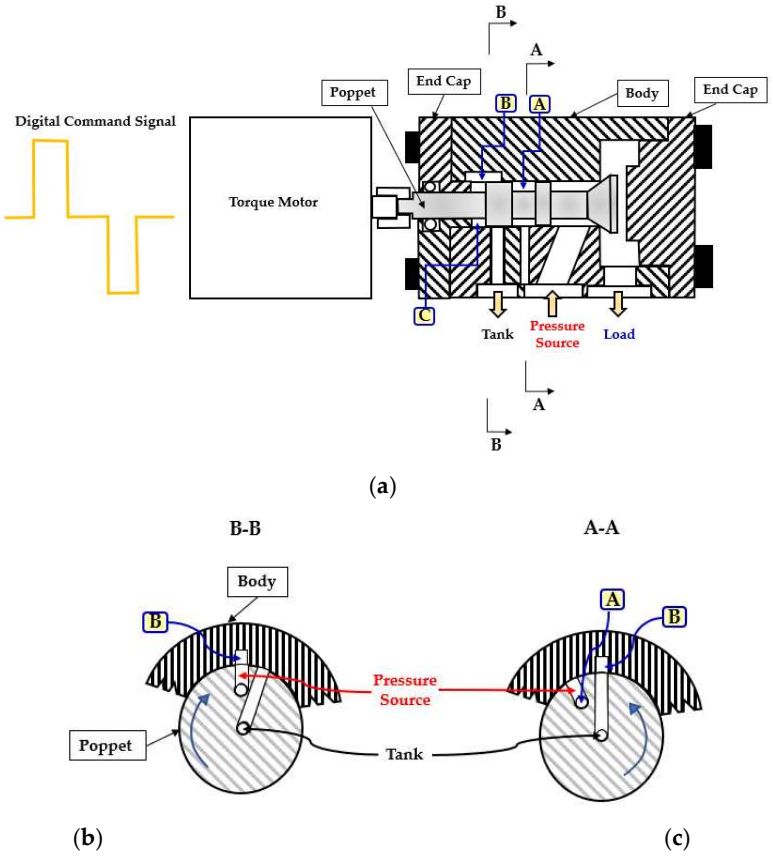

Fig. 50. Redrawn schematic representation of the 2/2 HFSVs realized in [180]: (**a**) Basic Configuration; (**b**) Operating principle to open the valve; (**c**) Operating principle to close the valve.

To assess the validity of the valve design, a prototype was fabricated, and experimental tests were conducted. The results showed that with a pulse signal frequency of 50 Hz, a duty cycle of 80%, and a pressure drop of 90 bar, the valve had a switching time of approximately 2.5 ms and produced a flow rate of around 18 L/min. However, the value of the flow rate decreased to 10 L/min when the pressure drop was set to 50 bar.

Three years later, the Chinese company Guizhou Honglin Machinery developed a 3/2 HFSV (ball type), whose schematic representation is shown in Fig.51(a) [132], [181]. When the coil (1) was energized, the electromagnetic force caused the armature (2) and the entire ball assembly (i.e., supply ball (3), separating pin (4), and returning ball (5) to move to the right. As a result, the port (A) was

connected to port (P) and separated from port (T), as depicted in Fig.51(b). Conversely, when the coil was de-energized, the hydraulic pressure of the inlet port (P) pushed back the ball assembly to the left side. As a result, the port (A) was connected to port (T) and separated from port (P), as illustrated in Fig. 51(c).

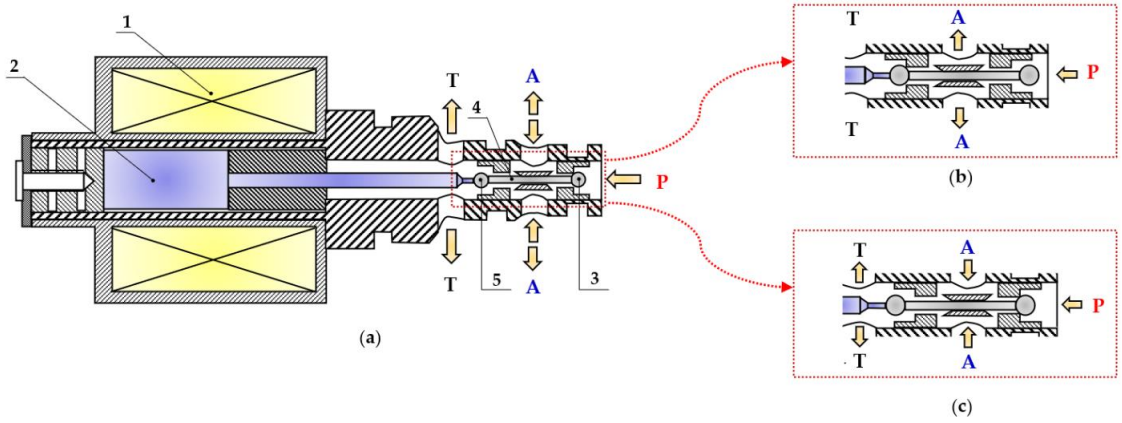

Fig. 51. Redrawn schematic representation of the 3/2 HFSV realized in [181]: (**a**) Basic configuration: (**b**) Open Position; (**c**) Closed Position.

According to manufacturer specifications, the opening and closing switching times of the valve were about 3.5 ms and 2.5 ms, respectively [132]. The maximum flow rate of 9 L/min was obtained at a pressure drop of 200 bar [132]. In recent years, this valve has been the subject of several scientific publications. Kong et al. enhanced the dynamic response of the 3/2 HFSV by replacing the single coil with multiple parallel solenoids [182]. By applying a driving voltage of 24 V at a pressure drop of 150 bar, the valve switching times were reduced from 1.5 ms to 1.16 ms for opening and from 1.54 ms to 1.3 ms for closing, respectively. However, the use of a parallel configuration also resulted in increased energy consumption and temperature of the valve. To minimize the energy consumption and temperature rise of the 3/2 HFSV, Zhong et al. proposed an intelligent PWM algorithm for controlling the valve in [155]. The experimental results showed that the algorithm had the potential to make the valve switching times faster, with the opening time being reduced by 23.6% and the closing time by 17%. Moreover, it significantly decreased energy consumption by 88.8% and limited the temperature rise by 69.9%.

In 2007, Tu et al. proposed a self-spinning rotary 3/2 HSFV (spool type) [183]. The operating principle of this rotary valve can be described by examining Fig.52. In particular, considering the illustration in Fig. 52(a), the inlet pressure rail on the valve sleeve supplied the rhombus inlet nozzles for generating fluid momentum. The helical barriers captured the fluid momentum and redirected it towards the centre of the valve spool. After reaching the valve spool centre, the fluid was compelled to move in the axial direction via the internal axial passages that guided it to the outlet turbines, as shown in Fig. 52(b). Then, the outlet turbine blades re-accelerated the fluid outward and tangential to the spool. As a result, a torque was generated on the spool, enabling its rotation. With the spool rotation, the inlet turbine continuously switched the fluid flow between the load and the tank, as

illustrated in Fig. 52(c.) The duty cycle of the DCS was regulated based on the spool axial position, which modulated the orifice area ratio between the two hydraulic pathways during each rotation. To study the performance of this valve configuration, a detailed dynamic model was realized in Matlab. The numerical predictions showed that the valve could achieved a switching frequency of 84 Hz, and it could produce a flow rate of 40 L/min at a pressure drop of 70 bar.

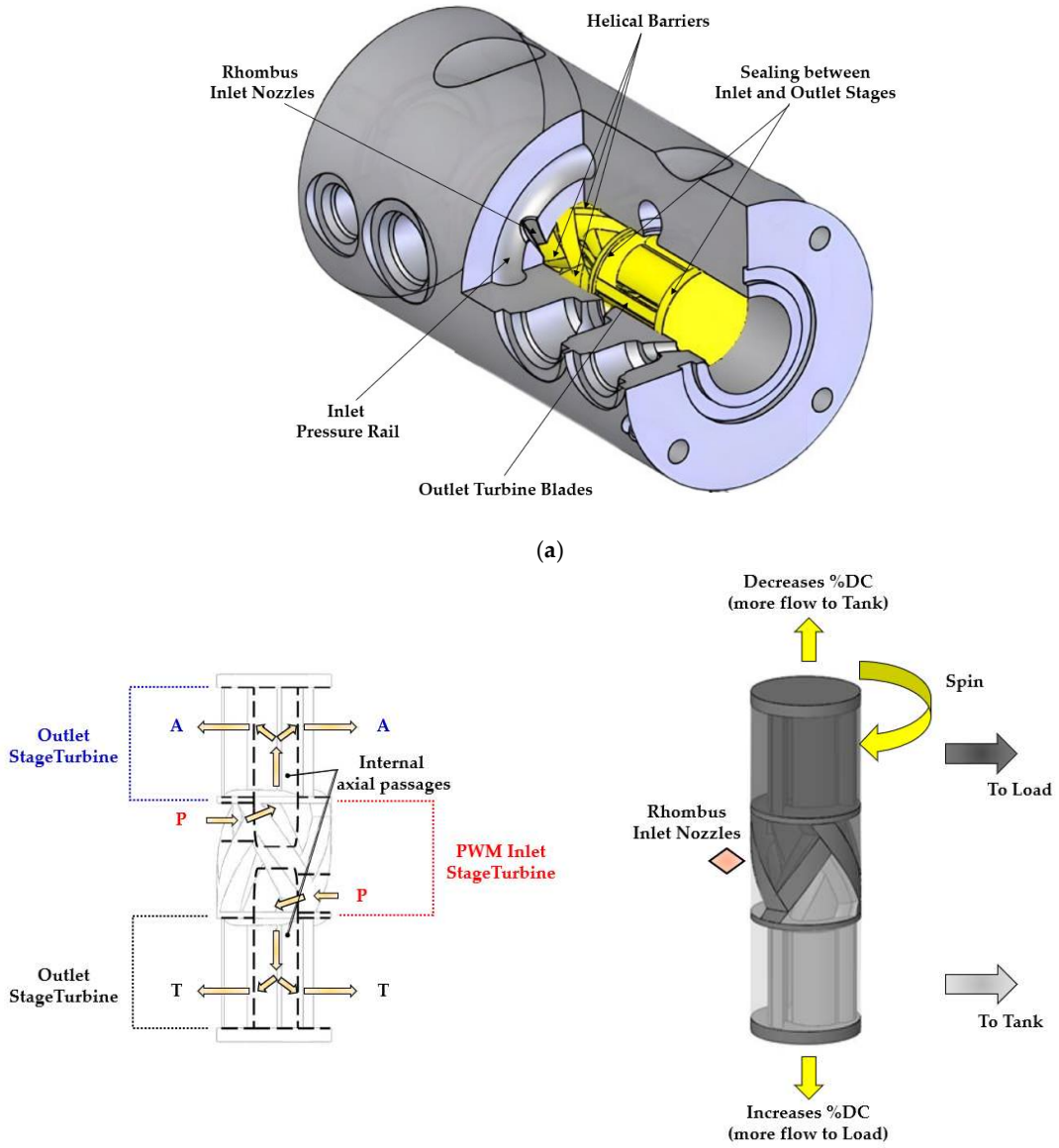

Fig. 52. Redrawn schematic representation of the self-spinning rotary 3/2 HFSV proposed in [183]: (**a**) Cutaway illustration of spool and sleeve assembly; (**b**) Internal geometry of the spool; (**c**) Schematic representation of the rotary spool.

In 2013, Gu et al. developed a 2/2 HFSV with a fixed poppet and a moving sleeve, as shown in Fig. 53 [184]. In the closed position, the Coil A was typically energized to counteract the flow force directed towards the right caused by the high inlet pressure from port (P). On the other hand, energizing the Coil B allowed the valve to open by moving the thin moving sleeve towards the right, thereby connecting the high-pressure port (P) to the outlet port (A).

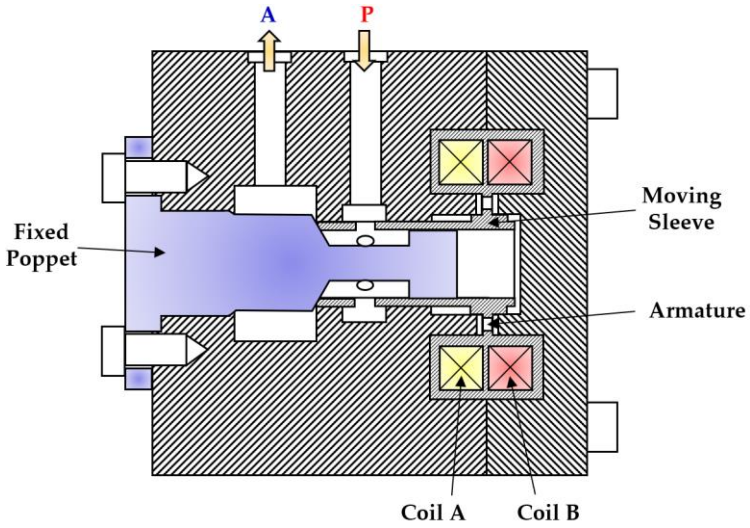

Fig. 53. Redrawn schematic representation of the 2/2 HFSV realized in [184].

The tested valve prototype achieved an opening switching time of 2.25 ms and a closing switching time of 2.15 ms. Additionally, at the maximum duty cycle of the DCS and a switching frequency of 50 Hz, it delivered a flow rate of approximately 64 L/min with a pressure drop of 10 bar.

In 2018, Yang et al. developed a novel miniature 2/2 HFSV (poppet type) [185], [186], [187], which is illustrated in Fig. 54. To increase the magnetic flux, the return spring was designed at the top of the valve. This design enabled the production of a significant electromagnetic force despite the valve's small size, resulting in excellent response speed. Moreover, the valve structure included a magnetic ring composed of soft magnetic material, which reduced the overall reluctance losses.

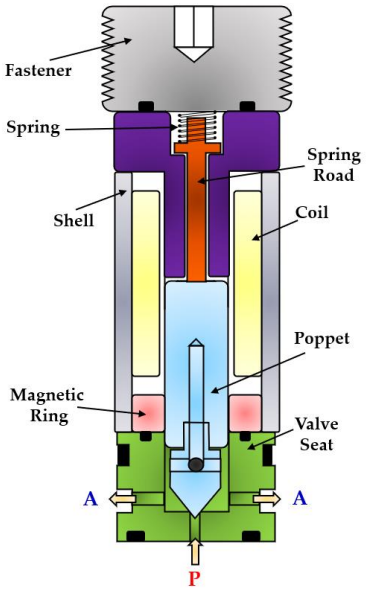

Fig. 54. Redrawn schematic representation of the 2/2 HFSV realized in [185], [186], [187].

The experimental results revealed that the valve exhibited a switching time of 1.5 ms. Nevertheless, due to the small diameter of the inlet orifice (0.5 mm), the flow rate at a pressure drop of 35 bar was limited to only 0.7 L/min.

Table 10 provides a useful comparison of the strengths and weaknesses of the different HFSVs driven by electromagnetic actuators, highlighting the performance of each type.

Table 10. Overview of HFSVs actuated by electromagnetic actuators.

Reference	HFSV Type	Description	Switching Frequency [Hz]	Switching Time [ms]	Flow Capacity [L/min] (@ Pressure drop [bar])
Cui et al. [180]	2/2	A rotating poppet allows to control the flow of hydraulic oil	50	2.5	18 (90)
Honglin Machinery [181]	3/2	A ball assembly of three parts enables the flow path to be alternate	-	3.5/2.5 (on/off)	9 (200)
Tu et al. [183]	3/2	A self-spinning rotary valve continuously switches the flow between the load and the tank	84	-	40 (70)
Gu et al. [184]	2/2	A fixed poppet and a thin moving sleeve cause the valve to open and close	50	2.25/2.15 (on/off)	64 (10)
Yang et al. [185], [186], [187]	2/2	A miniature poppet valve with top spring and soft magnetic ring for low reluctance losses	-	1.5	0.7 (35)

2.3.2.1.2 HFSVs with PEAs

The need for high switching speeds led researchers to explore the possibility of using smart materials for actuating HFSVs. In particular, their focus was on piezo-electric actuators. Indeed, the excellent

characteristics of these actuators, such as simple design, reduced moving parts, high reliability, and fast response, make them useful for developing this type of digital hydraulic valves [188].

Back in 1990s, Yokota et al. conducted a research study on the application of PEAs to develop a novel 3/2 HFSV (poppet type) [80], [189]. A cross-section view of the valve is shown in Fig. 55. There were two piezo-stacks that allowed to move a double poppet through steel balls in a push-pull mode from both sides. The multilayer PEAs offered a free stroke of 0.015 mm and a blocking force of 850 N at a maximum operating voltage of 100 V. The displacement of the double poppet was measured by means of a non-contact reluctance-type position sensor. In order to obtain high-speed response, feedforward control was utilized. The authors stated that this valve had a switching frequency of 2 kHz and a switching time of 0.06 ms in both directions, and it could deliver 7.2 L/min at a pressure drop of 100 bar. They recommended the use of this HFSV as a pilot stage for other hydraulic components.

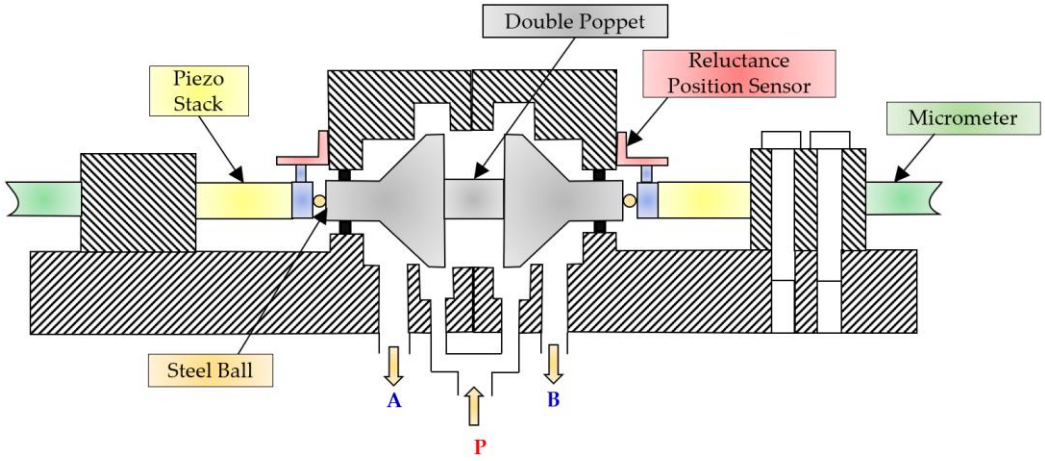

Fig. 55. Redrawn schematic representation of the 3/2 HFSV realized in [80], [189].

To address the issue of high costs associated with the use of two piezo stack actuators, Yamada et al. developed a 2/2 HFSV prototype that employs a spring mechanism and a single PEA to obtain bidirectional poppet control [190]. A cross-section view of the prototype is shown in Fig. 56. Since the main weakness of piezo stack actuators is their low stroke, a hydraulic amplifier was implemented to copy with this problem and actuate the valve. When a DCS was applied to the multilayer PEA (1), the press piston (2) moved towards the right, compressing the oil in the oil chamber (3). This pressurized oil allowed the valve to fully open by pushing the poppet (4) to the right. The poppet movement was countered by a spring (5), which allowed the valve to close when the DCS to the stack was removed. During the closed position, the oil pressure in the oil chamber decreased, and the oil could be recharged through the check valve (6). Other important components were the pre-compression spring (7), the check valve (8), and the LVDT (9). The pre-compression spring (7) ensured the correct value of preload to the piezo stack, while the check valve (8) acted as a pressure relief valve by allowing the red path to remain under a certain value of pressure. The LVDT (9) was used to measure the poppet position and achieve closed loop control.

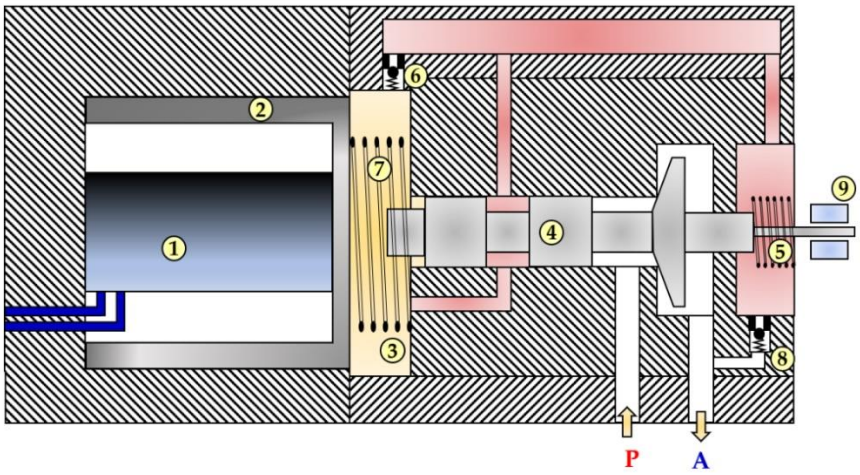

Fig. 56. Redrawn schematic representation of the 2/2 HFSV realized in [190].

The experimental results showed that the valve could operate at a frequency of 500 Hz, with a switching time less than 0.7 ms. At a pressure drop of 100 bar and a switching frequency of 100 Hz, the flow rate increased in proportion to the duty cycle until reaching a maximum of 3 L/min at a duty cycle of 75%. However, above this duty cycle value, the flow rate sharply decreased due to the low "off" time of the valve, which did not allow the oil to adequately recharge the oil chamber. As a result, the hydraulic amplification was not enough to open the valve.

In order to overcome the limitations in duty cycle and achieve higher flows, Ouyang et al. utilized three piezo stack actuators in a 2/2 HSFV to open and close a poppet [191]. The operating principle is depicted in Fig. 57 (from left to right). When both piezo stacks (1) were activated, the combined output force of 3 kN permitted the poppet (2) to initiate a slight opening. At that point, the outlet pressure increased rapidly, while the resistance forces (namely the flow forces and the pressure forces due to the supply pressure) decreased quickly. Consequently, the poppet continued to move until it reached its end stop with the help of the spring (3). To return the poppet to its original position, the DCS was removed from the two piezo stacks (1) and applied to piezo stack (4). This latter stack generated an instant force of 3 kN, which impacted the poppet, causing it to move downwards. Subsequently, the force of the spring (5) allowed the poppet to close the valve.

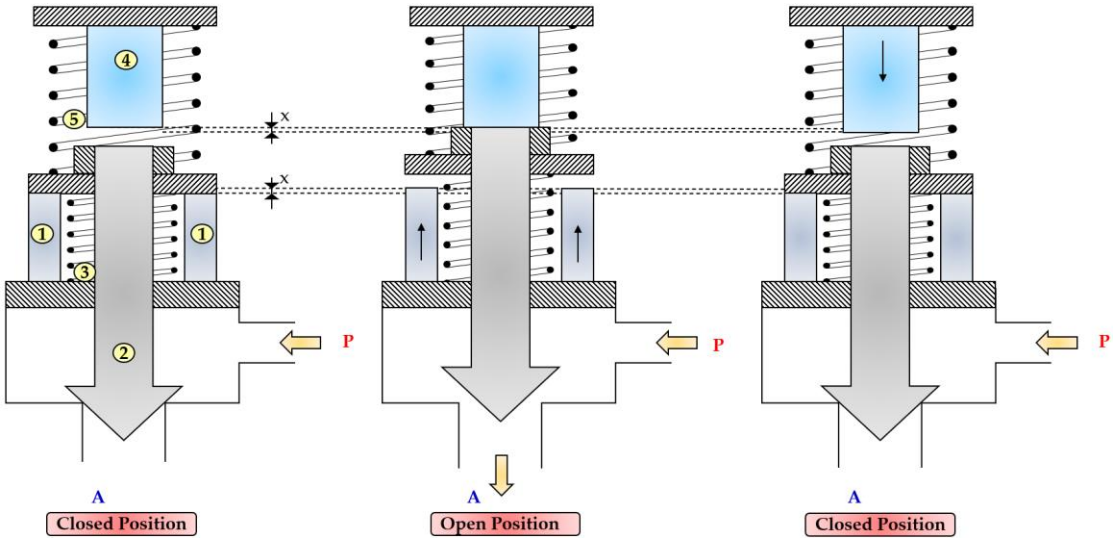

Fig. 57. Redrawn working cycle of the 2/2 HFSV proposed in [191]: Closed position (left); Open position (middle); Closed position (right).

This valve design successfully overcame the issue of micro-displacement of piezo stack actuators. While both piezo stacks (1) and (4) provided a free stroke of 0.032 mm under a maximum voltage of 120 V, the poppet stroke could reach displacements up to 1 mm. To assess the validity of this valve configuration, a detailed mathematical model was realized. The simulations showed that the valve was capable of producing 10 L/min at a pressure drop of 200 bar and a switching frequency of 200 Hz. The graphs also revealed that the switching time of the valve was less than 1 ms.

Table 11 provides an overview of HFSVs actuated by smart materials, highlighting the advantages and disadvantages of the piezoelectric actuation. In contrast to solenoid driven HFSVs, HFSVs utilizing PEAs can achieve higher switching frequency and faster switching time. For example, the piezoelectric HFSV developed by Yokota et al. can switch at a frequency of 2 kHz [80], [189]. However, due to the limited displacement of PEAs, additional piezostacks or displacement mechanism amplifiers are often required, as seen in the valve layouts proposed by Ouyang et al. [191] and Yamada et al. [190], which can increase the valve costs. Additionally, all the innovative piezoelectric HFSVs exhibit very low flow rates at high pressure drops, generating high power consumption.

Table 11. Overview of HFSVs actuated by PEAs.

Reference	HFSV Type	Description	Switching Frequency [Hz]	Switching Time [ms]	Flow Capacity [L/min] (@ Pressure drop [bar])
Yokota et al. [80], [189]	3/2	Two piezo stacks allow to drive a double poppet in a push-pull mode from both sides of the valve	2000	0.06	7.2 (100)
Yamada et al. [190]	2/2	A piezo stack with hydraulic mechanism amplification enables the poppet valve to be actuate	500	< 0.7	3 (100)
Ouyang et al. [191]	2/2	Three piezo stacks allow to open and close the poppet valve	200	< 1	10 (200)

2.3.2.1.3 Potential Application Scenarios of High Frequency Switching Digital Hydraulic Valves

The previous Tables 10 and 11 have illustrated that both HFSVs equipped with electromagnetic actuators and smart materials are typically associated with small flow rates. As a result, researchers have explored their potential use as control components of other hydraulic components, such as for the main spool of proportional and servovalves [192], [193]. A remarkable example is the digital servovalve proposed by Gao et al., which effectively addressed the issues of conventional analogue spool valves, such as oil contamination, high complexity, and low energy efficiency [194]. In this prototype, two 2/2 HFSVs replaced the traditional torque motor structure, as illustrated in Fig. 58. An LDVT was used to measure the position of the main spool and achieve closed loop control. The authors analysed the effects of control parameters, namely the duty cycle and the switching frequency of the PWM signal and found that increasing the duty cycle improved the main spool displacement, while a higher switching frequency reduced its oscillations. Furthermore, the step test response demonstrated that the main spool could reach the set point in just 3.5 milliseconds. However, due to the hysteresis of the electromagnetic actuators, the switching frequency of the two 2/2 HFSVs was limited to 100 Hz, resulting in reduced position tracking accuracy for the main spool.

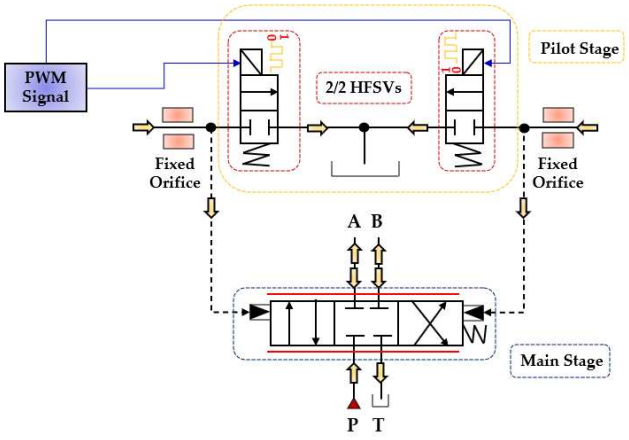

Fig. 58. HFSVs as pilot stage in a novel digital servovalve, adapted from [194].

HFSVs also play a significant role in DHBCs, which, in addition to HFSVs, leverage the reactive behavior of two important hydraulic components, namely accumulators and inertance tubes, as shown in Fig. 59. The capacitive and inertial effect of these hydraulic components, along with the high switching speeds of HFSVs, enables precise adjustment of system pressure and flow rates, energy recovery, and overall system efficiency improvements [195]. Scheidl et al. explored these converters as replacements for conventional spool valves in advanced casting systems, aiming to improve the control of mold oscillations [174]. This implementation, indeed, resulted in reduced energy consumption and lower installation costs. For further details on switched inertance concepts, refer to [196], [197].

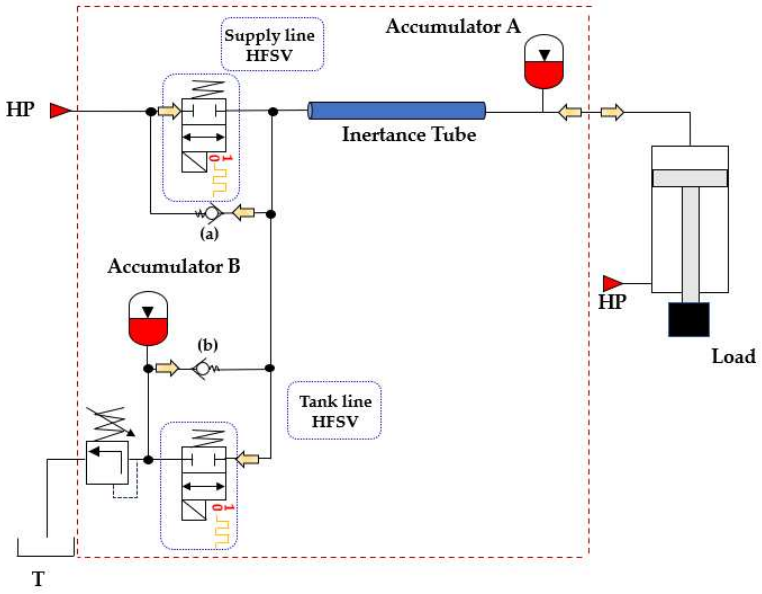

Fig. 59. Digital hydraulic buck converters, adapted from [195].

The use of HFSVs is also instrumental in actively and intelligently controlling the displacement, force, and torque delivered by pumps, cylinders, and motors [122]. These digital hydraulic systems have demonstrated their capacity to enhance energy system efficiency, as demonstrated in various scientific publications [198], [199]. A notable example is the digital hydraulic system proposed by Rannow and Li [200], which is shown in Fig. 60. In this system two HFSVs, along with a check valve and a soft switch lock-release mechanism, efficiently controlled a hydraulic load, reducing overall system losses by 64% even when the HFSVs operated at a relatively low switching frequency of just 20 Hz.

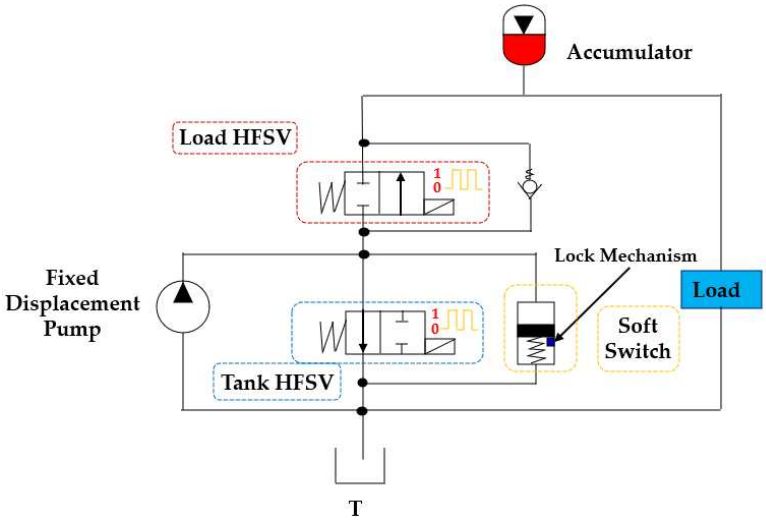

Fig. 60. Redrawn of the digital hydraulic system proposed in [200].

2.3.2.2 Research Progress in Parallel Digital Hydraulic Valves

The idea of using multiple valves in parallel to control the flow of hydraulic fluid date back approximately 100 years ago to the patent of Rickenberg in 1930. He was one of the pioneers to propose the parallel use of three solenoid valves with different flow capacities in his patent application [201]. On the other hand, Bower was the first to use real PCM control with a dual-acting actuator in 1961 [202]. One year later, Murphy and Weil introduced a four-way digital valve that could independently control the load using a DFCU [203]. In 1978, Virvalo demonstrated the application of a DFCU in regulating the velocity of a hydraulic cylinder [204]. However, practical implementation of parallel digital hydraulic valves was challenging at the time due to the limitations of computer technology.

In the new millennium, instead, there has been a substantial increase in research and applications related to parallel digital hydraulic valves. One of the most prominent contributors in this field is the research group led by Matti Linjama at Tampere University of Technology. Their efforts have been focused on developing innovative DFCU structures [205], [206] and implementing advanced control algorithms to enhance the overall DFCU performance [207], [208], [209].

In recent years, advancements have been made in the development of DFCU prototypes that are capable of integrating more switching valves. In 2014, Paloniitty et al. introduced a DFCU containing 16 on/off valves, as shown in Fig. 61 [210]. The DFCU flow rate was controlled by the PNM coding scheme, and it achieved a flow rate of approximately 25 L/min at a pressure drop of 35 bar, with a switching time of less than 4 ms [211]. To improve the resolution of the flow rate, a novel DFCU was proposed by Linjama et al. in 2015 that integrated 64 on/off valves [212].

(**a**) (**b**)

Fig. 61. DFCU with sixteen on/off valves in parallel developed by Paloniitty et al. [210]: (**a**) prototype; (**b**) utilized on/ff valve.

Two years later, Ketonen et al. introduced a 4/3 DFCU Valve with high flow characteristics and capable of replacing conventional spool valves in many mobile and industrial applications. [213]. As shown in Fig. 62(a), each of the four DFCU consisted of 7 On/Off valves from Bucher Hydraulic and was capable of producing 127 states, resulting in a total of 508 possible flow rate combinations for the entire 4/3 DFCU Valve. The Bucher Hydraulic On/Off valve, illustrated in Fig. 62(b), provided a flow rate of 60 L/min at a pressure drop of 15 bar. The entire prototype presented a dimension of 402x343x96 mm. The experimental results showed that, by employing PCM and PNM coding schemes, the measured maximum flow rate of each DFCU could reach up to 200 L/min at a pressure difference of 15 bar. The authors stated that the 4/3 DFCU Valve could offer excellent fault tolerance performance and could be an efficient energy solution to control hydraulic actuators in range up to 400 L/min and pressures up to 350 bar.

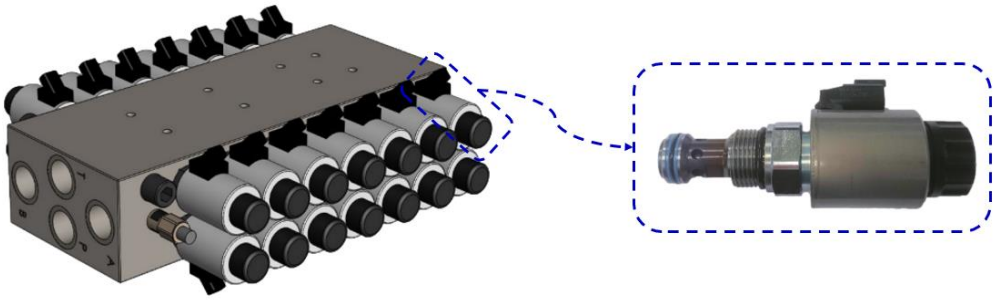

(**a**) (**b**)

Fig. 62. 4/3 DFCU Valve with multiple On/Off valves in parallel developed by Ketonen et al. [213]: (**a**) prototype; (**b**) utilized On/Off valve.

2.3.2.2.1 Potential Application Scenarios of Parallel Digital Hydraulic Valves

Recently, in an effort to enhance the performance of electro-hydraulic servovalves used in aircraft fuel systems and address issues associated with these conventional spool valves, Gao et al. replaced the traditional torque motor with two DFCUs to actuate the main spool in a novel digital fuel metering servovalve [214]. As shown in the hydraulic schematic of Fig. 63, each DFCU controlled five parallel-connected on/off valves through PCM coding scheme. A detailed numerical model was developed to investigate the performance of this valve design and, the numerical results revealed that the main spool could reach the desired set point in just 4.1 ms.

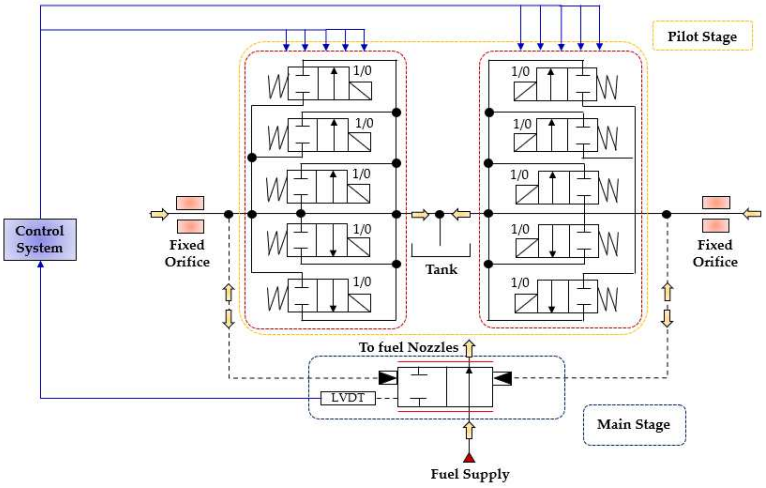

Fig. 63. DFCUs as pilot stage in a novel digital servovalve, adapted from [214].

DFCUs can also be used to control independently velocity and pressure level of an actuator. A practical example of this can be seen in the work of Linjama et al., where a 4/3 DFCU was used to regulate the flow rate to a heavily loaded cylinder, as depicted in Fig. 64 [215]. The PCM scheme was employed to control all four flow paths independently, using five on/off valves in parallel for each DFCU, which provided a total of 128 potential flow rate states. This parallel digital hydraulic system, due to its minimal pressure losses, has the potential to be more energy-efficient compared to conventional valve-controlled hydraulic systems that rely on throttling for precise control.

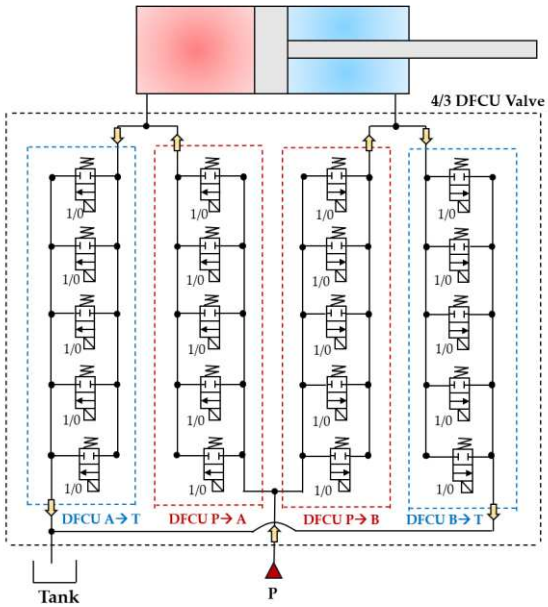

Fig. 64. DFCUs used to control independently velocity and pressure level of an actuator, adapted from [215].

Following a similar approach, Huova et al. used DFCUs to achieve discrete and intelligent control of a variable displacement linear actuator (or multi-chamber cylinder) [216]. Specifically, the authors

employed a pressurized tank line and a constant pressure supply line to effectively drive the three-chamber hydraulic cylinder, as depicted in Fig. 65. To control each chamber, two DFCUs were utilized, with one controlling the flow rate between the chamber and the supply line, and the other controlling the flow rate between the chamber and the tank line. The authors stated that the energy loss in this parallel digital hydraulic system, considering a constant supply pressure, was reduced by 30% to 60% compared to conventional hydraulic cylinders. Moreover, multi-chamber cylinders were integrated into construction machinery, resulting in a considerable reduction in fuel consumption [217].

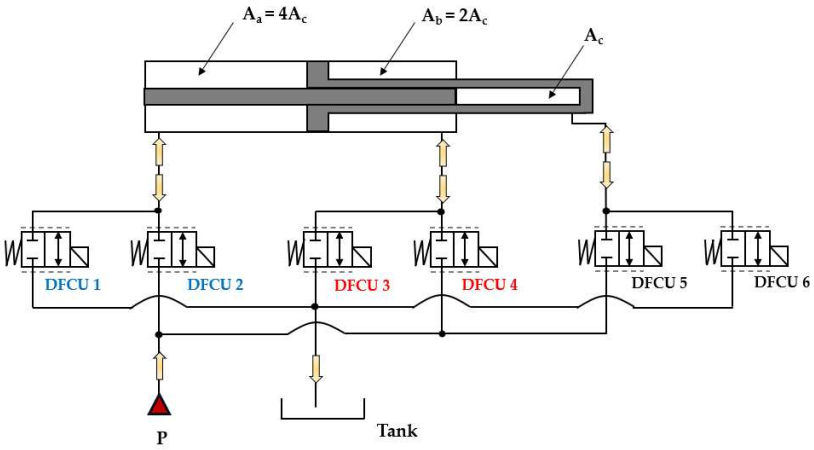

Fig. 65. DFCUs used to control a multi-chamber cylinder, adapted form [216].

2.3.3 Challenges and Future Directions in Digital Hydraulic Technology

Despite the considerable advantages over conventional hydraulic technology, achieving widespread adoption of digital hydraulic technology across diverse industries in the coming years requires addressing several challenges [44]. Fig. 66 illustrates the primary obstacles faced by both parallel and high-frequency switching digital hydraulic technology.

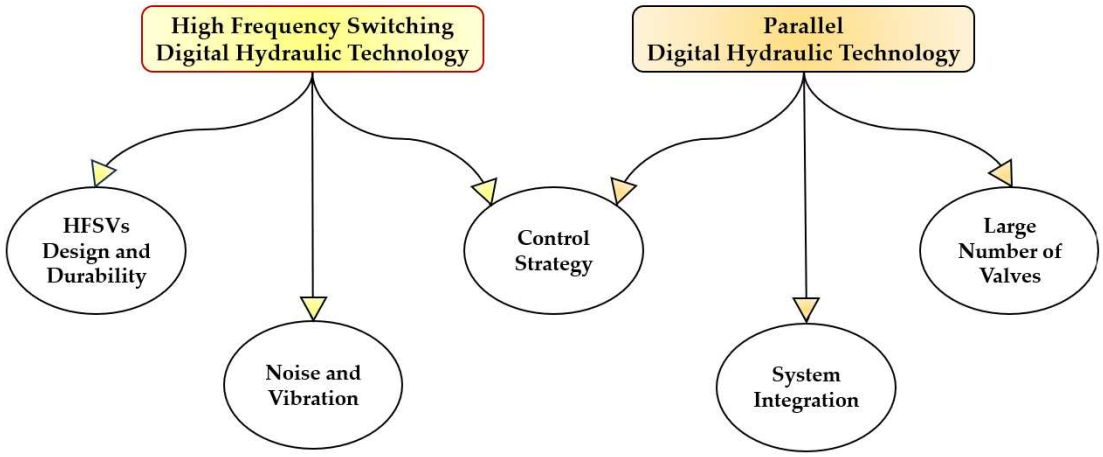

Fig. 66. Key Challenges in High Frequency Switching and Parallel Digital Hydraulic Systems [44].

Concerning high-frequency switching digital hydraulic technology, a critical challenge lies in the design and durability of HFSVs. These valves must withstand rapid switching speeds, deliver large flow rates, maintain durability, and resist wear and fatigue. Moreover, the high frequency switching of these components can introduce issues such as noise, vibration, and pressure peaks in the system.

Regarding parallel digital hydraulic technology, the use of a large number of switching valves in DFCUs can result in challenges related to system size, cost, and complexity. Additionally, similar to high-frequency switching digital hydraulic technology, developing and implementing a control strategy can be complex, requiring unconventional approaches compared to conventional hydraulic technology.

Finally, the integration of digital hydraulic technologies into existing machinery poses challenges related to compatibility and space constraints.

2.4 Precision Fluid Pumps powered by PEAs

PEAs can be also considered an ideal choice for developing innovative precision fluid pumps. Among potential advanced and smart driving mechanisms, PEAs stand out due to their high output force, rapid dynamic response, high reliability, simple structure, and lightweight design. A comparison of various smart driving mechanisms used for precision fluid pumps is presented in Table 12 [36].

Table 12. Performance comparisons of precision fluid pumps under various driving methods [36].

Driving method	Thermal	Electrostatic	Electromagnetic	Shape memory	Piezoelectric Stack	Piezoelectric Membrane
Load	small	small	small	medium	large	small
Stroke	medium	small	large	large	small	medium
Response	medium	short	medium	long	short	short
Flowrate	medium	low	high	medium	low	high
Pressure	medium	small	large	medium	large	small
Frequency	low	high	medium	low	high	medium
Structure	simple	simple	complex	simple	simple	simple
Reliability	medium	excellent	good	poor	good	good
Anti-Interferance	weak	strong	weak	weak	strong	strong

Piezoelectric pumps (or piezopumps) are one of the most common types of precision fluid pumps that utilize the inverse piezoelectric effect to convert electrical energy into mechanical energy in order to pressurize and move fluids. Piezopumps feature a simple structure, are easy to miniaturize, consume minimal energy, and produce no electromagnetic noise. Their long service life and high reliability make them ideal for integration into Micro-Electro-Mechanical Systems (MEMS).

As a result, piezoelectric pumps hold great potential in fields like biomedicine, robotics, aerospace, electronics, chemistry, and automotive engineering [218], [219], [220], [221]. Within

piezoelectric pumps a classification can be made between "valved piezopumps" and "valveless piezopumps," depending on whether the pump incorporates movable valves [222].

The performance of various piezopumps developed by researchers over the years, following this classification, is now reviewed. Special attention is given to key performance metrics such as maximum flowrate (Q_{max}), maximum backpressure (p_{max}), and the type of pumping media used, as these are critical for evaluating these pumps. Another key metrics are the driving voltage (U_{pa}) and frequency (f_{pa}), as they impact the electronics needed to operate the pump effectively.

2.4.1 Valveless Piezopumps

Valveless piezopumps offer several key advantages over their valved counterparts, including longer lifespan, greater structural stability, and easier miniaturization [223]. These pumps enable one-way fluid transfer by utilizing the difference in resistance between forward and reverse flow in specially designed channels at the inlet and outlet of a pumping chamber. This design effectively replaces conventional valves, eliminating wear and fatigue associated with check valves and reducing the risk of clogging [224]. Additionally, the absence of valves reduces the probability of crushing damage to the possible transported substance [225].

Fig. 67 illustrates the classifications of valveless piezoelectric pumps. Based on their structural characteristics, they can be divided into three main types [226]:

- External flow tube type: This type achieves one-way fluid flow using a piezomembrane actuator and specialized external tubes, such as nozzle/diffuser tube [227], Y-shaped tubes [228], spiral tubes [229], and other specially designed flow tubes [230];
- Built-in structure type: In this type, the flow resistance elements are placed inside the pump chamber. Common examples include asymmetric slope elements [231], hemisphere segments [232], and conical spiral cavities [233];
- Bionic type: Inspired by biological structures, this design mimics natural mechanisms to achieve unidirectional flow. Examples include fishtail bimorph structures [234] and built-in compliant structures [235].

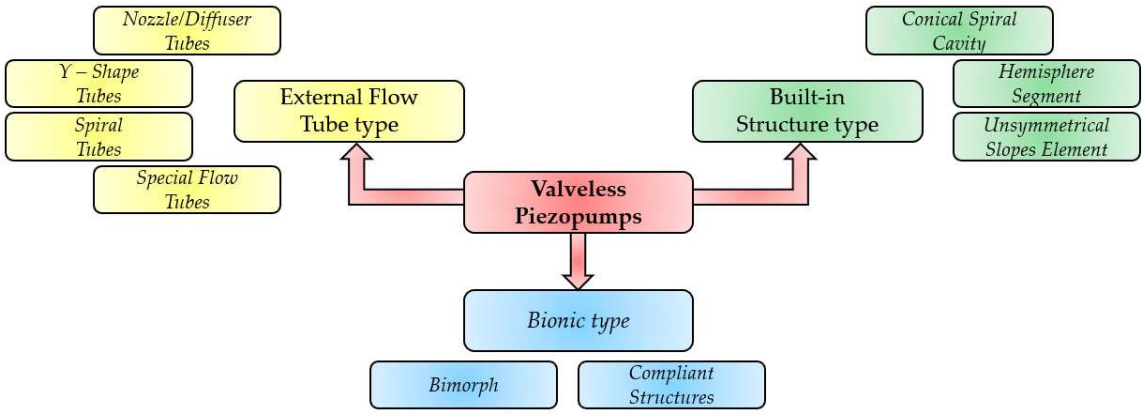

Fig. 67. Classification of valveless piezoelectric pumps [226].

2.4.1.1 Valveless Piezopumps with External Flow Tubes

To understand how valveless piezopumps with external flow tubes work, Fig. 68 shows the functioning of a valveless nozzle/diffuser piezopump. It is important to note that the other types of valveless piezopumps with external flow tubes operate in a similar way, so their principles will not be explained in detail. The valveless nozzle/diffuser pump, which is considered to be a reciprocating positive displacement pump, operates in two distinct modes within each cycle, based on the deflection of the piezomembrane actuator:

- Supply Mode: The diaphragm moves upward, lowering the pressure inside the pumping chamber. Fluid enters the chamber through both the inlet and outlet, but due to the design, the kinetic energy loss is lower in the forward direction (diffuser action) than in the reverse direction (nozzle action). As a result, more fluid flows into the chamber through the inlet (Q+) than the outlet (Q-), effectively filling the chamber.
- Pump Mode: The diaphragm moves downward, increasing the pressure within the chamber. Fluid is then pushed out through both the inlet and outlet. Again, because the forward flow (through the outlet, Q+) experiences less energy loss than the reverse flow (through the inlet, Q-), more fluid exits through the outlet.

This difference in kinetic energy loss between the nozzle and diffuser during each cycle creates a pressure drop, leading to flow rectification and ensuring unidirectional fluid movement. In this way, the reciprocating motion of the piezomembrane actuator, powered by an alternating sine-wave voltage signal, drives a steady flow of fluid through the chamber from the inlet to the outlet.

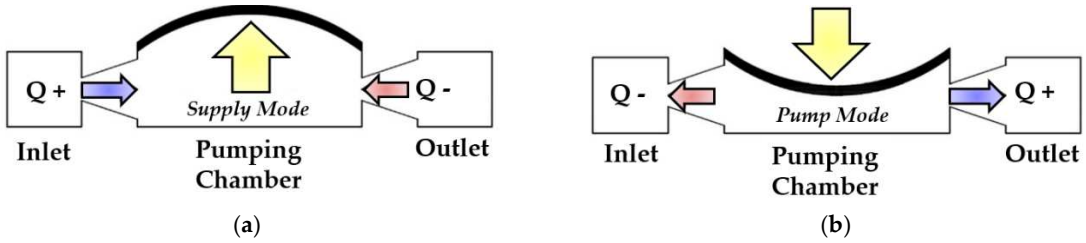

Fig. 68. Working principle of a valveless nozzle/diffuser piezopump: (**a**) Supply mode; (**b**) Pump mode.

The first valveless nozzle/diffuser piezo pump was developed by Stemme et al. in 1993 [236]. This prototype had a chamber with a diameter of 19 mm and conical flow tubes. When tested with water as the pumping medium, it achieved a maximum flow rate of 16 mL/min and a pressure of 0.2 bar at a driving frequency of 100 Hz.

Five years later, Olson et al. enhanced the design by using cone-shaped tubes and connecting two parallel pumping chambers operating in antiphase [237]. This improved the pump's performance, achieving a maximum pressure of 0.74 bar and a flow rate of 2.3 mL/min for water at a frequency of around 4 kHz.

In 2003, Nguyen et al. designed and built a valveless nozzle/diffuser piezo pump based on a printed circuit board [238]. When tested with water at 100 Hz, the pump achieved a flow rate of 3 mL/min and a pressure of 0.07 bar.

These experiments demonstrated that while valveless diffuser/nozzle piezopumps with conical flow tubes had simple structures and could be easily miniaturized, their performance was significantly limited. In this way, in 2007, Izzo et al. addressed this issue by developing a valveless piezoelectric pump with a special flow tube [239]. Tested with ethyl alcohol at a driving frequency of 2250 Hz, the pump reached a flow rate of 0.64 mL/min and a pressure of 0.173 bar.

Continuing this line of improvement, five years later, Huang et al. introduced a valveless piezo pump with Y-shaped tubes, designed to reduce the vortex effect seen in traditional conical flow tubes [240]. This pump, tested with water at a driving frequency of 10 Hz, achieved a maximum flow rate of 35.5 mL/min and a pressure of 0.0055 bar, making it suitable for transporting living cells.

Table 13 shows the performance comparisons of the analysed valveless piezopumps with external flow tubes.

Table 13. Performance comparisons of the analysed valveless piezopumps with external flow tubes.

Reference	Type of Valveless Piezopump	Driving Voltage (U_{pa}) [V]	Driving Frequency (f_{pa}) [Hz]	Maximum Pressure (p_{max}) [bar]	Maximum Flow Rate (Q_{max}) [mL/min]	Pumping Medium
Stemme et al. [236]	Nozzle/Diffuser	–	100	0.2	16	Water
Olson et al. [237]	Nozzle/Diffuser	200	4000	0.74	2.3	Water
Nguyen et al. [238]	Nozzle/Diffuser	100	100	0.07	3	Water
Izzo et al. [239]	Special Flow	100	2250	0.173	0.64	Ethyl alcohol
Huang et al. [240]	Y – Shape	100	10	0.0055	35.5	Water

To summarize, the external flow tubes limit further miniaturization of this kind of valveless piezoelectric pumps. Additionally, its typically low flow rate restricts its suitability for high-flow applications.

2.4.1.2 Valveless Piezopumps with Built-in Structures

The operating principle of a valveless piezo pump with a built-in structure, specifically one with asymmetrical slopes, is illustrated in Fig. 69. It is important to note that other types of valveless piezo pumps with similar structures operate on comparable principles, so their mechanisms are not detailed here.

In this design, the piezopump works as a reciprocating positive displacement pump. The key feature is the asymmetrical angled surfaces: one side has a slope angle of α_1, and the opposite side has a different slope angle, α_2 (where $\alpha_1 \neq \alpha_2$). These angled surfaces are placed at the bottom of the pumping chamber, directly facing the piezo membrane actuator. This asymmetry enables non-valve control of unidirectional fluid flow.

Specifically, because α_1 is not equal to α_2, the flow resistance is different when fluid flows through. As a result, the fluid flow rate entering or leaving the chamber from the left and right conduits of the pump differs during the supply and pump modes, creating a net flow in one direction.

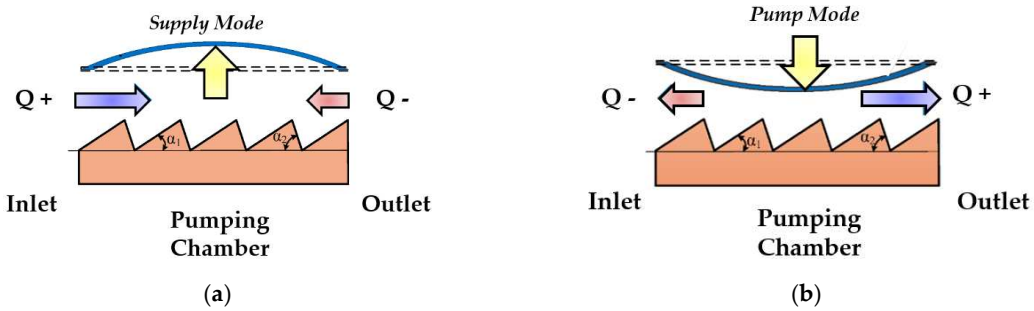

Fig. 69. Working principle of a valveless piezopump with unsymmetrical slopes: (**a**) Supply mode; (**b**) Pump mode.

In 2011, Zhang et al. introduced a valveless piezoelectric pump with rotatable, unsymmetrical slopes, capable of mixing different fluids [241]. By rotating the slopes, this design controls the ratio of fluids entering the pump chamber. The prototype was tested at 220 V and 50 Hz, with a chamber diameter of 30 mm and slope angles of $\alpha_1 = 30°$ and $\alpha_2 = 90°$ on each side. Under these conditions, the pump achieved a maximum flow rate of 32.32 mL/min.

In 2013, Ji et al. developed a novel valveless piezoelectric pump featuring six hemisphere segments in a water-filled chamber [232]. With a diameter of the piezomembrane actuator equal to 30 mm, the experimental tests revealed that the pump reach a maximum flow rate of 30 mL/min at 6 Hz and 110 V, while a pressure difference of 0.0026 bar was achieved at 6 Hz and 160 V.

Six years later, Zhao et al. improved the flow rate of this type of pump by optimizing the hemisphere segments, creating a crescent-shaped structure using 3D printing [242]. The pump prototype reached a maximum flow rate of 286 mL/min at 220 V and 82 Hz.

Recently, He et al. designed another valveless pump with rotatable asymmetrical slopes, achieving a maximum flow rate of 220.6 mL/min at 190 V and 45 Hz [243]. The highest output pressure was 0.0067 bar, measured at 190 V and 130 Hz. Table 14 summarizes the properties of valveless piezoelectric pumps with built-in structures.

Table 14. Performance comparisons of the analysed valveless piezopumps with built-in structures.

Reference	Type of Valveless Piezopump	Driving Voltage (U_{pa}) [V]	Driving Frequency (f_{pa}) [Hz]	Maximum Pressure (p_{max}) [bar]	Maximum Flow Rate (Q_{max}) [mL/min]	Pumping Medium
Zhang et al. [241]	Unsymmetrical Slopes	220	50	–	32.32	–
Ji et al. [232]	Hemisphere Segment	160 – 110	6	0.0026	30	Water
Zhao et al. [242]	Hemisphere Segment	220	82	–	286	Water
He et al. [243]	Unsymmetrical Slopes	190	130 – 45	0.0067	220.6	Water

To summarize, integrating flow resistance structures within the pumping chamber and using standard flow tubes at the inlet and outlet enhances the efficiency of this type of valveless

piezoelectric pump, resulting in a significantly higher flow rate compared to valveless piezopumps with external flow tubes.

2.4.1.3 Bionic Valveless Piezopumps

The working principle of a bionic valveless piezopump with compliant structures is illustrated in Fig. 70. This pump comprises a pumping chamber, a piezomembrane actuator, two flow channels, and compliant structures on each side of the chamber.

In the supply mode, the piezomembrane moves upward, expanding the chamber volume, which opens the inlet gap while reducing the outlet gap. As a result, more fluid is directed through the inlet channel (Q+) than the outlet (Q-).

During the pump mode, the piezomembrane moves downward, reducing the chamber volume. This action widens the outlet gap and narrows the inlet gap, pushing more fluid through the outlet (Q+) than the inlet (Q-). Based on this principle, the pump functions as a reciprocating positive displacement pump.

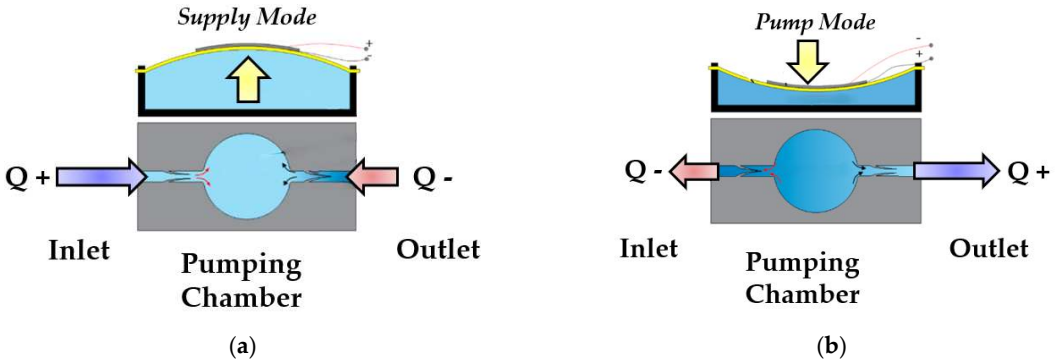

Fig. 70. Working principle of a bionic valveless piezopump with compliant structures: (**a**) Supply mode; (**b**) Pump mode.

The bimorph bionic valveless piezopump, shown in Fig. 71, represents an alternative type inspired by the swimming motion of fish. Fish naturally create propulsion by moving their bodies or fins, generating a trail of vortices. When this motion is held in place, fluid flow occurs, effectively mimicking a pump. Similarly, this piezopump uses a bimorph PEA (a thin, oscillating plate) to replicate the fish's movement in a fluid environment. Powered by AC voltage, the bimorph actuator oscillates, continuously adding energy to the fluid and enhancing its momentum. This design enables the pump to act as a dynamic pump, delivering a continuous flow.

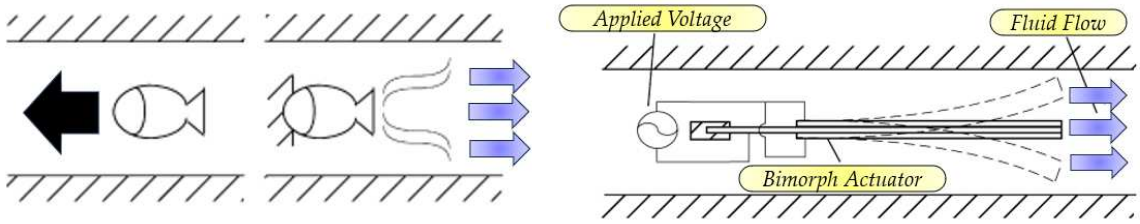

Fig. 71. Bionic bimorph valveless piezopump: (**a**) Fish propulsion; (**b**) Pump scheme.

In 2009, Pires et al. developed a bionic valveless piezopump with a bimorph actuator inserted in water [244]. Testing showed the pump reached a maximum flow rate of 103 mL/min and a maximum pressure of 0.0012 bar at a frequency of 320 Hz and 60 V.

Three years later, Hu et al. significantly improved the performance, creating a pump prototype that achieved 560% of Pires et al.'s flow rate. Their tests demonstrated a maximum flow rate of 576 mL/min and a pressure of 0.0088 bar at 80 V and 1360 Hz [245].

In 2019, Bao et al. introduced a compliant-structured bionic valveless piezopump, reaching a maximum flow rate of 3.6 mL/min and a pressure of 0.0199 bar at 210 V and 80 Hz [235].

Table 15 shows the performance comparisons of the analysed bionic valveless piezopumps.

Table 15. Performance comparisons of the analysed bionic valveless piezopumps.

Reference	Type of Valveless Piezopump	Driving Voltage (U_{pa}) [V]	Driving Frequency (f_{pa}) [Hz]	Maximum Pressure (p_{max}) [bar]	Maximum Flow Rate (Q_{max}) [mL/min]	Pumping Medium
Pires et al. [244]	Bimorph	60	320	0.0012	103	Water
Hu et al. [245]	Bimorph	80	1360	0.0088	576	Water
Bao et al. [235]	Compliant Structures	210	80	0.0199	3.6	Water

To summarize, bionic valveless piezoelectric pumps achieve one-way fluid flow by mimicking biological structures. These pumps offer several benefits, including simplicity, ease of miniaturization, cost-effectiveness, and the added advantage of minimizing backflow.

2.4.2 Valved Piezopumps

Valved piezoelectric pumps typically use a pair of unidirectional valves positioned at the inlet and outlet to control fluid flow. These valves alternately open and close, creating directional fluid movement. Based on how the valves are controlled, these piezopumps can be further categorized

into passive valve piezoelectric pumps, which rely on natural flow response, and active valve piezoelectric pumps, which use an external control mechanism, as shown in Fig. 72.

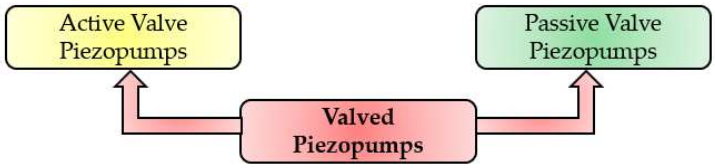

Fig. 72. Classification of Valved Piezopumps.

2.4.2.1 Passive Valve Piezopumps

In passive valve piezoelectric pumps, the opening and closing of the valves are controlled by the periodic pressure changes within the pumping chambers. Over time, various designs have emerged, including ball valves, cantilever valves, bridge valves, wheel valves, umbrella valves, and dimple valves.

The passive ball valve piezopump developed by Carrozza et al. demonstrates good mechanical strength and cost-effective production, although it has relatively low efficiency [246]. Experimental testing of this pump, using water as the fluid medium, revealed a maximum flow rate of 2.7 mL/min and a maximum back pressure of 0.35 bar at a driving frequency of 70 Hz and a voltage of 300 V supplied to the piezo membrane actuator.

To enhance the frequency performance of passive valve piezopumps, researchers have increasingly transitioned from ball check valves to reed valves. Reed valves utilize a flexible material to serve both the spring and sealing functions, thereby reducing the moving mass and increasing the bandwidth. However, there is no consensus on the best type or design for these valves. Various designs have been explored, including cantilever designs by Kan et al. [247], bridge designs by Feng et al. [248], dimple designs by Luo et al. [249], wheel designs by Truong et al. [250], and umbrella designs by Peng et al. [251]. The diversity of designs reflects the ongoing search for effective solutions in this field. A performance comparison of these different passive valve piezopumps is presented in the following Table 16.

Table 16. Performance comparisons of the analysed passive valve piezopumps.

Reference	Type of Passive Valve Design	Driving Voltage (U_{pa}) [V]	Driving Frequency (f_{pa}) [Hz]	Maximum Pressure (p_{max}) [bar]	Maximum Flow Rate (Q_{max}) [mL/min]	Pumping Medium
Carrozza et al. [246]	Ball	300	70	0.35	2.7	Water
Kan et al. [247]	Cantilever	50	3000	0.27	3.5	Water
Feng et al. [248]	Bridge	100	6000	0.04	0.7	–
Luo et al. [249]	Dimple	150	875	0.1525	16.4	Water
Truong et al. [250]	Wheel	300	100	0.16	2.9	Water
Peng et al. [251]	Umbrella	210	120	0.3247	1845	Water

2.4.2.1.1 Single Cylinder Piezohydraulic Pumps

In fluid power applications, where high flow rates and back pressures are required, piezostack actuators are preferred over piezomembrane actuators as the driving power source mechanism, especially when combined with a valve-based configuration [252], [253]. Piezopumps that use piezostack actuators as their driving power source are also known as piezohydraulic pumps.

In a conventional single cylinder (single pumping chamber) piezohydraulic pump, a piezostack actuator drives a piston, and a pair of passive check valves (inlet and outlet) control the fluid flow into and out of the pumping chamber. The working cycle of such a piezopump, illustrated in Fig. 73, consists of four stages:

A) Compression Stage: Both inlet and outlet check valves (3 – 4) are closed. When the voltage signal is applied to the piezostack actuator (1), it expands, compressing the fluid by means of the piston (2), thereby increasing the pressure in the pumping chamber (5);
B) Delivery Stage: When the pumping chamber pressure matches the outlet pressure, the outlet check valve opens, allowing fluid to flow out.
C) Expansion Stage: Removing the voltage signal causes the piezostack actuator to contract, reducing the pumping chamber pressure to the inlet level.
D) Intake Stage: The inlet check valve opens when the inlet pressure and pumping chamber pressure equalize, letting fluid back into the chamber.

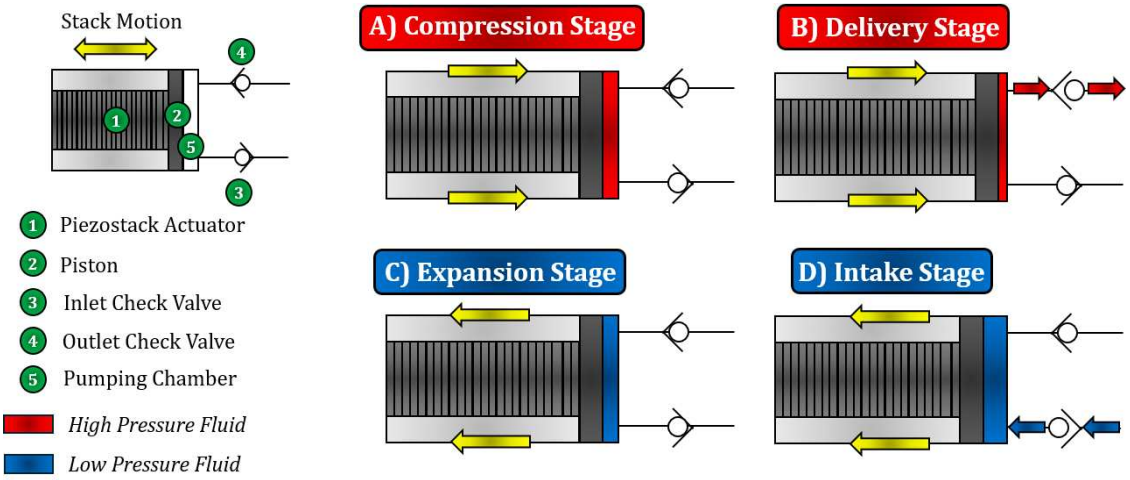

Fig. 73. The four-stage working cycle of a conventional piezohydraulic pump.

Leveraging the broad operating frequency of piezoelectric materials, and thus, supplying the piezostack actuator with a high-frequency sinusoidal voltage signal (exceeding 1 kHz) allows for a substantial flow despite the stack's limited displacement. Indeed, increasing the operating frequency turns out to be as a simple and convenient approach to enhance the performance of piezoelectric pumps without the need to increase their size or input power [254].

An important example was the piezohydraulic pump developed by Kan et al. This pump featured a reinforced chamber diaphragm, consisting of a membrane and a rigid disk. Analytical results indicated that the pump's performance depended on the thickness of the diaphragm and the radius ratio. As the membrane thickness decreased, both the flow rate and backpressure increased; however, the radius ratio had varying effects on these performance parameters. Testing a prototype with water at a driving voltage of 150 V demonstrated that, at a high driving frequency of 280 Hz, the pump achieved a flow rate of 395 mL/min with a 12 mm radius disk.

However, at high driving frequencies, these kinds of piezopumps are prone to severe cavitation [255], which can lead to component damage, reduced efficiency, vibrations, and noise [256]. Cavitation, which involves the formation, growth, and implosive collapse of vapour bubbles under high-pressure conditions, significantly limits the performance of piezopumps working at high flow rates [257]. Zhang et al. found that during the intake stage, as the pumping chamber volume increases and pressure decreases, dissolved gas escapes from the liquid, leading to cavitation [255]. He et al. explored the negative impacts of cavitation on piezopumps, noting that it reduces the bulk modulus of the working fluid, thereby severely decreasing pump efficiency [258]. In efforts to mitigate cavitation, Pecar et al. utilized a sinusoidal excitation signal waveform, which, despite resulting in lower output flow rates, effectively reduced the risk of cavitation compared to square-wave excitation [259], [260].

2.4.2.1.2 Multi-Cylinder Piezohydraulic Pumps

To further enhance performance, increasing the size of the piezo stack could theoretically boost the pump's power output. However, practical constraints such as thermal management, cost, and manufacturability limit this approach. A more feasible solution is to use multiple cylinders, each driven by an individual piezo stack. This setup allows any advancements in the single cylinder design to be applied directly to a multi-cylinder (multi-pumping chamber) piezopumps.

Multiple cylinders can be configured in parallel to increase flow, in series to increase pressure (as shown in Fig. 74), or dynamically switched between these arrangements using valves, depending on specific performance goals.

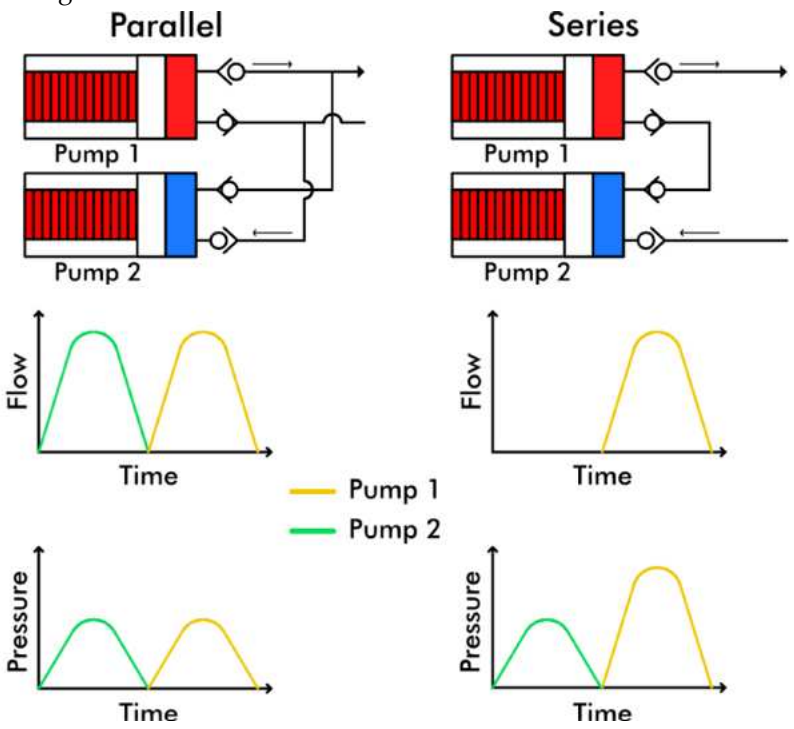

Fig. 74. Series and parallel multi-cylinder piezopump arrangements

Early work by Ullmann looked at the effect of different connections between two pump cylinders joined with diffuser nozzles [261]. It was expected that the series connection would double the pressure difference and the parallel connection would double the flow rate, as shown in Fig. 74. However, it was found that with the diffuser nozzles, the series connection also gave a flow increase. In all instances, the pumping elements were operated in-phase after this was found to be advantageous for the series-connected pump. No explanation was given as to why this result was expected to be generalised across all architectures. It is also unclear whether the results were tied specifically to the use of diffuser nozzles in place of valves or whether they apply to multi-cylinder piezopumps in general.

Alongside the connection of the cylinders, the phasing between the cylinders is a design variable that is not relevant to single cylinder pumps. These two variables, the output connection and phasing, have therefore formed the subject of most multi-cylinder piezopump research. The phase is a

continuous variable but, at its extremes, the pistons in a two-cylinder pump move together (in-phase) or in opposite directions (anti-phase), with stages 1 and 3 occurring simultaneously in the two cylinders. Fig. 75 depicts this in a parallel-connected pump.

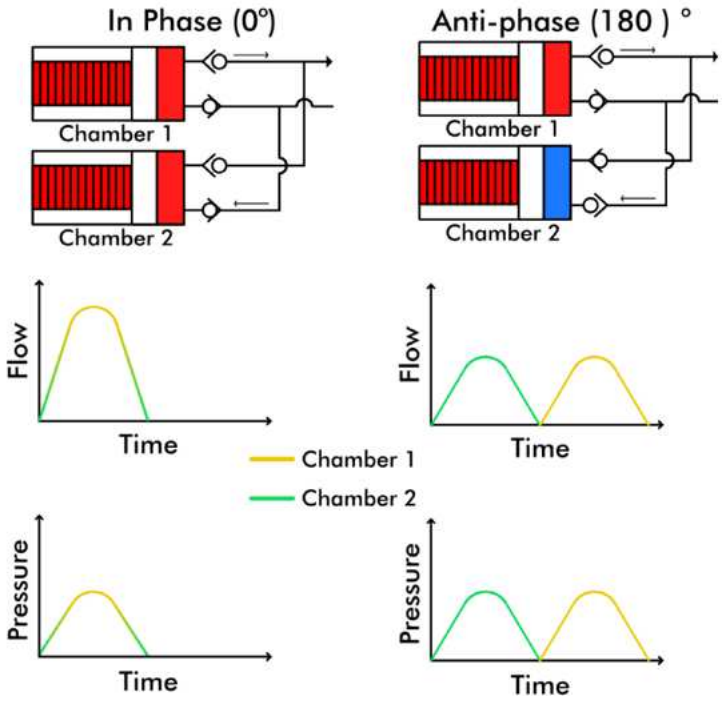

Fig. 75. Phasing extremes of a parallel-connected multi-cylinder piezopump.

Li et al. used two cylinders to drive a hydraulic actuator and experimentally investigated the difference in performance with parallel and series connections and in-phase and anti-phase setups [262]. They found that, in all cases, driving the two cylinders in anti-phase gave better performance than in-phase, but the size of the hydraulic actuator dictated whether a series or parallel connection was preferable to achieve the desired force and velocity. This is expected, with a parallel connection generally giving large flows but at lower pressures, which are more suited to larger actuator piston areas. Whilst unsurprising, these conclusions highlight the potential capabilities of a piezopump that can be reconfigured to achieve a wider operating envelope. The parallel configuration could be used for rapid advancement and the series connection utilised for higher force movements. There are several applications where the need for a high velocity and high force do not coincide that could make use of such a device. It was estimated from the actuator's force and displacement that the serial-connected pump was able to produce 53 bar and the parallel-connected pump 1.65 L/min.

2.4.2.2 Active Valve Piezopumps

In active valve piezoelectric pumps, the opening and closing of the valves are actively controlled by PEAs. Some studies have suggested using active valves instead of passive ones to reduce phase lag. For instance, the active valve piezopump designed by Lee et al. achieved a pressure of 83 bar and a flow rate of 204 mL/min at a frequency of 1000 Hz [263]. Similarly, the active valve piezopump

developed by Lemke et al. attained a pressure of 0.505 bar and a flow rate of 4.36 mL/min at a driving voltage of 45 V [264]. Additionally, Cazorla et al. introduced an active valve piezopump powered by a piezo membrane actuator, achieving a pressure of 0.04 bar and a flow rate of 0.0036 mL/min at 24 V, with a remarkably low power consumption of just 0.3 mW [265]. Table 17 summarizes the performance of the analysed active valve piezopumps.

Table 17. Performance comparisons of the analysed active valve piezopumps.

Reference	Type of Valve	Driving Voltage (U_{pa}) [V]	Driving Frequency (f_{pa}) [Hz]	Maximum Pressure (p_{max}) [bar]	Maximum Flow Rate (Q_{max}) [mL/min]	Pumping Medium
Lee et al. [263]	Active	–	1000	83	204	Water
Lemke et al. [264]	Active	45	35	0.505	4.36	Water
Cazorla et al. [265]	Active	25	1	0.04	0.0036	Water

2.4.3 Comparison of Valveless and Valved Piezopumps

Valved piezopumps excel in delivering high flow rates and pressures, which makes them promising for uses such as cooling systems, fuel distribution, and aerospace applications. Despite these advantages, valved piezopumps, particularly passive valve piezopumps, are susceptible to fatigue and wear when operating at high frequencies. Additionally, these piezopumps may reduce the survival rate of possible transported living organisms.

In contrast, valveless piezopumps have no moving parts, allowing them to operate at much higher frequencies and handle fluids with micro particles, making them especially advantageous for applications in biomedicine and chemical analysis. However, valveless performance is hindered by liquid backflow, resulting in flow rates generally lower than 100 mL/min and output pressures below 0.05 bar.

2.4.4 Application of Piezopumps

As shown in Fig. 76, piezoelectric pumps are used in four main fields: electronic instruments, industrial production, scientific applications and fuel supply [218].

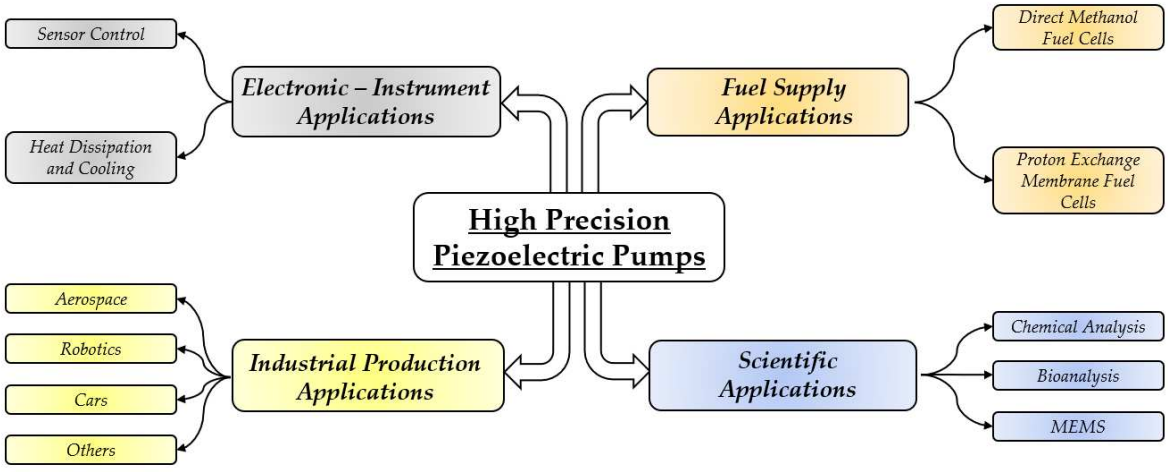

Fig. 76. Applications of high precision piezoelectric pumps.

2.4.4.1 Electronic – Instrument Applications

Piezoelectric pumps are utilized in two main areas within electronic instruments: sensing control and heat dissipation cooling.

In the realm of sensing control, flow sensing is crucial for piezopump applications, which can be categorized into indirect and direct flow sensing. Indirect flow sensing involves measuring flow rates using intelligent speed measuring instruments. For example, Dinh et al. incorporated a p-type silicon hotwire as a flow rate sensor within a micropump, achieving a resolution in the microliter range, making it suitable for microfluidic applications [266].

On the other hand, direct flow sensing, also known as piezoelectric self-sensing, was exemplified by Zhang et al., who introduced a novel micropump concept utilizing space-division multiplexing [267]. In this design, the electrode of the PEA is split into a driving element and a sensing element, allowing the sensor to be integrated into the micropump. This integration enables the prediction of changes in flow rate and pressure.

In the area of cooling, as electronic components shrink and the power density of microprocessors continues to rise, there is a growing need for improved cooling systems to effectively dissipate heat. Microfluidic electronic cooling systems using piezopumps offer efficient cooling solutions. In 2018, for instance, Chen et al. proposed a computer chip water cooling system powered by a piezoelectric pump [268]. This design aimed to enhance the applicability, maintainability, and cooling efficiency of water-cooling systems, presenting a novel approach to effectively cool computer chips.

2.4.4.2 Scientific Applications

In the realms of chemical analysis, bioanalysis, and MEMS, piezoelectric pumps hold significant promise due to their miniaturization, precise flow control, low energy consumption, and minimal backflow pressure.

The miniaturization of chemical processes into "lab-on-a-chip" or micro total analysis systems has gained significant interest due to their reduced reagent use, smaller space requirements, and quicker

analysis times. In this context, Ma et al. developed a piezopump, which demonstrates impressive capabilities, including a liquid transfer rate of 8.4 nL/s, a maximum flow rate of 102 nL/s, and pressures up to 0.02 bar [269]. This pump's exceptional performance and reliability underscore its significant potential for chemical analysis applications.

High-precision fluid transport and distribution are essential in modern science and technology, particularly within the biomedical field, which encompasses laboratory drug proportioning systems, bioanalytical techniques, and high-throughput screening methods. Micropumps are valuable in micro biochemical analysis systems due to their capability to manipulate and deliver small volumes of liquid. For example, piezoelectric pumps are utilized to accurately transfer insulin for diabetic patients, where micropumps play a critical role in drug delivery and dosing systems [270].

2.4.4.3 Industrial Production Applications

In various industrial sectors like aerospace, automotive, robotics, and drives, there is an increasing focus on small piezoelectric precision actuators, which offer high accuracy, quick response times, and strong electromagnetic interference resistance.

Sell et al. developed an innovative pieohydraulic pump capable of delivering a high-power output ranging from 10 W to 100 W [271]. This pump was designed for aerospace applications, specifically to provide the necessary flow rate to actuate accessory actuators in landing gear systems. By doing so, it aimed to enhance flight efficiency by reducing non-propulsive power consumption and minimizing aircraft weight.

In robotics, miniaturizing conventional suction mechanisms can be quite challenging. To address this issue, piezoelectric pumps can be integrated into suction pads. For example, in 2018, Hwang et al. designed a new suction pad featuring a valveless piezoelectric pump [272].

Applications also extend to engine gas distribution mechanisms. In 2009, Kim and Wang designed a non-linear gliding pattern for the force detection system in a piezohydraulic pump-based drive system [273].

2.4.4.4 Fuel Supply Applications

Fuel cells are miniaturized devices that convert chemical energy into electrical energy. Piezopumps play a crucial role in transferring the fuel needed to generate this electricity, particularly in Direct Methanol Fuel Cells (DMFC) and Proton Exchange Membrane Fuel Cells (PEMFC). These fuel cells offer several advantages, including higher power density, longer service life, and near-instantaneous charging compared to conventional cells [274].

For both DMFC and PEMFC devices, piezopumps must meet specific requirements, such as low power consumption and adequate fuel flow rates. Zhang et al. developed a miniaturized DMFC that utilizes a valveless micropump to ensure a sufficient fuel supply while simultaneously removing carbon dioxide generated by the fuel cell [275].

3. AIRCRAFT FUEL SYSTEM MODELLING

This chapter outlines the aircraft fuel system layout and simulation model developed for gas turbine engines (both turboprop and turbofan) as part of this research. Designed in the Simulink environment, a widely used industrial software, the model enables manufacturers and researchers to assess the performance of FMU, with a particular focus on conventional servovalves that play a crucial role in controlling fuel flow rate to combustion chamber/IGV actuator under various operating conditions. The chapter provides an in-depth description of the model, detailed performance results for selected scenarios, and a system power consumption analysis that identifies primary sources of loss. These findings offer valuable insights for EU initiatives targeting reductions in aircraft power consumption and addressing the CO_2 impact of conventional gas turbine engines. Results were shared at the ATI conference at the Polytechnic University of Bari in September 2022 [42] and the ASME/BATH conference on Fluid Power and Motion Control in Sarasota, USA, in October 2023 [43].

3.1 Aircraft Fuel System Layout

The proposed aircraft fuel system layout is shown in Fig. 77. This design resembles the General Electric CJ610 fuel system, previously illustrated in Fig. 9 of Chapter 2 [23]. The hydraulic schematic is drawn using ISO symbols.

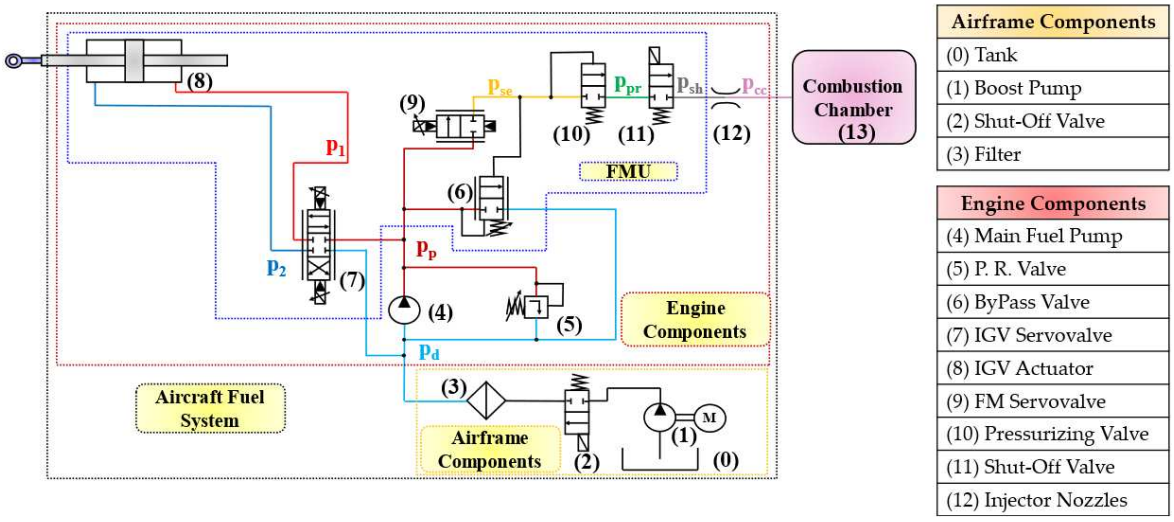

Fig. 77. Aircraft fuel system layout analysed in this research project.

3.2 Simulink Model

A simulation code, reproducing the fuel system layout of Fig. 77, has been produced in Simulink, software developed by MathWorks® based in Natick, MA, USA. In particular, the Simscape Fluids library has been used. The code graphical scheme is shown in Fig. 78.

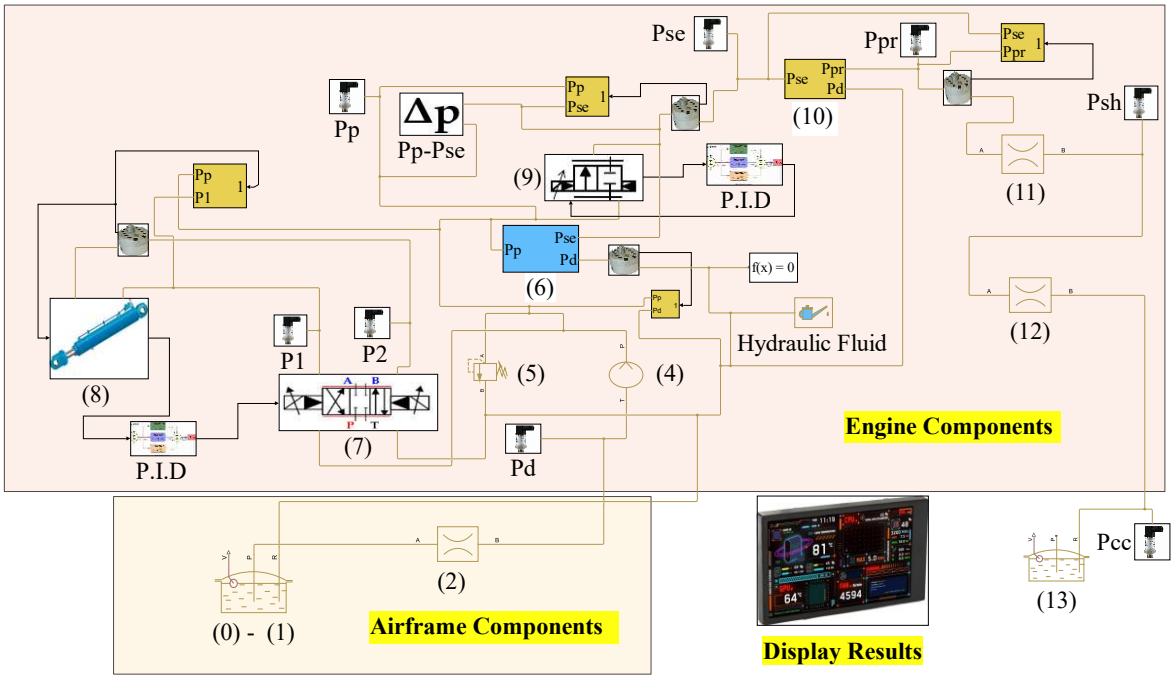

Fig. 78. Simulink model reproducing the aircraft fuel system proposed.

The resulting set of ordinary differential equations describing the dynamics of the system with respect to time are solved by the solver Ode 15s (Stiff/NDF) with time steps of 0.1 ms..

3.2.1 Airframe Components

To simplify the simulation of the airframe components, the fuel tanks (0) and boost pumps (1) are combined and represented by the "Reservoir" block. This block acts as a pressurized hydraulic reservoir and its pressure (i.e., the boost pressure, p_d) can be set within the block. On the other hand, the airframe shut-off valve (2) is simulated using the "Constant Area Hydraulic Orifice" block. In the model, this valve is assumed to be fully open, with negligible pressure drops across it. This means that the boost pressure (p_d) is the pressure that the fluid has at the inlet of the main fuel pump (4).

3.2.2 Engine Components

3.2.2.1 Main Fuel Pump – Pressure Relief Valve

The main fuel pump (4) is typically a gear-type positive displacement pump and in certain aircraft fuel systems, it consists of a high-pressure (HP) gear pump and a low-pressure (LP) centrifugal pump. The LP pump is used to increase the fuel pressure at the HP pump inlet, ensuring and facilitating proper fuel suction [23]. To prevent any damage to the system, a pressure relief valve (5)

is installed in the pump housing. In the simulation model, the main fuel pump is represented by the "Hydraulic Constant Flow Rate Source" block, considering only the HP pressure pump, while the pressure relief valve is represented by the "Pressure Relief Valve" block. The former maintains a specified flow rate at its outlet, regardless of the pressure difference. In contrast, the latter allows setting a maximum pressure, p_{max}, that keeps the valve closed until the inlet pressure is below this value. The flow rate delivered by the main fuel pump, Q_p, can be set within the "Hydraulic Constant Flow Rate Source" block.

The power absorbed by this pump, P_a, is evaluated using the following equation [42]:

$$P_a = \frac{Q_p(p_p - p_d)}{\eta_p}. \tag{4}$$

where p_p is the pressure downstream of the main fuel pump, and η_p is its efficiency.

3.2.2.2 Bypass Valve

The fuel delivered by the main fuel pump encounters a bypass valve (6) as it enters the FMU. This valve is designed to maintain a constant differential pressure between the fuel pump pressure, p_p, and the main metered fuel pressure, p_{se}. Fig. 79 shows that the bypass valve consists of a spool that operates in a ported sleeve, which is actuated by a spring. The latter regulates the movement of the spool, allowing a specific quantity of fuel to be redirected back to the inlet of the main fuel pump, and this quantity of fuel changes based on the operating conditions. Consequently, this mechanism ensures that an almost constant differential pressure is maintained across the FM servovalve, resulting in a proportional relationship between the degree of its opening and the fuel flow through its main stage.

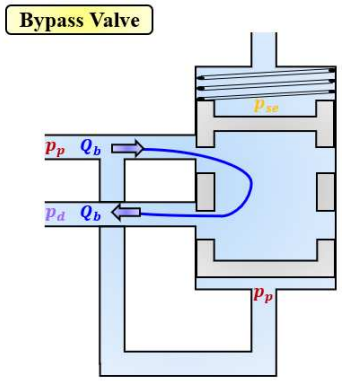

Fig. 79. Schematic representation of the Bypass Valve including the main parameters used in the numerical model.

To determine the differential pressure across the FM servovalve (i.e., $p_p - p_{se}$), various forces acting on the spool of the bypass valve must be taken into account, including the flow force, inertia force, and damping force [42]. When the spool is stationary and the flow force is neglected, the differential pressure is given by [42]:

$$\left(p_p - p_{se}\right) = \frac{k_b(x_{0,b} + x_b)}{A_b}, \tag{5}$$

where A_b is the effective area of the spool; $x_{0,b}$, k_b and x_b are the preload, the stiffness, and the deformation of the spring, respectively. The suffix "b" denotes the quantities regarding the bypass valve.

To evaluate the fuel flow rate, Q_b, which flows through this valve, the following equation can be used:

$$Q_b = C_{D,b} w_b x_b \sqrt{\frac{2(p_p - p_d)}{\rho}}, \tag{6}$$

where $C_{D,b}$ is the discharge coefficient, whereas w_b is the slot width of the bypass valve.

When fuel flows through the bypass valve, it experiences a pressure drop, which results in power consumption. Equation (7) provides a means to calculate the extra power required by the main pump to overcome the pressure drop caused by the bypass valve. Therefore, the power loss in the bypass valve, $P_{d,b}$, can be determined as follows [42]:

$$P_{d,b} = \frac{Q_b(p_p - p_d)}{\eta_p}. \tag{7}$$

3.2.2.3 IGV Servovalve – FM Servovalve

The IGV servovalve (7) and the FM servovalve (9) are crucial components of the FMU. The former controls the position of the IGVs by supplying fuel flow to the IGV actuator (8). On the other hand, the latter regulates the amount of fuel injected into the combustion chamber (13). Both the FM servovalve and the IGV servovalve offer the option of incorporating a feedback spring for mechanical feedback or using a LVDT for electrical feedback [21]. For this analysis, both servovalves are assumed to be equipped with an LVDT, meaning that the feedback spring is not considered. In particular, the main equations describing their operating principles are presented in three subsections. The first subsection (3.2.2.3.1) contains the equations used for the pilot stage of both electrohydraulic servovalves, while the second (3.2.2.3.2) and third (3.2.2.3.3) subsections describe the equations used for the main stage of the IGV and FM servovalves, respectively.

3.2.2.3.1 IGV Servovalve – FM Servovalve: Pilot Stage

The equations provided in this subsection can be utilized to model the pilot stages of both electrohydraulic servovalves as they share the same architecture. As shown in Fig. 80, the pilot stage is a double flapper/nozzle system which is mainly composed of a torque motor, a flapper and a flexure tube [21]. The torque motor is a small electromagnetic actuator which is made up of coils, pole pieces, and an armature. The latter is linked to the flapper and a non-magnetic flexure tube supports the flapper while keeping the torque motor separate from the hydraulic fluid [21].

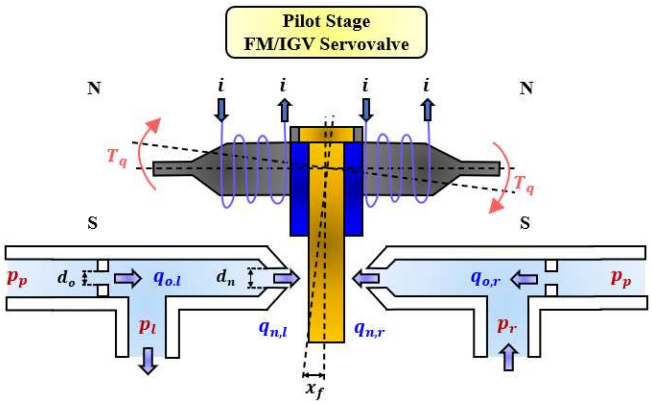

Fig. 80. Schematic representation of the pilot stage of both electrohydraulic servovalves including the main parameters used in the numerical model.

The simulation parameters shown in Fig. 80 and the following equations are not specific to either the IGV servovalve or the FM servovalve and can be applied to both. However, to differentiate between the two, a specific suffix must be added. In this analysis, to refer to the IGV servovalve, the suffix *"IGV"* is used, while the suffix *"FM"* is used for the FM servovalve.

When a low input current (i) flows through the coils of the torque motor, the ends of the armature become polarized. This generates a torque (T_q) that makes the armature and consequently the flapper to rotate from the central position towards one of the two nozzle [21]. To determine the torque produced, the following equation can be used [42]:

$$T_q = K_1 i, \tag{8}$$

where K_1 is a conversion factor, provided by Moog [42].

According to the model, a positive current produces a positive torque which allows the flapper to move towards the left nozzle (indicated with a positive sign). Conversely, a negative current produces a negative torque which allows the flapper to move towards the right nozzle (indicated with a negative sign). The flapper small displacement leads to the assumption of linear and translational movement, for simplicity [21].

The relationship between the produced torque (T_q) and the resulting flapper displacement (x_f) is modelled using a second-order transfer function G(s) [276], [277]:

$$G(s) = \frac{x_f}{T_q} = \frac{{}^{1}/_{K_f}}{1 + s\left(\frac{2\xi}{\omega_n}\right) + \left(\frac{s}{\omega_n}\right)^2}, \tag{9}$$

where s is the complex variable and K_f is the stiffness of the flapper; ω_n and ξ are the natural frequency and the damping ratio of the torque motor.

In the pilot stage, the orifices can have a fixed or variable area. The equations that govern the flow of fuel through these orifices are provided below [21]:

$$q_{o,r} = C_{D,o}\frac{\pi d_o^2}{4}\sqrt{\frac{2(p_p - p_r)}{\rho}}, \tag{10}$$

$$q_{o,l} = C_{D,o}\frac{\pi d_o^2}{4}\sqrt{\frac{2(p_p - p_l)}{\rho}}, \tag{11}$$

$$q_{n,r} = C_{D,n}\pi d_n(x + x_f)\sqrt{\frac{2(p_r - p_d)}{\rho}}, \tag{12}$$

$$q_{n,l} = C_{D,n}\pi d_n(x - x_f)\sqrt{\frac{2(p_l - p_d)}{\rho}}. \tag{13}$$

where p_r and p_l are the pressures acting on the right and left end faces of the sliding spool, respectively; x denotes the clearance between the flapper and the nozzles; d is the orifice/nozzle diameter. The suffix "o" is used to denote the two fixed orifices, while the suffix "n" is used for the two variable orifices.

3.2.2.3.2 IGV Servovalve: Main Stage

With reference to Fig. 81, assuming that the main stage spool moves from the left (l) to the right (r), the equilibrium of the forces acting on the spool can be written as [21]:

$$(p_{l_{IGV}} - p_{r_{IGV}})A_{s,IGV} - F_{f,IGV} - M_{IGV}\ddot{X}_{IGV} - C_{IGV}\dot{X}_{IGV} = 0, \tag{14}$$

where $(p_{l_{IGV}} - p_{r_{IGV}})\ A_{s,IGV}$ is the actuation force generated by the differential pressure $(p_{l_{IGV}} - p_{r_{IGV}})$ acting on the sliding spool lateral surfaces of area $A_{s,IGV} = \frac{\pi D_{IGV}^2}{4}$; D_{IGV} denotes the diameter of the sliding spool; $F_{f,IGV}$ is the flow force that opposes the actuation force; $M_{IGV}\ddot{X}_{IGV}$ and $C_{IGV}\dot{X}_{IGV}$ are the inertia force and the damping force (accounting for friction), respectively; M_{IGV} and C_{IGV} indicating the mass and the damping factor of the sliding spool, respectively.

To evaluate the damping factor of the sliding spool, which is due to the frictional forces acting on it, the following relation can be used [42]:

$$C_{IGV} = \frac{\mu\pi D_{IGV} l_{IGV}}{c_{IGV}\sqrt{1 - \left(\frac{\varepsilon_{IGV}}{c_{IGV}}\right)^2}}, \tag{15}$$

where μ is the dynamic viscosity of the jet fuel, and l_{IGV} is the length of the sliding spool; $c_{IGV}$is the radial clearance and ε_{IGV} is the radial eccentricity.

The flow force is calculated by using the following simplified equation [48]:

$$F_{f,IGV} = 2\rho\frac{Q_{IGV}^2}{A_{r,s_{IGV}}}cos\vartheta, \tag{16}$$

where the factor 2 is due to two metering chambers being opened simultaneously (P → A and B → T, for a right displacement of the sliding spool, or P → B and A → T, for a left displacement of the sliding spool), Q_{IGV} is the volumetric flow rate, $A_{r,s_{IGV}}$ is the restriction area through each metering

chamber, and θ is the velocity angle with respect to the horizontal direction at section $A_{r,s_{IGV}}$. The value of the restriction area is determined as follows [48]:

$$A_{r,s_{IGV}} = b_{IGV} X_{IGV} \; if \; X_{IGV} \geq c_{IGV}, \tag{17}$$

$$A_{r,s_{IGV}} = A_{l,s_{IGV}} = b_{IGV} c_{IGV} \; if \; X_{IGV} < c_{IGV}, \tag{18}$$

where b_{IGV} is the overall slot width and $A_{l,s_{IGV}}$ is the sliding spool leakage area. The restriction area has the same value in both the (P→A) and (B→T) paths. In this analysis, the impact of fluid erosion and any geometrical imperfections that might cause an increase in the leakage area, as discussed in [38] has been left out of consideration.

The flow rate through each metering section of the main stage is calculated using the orifice equation:

$$Q_{IGV} = C_{D_{IGV}} A_{r,s_{IGV}} \sqrt{\frac{2\Delta p}{\rho}}, \tag{19}$$

where $C_{D_{IGV}}$ is the discharge coefficient and Δp denotes the pressure drop across the IGV servovalve, which can be calculated as follows:

$$\Delta p = p_p - p_1 = p_2 - p_d = \frac{p_p - p_d}{2}, \tag{20}$$

where p_1 and p_2 are the pressures at Port A and Port B, respectively.

To calculate the extra power consumed by the main fuel pump because of the pressure drop in the main stage of the IGV servovalve, without taking into account the internal leakage of the pilot stage, the following equation can be used to determine the power dissipated by the IGV servovalve main stage [49]:

$$P_{d,IGV} = 2 \frac{Q_{IGV} \Delta p}{\eta_p}, \tag{21}$$

To control the position of the IGV actuator, a closed-loop control system is simulated using a Proportional-Integral (PI) controller. The controller modifies the low input current to the IGV servovalve to attain the desired position of the IGV actuator. The low input current (i_{IGV}) is determined by the following equation:

$$i_{IGV} = K_{p,IGV} e_{IGV}(t) + K_{I,IGV} \int_0^t e_{IGV}(t) dt. \tag{22}$$

where $e_{IGV}(t)$ is the error, namely, the difference between the set point and the actual value of the IGV actuator position, X_A; $K_{p,IGV}$ and $K_{I,IGV}$ denote the proportional and integral gain of the IGV controller, respectively.

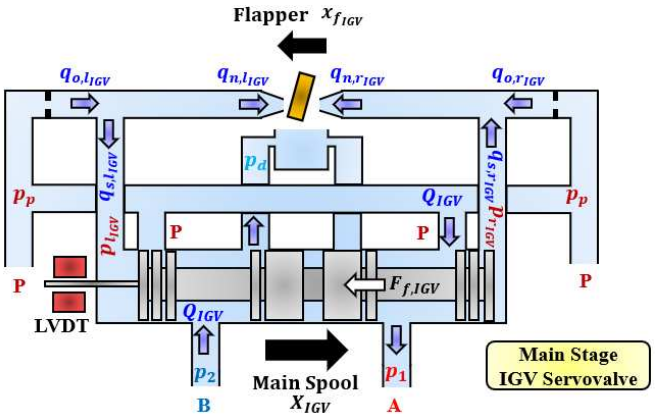

Fig. 81. Schematic representation of the main stage of the IGV Servovalve including the main parameters used in the numerical model.

In the schematic representation of Fig. 81, $q_{s,l_{IGV}}$ and $q_{r,l_{IGV}}$ denote the pilot flow entering (positive sign) or exiting (negative sign) the IGV servovalve main stage on the left and right side, respectively.

3.2.2.3.3 FM Servovalve: Main Stage

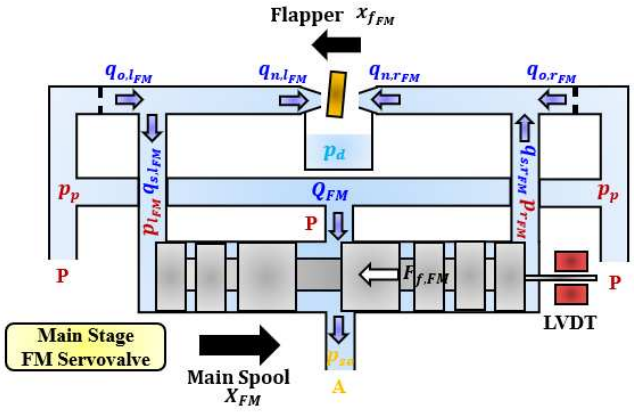

Fig. 82. Schematic representation of the main stage of the FM Servovalve including the main parameters used in the numerical model.

The equations below explain how the main stage of the FM servovalve operates, considering the movement of the main spool from left (l) to right (r) as depicted in Fig. 82.

To compute the damping factor (C_{FM}) of the main spool and determine the equilibrium of forces on it, equations (14 – 15) can be utilized by using the suffix *"FM"* instead of *"IGV"*.

The flow force, $F_{f,FM}$, and the main metered fuel flow rate, Q_{FM}, through the metering section of the main stage can be evaluated by the following equations:

$$F_{f,FM} = \rho \frac{Q_{FM}^2}{A_{r,s_{FM}}} cos\vartheta, \tag{23}$$

$$Q_{FM} = C_{D_{FM}} A_{r,s_{FM}} \sqrt{\frac{2(p_p - p_{se})}{\rho}}, \tag{24}$$

To evaluate the restriction area of the metering section, $A_{r,s_{FM}}$, for the FM servovalve, equations (17 – 18) can be used by replacing the suffix *"IGV"* with *"FM"*.

To calculate the additional power absorbed by the main fuel pump as a result of the pressure drop in the main stage of the FM servovalve, without taking into account internal leakage, the power loss through the FM servovalve main stage can be computed using the following equation [42]:

$$P_{d,FM} = \frac{Q_{FM}(p_p - p_{se})}{\eta_p}, \tag{25}$$

By means of a closed loop control system, a proportional-integral (PI) controller adjusts the low input current (i_{FM}) to obtain the desired main spool position (X_{FM}) according to the calculated error $e_{FM}(t)$:

$$i_{FM} = K_{p,FM} e_{FM}(t) + K_{I,FM} \int_0^t e_{FM}(t) dt. \tag{26}$$

where $K_{p,FM}$ represents the proportional gain of the FM servovalve controller, while $K_{I,FM}$ corresponds to the integral gain of the FM servovalve controller.

Once again, in the schematic representation of Fig. 82, $q_{s,l_{FM}}$ and $q_{r,FM}$ represent the pilot flow entering (positive sign) or exiting (negative sign) the FM servovalve main stage on the left and right side, respectively.

3.2.2.4 IGV Actuator

The IGV actuator (8) is mounted on the compressor casing and plays a fundamental role in adjusting the angle position of the IGVs. Fig. 83 illustrates that the IGV actuator is a double-ended double-acting (synchronous) cylinder, which means it has a symmetrical behaviour. In the numerical model, the simulation is limited to a single IGV actuator, which is a common configuration for turboprop and turbojet engines. However, the simulation can be expanded to include multiple actuators if they are present in the fuel system.

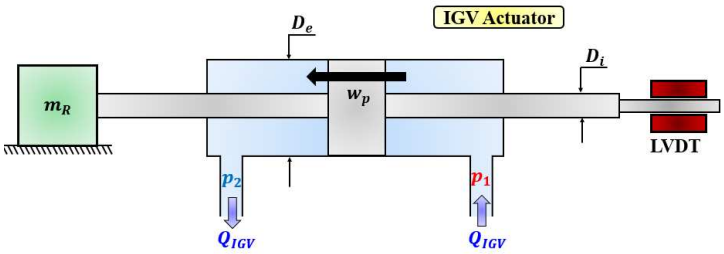

Fig. 83. schematic representation of the IGV Actuator including the main parameters used in the numerical model.

When the IGV servovalve provides fuel flow rate to the IGV actuator, causing the piston to move from right to left, the forces acting on the piston can be balanced as shown below:

$$(p_1 - p_2)A_A - (m_A + m_r)\ddot{X}_A - (C_A + C_r)\dot{X}_A = 0, \tag{27}$$

where $(p_1 - p_2)A_A$ is the actuation force generated by the differential pressure $(p_1 - p_2)$ acting on the lateral surfaces of piston area $A_A = \frac{\pi(D_e^2 - D_i^2)}{4}$; D_e and D_i denotes the diameter of the cylinder and the piston rod, respectively; m_A and m_r represent the mass of the piston and the mass of the IGVs actuation mechanism, respectively; C_A and C_r indicate the damping factor of the piston and of the IGVs actuation mechanism, respectively. In the model, the piston position, X_A, is measured by an ideal translational motion sensor; the sensor is considered to be ideal as the corresponding Simulink block neglects the effects of inertia, friction, time delays, and power consumption associated with it.

The piston velocity (w_p) can be evaluated using the following equation:

$$w_p = \frac{Q_{IGV}}{A_A}. \tag{28}$$

3.2.2.5 Pressurizing Valve

The pressurizing valve (10) serves to build up the main metered fuel pressure (p_{se}) to a predetermined minimum value $(p_{se,crack})$ before allowing metered fuel pressure (p_{pr}) to flow towards the engine shut off-valve.

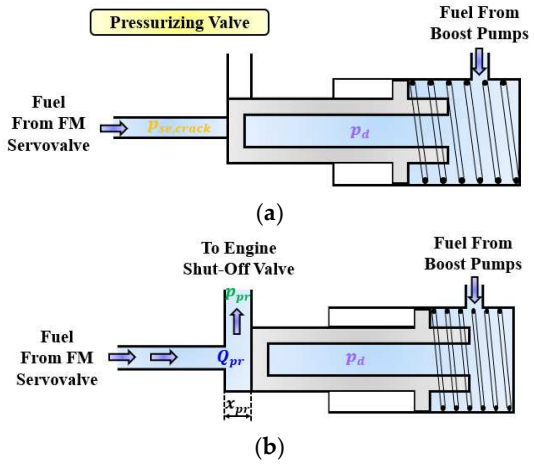

Fig. 84. Schematic representation of the Pressurizing Valve including the main parameters used in the numerical model: (**a**) Closed position; (**b**) Fully open position.

The operating principle of the pressurizing valve is shown in Fig. 84. The pressurizing valve is not meant to have any metering effect on the fuel, but there is a slight decrease in pressure across it, which is why p_{pr} is indicated as metered fuel pressure. At the start of the engine, the pressurizing valve is closed by the boost pressure (p_d), and the preload force of the spring $(k_{pr}x_{0,pr})$ to prevent low-pressure fuel from flowing to the fuel nozzles. The value of the cracking pressure $(p_{se,crack})$, which is the main metered fuel pressure at which the pressurizing valve starts to open, depends on

the equilibrium of the forces acting on the piston of the valve, including the flow force, inertia force and damping force [278]. When the piston is not moving, and neglecting the flow force, the cracking pressure is equal to:

$$p_{se,crack} = \frac{k_{pr} x_{0,pr}}{A_{pr}} + p_d, \tag{29}$$

where A_{pr} is the effective area of the piston; $x_{0,pr}$ and k_{pr} are the preload and the stiffness of the spring, respectively. The suffix "pr" denotes the quantities regarding the pressurizing valve.

The metered fuel flow rate, $Q_{pr,}$ that flows across the pressurizing valve towards the engine shut-off valve is given by [278]:

$$Q_{pr} = C_{D,pr} w_{pr} x_{pr} \sqrt{\frac{2(p_{se} - p_{pr})}{\rho}}, \tag{30}$$

where $C_{D,pr}$ is the discharge coefficient, whereas w_{pr} is the slot width of the pressurizing valve, and x_{pr} is the piston position (equal to the deformation of the spring).

The behaviour of the pressurizing valve can be described as follows: when it is not fully open, the metered fuel flow rate (Q_{pr}) across the valve has a linear relationship with the main metered pressure (p_{se}). Instead, once the valve is fully open, this relationship becomes quadratic. To determine the value of the main metered pressure ($p_{se,lin}$) at which the valve reaches its fully open position, the following equation can be used:

$$p_{se,lin} = \frac{k_{pr} x_{pr}}{A_{pr}} + p_{se,crack}, \tag{31}$$

The additional power absorbed by the main pump because of the pressure drop in the pressurizing valve can be evaluated as follows:

$$P_{d,pr} = \frac{Q_{pr}(p_{se} - p_{pr})}{\eta_p}. \tag{32}$$

3.2.2.6 Engine Shut-Off Valve – Fuel Nozzles – Combustion Chamber

The engine shut-off valve (11) is responsible for controlling the fuel flow to the engine, allowing it to be started or stopped as needed. The fuel nozzles (12) are the final components of the fuel system, responsible for atomizing or vaporizing the fuel to ensure efficient combustion. To model the behaviour of these components, two "Constant Area Hydraulic Orifice" blocks are used, while a "Reservoir" block is employed to simulate the combustion chamber (13). The flow rates passing through the engine shut-off valve (Q_{sh}) and the fuel nozzles (Q_{fn}) can be calculated using the following equations [42]:

$$Q_{sh} = C_{D,sh} A_{r,sh} \sqrt{\frac{2(p_{pr} - p_{sh})}{\rho}}, \tag{33}$$

$$Q_{fn} = C_{D,fn} A_{r,fn} \sqrt{\frac{2(p_{sh} - p_{cc})}{\rho}}. \quad (34)$$

where C_D is the discharge coefficient, whereas A_r is the restriction area (orifice area). The suffix "*sh*" and "*fn*" denote the engine shut-off valve and the fuel nozzles, respectively; p_{sh} is the pressure downstream of the engine shut-off valve (equal to the nozzles inlet pressure) and p_{cc} is the pressure in the combustion chamber; the latter value is set in the "Reservoir" block.

3.3 Numerical Results

In this section, the numerical results are presented and discussed. Table 18 provides the input values of the operating and geometrical parameters used in the simulations. These values are typical of fuel systems for a large-size turboprop engine and have been determined through a comprehensive review of relevant literature for each component [23], [276], [277], [279]. Furthermore, Table 19 displays the output variables that will be acquired from the simulations.

Table 18. Simulated input parameters and corresponding nomenclature.

Component	Input Parameter – (Symbol)	Value	Unit
Fuel (Jet Fuel)	Temperature (T)	90	°C
	Density (ϱ)	784.3	kg/m^3
	Viscosity (μ)	$7.7 \cdot 10^{-4}$	kg/(ms)
Boost Pumps (1)	Boost Pressure (p_d)	3	bar
Main Fuel Pump (4)	Flow Rate (Q_p)	40	L/min
	Pump Efficiency (η_p)	0.8	-
Pressure Relief Valve (5)	Max. Pressure (p_{max})	200	bar
Bypass Valve (6)	Spring Preload ($x_{0,b}$)	10.8	mm
	Spring Stiffness (k_b)	2500	N/m
	Spring def. max ($x_{b,max}$)	5	mm
	Spool Mass (m_b)	15	g
	Damping Factor (C_b)	20	Ns/m
	Spool Area (A_b)	78.54	mm^2
	Slot Width (w_b)	5	mm
Pilot Stage IGV/FM Servovalve (7) – (9)	Torque Motor Gain ($K_{I,IGV/FM}$)	0.025	in·lbf/mA
	Torque Motor Natural Frequency ($\omega_{n,IGV/FM}$)	730	Hz
	Torque Motor Damping Ratio ($\xi_{IGV/FM}$)	0.4	-
	Input Current ($i_{IGV/FM}$)	±10	mA
	Flapper Stiffness ($K_{f,IGV/FM}$)	93	in·lbf/in
	Flapper Clearance ($x_{IGV/FM}$)	0.1	mm
	Fixed Orifice Diameter ($d_{o,IGV/FM}$)	1.01	mm
	Nozzles Diameter ($d_{n,IGV/FM}$)	0.5	mm
Main Stage IGV Servovalve (7)	Spool Diameter (D_{IGV})	10	mm
	Spool Mass (M_{IGV})	30	g
	Spool Damping (C_{IGV})	1	Ns/m
	Spool Displacement (X_{IGV})	±1	mm
	Spool Length (l_{IGV})	80	mm
	Radial Clearance (c_{IGV})	3	µm

	Radial Eccentricity (ε_{IGV})	1	μm
	Leakage Area ($A_{l,s\ IGV}$)	$4 \cdot 10^{-2}$	mm^2
	Flow Angle (θ_{IGV})	69	deg
	Overall Slot Width (b_{IGV})	15	mm
IGV Actuator (8)	Piston Rod Diameter (D_i)	10	mm
	Cylinder Diameter (D_e)	40	mm
	Piston Stroke ($X_{A,max}$)	40	mm
	Piston Mass (m_A)	5	kg
	Piston Damping (C_A)	10	Ns/m
	IGV System Mass (m_r)	100	kg
	IGV System Damping (C_r)	10	Ns/m
Main Stage FM Servovalve (9)	Spool Diameter (D_{FM})	6	mm
	Spool Mass (M_{FM})	10	g
	Spool Damping (C_{FM})	1	Ns/m
	Spool Displacement (X_{FM})	1	mm
	Spool Length (l_{FM})	60	mm
	Radial Clearance (c_{FM})	3	μm
	Radial Eccentricity (ε_{FM})	1	μm
	Leakage Area ($A_{l,s\ FM}$)	$2.9 \cdot 10^{-2}$	mm^2
	Flow Angle (θ_{FM})	69	deg
	Overall Slot Width (b_{FM})	9.42	mm
Pressurizing Valve (10)	Spring Preload ($x_{0,pr}$)	2	mm
	Spring Stiffness (k_{pr})	10000	N/m
	Spring def. max ($x_{pr,max}$)	4	mm
	Spool Mass (m_{pr})	10	g
	Spool Damping Factor (C_{pr})	10	Ns/m
	Piston Area (A_{pr})	133	mm^2
	Slot Width (w_{pr})	1.5	mm
Engine Shut-Off Valve (11)	Restriction Area ($A_{r,sh}$)	15	[mm^2]
Fuel Nozzles (12)	Restriction Area ($A_{r,fn}$)	2.5	[mm^2]
Combustion Chamber (13)	Pressure (p_{cc})	12	[bar]

Table 19. Output variables nomenclature.

Component	Output Variable	Symbol
Main Fuel Pump (4)	Pressure	p_p
	Power Absorbed	P_a
Bypass Valve (6)	Flow Rate	Q_b
	Power Dissipated	$P_{d,b}$
Pilot Stage IGV/FM Servovalve (7) - (9)	Current	$i_{IGV/FM}$
	Torque	$T_{q\ IGV/FM}$
	Flapper Displacement	$x_{f\ IGV/FM}$
	Left Nozzle Flow Rate	$q_{n,l\ IGV/FM}$
	Left Orifice Flow Rate	$q_{o,l\ IGV/FM}$
	Right Nozzle Flow Rate	$q_{n,r\ IGV/FM}$
	Right Orifice Flow Rate	$q_{o,r\ IGV/FM}$
Main Stage IGV/FM Servovavle (7) – (9)	Left Spool Pressure	$p_{l\ IGV/FM}$
	Right Spool Pressure	$p_{r\ IGV/FM}$
	Total Pressure Drop (IGV Servovalve)	Δp
	Main Metered Pressure (FM Servovalve)	p_{se}

	Left Spool Flow	$q_{l,s\ IGV/FM}$
	Right Spool Flow	$q_{r,s\ IGV/FM}$
	Spool Position	$X_{IGV/FM}$
	Flow Force	$F_{f,IGV/FM}$
	Flow Rate	$Q_{IGV/FM}$
	Power Dissipated	$P_{d,IGV/FM}$
IGV Actuator (8)	Piston Delta Pressure	$(p_1 - p_2)$
	Piston Position	X_A
	Piston Velocity	w_P
Pressurizing Valve (10)	Cracking Pressure	$p_{se,crack}$
	Linear Trend Pressure	$p_{se,lin}$
	Metered Pressure	p_{pr}
	Flow Rate	Q_{pr}
	Power Dissipated	$P_{d,pr}$
Engine Shut-Off Valve (11)	Downstream Pressure	p_{sh}
	Flow Rate	Q_{sh}
Fuel Nozzles (12)	Flow Rate	Q_{fn}

To test the performance of the fuel system, closed-loop step tests were carried out, in which two controlled variables were adjusted. The positions of the FM servovalve main stage spool (referred to as X_{FM}) and the IGV actuator piston position (defined as X_A) were modified by changing the currents i_{FM} and i_{IGV} applied to the torque motor of the pilot stages of the two electrohydraulic servovalves.

The FM servovalve PI controller parameters were $K_P = 9$ and $K_I = 150$, while the IGV PI controller parameters were $K_P = 0.2$ and $K_I = 0.0025$. These specific values for the controller parameters were determined by a trial-and-error approach. The back calculation anti-windup method was implemented in the PI controller. The derivative action, as often occurs, was not considered because it is too sensitive to noise.

To perform the step tests, the set points for both control variables were changed five times each. For the FM servovalve, the set point was increased from 0 to 0.9 mm, then decreased from 0.9 to 0.7 mm, from 0.7 to 0.5 mm, from 0.5 to 0.3 mm, and finally returned to 0 mm. Each set point was maintained for 0.5 seconds, as shown in Fig. 85. Similarly, for the IGV actuator, whose piston was initially located in the neutral position (i.e., at the center of the cylinder, $X_A = 0$ mm), the set point was increased from 0 to 5 mm, then from 5 to 10 mm, from 10 to 15 mm, from 15 to 20 mm, and finally returned to 0 mm. Each set point was also maintained for 0.5 seconds, as shown in Fig. 86.

Fig. 85 to 89 present the time histories of the numerical results of the main parameters concerning the FM servovalve, IGV servovalve, and IGV actuator. Specifically, Fig. 85 and 87 focus on the main stage and pilot stage of the FM servovalve. Fig. 88 and 89 are related to the main stage and pilot stage of the IGV servovalve. Fig. 86 pertains to the IGV actuator.

Firstly, the graphs related to the FM servovalve are analysed. Observing Fig. 87, it is evident that when the FM servovalve pilot stage is not energized, the flapper remains stationary at $x_{f,FM} = 0$ mm (scaled by 15 in the graph for clarity). In this state, the combined quiescent flow from the two variable nozzles ($q_{n,r_{FM}}$ and $q_{n,l_{FM}}$) returning to the inlet of the main fuel pump is equal to 0.92 L/min, where $q_{n,r_{FM}} = q_{n,l_{FM}} = 0.46$ L/min. In the first positive step (at 3.5 s), the control system energizes the torque motor by transmitting a positive current (i_{FM}) to the coils of the FM servovalve pilot stage. The

generated electromagnetic field causes the armature to rotate due to a positive torque ($T_{q,FM}$). As the flapper is hinged to the armature, it moves towards the left nozzle, reducing the flow rate through it and increasing the flow rate through the right nozzle. On the other hand, for the other four negative steps, the opposite happens. Note that the current applied to the pilot stage remains non-zero in steady-state conditions to generate a pressure difference at the spool ends that counteracts the flow force acting on the main spool.

Referring to Fig. 85, specifically during the first significant positive step, the main spool position (X_{FM}) remarkably reaches 90% of the set points in less than 20 ms. As a consequence of the main spool displacement, the value of the main metered flow rate (Q_{FM}) flowing through the FM servovalve main stage towards the pressurizing valve undergoes changes. The graph also displays the pilot flow entering (positive sign) or exiting (negative sign) the FM servovalve main stage on the left ($q_{s,l_{FM}}$) and right ($q_{s,r_{FM}}$) side, which aligns well with the predicted main spool displacement.

When examining the predictions of the IGV servovalve pilot stage, Fig. 89 shows that they resemble those of the FM servovalve pilot stage, apart from the order in which the positive and negative steps occur, which are consistent with the IGV actuator set points, shown in Fig. 86. Once again, during the positive steps, the control system sends a positive current (i_{IGV}) to the coils of the IGV servovalve pilot stage, which generates a positive torque ($T_{q,IGV}$). This torque moves the flapper towards the left nozzle, causing the flow rate through the left nozzle ($q_{n,l_{FM}}$) to decrease and the right nozzle ($q_{n,r_{FM}}$) to increase. The opposite happens during the negative step. To make the plot clearer, the flapper displacement ($x_{f,IGV}$) is multiplied by 15.

The IGV servovalve main stage is designed to regulate the flow of fuel through its ports. When the flapper displacement is positive, the main spool moves from left to right (X_{IGV} is denoted by a positive value), allowing fuel to flow from Port (P) to Port (A), and from Port (B) to Port (T). Conversely, when the flapper displacement is negative, the main spool moves from right to left (X_{IGV} is denoted by a negative value), allowing fuel to flow from Port (P) to Port (B), and from Port (A) to Port (T). There are two important factors that affect the fuel flow rate through the IGV servovalve (Q_{IGV}). The first is the required position of the IGV actuator piston, which affects the opening degree of the IGV servovalve. The second is the required position of the FM servovalve main spool, which affects the pressure at the inlet of the IGV servovalve. Since both servovalves are connected to the same fuel line from the main fuel pump, the pressure in this fuel line (i.e., the pump pressure, p_p) will vary based on the FM servovalve main spool position. Examining Fig. 88, it is clear that the fuel flow rate used by the IGV Actuator, Q_{IGV} ($PA - BT$), decreases from the first to the fourth positive step, even though the step size remains the same. This decrease occurs because, although the main spool position of the IGV servovalve reaches the same value during these four positive steps ($X_{IGV} = 0.11$ mm), the pump pressure decreases progressively from the first to the fourth step because of the corresponding decrease in the FM servovalve main spool position. To provide greater clarity, the time history of the pressure pump (p_p) has been plotted in Fig. 92. The last step achieves the highest flow rate, Q_{IGV} ($PB - AT$), of the five steps and allows the piston of the IGV actuator to return to the starting position. This happens because, even though the pump pressure

at the IGV servovalve inlet is at its lowest point among the five steps, the IGV actuator piston position experiences the largest step size, resulting in the highest opening degree of the IGV servovalve ($|X_{IGV}| = 0.44$ mm). Once again, the predicted pilot flows ($q_{s,l_{IGV}}$ and $q_{s,r_{IGV}}$) are in agreement with the predicted main spool position.

With regard to the IGV actuator, it can be observed from Fig. 86 that the control system enables the IGV actuator piston (X_A) to attain the set points in less than 150 milliseconds in all simulated step tests. Additionally, the velocity of the piston (w_p) varies consistently with the fuel flow rate (Q_{IGV}) across all the five steps.

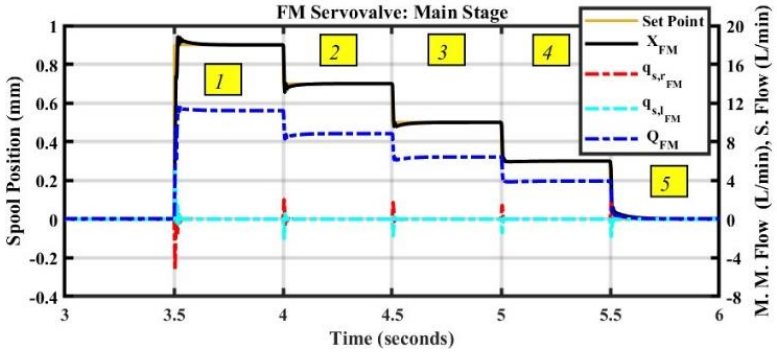

Fig. 85. Main stage FM Servovalve predictions: set point (mm), spool position (mm), spool flow rate (L/min), main metered flow rate (L/min).

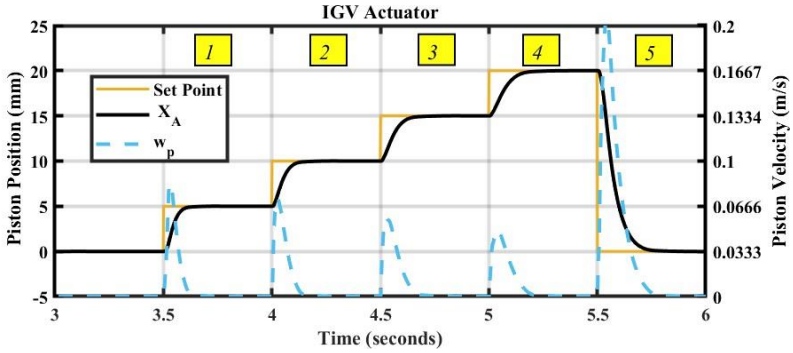

Fig. 86. IGV Actuator predictions: set point (mm), piston position (mm), piston velocity (m/s).

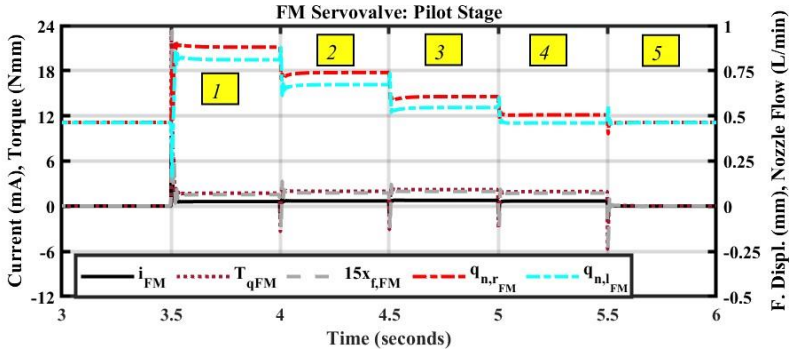

Fig. 87. Pilot stage FM Servovalve predictions: current (mA), torque (Nmm), flapper displacement (mm), nozzles flow rate (L/min).

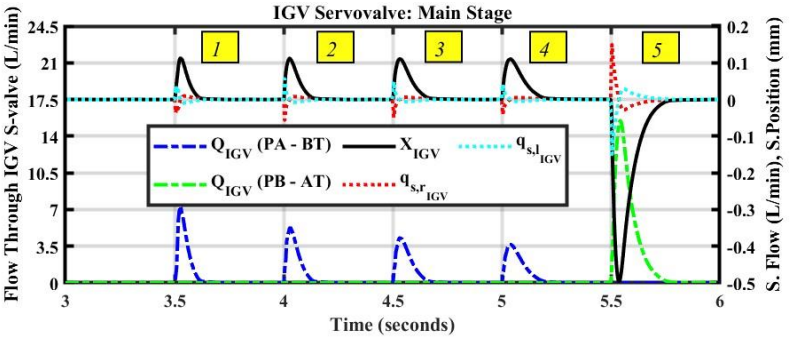

Fig. 88. Main stage IGV Servovalve predictions: flow through IGV Servovalve (L/min), spool position (mm), spool flow rate (L/min).

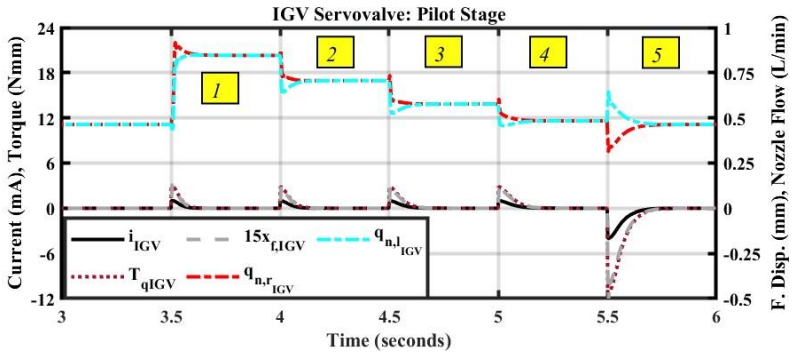

Fig. 89. Pilot stage IGV Servovalve predictions: current (mA), torque (Nmm), flapper displacement (mm), nozzles flow rate (L/min).

The numerical results of the bypass valve are presented in Fig. 90. At the first, before energizing the pilot stages of both servovalves, the bypass valve position (x_b) is approximately 2.5 mm. This configuration enables all the flow rate generated by the main fuel pump (except for the quiescent flows needed in the pilot stage of the two servovalves) to be bypassed back to the main fuel pump inlet. On the other hand, the spring-piston mechanism inside the bypass valve ensures an almost

constant pressure difference of 4 bar across the FM servovalve (3.7 bar < $p_p - p_{se}$ < 4.2 bar). This pressure difference slightly changes with the flow rate through the bypass valve, Q_b.

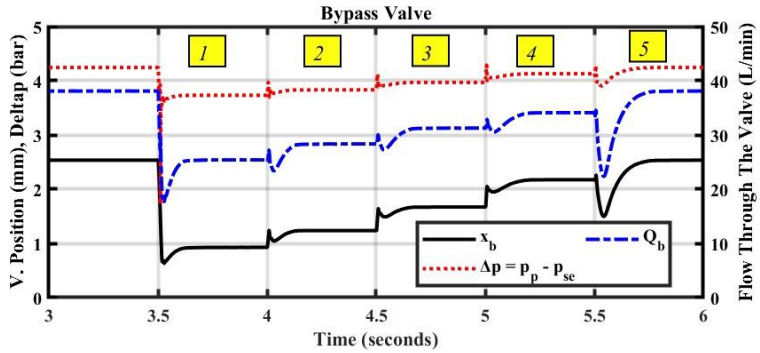

Fig. 90. Bypass Valve predictions: valve position (mm), delta-pressure (bar), flow through the valve (L/min).

The pressurizing valve predictions are shown in Fig. 91 and 92. In particular, Fig. 91 shows the pressurizing valve characteristic, which has been obtained during the first positive steps (when the FM servovalve set point is changed from 0 to 0.9 mm and the IGV actuator set point is changed from 0 to 5 mm), but holds general validity for all the five steps. The pressurizing valve opens at a minimum main metered pressure of $p_{se,crack}$ =18 bar and reaches its fully open position at a main metered pressure of $p_{se,lin}$ = 21 bar. During the transition phase between the closed and fully open position, the valve behaviour is linear, showing a direct relationship between the main metered pressure (p_{se}) and the metered fuel flow rate ($Q_{pr} = Q_{FM}$). Instead, for pressures above $p_{se,lin}$, the relationship becomes quadratic.

The graph of Fig. 92 indicates that the valve is fully open (x_{pr} = 4 mm) from the first to the third step due to p_{se} being greater than $p_{se,lin}$. However, during fourth step, the valve fails to reach its fully open position (x_{pr} = 2.5 mm) because $p_{se,crack} < p_{se} < p_{se,lin}$.

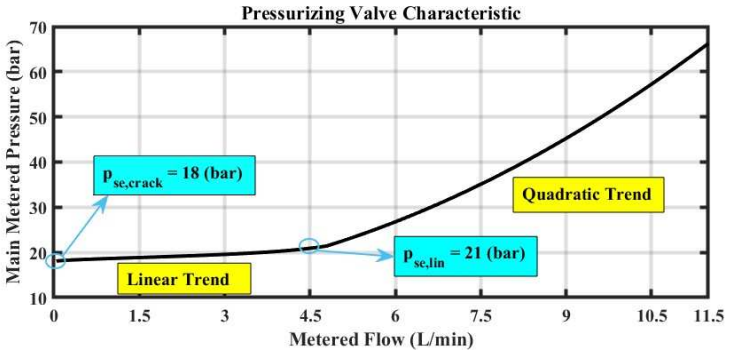

Fig. 91. Pressurizing valve characteristic: Linear and Quadratic Trend.

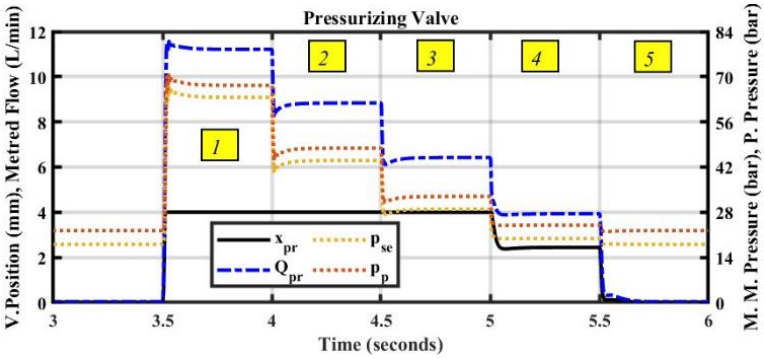

Fig. 92. Pressurizing Valve predictions: valve position (mm), metered flow rate (L/min), main metered pressure (bar), pump pressure (bar).

In Fig. 93, the pressure histories at various points of the fuel system are plotted over time. These points include the pressurizing valve outlet (p_{pr}), the engine shut-off valve outlet or injector nozzles inlet (p_{sh}), and the combustion chamber (p_{cc}), which remains constant since it is set to 12 bar. It can be observed that the pressure drops across the shut-off valve ($p_{pr} - p_{sh}$) and the injector nozzles ($p_{sh} - p_{cc}$) increase with the main metered flow rate (Q_{FM}) according to equations 33 and 34.

In conclusion, Fig. 94 presents the predicted power consumption for various components of the system, such as the main stage of the FM servovalve ($P_{d,FM}$), the main stage of the IGV servovalve ($P_{d,IGV}$), the pressurizing valve ($P_{d,pr}$), and the bypass valve ($P_{d,b}$). These sources of power consumption are due to the pressure drop generated in each component. In addition, the power absorbed by the main fuel pump (P_a) is plotted in Fig. 94. The graph indicates that the bypass valve and the IGV servovalve—a four-way, three-position (4/3) type—are the primary sources of power consumption under the given operating conditions, consuming approximately 3.5 kW and 1 kW, respectively. For the IGV and FM servovalves, the analysis focuses only on the power consumption due to internal leakage in the main stage, excluding the more significant energy consumption from the quiescent flow in the pilot stage. This finding highlights the challenges associated with two-stage servovalves regarding power efficiency. Therefore, modifications to their design and operation could lead to substantial energy savings, resulting in more efficient aircraft.

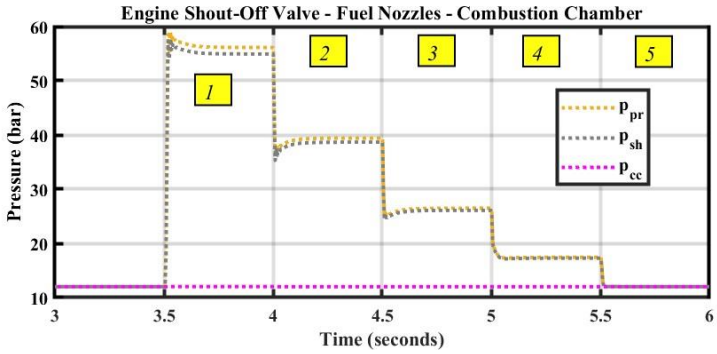

Fig. 93. Engine Shut-Off Valve, Fuel Nozzles, Combustion Chamber pressure (bar).

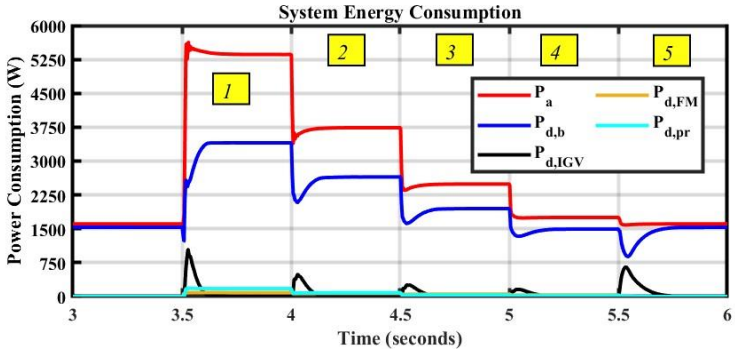

Fig. 94. System power consumption: Main Fuel Pump power (W), Bypass Valve, IGV Servovalve Main Stage, FM Servovale Main Stage, Pressurizing Valve power dissipated (W).

3.4 Discussion

These first research studies [42], [43] thoroughly examined the performance of an entire aircraft fuel system based on the General Electric CJ610 type. They analysed and simulated both airframe and engine components, including the main fuel pump, pressure relief valve, bypass valve, FM servovalve, pressurizing valve, engine shut-off valve, fuel nozzles, as well as the IGV servovalve and IGV actuators. These components were simulated using Simulink and the Simscape Fluids (Hydraulics) library, allowing for accurate closed-loop control simulations.

In the simulated step tests, the controlled variables were the sliding spool position of the FM servovalve and the piston position of the IGV actuator, while the control variables were the input currents sent to the pilot stages of the FM and IGV servovalves. The control system demonstrated high performance, achieving the desired set points for the FM servovalve and the IGV actuator in just 20 ms and 150 ms, respectively.

The code simulated the aircraft fuel system's dynamics and evaluated its energy efficiency. The investigation identified the bypass valve and IGV servovalve as the main energy consumers, dissipating about 3.5 kW and 1 kW, respectively. The analysis focused on internal leakage in the main stage of the IGV and FM servovalves, excluding the larger consumption from the quiescent flow in the pilot stage, highlighting efficiency challenges with two-stage servovalves. The findings suggested that redesigning conventional servovalve architectures could lead to significant energy savings and enhance the fuel system's sustainability and efficiency.

In conclusion, the developed numerical code is applicable to different turbine engine types (e.g., by including more actuators and changing the operating data), making it a valuable tool for both manufacturers and researchers to assess fuel system performance and explore optimization strategies.

4. DEVELOPMENT OF TWO INNOVATIVE HFSVs

Despite their widespread use in industrial and aeronautical applications, commercially available spool valves—both servovalves and proportional valves—are inefficient due to high power consumption, as thoroughly explained in Chapter 1. For instance, as evaluated the research studies in Chapter 3, servovalves heavily influence the energy performance of FMUs in aircraft fuel systems. Chapter 2 has introduced a recent research focus on replacing these spool valves with HFSVs, which could advance digital hydraulic technology in industrial and aeronautical applications.

Although digital hydraulic technology offers significant advantages, it currently lacks substantial industrial and aeronautical applications due to manufacturing challenges associated with HFSVs. These valves must achieve high switching frequencies and speeds (under 5 ms), minimize pressure losses, and deliver high flow rates while maintaining a compact size. Indeed, despite their high switching speeds and frequencies, the piezoelectric HFSVs reviewed in Chapter 2 deliver insufficient flow rates, making them unsuitable as direct replacements for conventional spool valves.

In this context, this Chapter presents a feasibility study of two potential HFSV architectures directly actuated by a commercially available ring stack—a multilayer PEA capable of generating the high actuation forces required for this application. The proposed valve architectures are assessed using well-established equations implemented in two Simulink models, allowing for accurate simulations of the hydraulic, mechanical, and electrical components of the valves. The chapter begins with a detailed description of the valve architectures and the corresponding numerical models developed, followed by validation of the ring stack actuator's hysteresis model against manufacturer-provided data. Finally, it presents the numerical results from both open-loop and closed-loop control systems.

The findings from these research studies have been shared at national [49] and international conferences [45] and published in prestigious journals [50].

4.1 Valve Architectures

To develop two novel HFSVs—specifically a two-way two-position (2/2) HFSV and a four-way two-position (4/2) HFSV—suitable for integration into the digital hydraulic circuit illustrated in Fig. 43 and Fig. 44 in Chapter 2, the following requirements must be met:

- ✓ Rapid Switching Time: The valves must be capable of switching between open and closed positions within a very short time interval, specifically less than 5 milliseconds;
- ✓ Low Pressure Drops: Even at high flow rates, the valves must generate minimal pressure drops in order to prevent energy dissipation. The desired target is to achieve a maximum pressure drop of 15 bar at a flow rate of 60 L/min;
- ✓ Robustness: The valves must be robust and reliable, capable of handling numerous operational cycles without compromising their functionality or durability.

To achieve the specified goals, a ring stack actuator is employed for the actuation of the valves. The specific ring stack actuator chosen for this purpose is manufactured by Noliac, namely the model NAC2125-HXX with the maximum height (H =200 mm) [280]. It is capable of producing the highest value of maximum free stroke (x_{max} = 325 µm). The maximum blocking force of this actuator is $F_{b,max}$ = 8450 N, while its stiffness is k_p = 26 N/µm. The detailed specifications are outlined in Table 20 [280], [281].

Table 20. NAC2125-HXX Ring Stack: Specifications [280].

Parameter	Symbol	Value	Unit
Outer Diameter	D	20	Mm
Inner Diameter	d	12	Mm
Height	H	200	Mm
Max. Operating Voltage	V_{max}	200	V
Max. Blocking Force	$F_{b,max}$	8450	N
Max. Free Stroke	x_{max}	325	µm
Capacitance	Cap	79300	nF
Stiffness	k_p	26	N/µm

The operation of the proposed HFSV architectures is depicted in Fig. 95. Specifically, Fig. 95a shows the working principle of the 2/2 HFSV, while Fig. 95b illustrates that of the 4/2 HFSV.

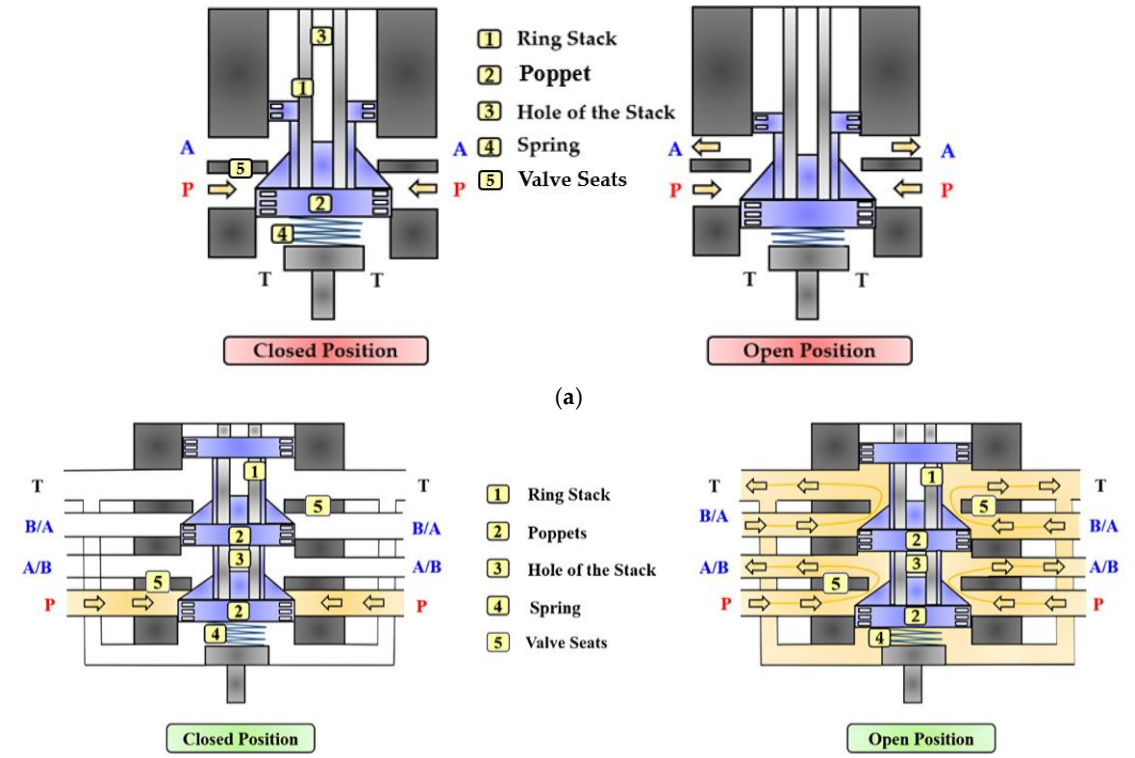

Fig. 95. Working principle of the proposed valve architectures: (**a**) 2/2 HFSV; (**b**) 4/2 HFSV

To avoid redundancy, only the working principle of the 4/2 HFSV will be described, as it closely resembles that of the 2/2 HFSV. Specifically, in the 4/2 HFSV design (Fig.95b), the valve remains closed thanks to the contact between the poppets (2) and the valve seats (5). To initiate valve opening, a digital signal is transmitted to activate the ring stack actuator (1). Consequently, the poppets, which are inserted through the hole of the stack (3), move downward, disengaging from their respective valve seats and allowing the valve to open. Additionally, the design includes a spring (4) with the dual function of maintaining close contact between the poppets and PEA and ensuring the correct pre-compression of the latter. This pre-compression is necessary because piezo stack actuators cannot handle large pulling forces, and applying a preload helps prevent damage.

When no voltage is applied to the ring stack actuator, no deformation occurs, and as a result, the valve remains closed, as depicted in Fig.95b (left). However, when a differential voltage is applied to the ring stack actuator, the poppets move from their original position, leading to the opening of the valve. Consequently, oil flow is permitted from Port P to Port A, and from Port B to Port T, as illustrated in Fig. 95b (right).

One critical aspect of HFSVs pertains to their frequent daily switching requirements. As a result, they must exhibit high resistance to wear and fatigue. In the selected 4/2 HFSV design, the poppets and their respective valve seats assume an important role in fulfilling these requirements. Any mismatch between these components could lead to adverse effects on sealing and the overall lifespan of the valve. To address this challenge, stainless steel is selected for the poppets, while nickel aluminium bronze is chosen for the valve seats, in line with recommendations provided by poppet valve manufacturers [282]. Furthermore, since the two poppets are integrated into a single body, achieving a reliable seal on both seats requires meticulous attention to geometric tolerances. This ensures a high-quality seal without adding unnecessary complexity or compromising functionality.

This focus on sealing performance is critical for minimizing leakage and maintaining system efficiency, setting this design apart from conventional spool valves, where achieving a perfect seal is generally not a priority.

4.2 Numerical Model of the 4/2 HFSV

The performance evaluation of the proposed valve architectures, specifically that illustrated in Fig.95, is conducted using well-established and referenced equations integrated within Simulink, utilizing the Simscape Fluids library [283]. Furthermore, since the model of the 4/2 HFSV extends from that of the 2/2 HFSV, only the 4/2 HFSV model will be described here. A detailed description of the 2/2 HFSV Simulink model is provided in [49]. The Simulink model of the 4/2 HFSV is shown in Fig. 96.

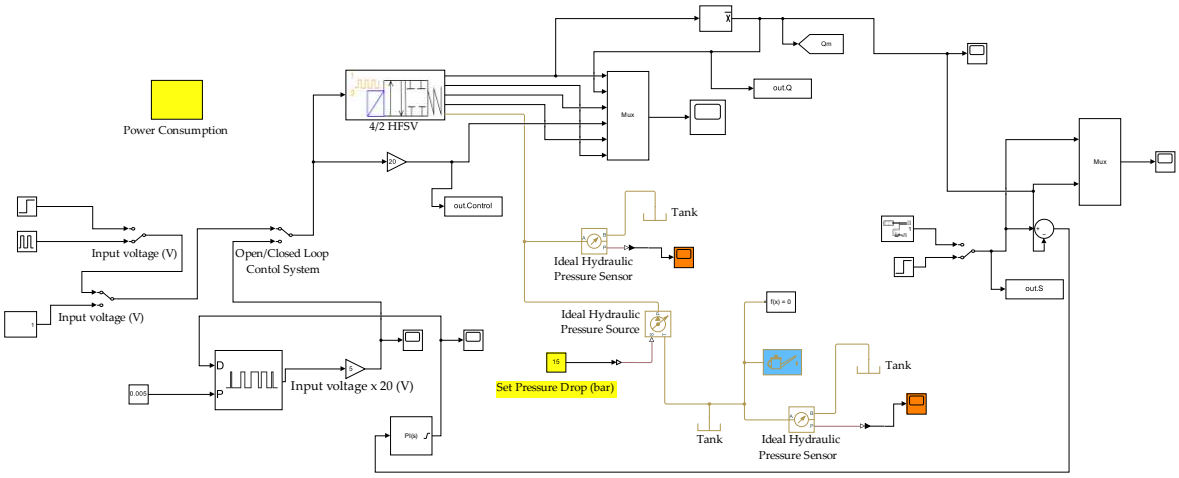

Fig. 96. 4/2 HFSV Simulink Model.

The equations implemented in Simulink are described in the following, referring to the actuation of the ring stack and the resulting opening of the valve, as shown in Fig. 97.

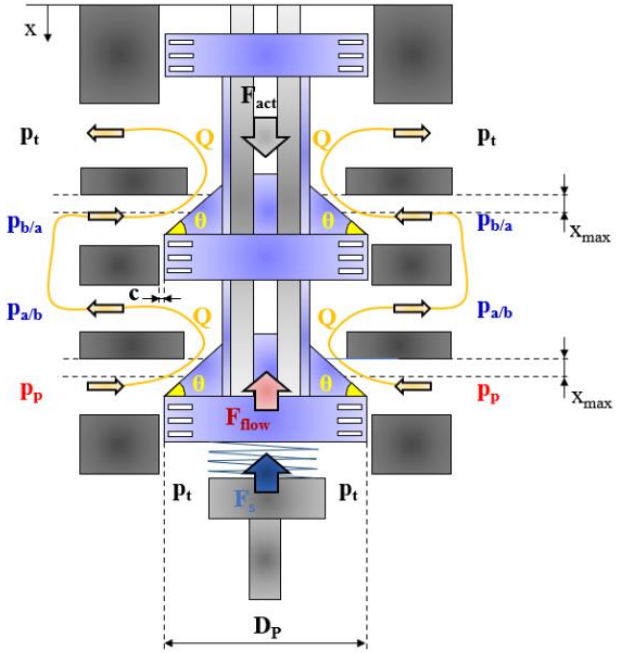

Fig. 97. Illustration of the modelled valve architecture in the open position, featuring the key system parameters employed and the main output variables obtained (please note that the radial clearance, denoted as "c," has been overestimated for clarity).

The ring stack necessitates an amplifier, which is responsible for converting a low-input control voltage, characterized by an overall period (τ), a switching frequency (f), an amplitude (V_c), and a duty cycle (DC), into a high-output voltage (V_{amp}). The relation between the output and the input voltage is simulated by using a second order transfer function $G(s)$ [49]:

$$G(s) = \frac{V_{amp}}{V_c} = \frac{k_a \omega_n^2}{s^2 + 2\xi\omega_n s + \omega_n^2}, \tag{35}$$

where s is the complex variable, while k_a, ω_n, and ξ are the gain, natural frequency and damping ratio of the amplifier, respectively. The current limit of the amplifier, I_{max}, is computed as follows [49]:

$$\left(\frac{dV_{amp}}{dt}\right)_{max} = \frac{I_{max}}{C_{ap}}, \tag{36}$$

where C_{ap} is the capacitance of the ring-stack.

The consideration of piezoelectric hysteresis involves the implementation of the Bouc-Wen hysteresis model, as described and used in reference [48]. This model enables the computation of the hysteresis nonlinear term, n:

$$\frac{dn}{dt} = \alpha \frac{dV_{amp}}{dt} - \beta \left|\frac{dV_{amp}}{dt}\right| n - \delta \frac{dV_{amp}}{dt} |n|, \tag{37}$$

where α, β and δ are parameters to be adjusted in order to adapt the hysteresis model to a specific case. The hysteresis non-linear term, n, is used to correct the blocking force, F_b, because of hysteresis, as follows [48]:

$$F_b = K_b K_{VF}(V_{amp} - n), \tag{38}$$

where K_b is a correction factor, to be tuned in order to match the numerical model with the experimental data provided by the manufacturer; whereas K_{VF} is a conversion factor (from voltage to force).

The blocking force, F_b, determines the actuation force, F_{act}, which can be calculated as follows [49]:

$$F_{act} = F_b - k_p x, \tag{39}$$

where k_p and x are the stiffness and the displacement of the actuator (the latter is equal to the poppets' displacement).

When the valve is actuated, the equilibrium of forces acting on the poppets can be expressed as:

$$F_{act} - F_s - F_{flow} - F_c - F_i = 0, \tag{40}$$

where:

- F_s is the force of the additional spring given by $F_s = k_s(x + \delta_0)$, with k_s and δ_0 representing the stiffness and the pre-compression of the additional spring;
- F_c is the viscous force given by $F_c = C\dot{x}$, with C representing the damping factor of the poppets (accounting for fluid viscosity);
- F_i is the inertia force given by $F_i = m\ddot{x}$, with m representing the mass of the moving parts.
- F_{flow} represents the flow forces acting on the poppets. Based on the momentum equation and architecture of the valve, the flow forces act in opposition to the actuation force, effectively working to close the valve. It is important to highlight that the contribution of the fluid

pressure from port P (p_p) is included in the calculation of flow forces. This term also accounts for viscous effects, ensuring a comprehensive representation of the forces acting on the valve.

To determine the damping factor of the poppets, C, which accounts for the frictional forces acting on them, the following relationship can be utilized [49]:

$$C = \frac{\mu\pi D_p l_p}{c\sqrt{1-\left(\frac{\varepsilon}{c}\right)^2}}, \tag{41}$$

where μ is the dynamic viscosity of the oil, D_p and l_p are the poppets' diameter and length of the part in contact with the case; c is the radial clearance and ε is the radial eccentricity.

The flow of fluid through the valve ports leads to the generation of steady-state and transient flow forces. Steady-state flow forces, which are hydrodynamic effects in stable flow conditions, can be further categorized as axial and radial flow forces [284]. In contrast, transient flow forces are instantaneous hydrodynamic phenomena that occur during sudden valve port opening or closing [285]. This analysis focuses only on steady-state flow forces, which occur as oil flows through the two metering chambers. The evaluation of these forces can be performed using the following equation [48], [286]:

$$F_{flow} = 2\rho\frac{Q^2}{A_r}cos\vartheta, \tag{42}$$

where the factor 2 considers the two metering chambers being opened simultaneously, ρ is the oil density, and θ is the velocity angle with respect to the horizontal direction; the volumetric flow rate, Q, and the restriction area, A_r, through each metering chamber can be calculated by the following equations [49]:

$$A_r = \pi D_p x sin\vartheta, \tag{43}$$

$$Q = C_D A_r\sqrt{\frac{\Delta p}{\rho}}, \tag{44}$$

where C_D is the discharge coefficient and Δp is the overall pressure drop across the valve. In the model, Port A and Port B are hydraulically connected and the pressure drop is neglected. Therefore, the pressure drop in Equation (42) becomes:

$$\Delta p = p_P - p_T = 2(p_B - p_T) = 2(p_P - p_A), \tag{45}$$

When oil flows through the metering chambers, it experiences a pressure drop, which results in power consumption. The ideal power average loss in the 4/2 HFSV, $P_{d,v}$ can be determined as follows [286]:

$$P_{d,v} = Q_M\Delta p, \tag{46}$$

where Q_M is the average flow rate provided by the valve.

The range of motion for the poppets is constrained by two stops, defining upper and lower bounds. Each stop incorporates a combination of a spring and a damper. When the poppets reach

their maximum displacement ($x = x_{max}$) or minimum displacement ($x = x_{min} = 0$), a force (F_{stop}) is exerted on the ring stack. The calculation for this force is evaluated as follows [49]:

$$F_{stop} = K_{stop}(x_{max} - x) + C_{stop}\frac{d}{dt}(x_{max} - x), \quad \text{for } x \geq x_{max} \tag{47}$$

$$F_{stop} = K_{stop}(x_{min} - x) + C_{stop}\frac{d}{dt}(x_{min} - x), \quad \text{for } x \leq 0 \tag{48}$$

To simulate the volume of oil between ports (P) and (A), as well as between ports (B) and (T), a block named "Constant Volume Hydraulic Chamber" is utilized. This block serves the purpose of mimicking a chamber with fixed volume and rigid walls, while also considering the compressibility of the fluid. The following equations are applied [49]:

$$V_{cham} = V_0 + \frac{V_0 p}{E}, \tag{49}$$

$$q_c = \frac{dV_{cham}}{dt} = \frac{V_0}{E}\frac{dp}{dt}, \tag{50}$$

where V_0 represents the geometrical volume of the chamber. This value is obtained by multiplying the internal diameter (D_0) by the overall internal length (L_0). On the other hand, V_{cham} represents the volume of oil in the chamber at a given pressure (p), while q_c represents the volumetric flow rate through the chamber. To calculate the actual bulk modulus (E), the following equation is used [49]:

$$E = E_0 \frac{1 + \sigma(\frac{p_a}{p})^{1/\gamma}}{1 + \sigma \frac{{p_a}^{1/\gamma}}{\gamma\, p^{(\gamma+1)/\gamma}} E_o}, \tag{51}$$

where E_0 is the pure liquid bulk modulus, p_a is the atmospheric pressure, γ is the gas-specific heat ratio (γ =1.4) and σ is the relative gas content at atmospheric pressure.

Both open and closed-loop control systems can be simulated. In the former control system, users have the flexibility to set the switching frequency (f), the overall period (τ), the duty cycle (DC), the amplitude (V_c) of the input control voltage, as well as the overall pressure drop across the valve (Δp). The resulting output variables include the average flow rate (Q_M) and the average power consumption ($P_{d,v}$). Conversely, in the latter control system, a PI controller is employed to adjust the duty cycle of the input pulse digital signal, aiming to achieve the desired average flow rate, based on the calculated error term $e(t)$:

$$DC = K_P e(t) + K_I \int_0^t e(t)dt \tag{52}$$

where K_P and K_I denote the proportional and integral gain, respectively. The controller does not incorporate the derivative action due to its susceptibility to noise in the process variable signal.

The Simulink solver, specifically Ode14x, calculates the states of the dynamic system at consecutive time intervals of 0.1 ms over a defined period.

To recap, Fig. 98 and Fig. 99 display two structured block diagrams that provide a visual representation of how the previous described equations flow in open and closed control systems, respectively. The colour of each block clarifies whether it represents the input variables, the input system parameters or the resulting output variables.

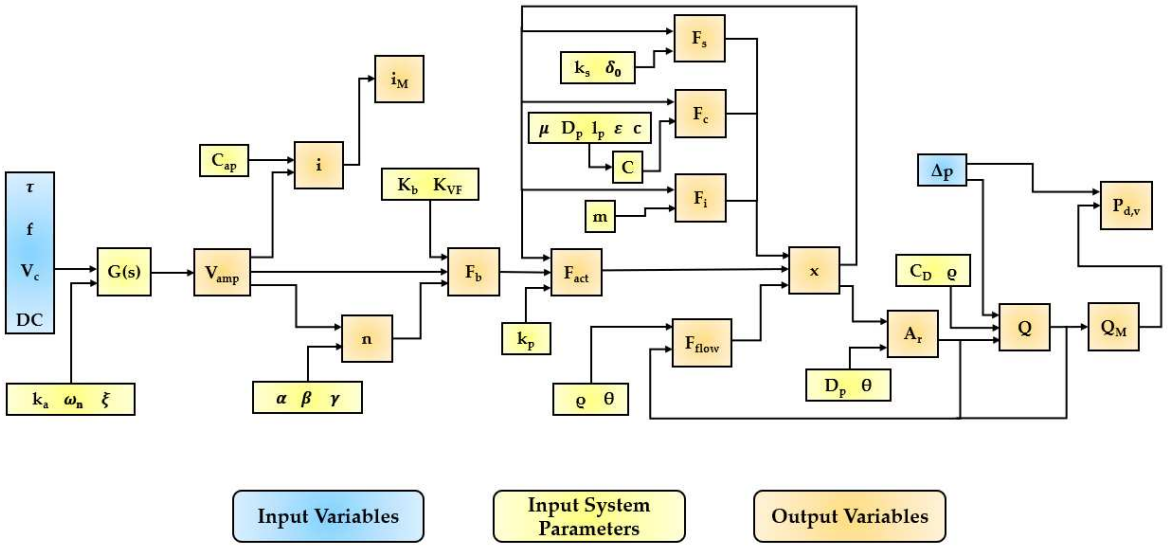

Fig. 98. Equation flow in the open-loop control system: input variables, input system parameters, and output variables.

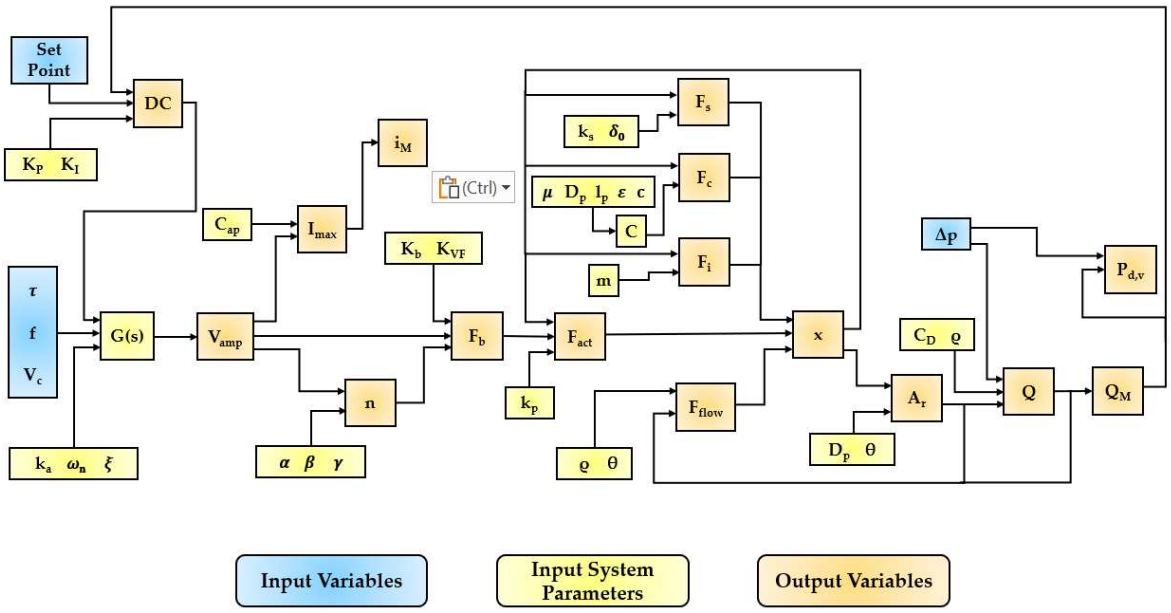

Fig. 99. Equation flow in the closed-loop control system: input variables, input system parameters, and output variables.

4.3 Numerical Results 4/2 HFSV

The following section presents and discusses the results of the numerical simulations conducted on both metering chambers of the 4/2 HFSV, specifically P → A and B→T. The initial step involved the validation of the hysteresis model using the data provided by Noliac on their website [280]. Fig. 100 visually represents the hysteresis curve, illustrating the relationship between the electric field supplied to the actuator and the resulting strain percentage. More precisely, Fig. 100a and Fig. 100b illustrate the percentage error between the ascending and descending branches obtained by the simulation and provided by manufacturer, respectively. Meanwhile, Fig. 100c offers a comprehensive comparison of the entire simulated hysteresis curve with the corresponding manufacturer's data. The manufacturer's curve, specifically, pertains to the piezoceramic material NCE51F, which is used in constructing the NAC 2125 HXX ring stack model. It is important to note that the strain percentage, indicated on the graph, applies exclusively to the active material. In practical multilayer PEAs, there are additional inactive layers present on each ceramic element, as well as on the top and bottom of the entire stack. Considering a total stack height of 200 mm, the active material is accounted for a length of 156 mm, with each active layer in the stack having a thickness of around 67 µm. In the graph, the hysteresis curve plotted in red with a continuous line represents the manufacturer's data. To obtain the simulated hysteresis curve (plotted in blue with a dotted line), the mentioned equations in Section 4.2 were used with tuned parameters $\alpha = 0.53$, $\beta = 0.009$, $\delta = 0.02$ and $K_b = 1.095$. A 1 Hz sinusoidal input control voltage with amplitude, ranging from 0 to +5 V, was applied in the simulation. No load was applied, meaning F_{flow}, F_s, F_c, F_i and Q were set all set to 0. The simulation utilized the characteristics of the NAC2125 H200 model, where $F_{b,max} = 8450\ N$ and $k_p = 26\ N/\mu m$. The amplifier employed in the simulations is characterized by $\omega_n = 10000\ rad/s$, $k_a = 40$ and $\xi = 1.5$. The close agreement between the simulation curve and the manufacturer's curve, with a percentage error of less than 15% in both the ascending and descending branches, demonstrates the accuracy of the hysteresis model.

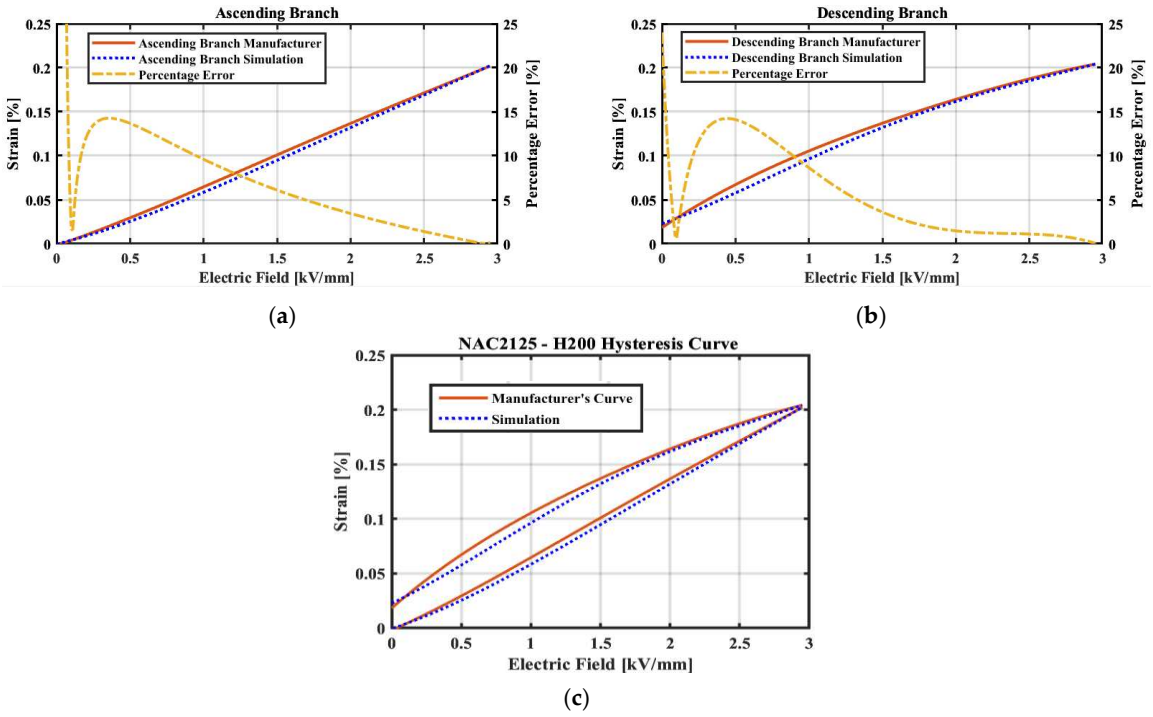

Fig. 100. Hysteresis curve provided by the manufacturer compared with the hysteresis curve obtained from the simulations: (**a**) Ascending branch; (**b**) Descending branch; (**c**) Entire hysteresis curve.

Once the hysteresis model was validated, the 4/2 HFSV architecture depicted in Fig. 97 was simulated using the numerical code described in Section 4.2.

In the simulation, the oil used was ISO VG 32, maintained at a temperature of 50 °C. The oil properties were characterized by a density $\rho = 851$ kg/m^3 and $\mu = 0.0187$ kg/(ms). The discharge pressure to the tank (p_t) was assumed to be constant and equal to 1 bar. Considering the dimensions of the ring stack actuator, the two poppets inserted through the hole of the stack were assumed to have a diameter $D_p = 60$ mm and an angle $\theta = 45°$. For the same reason, the length of the part in contact with the case (l_p) was assumed to be 50 mm, with a clearance (c) of 1 μm. Taking the piezoelectric actuation into a account, a mass m = 100 g was considered to represent the moving parts. The damping factor of the poppets was calculated using Equation (41): assuming negligible eccentricity (ε), the calculated damping factor is $C = 60$ Ns/m. The chamber accounting for fluid compressibility, given the dimensions of the poppets, was assumed to have $D_0 = D_p = 60$ mm and $L_0 = l_p = 50$ mm, thus obtaining $V_0 \approx 2 \cdot 10^{-4}$ m^3. Regarding the discharge coefficient, it was assumed to remain constant at $C_D = 0.7$, under the hypothesis of turbulent flow [21].

To achieve a preload equal to 20% of the maximum blocking force [25], the additional spring was assumed to have a stiffness of $k_s = 190000$ N/m. It was pre-compressed by $\delta_0 = 8.90$ mm. The maximum displacement, represented by the mechanical stop, was defined as $x_{max} = 0.325$ mm, which corresponds to the maximum free stroke of the ring stack. For the mechanical stops, the spring stiffness was set to $K_{stop} = 10^7$ N/m, while the damping was assigned a value of $C_{stop} = 5000$ Ns/m.

The operating parameters for the ring stack actuator were reported in the previous Table 20, while the input system parameters, including the hysteresis parameters for the ring stack, can be found in the following Table 21. Additionally, Table 22 shows the input and output variables that will be set and obtained from the simulations for both open and closed-loop control systems.

Table 21. Simulated input system parameters and nomenclature.

Component	Parameter	Symbol	Value	Unit
Oil (ISO VG 32)	Temperature	T	50	°C
	Density	ϱ	851	kg/m^3
	Viscosity	μ	0.0187	kg/(ms)
Discharge Line	Discharge Pressure	p_t	1	bar
Amplifier	Natural Frequency	ω_n	10000	rad/s
	Gain	k_a	40	-
	Damping Ratio	ξ	1.5	-
Ring Stack	Hysteresis Parameter	α	0.53	-
	Hysteresis Parameter	β	0.009	-
	Hysteresis Parameter	δ	0.02	-
	Hysteresis Parameter	K_b	1.09	-
4/2 HFSV	Conversion factor K_{VF}	K_{VF}	42.25	N/V
	Mass Moving Parts	m	100	g
	Poppets' Diameter	D_p	60	mm
	Length Parts Contact Case	l_p	50	mm
	Clearance	c	1	μm
	Eccentricity	ε	0	μm
	Poppets' Damping Factor	C	60	Ns/m
	Poppets' Angle	θ	45	°
	Chamber Volume	V_{cham}	$2 \cdot 10^{-4}$	m^3
	Discharge Coefficient	C_D	0.7	-
	Stiffness Additional Spring	k_s	190000	N/m
	Pre-compression	δ_0	8.9	mm
	Spring stiffness Stop	K_{stop}	10^7	N/m
	Damping Factor Stop	C_{stop}	5000	Ns/m

Table 22. Input and output variables nomenclature for both open and closed-loop control systems.

Variables	Open Loop	Closed Loop	Symbol	Unit
Overall Period	Input	Input	τ	ms
Switching Frequency	Input	Input	f	Hz
Amplitude	Input	Input	V_c	V
Duty Cycle	Input	Output	DC	-
Overall Pressure Drop	Input	Input	Δp	bar
Set Point	-	Input	Set Point	L/min
Amplified Voltage	Output	Output	V_{amp}	V
Current	Output	Output	i	A
Average Current	Output	Output	i_M	A
Hysteresis Term	Output	Output	n	V
Blocking Force	Output	Output	F_b	N
Actuation Force	Output	Output	F_{act}	N
Inertia Force	Output	Output	F_i	N
Viscous Force	Output	Output	F_c	N

Add. Spring Force	Output	Output	F_s	N
Flow Force	Output	Output	F_{flow}	N
Poppets' Position	Output	Output	x	μm
Flow Rate	Output	Output	Q	L/min
Average Flow Rate	Output	Output	Q_M	L/min
Average Power Con.	Output	Output	$P_{d,v}$	W

All the numerical results were obtained by maintaining the period of the input pulse digital signal (or input control voltage) constant, specifically set at $\tau = 5$ ms, resulting in a switching frequency equal to $f = 200$ Hz.

Firstly, the impact of the amplitude of the input control voltage on the performance of the 4/2 HFSV was investigated. Fig. 101 shows open-loop predictions conducted with varying amplitudes of the input pulse digital signal during four different periods: 0 to 2 V, 0 to 3 V, 0 to 4 V, and 0 to 5 V. The analysis took into account an overall pressure drop across the valve of $\Delta p = 15$ bar and a duty cycle of the input pulse digital signal set at $DC = 60\%$. Specifically, Figure 101a shows the time history of the quantities provided to the ring stack actuator. These quantities include the amplitude of the input control voltage, V_c (multiplied by 20 for clarity), the amplified voltage, V_{amp}, the current, i, and the average current, i_M. Furthermore, the time history of the resulting blocking force achieved, F_b, is also depicted in the graph. Fig. 101b illustrates the time history of the forces related to the actuation of the ring stack. Specifically, it presents the actuation force developed by the ring stack, denoted as F_{act}, along with the resistant forces. These resistant forces include the viscous force, F_c, the inertia force, F_i, the force of the additional spring, F_s, and the flow forces, F_{flow}. Fig. 101c displays the time history of poppets' position, x, the obtained instantaeous flow rate, Q, the obtained average flow rate, Q_M, and the average ideal power dissipated by the valve, $P_{d,v}$.

Referring to Fig. 101a, the amplitude of input control voltage, V_c, is amplified to a higher pulse voltage, V_{amp}, by the amplifier within approximately 1 ms. This amplified voltage is then corrected by the hysteresis non-linear term, n, and then converted into the blocking force, F_b, using the conversion factor, K_{VF}, and the hysteresis correction factor, K_b. It is worth noting that a higher amplitude of the input control voltage results in a higher blocking force. Specifically, when the amplitude of the input control voltage reaches its maximum value of 5 V, the maximum value of the blocking force is obtained. However, due to the hysteresis of the ring stack actuator the blocking force does not return to zero when the input control voltage is removed. Moreover, the graph reveals that as the amplitude of the input control voltage increases, the current, i, experiences a higher peak value. In particular, during the fourth period, the peak of current reaches its maximum value of 43.5 A. However, it is important to note that this peak of current occurs only for a short duration, and the average current, i_M, remains relatively low, below 6 A.

When examining the predictions of Fig. 101b, it becomes apparent that both the viscous force, F_c, and the flow force, F_{flow}, have negligible effects on the actuation capability of the ring stack actuator. This is because these forces are considerably smaller than the actuation force, F_{act}, which is determined by the difference between the blocking force, F_b, and the ring stack spring force, $k_p x$. Therefore, also the actuation force does not return to zero when the input control voltage is removed.

On the other hand, the force of the additional spring, F_s, and the inertia force, F_i, play significant roles in the actuation of the ring stack. The force of the additional spring is particularly influential due to the value of the preload, δ_0. In addition, the oscillations in the actuation force are caused by the inertia force, attributed to the relatively lower damping factor, C, calculated for the poppets. Therefore, it is crucial to ensure that the mass of the moving parts, m, is not excessively large in order to minimize these oscillations and enhance the performance of the 4/2 HFSV.

With regard to the predictions of Fig. 101c, the actuation force, F_{act}, allows the poppets to move and reach the open position in less than 1 ms. Due to the oscillations in the actuation force, the poppets oscillate around the open position, which may not be equal to the maximum free stroke, x_{max}, due to the presence of resistant forces. However, despite the hysteresis of the ring stack actuator, the force stored in the additional spring, F_s, is substantial enough to ensure that the poppets can close the valve when the input control voltage is removed. The poppets' position, x, exhibits a similar trend to the obtained instantaneous flow rate, Q, indicating a correlation between the two variables. It is worth noting that the amplitude of the input control voltage, V_c, directly influences the obtained average flow rate, Q_M. As the amplitude increases, the average flow rate also increases. During the fourth period, when the amplitude of the input control voltage reaches its maximum value (i.e., $V_c = 5$ V), an average flow rate of $Q_M = 34.74$ L/min is achieved. Given that the overall pressure drop across the valve remains constant, the ideal average power dissipated by the valve, $P_{d,v}$, follows a similar trend to the average flow rate. It is important to note that, when the input control voltage is equal to its maximum, an ideal average power consumption of only $P_{d,v} = 868.4$ W can be observed.

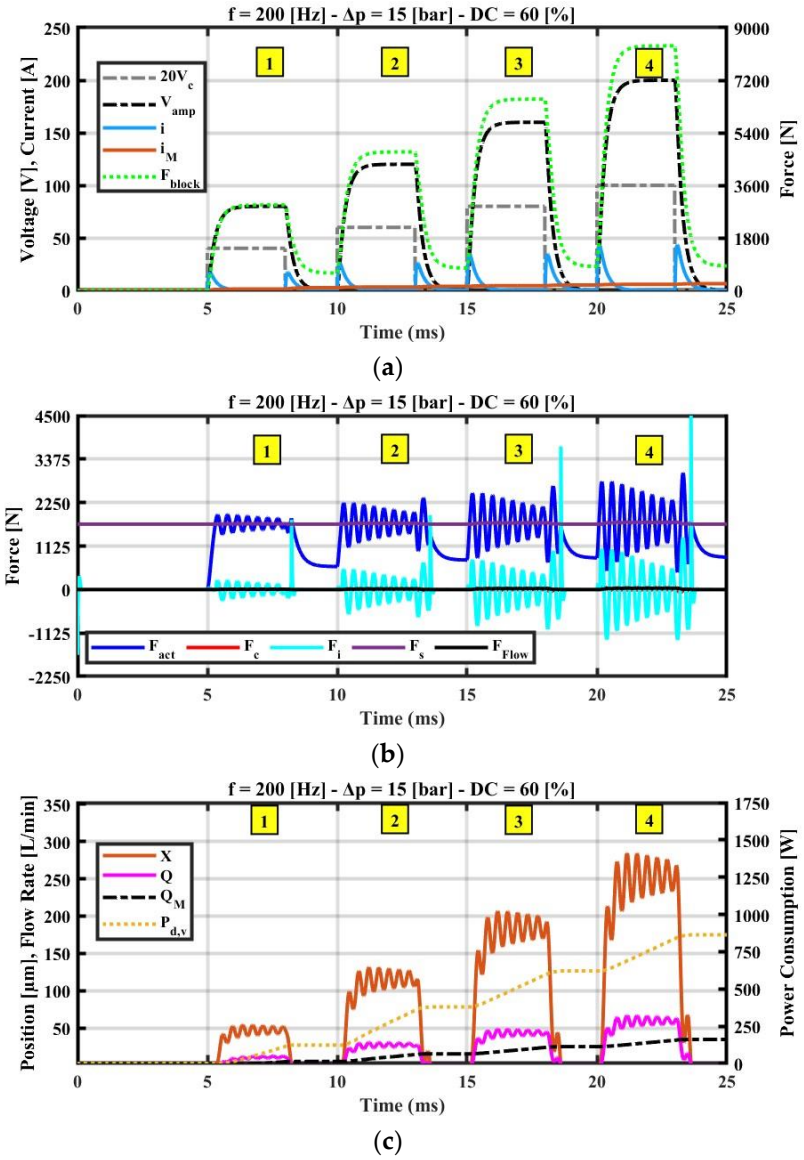

Fig. 101. Open-loop predictions simulated for different values of V_c (f = 200 Hz, Δp = 15 bar, DC= 60%): (**a**) Amplitude of the Input Control Voltage, Amplified Voltage, Current, Average Current, Blocking Force; (**b**) Actuation Force, Viscous Force, Inertia Force, Additional Spring Force, Flow Force; (**c**) Poppets' Position, Flow Rate, Average Flow Rate, Ideal Average Power Dissipated by the Valve.

The results shown in Fig. 102 provide an evaluation of how the performance of the 4/2 HFSV is affected by the duty cycle of the input control voltage. To conduct these evaluations, open-loop step tests were performed, resembling the tests shown in Fig. 101, but this time changing the duty cycle of the input pulse digital signal. Four different periods, with different values of the duty cycle, were examined, specifically DC = 30%, DC = 40%, DC = 60%, and DC = 80%. The analysis considered an overall pressure drop across the valve of Δp = 15 bar and an amplitude of the input control voltage of V_c = 5 V. It is evident that increasing the duty cycle, DC, leads to a higher average flow rate, Q_M,

and, consequently, an increase in the ideal average power dissipated by the valve, $P_{d,v}$. Specifically, during the fourth period with a duty cycle of 80%, an average flow rate of $Q_M = 46.78$ L/min and an ideal average power consumption of $P_{d,v} = 1170$ W were achieved.

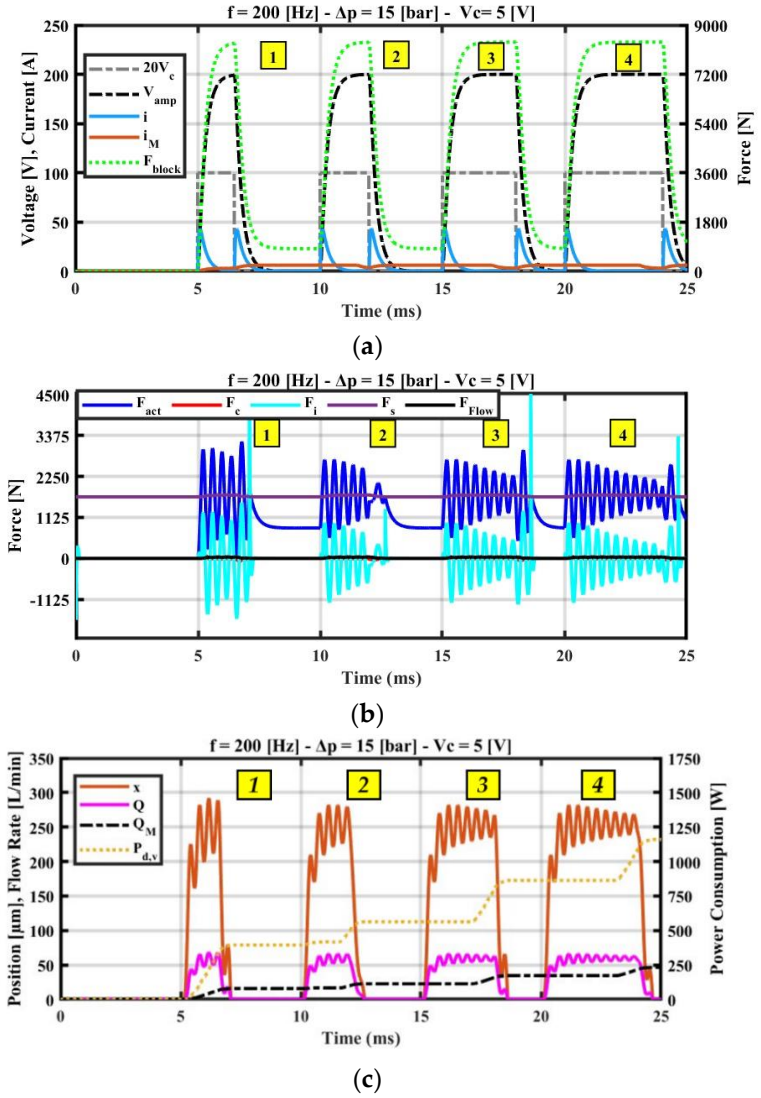

Fig. 102. Open-loop predictions simulated for different values of DC (f = 200 Hz, Δp = 15 bar, V_c= 5 V): (**a**) Amplitude of the Input Control Voltage, Amplified Voltage, Current, Average Current, Blocking Force; (**b**) Actuation Force, Viscous Force, Inertia Force, Additional Spring Force, Flow Force; (**c**) Poppets' Position, Flow Rate, Average Flow Rate, Ideal Average Power Dissipated by the Valve.

To resume the impact of the amplitude (V_c) and duty cycle (DC) of the input control voltage, Fig. 103 illustrates the average flow rate (Q_M) provided by the valve as the amplitude and duty cycle of the input control voltage vary. The analysis considers an overall pressure drop across the valve of $\Delta p = 15$ bar. The simulations demonstrate that as both the amplitude and duty cycle of the input control voltage increase, the average flow rate also increases. Specifically, when applying the

maximum duty cycle and maximum amplitude of the input control voltage to the ring stack actuator, the valve achieves an impressive average flow rate of $Q_M = 60$ L/min. In addition, it is evident in Fig. 103, that the valve ensures linearity between the average flow rate and duty cycle, even at wide openings, despite the conical shape of the poppets. This feature is crucial, as any loss of linearity at larger openings could compromise the precision of flow control, especially in applications that demand highly accurate performance across the full range of valve openings, as is often the case in the aeronautical sector.

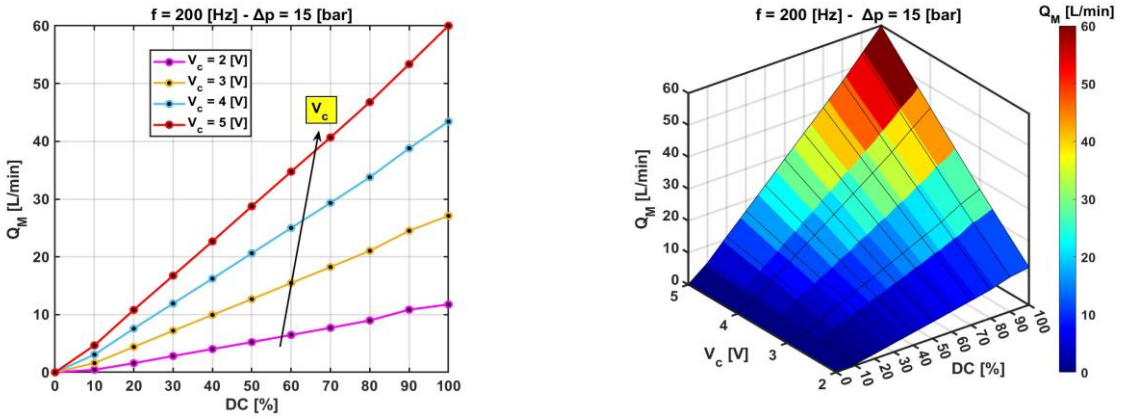

(**a**) (**b**)

Fig. 103. Open-loop predictions simulated for different values of V_c and DC (f = 200 Hz, Δp = 15 bar): (**a**) 2D plot of the Average Flow Rate; (**b**) 3D plot of the Average Flow Rate.

Fig. 101, 102 and 103 depict open-loop simulations conducted with an overall pressure drop across the valve set at $\Delta p = 15$ bar. The chosen pressure drop value aims to design a valve that can provide high flow rates while maintaining low pressure drops. Therefore, a pressure drop of 7.5 bar for each metering chamber (P→A and B→T) was considered appropriate for this purpose, leading to a total pressure drop of 15 bar across the valve.

Fig. 104 and 105 evaluate the influence of the inlet pressure (p_p) on the average flow rate (Q_M) and the ideal average power dissipated by the valve ($P_{d,v}$). Each figure focuses on a specific quantity, with Fig. 104 presenting the average flow rate and Fig. 105 illustrating the ideal average power dissipated by the valve. The analysis involves varying the duty cycle (DC) while keeping the amplitude of the input control voltage constant at V_c =5 V. Different values of $\Delta p = p_p - p_t$ are considered in the investigation, specifically $\Delta p = 10$ bar, $\Delta p = 15$ bar, $\Delta p = 20$ bar, $\Delta p = 25$ bar. It is worth noting that as the overall pressure drop across the valve increases, the average flow rate also increases. For example, at $DC = 100\%$ and $\Delta p = 25$ bar, the average flow rate reaches its maximum value of $Q_M = 77$ L/min. However, it is important to consider a trade-off between average flow rate and average power consumption. Since the ideal average power dissipated by the valve ($P_{d,v}$) is calculated as the product of the average flow rate (Q_M) and the pressure difference (Δp), the ideal average power consumption becomes significantly high. For the mentioned case of $DC = 100\%$ and $\Delta p = 25$ bar, the ideal average power dissipation amounts to $P_{d,v} = 3208$ W.

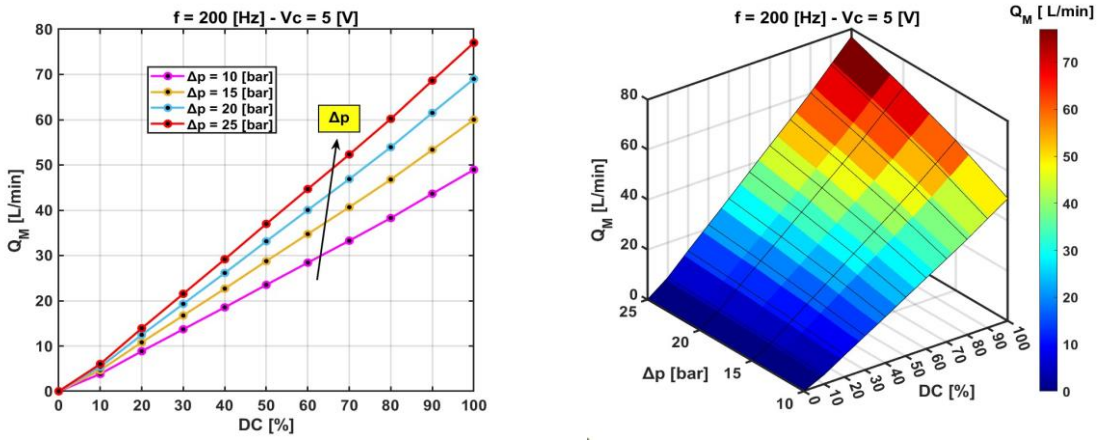

(**a**) (**b**)

Fig. 104. Open-loop predictions obtained for different values of Δp and DC (f = 200 Hz, V_c = 5 V): (**a**) 2D plot of the Average Flow Rate; (**b**) 3D plot of the Average Flow Rate.

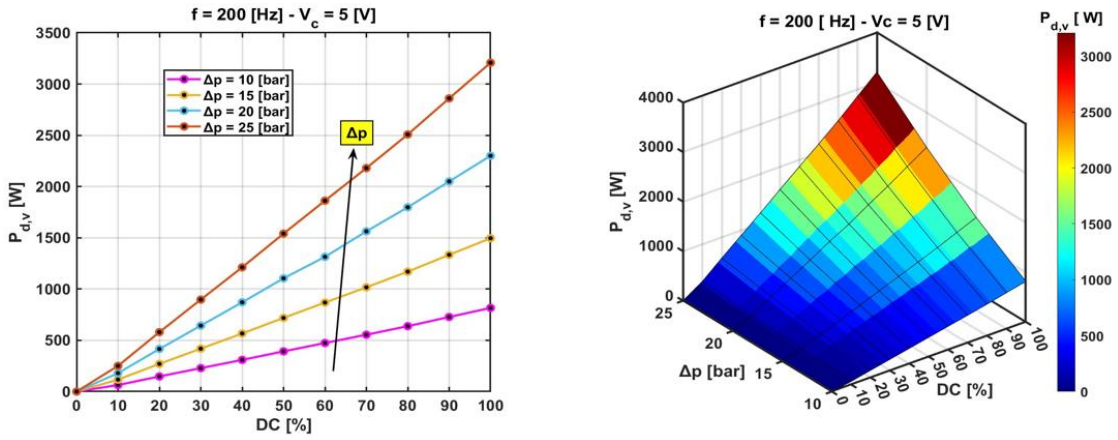

(**a**) (**b**)

Fig. 105. Open-loop predictions obtained for different values of Δp and DC (f = 200 Hz, V_c = 5 V): (**a**) 2D plot of the Ideal Average Power Dissipated by the Valve; (**b**) 3D plot of the Ideal Average Power Dissipated by the Valve.

For real applications, closed-loop control is essential to ensure proper control. In this scenario, closed-loop control was simulated using a simple PI controller. The controller adjusts the duty cycle of the input control voltage, which has an amplitude of V_c = 5 V, based on Equation (52), to achieve the desired average flow rate (set point). The PI controller parameters, K_P and K_I, were determined using the Ziegler-Nichols method and set to 0.01125 and 3.6, respectively. The back calculation anti-windup method was employed.

In the simulated closed-loop step tests, the set point was adjusted three times, specifically from 0 to 20 L/min (Fig. 106a), from 0 to 30 L/min (Fig. 106b), and from 0 to 40 L/min (Fig. 106c). The overall

pressure difference across the valve, $\Delta p = p_p - p_t$ was set to 15 bar for these tests. The parameters specified in Table 20 and Table 21 were used in these simulations as well.

These graphs provide clear evidence of the effectiveness of the closed-loop control system. It is evident that the system efficiently reached the desired set point by making only three changes in the duty cycle of the input control voltage. Remarkably, this achievement was accomplished in less than 15 ms.

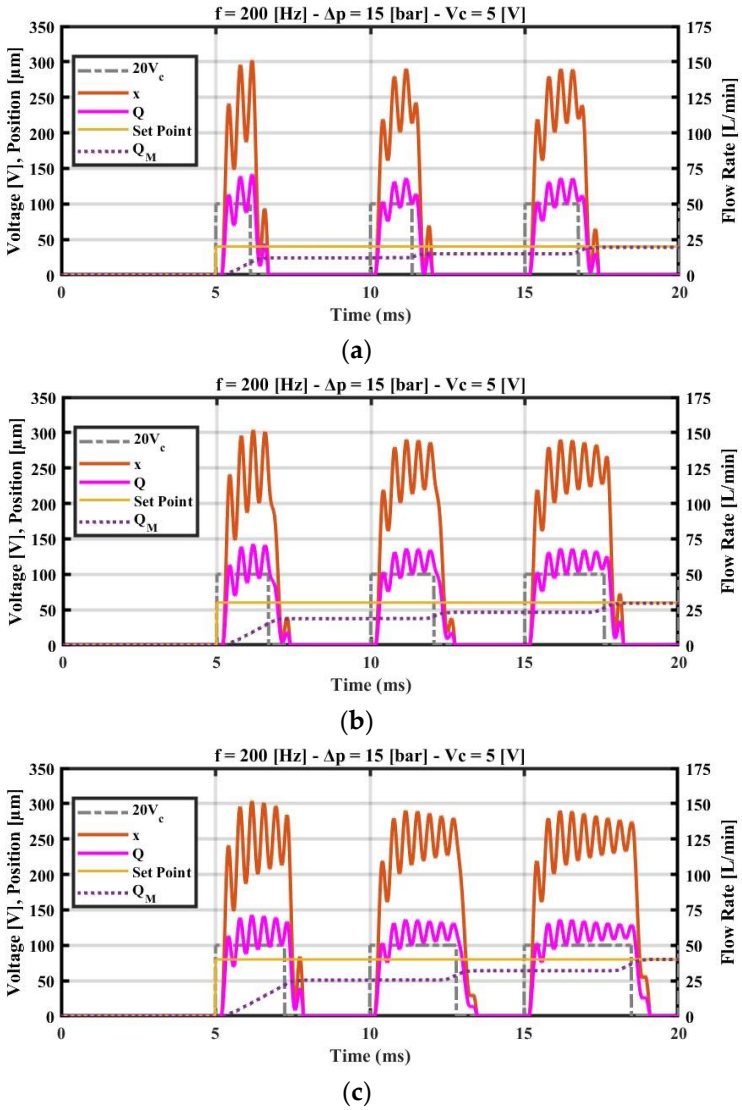

Fig. 106. Closed-loop results (f = 200 Hz, Δp = 15 bar, V_c = 5 V): (**a**) Q_M = 20 L/min; (**b**) Q_M = 30 L/min; (**c**) Q_M = 40 L/min.

4.4 Numerical Results 2/2 HFSV

For the numerical results of the 2/2 HFSV, the same input system parameters of Table 21 have been applied, with only open-loop simulations conducted. Notably, when an overall pressure drop across the valve of $\Delta p = 10$ bar was applied and the input control voltage amplitude set to $V_c = 5$ V with a frequency of $f = 200$ Hz and a duty cycle of $DC = 100\%$, a maximum flow rate of 70 L/min was achieved. Additionally, the valve's switching time was within 1 ms. For more details, please refer to the following paper [49].

4.5 Discussion

These research studies [49], [50] explored the potential application of a commercially available ring stack actuator to drive two innovative HFSVs—a 2/2 HFSV and a 4/2 HFSV—as replacements for conventional proportional and servovalves in industrial and aeronautical applications. By harnessing the benefits of PEAs, such as rapid response and lightweight design, the demanding requirements of these digital hydraulic valves were successfully met.

The performance of the proposed HFSV architectures was assessed through well-established equations within Simulink. The Bouc-Wen model accurately simulated the ring stack actuator's hysteresis, validated by experimental data showing less than 15% error in both ascending and descending branches.

The analysis of the 2/2 HFSV presented open-loop simulation results only, while the 4/2 HFSV included both open and closed-loop control assessments. These simulations revealed both strengths and challenges for each design.

Advantages include design simplicity, as the ring stack actuator directly controls the opening and closing of the poppets by varying the input pulse signal. The PEA provides sufficient force to overcome opposing forces, ensuring rapid response times, with valves reaching the open position in under 1 ms. Furthermore, the actuator hysteresis does not hinder performance, as the additional spring provides enough force to ensure proper valve closure.

Open-loop tests for the 2/2 HFSV demonstrated a maximum flow rate of 70 L/min at a switching frequency of 200 Hz, with a pressure drop of 10 bar and a 100% duty cycle. For the 4/2 HFSV, increasing the input pulse amplitude, duty cycle, and pressure drop led to higher average flow rates but also increased power consumption. The optimal trade-off was identified at a 100% duty cycle, 5 V input voltage, and a pressure drop of 15 bar, resulting in an average flow rate of 60 L/min and power dissipation of only 1500 W, meeting HFSV requirements.

Closed-loop tests on the 4/2 HFSV evaluated control effectiveness across set points of 20 L/min, 30 L/min, and 40 L/min. The control system successfully reached each set point within 15 ms by adjusting the input voltage duty cycle only three times.

Challenges include the high costs, large size, and the requirement for high-performance amplifiers for PEAs. Mass production of these actuators could be a potential solution to mitigate costs.

In conclusion, these studies demonstrated the feasibility and significant energy-saving potential of digital hydraulics in industrial and aeronautical applications as a replacement for conventional spool valves, marking it as a promising technology for future fluid power applications.

Chapter 5

5. DEVELOPMENT OF AN INNOVATIVE DIRECT DRIVE SERVOVALVE

This chapter addresses the key challenges of direct drive servovalves by presenting a feasibility study that explores the use of commercially available APAs as substitutes for LFMs. The possibility of using APAs in place of LFMs is very attractive given the fast response speed and low weight of APAs, which are equipped with mechanical amplification systems to obtain good levels of displacement. A very effective amplification system has recently been produced by some manufacturers and is based on a temperature independent diamond structure. In this paper, simulations are performed of a four-way three-position (4/3) servovalve directly actuated by such a PEAs with diamond structure. To this end, the performance of the valve architecture proposed is evaluated using well-established equations implemented in Simulink through the libraries of Simscape Fluids. From the analysis of the inherent characteristics of the APA and from the results of the simulations, advantages and disadvantages of this possible architecture are drawn and discussed in detail.

The results of this study have been published in a renowned journal [48].

5.1 Valve Layout

A few manufacturers produce APAs designed to provide good levels of displacement thanks to mechanical amplification systems. The amplification system based on the configuration called "diamond structure, produced by Noliac [280], [281] , is one of the most effective because of its low weight, temperature independence, and good levels of displacement and actuation force achievable. The structure, as shown in Fig. 107, consists of four piezo-stacks elements connected in pairs with a moving slider which is in the central (neutral) position when no differential voltage is applied. Furthermore, there is an internal mechanism which creates a preload to ensure the correct position of each member during operation. When a differential voltage is applied to the two pairs of piezo stacks, the length of a pair is increased, while the length of the other one is decreased, thus causing the movement of the slider from the central (neutral) position.

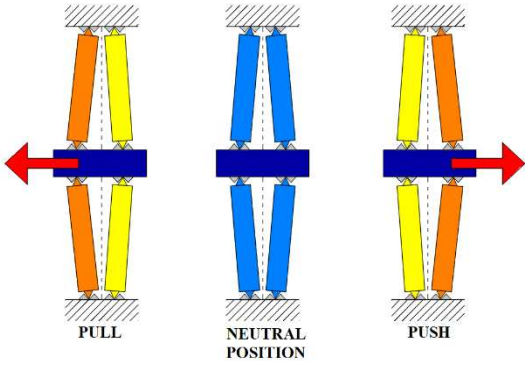

Fig. 107. Operating principle of an amplified stack actuator with a diamond structure [280].

This system can operate in two different modes depending on how the input voltage is applied. The first way is to provide the actuator with a voltage signal which may vary from −100 V to +100 V. The neutral position occurs for zero voltage applied; positive values move the slider in a direction, whilst negative values move the slider in the opposite direction. In the second way of operation, the input voltage is varied from 0 to +200 V, and the neutral position is obtained for a voltage equal to +100 V; when the voltage is greater or less than +100 V, the slider moves in one direction or the other.

As stated by the manufacturer, the APA has the same performance regardless of the direction of movement. Furthermore, any change in the operating temperature will have no effect on the displacement despite stack thermal expansion due to the symmetry of the mechanism [280], [281], and this is a significant advantage compared to lever mechanisms, which do not have any temperature compensation system [88], [90].

Noliac produces three APAs with a diamond structure. In Table 23, the main characteristics of the three APAs produced by Noliac are shown, such as size, maximum blocking force, maximum free stroke, and stiffness [280], [281].

Table 23. Amplified stack actuators produced by Noliac: specifications [280], [281].

Parameter	Unit	NAC2641	NAC2643	NAC2645
Length (l_{APA}) × Width (w_{APA}) × Height (h_{APA})	mm	14 × 70.5 × 26.1	14 × 102.4 × 28	14 × 134.2 × 30.6
Max. free stroke (working in one direction), x_{max}	μm	300	625	950
Max. free stroke (working in two directions), $\pm x_{max}$	μm	±150	±312.5	±475
Stiffness, k_p	N/μm	1.3	0.9	0.7
Max. blocking force, $F_{b,max}$	N	195	281	332
Max. actuation force at 20 °C, $F_{act,max}$	N	250	250	250
Max. actuation force at 50 °C, $F_{act,max}$	N	200	200	200
Overall mass, $2m_p$	g	84	122	160
Capacitance, Cap	μF	7.2	13	20

The size of the APAs increases with the maximum free stroke produced (x_{max}). Model NAC2645 is the largest; however, its overall weight is only 160 g, thus being much lighter than typical valve electric actuators (both solenoids and LFMs).

The maximum free stroke (x_{max}) is the maximum displacement theoretically obtained for a null actuation force, namely, when no load is applied. If the APA works in both directions (push and pull mode), the maximum free stroke is one half of that obtained when the APA works in one direction only (either push or pull mode). In the case of a push and pull mode of operation, the maximum free stroke provided by model NAC2645 is ± 0.475 mm, which is very similar to the displacement obtained by a LFM (about ±0.5 mm [21]). Therefore, the values of the displacement are compatible with the direct actuation of a spool valve.

The blocking force F_b is the actuation force produced when the slider is blocked, the blocking force increases proportionally to the amplified voltage applied to the actuator, and the maximum blocking

force $F_{b,max}$ is obtained when the voltage is at its maximum. The actuation force F_{act} is given by the difference between the blocking force F_b and the internal elastic force of the APA, which is characterized by a stiffness k_p. The manufacturer advises against exceeding a limit for the actuation force in order to protect the internal mechanism. This limit in the actuation force, which changes with the temperature, being $F_{act,max}$ = 250 N at 20 °C and $F_{act,max}$ = 200 N at 50 °C, is sufficiently high to allow the opposing forces in a spool valve (i.e., flow forces and friction) to be counteracted; however, this represents a limitation as far as the chip shear capability is concerned, since the force required to shear contamination particles that can be caught between the edges of a metering section can exceed 200 N. This is the same drawback occurring with solenoids and LFMs. If high chip shear forces are needed, two APAs can be employed to move the sliding spool.

Fig. 108 shows two different solutions to directly actuate a four-way three-position (4/3) servovalve, (the most used in industrial and aircraft applications [21]), employing the APAs with a diamond structure.

The first solution (Fig. 108a) makes use of only one APA, operating in pull/push mode, whose slider is directly connected with the spool. When the slider pushes the spool to the right, flow modulation is allowed from Port P to Port B, and from Port A to Port T. Alternatively, when the slider pulls the spool to the left, Port P is connected to Port A, while Port B is connected to Port T. To compensate for the low stroke and to achieve reasonable values of flow rate, large slots can be used, as occurs with direct drive servovalves actuated by LFMs. A LVDT must be used to compensate for hysteresis and to achieve closed-loop spool position control.

Figure 108b shows another architecture characterized by two APAs, each connected to the end faces of the spool. With this solution, larger blocking forces can be achieved, since both APAs can generate a force (one pushing the spool, the other one pulling the spool). This solution can increase the chip shear force capability of the valve. However, this solution is more complicated and expensive than the previous one. Again, an LVDT is to be used for closed-loop control to compensate for hysteresis.

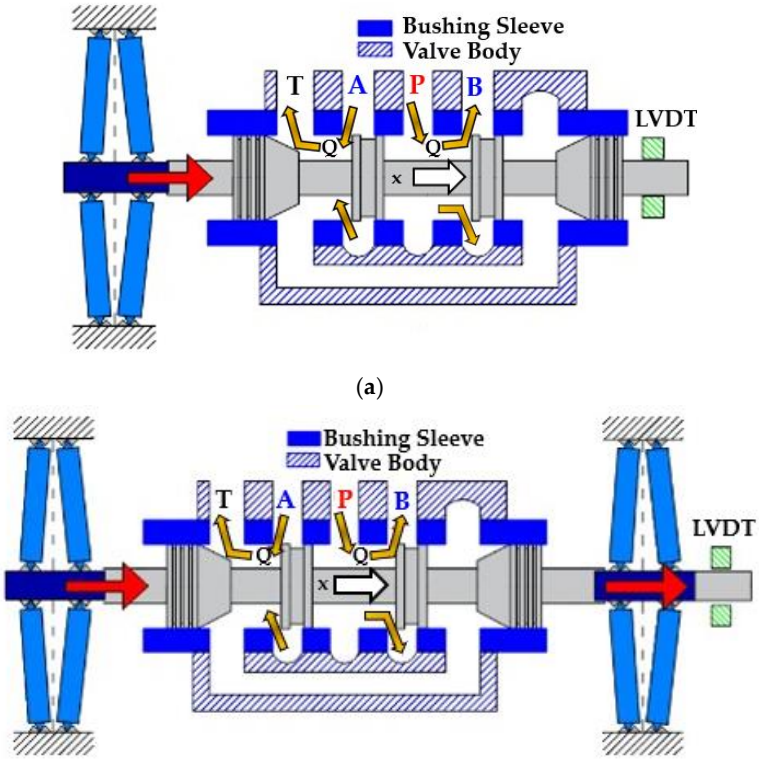

Fig. 108. Two schemes of application of APAs with diamond structure for the direct actuation of a 4/3 servovalve: (**a**) one actuator; (**b**) two actuators.

In both designs shown in Fig. 108 (a and b), a linear relationship between flow rate and current under a constant pressure drop is achieved. This is because the main stage of the proposed valve designs remains unchanged compared to conventional direct drive servovalves.

5.2 Numerical Model

In this research study, the performance of the simpler architecture proposed, namely, that shown in Fig. 108a, has been assessed using well-established equations implemented in Simulink through the libraries of Simscape Fluids. The Simulink model of the direct drive servovalve actuated by an APA with a diamond structure is shown in Fig. 109.

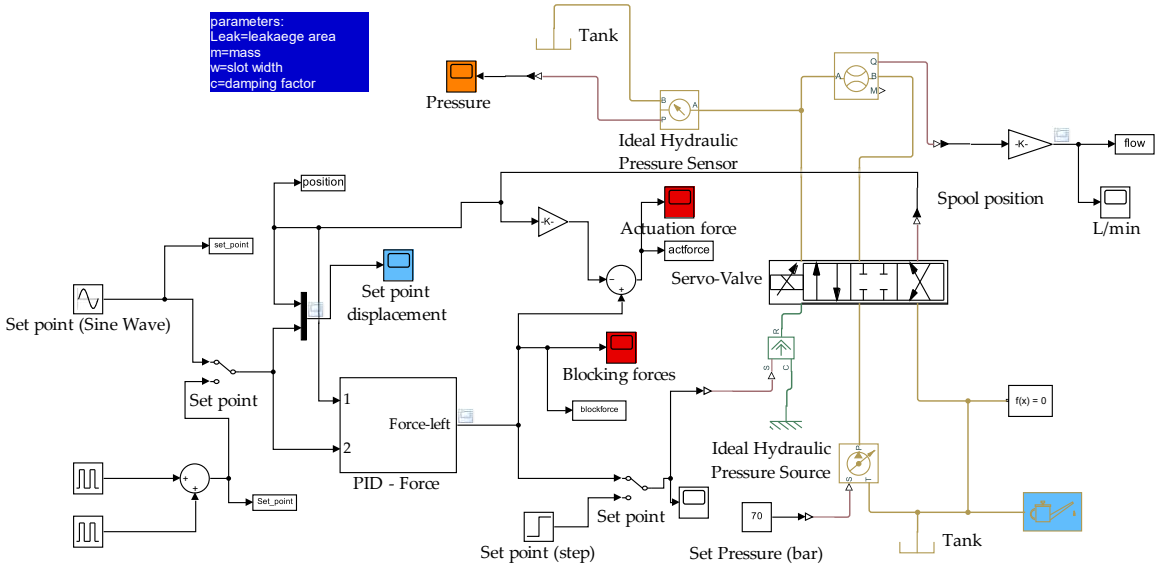

Fig. 109. Simulink model of the proposed 4/3 piezo valve architecture.

The main equations implemented in Simulink are described in the following, with reference to the spool moving only from the left to the right for the sake of simplicity, as shown in Fig. 110.

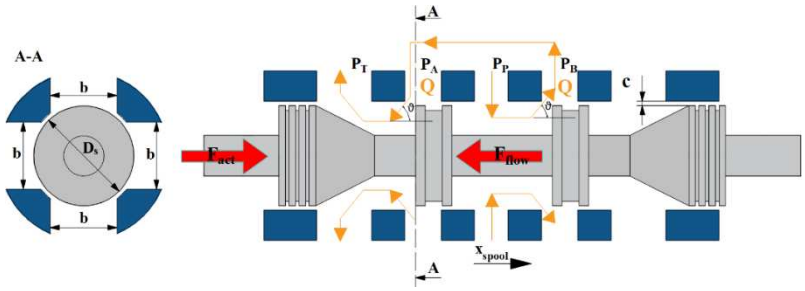

Fig. 110. Sketch including the main parameters used in the numerical model.

An amplifier is needed to transform a low input control voltage, V_c, (ranging from −5 to +5 V in this study) into a high output voltage V_{amp} (ranging from −100 V to +100 V). A second order transfer function $G(s)$ is used to model the relation between V_{amp} and V_c, as already done in previous studies:

$$G(s) = \frac{V_{amp}}{V_c} = \frac{K_a \omega_{n,a}^2}{s^2 + 2\xi_a \omega_{n,a} s + \omega_{n,a}^2}, \tag{53}$$

where s is the complex variable, while K_a, $\omega_{n,a}$and ξ_a are the gain, natural frequency and damping ratio of the amplifier, respectively. To model the current limit, the rate of change of voltage is limited according to Equation (54):

$$\left(\frac{dV_{amp}}{dt}\right)_{max} = \frac{I_{max}}{C_{ap}}, \tag{54}$$

where C_{ap} is the capacitance of the APA.

Piezoelectric hysteresis is taken into account by implementing the Bouc–Wen hysteresis model, described and used in [103], which allows for the calculation of the hysteresis non-linear term n:

$$\frac{dn}{dt} = \alpha \frac{dV_{amp}}{dt} - \beta \left|\frac{dV_{amp}}{dt}\right| n - \delta \frac{dV_{amp}}{dt} |n|, \tag{55}$$

where α, β and δ are parameters to be adjusted in order to adapt the hysteresis model to a specific case. The hysteresis non-linear term n is used to correct the blocking force, F_b, because of hysteresis, as follows [103]:

$$F_{act} = F_b - k_p x, \tag{56}$$

where k_p is the stiffness of the actuator and x is the displacement of the slider (equal to the spool position).

The equilibrium of the forces acting on the spool can be written as follows [286]:

$$F_{act} - F_f - \left(C_p + C_s\right)\dot{x} - (m_p + m_s)\ddot{x}, \tag{57}$$

where x is the displacement of the spool; C_p and C_s are the damping factors of the APA and of the spool, respectively; m_p and m_s denote the mass of the moving parts of the APA (assumed to be one half of the overall mass ofthe APA) and the mass of the spool, respectively. In the model, the spool position is measured by an ideal translational motion sensor; the sensor is assumed idealsince the corresponding Simulink block does not account for inertia, friction, delays, andenergy consumption of the sensor. To evaluate the damping factor of the spool, which is due to the frictional forces acting on the spool, the following relation can be used [287]:

$$C_s = \frac{\mu \pi D_s l_s}{c\sqrt{1 - \left(\frac{\varepsilon}{c}\right)^2}}, \tag{58}$$

where μ is the dynamic viscosity of the oil, D_s and l_s are the diameter and length of the spool, respectively; c is the radial clearance and ε is the radial eccentricity.

The flow force is calculated by using the following simplified equation [288]:

$$F_f = 2\rho \frac{Q^2}{A_{r,s}} cos\vartheta, \tag{59}$$

where the factor 2 considers two metering chambers being opened simultaneously, ρ is the oil density, Q is the volumetric flow rate, and ϑ is the velocity angle with respect to the horizontal direction; $A_{r,s}$ is the restriction area in each metering chamber, calculated as follows:

$$A_{r,s} = bx \; if \; x \geq c, \tag{60}$$

$$A_{r,s} = A_{l,s} = bx \; if \; x < c, \tag{61}$$

where b is the overall slot width, and $A_{l,s}$ is the spool leakage area [38].

The flow rate through each metering section of the main stage is calculated using the orifice equation [287]:

$$Q = C_D A_{r,s} \sqrt{\frac{\Delta p}{\rho}}, \tag{62}$$

where C_D is the discharge coefficient and Δp is the pressure drop across the restriction area $A_{r,s}$. In the model, Port A and Port B are hydraulically connected and the pressure drop $(p_B - p_A)$ is neglected. Therefore, the pressure drop in Equation (62) becomes:

$$\Delta p = p_A - p_T = p_P - p_B = (p_P - p_T)/2, \tag{63}$$

The values of p_P and p_T are constants for the supply and tank pressures, respectively.

Open-loop control can be simulated, in which the input voltage V_c can be set, and the output is the spool position. Otherwise, closed-loop control can be simulated, in which a PI controller adjusts the voltage V_c to obtain the desired spool position according to the calculated error $e(t)$:

$$V_c = K_P e(t) + K_I \int_0^t e(t)dt \tag{64}$$

where K_P and K_I denote the proportional and integral gain, respectively. The derivative action is not considered in the controller since it is highly sensitive to noise in the process variable signal.

The Simulink solver (Ode 14x) computes the dynamic system's states at successive time steps (0.1 ms) over a specified time span, using information provided by the model. Ode14x uses a combination of Newton's method and extrapolation from the current value to compute the model's state at the next time step, as an implicit function of the state and the state derivative at the next time step. This solver requires more computation per step than an explicit solver but is more accurate for a given step size.

5.3 Numerical Results

The results of the numerical simulations are now presented and discussed. Firstly, the hysteresis model was validated against the data provided by Noliac on their website [280], [281]. Fig. 111 shows the hysteresis curve (displacement of the slider x vs. amplified voltage V_{amp}) provided by the manufacturer for model NAC2643 (the only hysteresis curve available), plotted as an orange curve. The simulated hysteresis curve (plotted in blue) was obtained using the above-mentioned equations with the tuned parameters α = 0.7, β = 0.013, δ = 0.03 and K_b = 1.19, by applying a 1 Hz sinusoidal input voltage V_c with a 5 V amplitude (from −5 V to +5 V), with no load applied (i.e., $F_f = C_s = C_p = m_s = Q = 0$), and using the characteristics of model NAC2643 ($F_{b,max}$ = 281 N, k_p = 900,000 N/m , m_p = 60 g). The amplifier employed in previous studies was assumed to be used in these simulations [289]; it is characterized by $\omega_{n,a}$ = 1400 rad/s and ξ_a = 1.5 (I_{max} = 1 A). Its cut-off frequency (calculated as the frequency at which the amplitude ratio is −3 dB) is 83 Hz. The good correspondence between the simulation curve and the manufacturer's curve shows the accuracy of the hysteresis model.

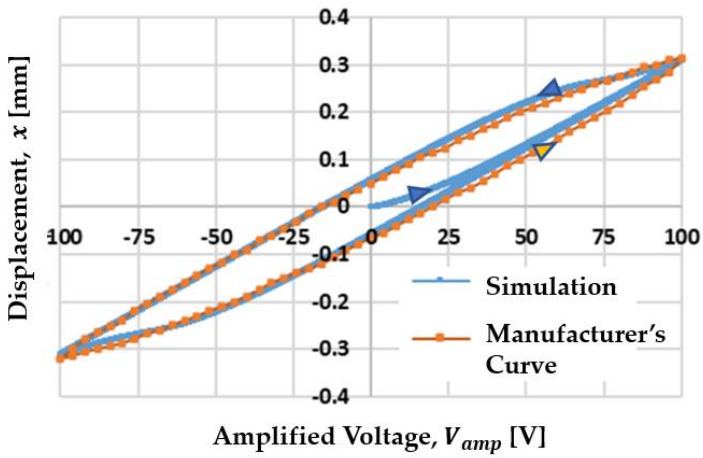

Fig. 111. Hysteresis curve provided by the manufacturer compared with the hysteresis curve obtained with the simulations (model NAC2643).

After the validation of the hysteresis model, the architecture of Fig. 108a was simulated using the full numerical code described in Section 5.2. The APA employed in the simulations was model NAC2645, being capable of producing the highest value of maximum free stroke (x_{max}= ±475 μm working in push/pull mode). The maximum blocking force of this model is $F_{b,max}$ = 332 N; its stiffness is k_p = 700,000 N/m. The overall mass of the APA comprising the case (which is the heaviest part, being realized in stainless steel [280], [281]) is 160 g; as already mentioned, in the simulations, the mass of the moving parts of the APA m_s was assumed to be one half of the overall mass, namely, m_p= 80 g. Given the very similar characteristics between model NAC2643 and model NAC2645, the same tuned parameters α = 0.7, β = 0.013, δ = 0.03 and K_b = 1.19 were used in this analysis to simulate the hysteresis of model NAC2645. In this regard, Fig. 112 shows how the hysteresis curve of model NAC2645 changes according to the frequency of the input voltage V_c (sine wave from -5 V to +5 V), with no load applied (i.e., $F_f = C_s = C_p = m_s = Q = 0$), and with $\omega_{n,a}$ = 1400 rad/s and ξ_a = 1.5 (I_{max} = 1 A).

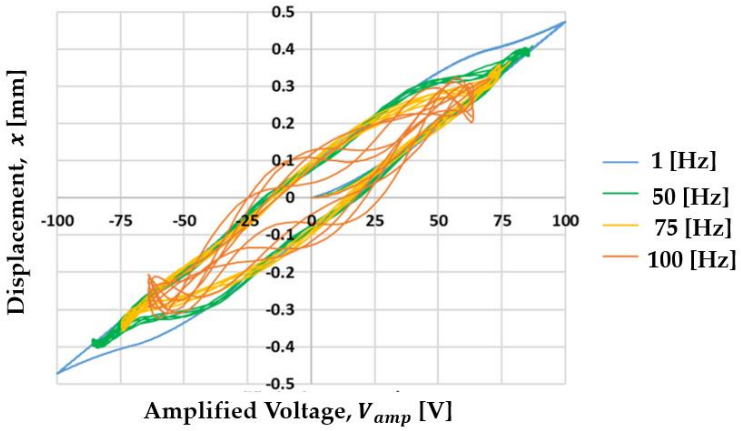

Fig. 112. Simulated hysteresis curves for model NAC2645 according to different input frequencies of V_c (sine wave from -5 V to +5 V).

Concerning the simulation of the entire valve architecture of Fig. 108a, a large size spool was used in the simulations, having a diameter of 15 mm and a mass of 30 g. The slot width was taken equal to 2/3 of the whole spool perimeter; therefore, b = 31.42 mm. The clearance was assumed to be c = 3 μm, being a typical value of servovalves [31], leading to $A_{l,s}$ = 0.09425 mm². The oil was assumed to be ISO VG 32 at 50 °C, characterized by ρ = 851 kg/m³ and μ = 0.0187 kg/(m s). The damping factor of the spool was calculated using Equation (58): assuming a spool length equal to l_s = 50 mm and an eccentricity equal to ε = 1 μm (common values for servovalves [21]), the calculated damping factor is C_s = 15 Ns/m.

Concerning the discharge coefficient, it was assumed, for simplicity, to be constant and equal to C_D = 0.7. Because of the large pressure drops used in the simulations, this assumption can be considered valid for a large part of the spool stroke, when the flow is turbulent and, for turbulent flows, the discharge coefficient in servovalves is constant, ranging from 0.65 to 0.7 regardless of the spool position [21], unlike the discharge coefficient in proportional valves which can have different values even for turbulent flows depending on the notch geometry and on the spool position [21]. The flow in the metering chamber of a servovalve is laminar only for very low values of the Reynolds number, usually for Re < 200 to 400 [21]; therefore, an error is introduced only at the very small opening degrees, without affecting the overall simulation. Similar considerations can be made for the flow angle, whose value was experimentally and numerically estimated to be around 69° for turbulent flows in servovalves [286]. Therefore, θ = 69° was imposed in Equation (59) to calculate the flow forces.

Concerning the simulation of the amplifier, it was operated from −100 V to + 100 V (the control voltage V_c being comprised between −5 V and +5 V, thus K_a = 20), the sign of the signal determining the direction of slider movement. All these parameters are reported in Table 24 for completeness.

Table 24. Input parameters employed in the simulations.

Parameter	Symbol	Unit	Value
Spool Diameter	D_s	mm	15
Spool Length	l_s	mm	50
Width of the Slots	b	mm	31.42
Spool Mass	m_s	g	30
Spool Damping Coefficient	C_s	Ns/m	15
Clearance	c	μm	3
Leakage Area	$A_{l,s}$	mm^2	0.09425
Discharge Coefficient	C_D	-	0.7
Flow Angle	θ	deg	69
Oil Density (ISO VG 32 at 50°C)	ρ	kg/m^3	851
Max. Blocking Force	$F_{b,max}$	N	332
Stiffness of the PEA	k_p	N/m	700000
Capacitance	C_{ap}	μF	20
Maximum Current	I_{max}	A	1
Gain of the Amplifier	K_a	-	20
Max. Amplified Voltage	V_{max}	V	100
Hysteresis Parameter	α	-	0.7
Hysteresis Parameter	β	-	0.013
Hysteresis Parameter	δ	-	0.3
Hysteresis Parameter	K_b	-	1.19

Fig. 113a shows the time history of the spool position simulated in a step test in which the control voltage V_c was initially changed from 0 V to +5 V, and then from +5 V to 0 V, with an inlet pressure p_P = 71 bar and a discharge pressure p_T = 1 bar (overall pressure drop $p_P - p_T$ = 70 bar), using the parameters of Table 24. Figure 113b shows the corresponding time history of the actuation force. The different curves were obtained for different values of the damping factor of the APA, namely, C_p = 10, 50, 90, 140 Ns/m, since the damping factor of APA depends on the geometry of the housing in which it is placed (affecting how the oil is displaced). Therefore, we can assume that it is possible to obtain these values by properly designing the geometry of the housing.

All the curves of the spool position in Figure 113a show oscillations, which are quite large for small values of C_p, while becoming negligible for larger values of C_p. Therefore, the response is very good for high values of C_p, with less than 10 ms being predicted on average to reach a stable condition. Instead, for low values of C_p, the output takes more time to reach a stable condition because of the large oscillations. This suggests that, if the housing of the APA produces low values of the damping factor, changes can be made to the housing in order to increase the damping factor and reduce possible oscillations of the spool. However, in all the cases (regardless of the value of C_p), the time interval taken to reach 90% of the maximum opening is very short, being of the order of 5 ms.

The spool displacement reached for V_c = +5 V is about 0.43 mm, which is similar to that achievable with LFMs (±0.5 mm), and a high value of flow rate is achieved at the maximum opening (51 L/min for $p_P - p_T$ = 70 bar). When the control voltage returns to 0 V, the simulated spool position is greater than zero because of the hysteresis occurring in the APA; this confirms that closed-loop controls must be employed to cope with hysteresis.

Concerning the actuation force, calculated as the difference between the blocking force (F_b) and the internal spring force ($k_p x$), the graph of Figure 113b reveals that the maximum value imposed by the manufacturer ($F_{act,max}$= 200 N at 50 °C) is never reached. This is due to the fact that the blocking force (black curve) has the same trend as the amplified voltage (red curve), and the maximum blocking force ($F_{b,max}$≃330 N) is obtained when V_{amp} = +100 V. Because of the time interval taken by the amplifier to transform +5 V into +100 V, the maximum blocking force is obtained approximately in correspondence of the maximum opening, when the elastic force is maximum; as a result, the actuation force is always well below 200 N. Notably, the values of the actuation force become negative after about 2 ms for low values of the damping factor. This happens when the internal spring force momentarily exceeds the blocking force.

The curves of Fig. 113a,b were obtained using an amplifier having $\omega_{n,a}$ = 1400 rad/s; it is evident that the response time of this amplifier has a great effect on the response of the valve, since the blocking force has the same trend as that of the amplified voltage. To evaluate the effects of using a different amplifier, Fig. 114a,b, respectively, show the time history of the sliding spool position and of the actuation force simulated for the same conditions as those of Fig. 113a,b, but using a different amplifier having $\omega_{n,a}$ = 2800 rad/s (while maintaining ξ_a = 1.5 and I_{max} = 1 A). Its cut-off frequency (calculated as the frequency at which the amplitude ratio is −3 dB) is 162 Hz. These curves show that the use of an amplifier with higher natural frequency can further improve the response time of the valve. Indeed, for high values of C_p, the time taken to reach a stable position is only slightly longer than 5 ms. In all the cases, regardless of the value of C_p, the time interval taken to reach 90% of the maximum opening is less than 3 ms, denoting a very fast response.

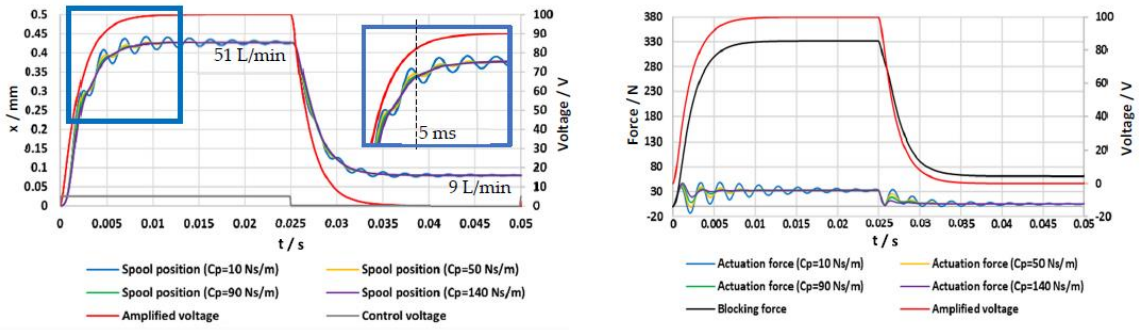

(**a**) (**b**)

Fig. 113. Open-loop step tests simulated for different values of C_p and $\omega_{n,a}$= 1400 rad/s (m_p = 80 g; $p_P - p_T$ = 70 bar): (**a**) spool position; (**b**) actuation force.

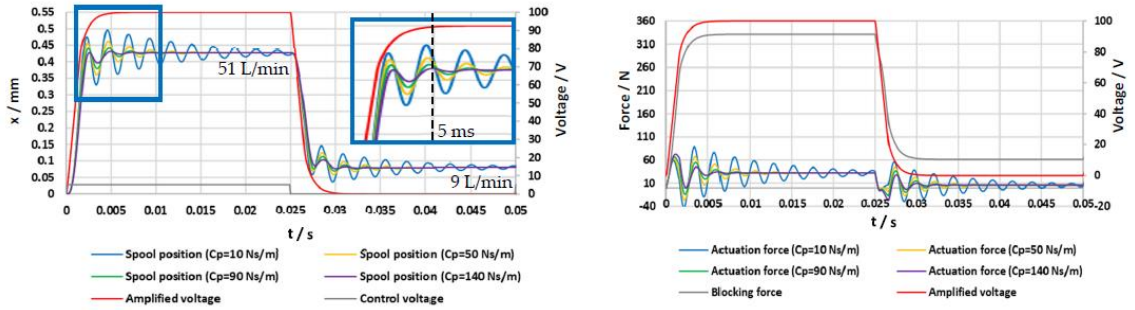

(**a**) (**b**)

Fig. 114. Open-loop step tests simulated for different values of C_p and $\omega_{n,a}$= 2800 rad/s (m_p = 80 g; $p_P - p_T$ = 70 bar): (**a**) spool position; (**b**) actuation force.

The results that are going to be presented from now on were obtained using the former amplifier, having $\omega_{n,a}$ = 1400 rad/s, keeping in mind that the transient response can further be shortened by using amplifiers with higher natural frequencies. Fig. 115 shows open-loop step tests, from V_c = 0 V to V_c = +5 V, predicted for different values of the overall pressure drop ($p_P - p_T$). The results were obtained using the parameters of Table 24, C_p = 90 Ns/m, m_p = 80 g, and $\omega_{n,a}$ = 1400 rad/s. As shown in the graphs, the response (initial part of the spool position curve) remains almost unchanged regardless of the pressure drop, which is typical of a direct drive valve. It is noteworthy that high levels of inlet pressure can be sustained by the valve, and hence, high flow rates can be reached (72 L/min at 200 bar). Note that the final spool position (for V_{amp} = +100 V) slightly decreases with the pressure drop, since the flow force increases with the pressure drop.

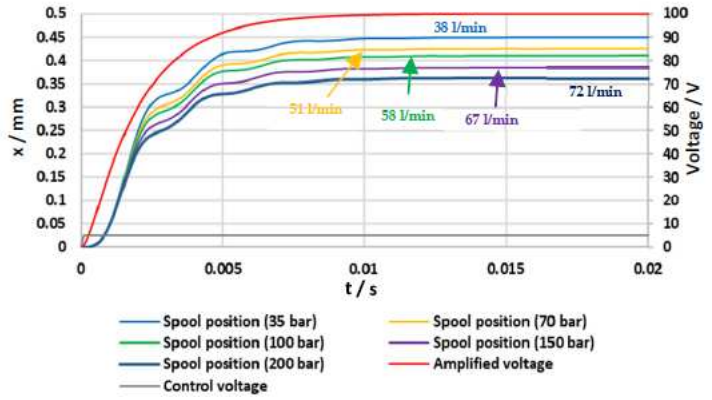

Fig. 115. Open-loop step tests simulated for different values of $p_P - p_T$ (C_p = 90 Ns/m; m_p=80g; $\omega_{n,a}$= 1400 rad/s).

In Fig. 113–115, the mass of the moving parts of the APA was set to m_p = 80 g. To evaluate the effects of the mass of the moving parts of APA upon the step response, Fig. 116 shows simulated open-loop step tests for different values of this mass, namely, m_p = 80, 130, 180, and 230 g (with V_c being changed from 0 V to +5 V; ($p_P - p_T$) = 70 bar; C_p= 90 Ns/m; $\omega_{n,a}$= 1400 rad/s). These graphs reveal that large oscillations of the spool position are predicted for large values of m_p. Therefore, it is

also important that the mass of the moving parts of the APA is taken not too large, in order to limit the oscillations of the spool position and, therefore, of the flow rate.

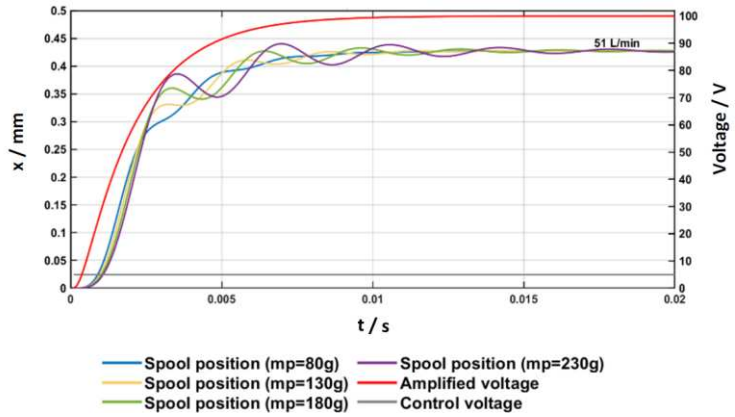

Fig. 116. Open-loop step tests simulated for different values of m_p ($p_P - p_T$ =70 bar, C_p= 90 Ns/m; $\omega_{n,a}$= 1400 rad/s).

All the results that have been presented up to this point were obtained through an open-loop control system, in order to assess the potential of the proposed architecture in terms of response speed. However, open-loop control is not able to cope with hysteresis, and closed-loop control is necessary for real applications. Therefore, closed-loop control was also simulated using a simple PI controller which changes the control signal (V_c) according to Equation (64) to reach the target position (set point). The parameters of the PI controller, which were determined taking advantage of the Ziegler–Nichols method, are K_p = 5.8 and K_I = 4100. The imposed saturation limits were V_c = ±5 V; the back calculation anti-windup method was used. As explained previously, this closed-loop control needs an LVDT to measure the spool position. Alternatively, in the literature, there are some open-loop control strategies with PEAs that do not need any position sensor, are easy to handle and cost effective [290].

In the simulated closed-loop step tests, the set point was changed with a step size of 0.2 mm and 0.4 mm (Fig. 117), and with a step size of 0.4 mm and 0.8 mm (Fig. 118). In these simulated closed-loop step tests, the overall pressure difference across the valve was set to $p_P - p_T$ =70 bar, with C_p= 90 Ns/m and m_p= 80 g. The parameters of Table 24 were used again in these simulations, along with $\omega_{n,a}$ = 1400 rad/s.

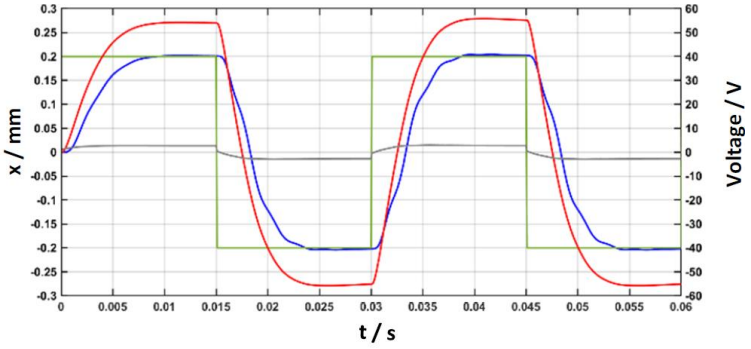

Fig. 117. Simulated closed-loop step tests ±0.2 mm ($p_P - p_T$=70bar, C_p = 90Ns/m, m_p = 80g; $\omega_{n,a}$ = 1400 rad/s).

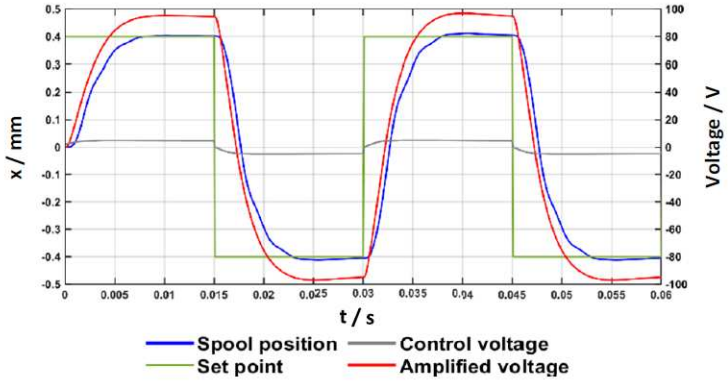

Fig. 118. Simulated closed-loop step tests ±0.4 mm ($p_P - p_T$=70bar, C_p = 90Ns/m, m_p = 80g; $\omega_{n,a}$ = 1400 rad/s).

These graphs show that the closed-loop control system allows the spool to reach the desired set points in short time intervals (overall, less than 10 ms to reach 90% of the set point). This reveals that such a simple closed-loop control system is capable of coping with the hysteresis that occurs in the APA.

The closed-loop frequency response of the valve is now discussed. The Bode Plot of hydraulic valves, in addition to depending on the supply pressure, usually depends on the amplitude of the input signal due to nonlinearities. Therefore, the Bode Plot is often obtained for an amplitude of the input signal equal either to 50% or to 100% of the maximum value [21]. The Bode Plot predicted for the proposed valve is shown in Fig. 119, including both the magnitude diagram (i.e., the amplitude ratio) and the phase diagram, obtained for $p_P - p_T$ = 70 bar, C_p = 90 Ns/m, m_p = 80 g, $\omega_{n,a}$= 1400 rad/s, along with the parameters of Table 24, and for an input sine wave (set point) having an amplitude of 0.4 mm (close to the maximum opening). The dimensionless amplitude ratio in dB was calculated using the formula $20log_{10}(x_{out}/x_{in})$, where$x_{in}$ = 0.4 mm is the amplitude of the input sine wave (set point) and x_{out} is the amplitude in mm of the output wave (actual spool position). The phase diagram reports the phase lag in degrees between the input wave and output wave.

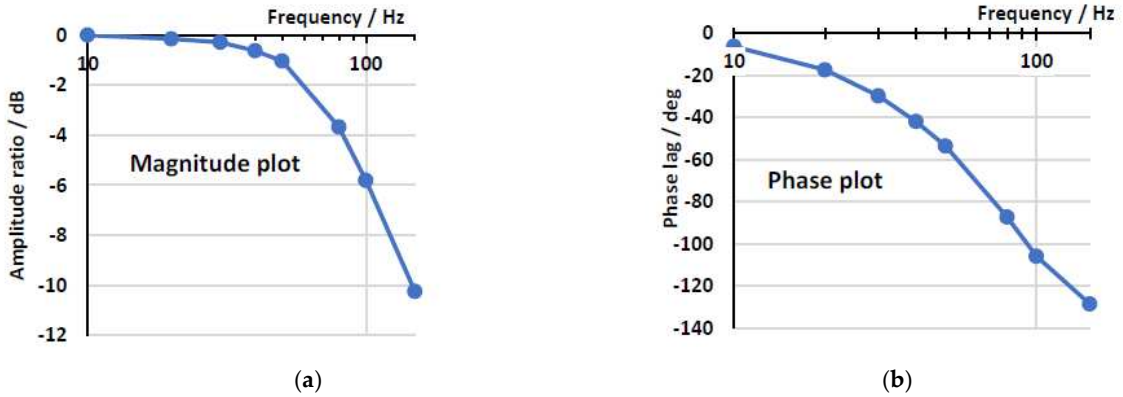

(**a**) (**b**)

Fig. 119. Bode Plot for input amplitude = 0.4 mm ($p_P - p_T$=70bar, C_p = 90Ns/m, m_p = 80g; $\omega_{n,a}$ = 1400 rad/s): (**a**) Magnitude plot; (**b**) Phase plot.

The plot shows that the predicted closed-loop frequency response is very good, with the phase shift being −54° for a frequency of 50 Hz, and −105° for a frequency of 100 Hz. The nonlinearity of the system is confirmed by Fig. 120 and 121, showing that the spool position is not exactly a sine wave.

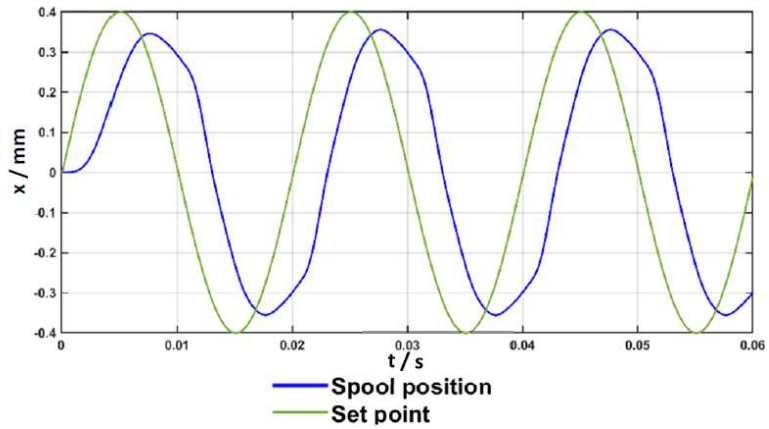

Fig. 120. Sine wave response for input amplitude = 0.4 mm and frequency = 50 Hz ($p_P - p_T$=70bar, C_p = 90Ns/m, m_p = 80g; $\omega_{n,a}$ = 1400 rad/s): spool position vs. time.

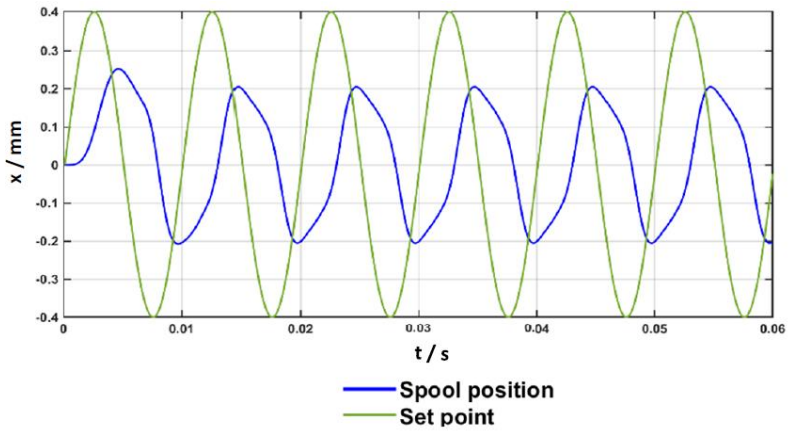

Fig. 121. Sine wave response for input amplitude = 0.4 mm and frequency = 100 Hz ($p_P - p_T$=70bar, C_p = 90Ns/m, m_p = 80g; $\omega_{n,a}$ = 1400 rad/s): spool position vs. time.

These results confirm the effectiveness of the proposed valve architecture: the main spool displacement reaches the set point very quickly. The dynamic characteristics of the system are also very good, with a frequency response comparable to, and slightly better than, that of conventional direct-drive servovalves, as previously detailed in Table 2 of Chapter 1. A comparison highlights that a conventional direct-drive servovalve, operating at 40 L/min with a pressure drop of 70 bar (and a supply pressure of 210 bar), exhibits a step response time of 15 ms and a -90° phase lag at 50 Hz. Additionally, its design is highly complex, and its size is substantial. In contrast, the innovative direct-drive servovalve, operating under the same conditions, achieves a step response time of less than 10 ms and a -90° phase lag at 55 Hz, with a simpler design and a more compact size.

5.4 Discussion

This study [48] of the PhD research project assessed the potential of using commercially available APAs with a diamond amplification mechanism for actuating direct-drive servovalves. This solution aimed to leverage the benefits of these actuators, such as rapid response and low weight. Specifically, two architectures were proposed, based on the number of APAs used (one or two). The performance of the simpler design, where a single APA pushed and pulled a spool within a four-way three-position (4/3) spool valve, was evaluated using well-established equations implemented in Simulink. Hysteresis was modelled accurately and validated against experimental data. The APA used in the simulations was the NAC2645 model from Noliac, providing displacement and force values similar to those of a LFM.

In the simulations, a spool with a 15 mm diameter and a 30 g mass was used. First, results from an open-loop control system were presented, followed by closed-loop spool position control to manage hysteresis. Both step and frequency responses were analysed.

The analysis of APA characteristics and simulation results highlighted favourable aspects of the proposed architecture. The actuation forces are sufficient to overcome the opposing ones that are present in a servovalve (friction and flow forces), and the piezo-electric actuation can guarantee a fast

response. In this regard, in the simulated open-loop tests, the time interval predicted to reach 90% of the maximum opening was less than 5 ms using an amplifier with 1400 rad/s natural frequency and less than 3 ms using an amplifier with 2800 rad/s natural frequency. Small oscillations in the response can be obtained, provided that the damping factor of the amplified piezo stack actuator, which can be changed by adjusting oil flow in the housing, is not too small. High inlet pressure levels can be sustained by the valve and therefore high flow rates can be achieved (about 70 L/min at 200 bar). The use of closed-loop control can allow hysteresis to be successfully coped with. A very good closed-loop frequency response was predicted, the phase shift being −105° for a frequency of 100 Hz and an amplitude of 0.4 mm, using an amplifier with 1400 rad/s natural frequency. The parameters of the closed-loop controller were determined taking advantage of the Ziegler–Nichols method; a descent approach could be used to further improve the results.

In conclusion, this analysis showed that APAs are feasible for directly actuating servovalves and offer promising features, particularly in response speed. Although the current cost of APAs is high (approximately 2000 euros), prices may decrease with larger-scale production in the future.

6. DESIGN AND TESTING OF HIGH-POWER PIEZOHYDRAULIC PUMPS

This part of the research focuses on the development of a multi-cylinder piezohydraulic pump, undertaken during the visiting Ph.D. period at the University of Bath (UK).

As outlined in Chapter 1, hydraulic actuation systems are widely used in industrial and aeronautical applications. Traditional valve-controlled hydraulic cylinders, however, are often inefficient due to power loss through control valves. This inefficiency has led to a shift from hydraulic power distribution from a centralized supply to electrical power distribution, aiming to reduce maintenance requirements, decrease weight, and improve efficiency. Despite these changes, hydraulic actuators remain highly valued for their power density, durability, and controllability, making it essential to find effective ways to convert electrical power to hydraulic power locally to drive an actuator.

Traditional hydraulic pumps, while powerful, are often inefficient and unsuitable for low-power applications, which has made piezoelectric pumps a promising alternative for converting electrical to hydraulic power in the sub-100 W range. Currently, the application of piezopumps is limited by their maximum power (typically only a few watts or less) and low flow rates. This research details the design, simulation, and testing of a single and a multi-cylinder piezohydraulic pump aimed at expanding the power capabilities of piezohydraulic technology. The motivation for this work is its potential use in aerospace, particularly for accessory actuators in landing gear systems. The chapter begins by presenting the design of a single cylinder piezohydraulic pump, along with its simulation model, architecture, test rig, and experimental results conducted by the research group of the University of Bath in 2022 [271], [291]. Following this, the Chapter introduces the innovative concept of a multi-cylinder piezohydraulic pump, designed to improve upon the performance of previously tested single cylinder model. The simulation model, test rig and experimental results are discussed, highlighting the advantages, limitations, and future developments.

This work was carried out in collaboration with the University of Bath's research group at the Centre for Power Transmission and Motion Control, and the findings were published in a respected journal [51].

6.1 Single Cylinder Piezohydraulic Pump

The design of the following single cylinder (single pumping chamber) piezohydraulic pump is derived from previous research studies conducted at the University of Bath [271], [291]. An initial design goal of Q_{Target} = 1.65 L/min at p_{Target} = 60 bar (P_{Target} = 100 W) has been set to guide pump development, though this target isn't tied to a specific application. For testing purposes, a ring stack actuator—the PI Ceramic PICA P025.50H, the largest available model—was selected, with key specifications detailed in Table 25 [292].

Table 25. PICA P025.50H Ring Stack: Specifications [292].

Parameter	Symbol	Value	Unit
Cross-sectional area		2.89	cm^2
Outer diameter		25	Mm
Inner diameter		16	Mm
Length		66	Mm
Maximum voltage		1000	V
Free stroke	x_{max}	80	Mm
Blocking force	$F_{b,max}$	9.6	Kn
Capacitance		1.2	Nf
Natural Frequency		17	kHz

As already discussed, a crucial characteristic of PEAs is that the blocking force occurs only at zero displacement, while maximum displacement is achieved at zero external force. Therefore, an optimal operating point is typically chosen midway between these extremes (as shown in Fig. 122), maximizing the power output [271].

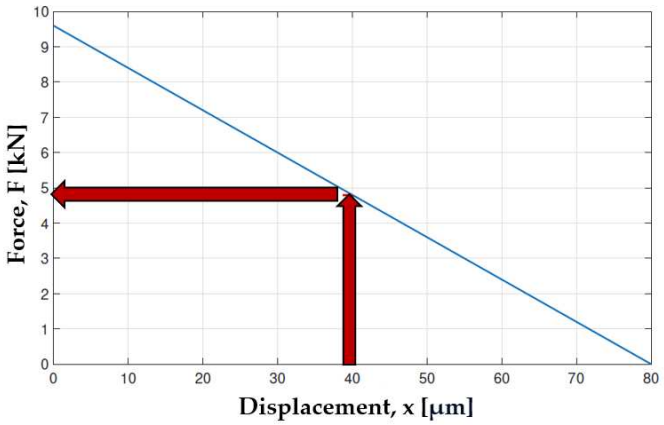

Fig. 122. Operating envelope of the PICA P025 [271].

Based on this operating point, with displacement x = 40 µm and actuation force F = 4.8 kN, the required piston area, A_p, to produce a pressure p_{Target} = 60 bar, can be calculated using:

$$A_p = \frac{F}{p_{Target}}, \tag{65}$$

This gives a piston area $A_p = 8 \cdot 10^{-4}$ m² which results in a piston diameter d_p = 31.9 mm. However, since this equation does not account for compressibility losses, it may overestimate the generated pressure. To compensate, it is prudent to reduce the diameter, which also helps to decrease the moving mass in the system—a crucial factor at high frequencies. A minimum reasonable diameter is d_p= 25 mm, which corresponds to a piston area $A_p = 4.91 \cdot 10^{-4}$ m² and a theoretical pressure p_{Target} = 98 bar. To prevent leakage, an O-ring will be used to seal the piston to the cylinder. Using this diameter, it is possible to estimate the driving frequency (f) of the pump:

$$f = \frac{Q_{Trget}}{xA_p}, \tag{66}$$

This results in a driving frequency of f = 840 Hz. Similar to the pressure calculation, this frequency does not include compressibility, making it a lower bound.

The choice of a ring stack actuator allows the inlet valve to be integrated into the piston face, resulting in a smaller pumping chamber compared to configurations where both the inlet and outlet valves are located in the chamber wall. Additionally, this design enables the piston rod to pass through the stack hole and be tensioned to the rear of the cylinder using Belleville washers.

Piezo stack actuators typically require preloads of around 150 bar for dynamic operation. Belleville washers are advantageous because they provide this high preload force in a more compact package than coil springs, helping to reduce internal volume.

A stack of three DIN 2093 D315163125 Belleville washers was used to preload the stack. These washers have an outer diameter of $d_{out,BW}$ = 31.5 mm, an inner diameter of $d_{in,BW}$ =16.3 mm, and a thickness of t_{BW} = 1.25 mm. To achieve the necessary preload on the piezostack, a deformation of 0.55 mm was utilized. This configuration results in a Belleville washers' stiffness of k_{BW} = 6.6 MN/m, which is about 5% of the stack stiffness and acts to limit the maximum force and displacement of the piston, consequently limiting the maximum pressure and flow of the pump. In addition, a spacer is required to properly position the springs on the piston shaft due to their large inner diameter, which adds extra moving mass.

In this design of a single cylinder piezohydraulic pump, disc-style reed valves with a thickness of t_{Valve} = 0.2 mm function as check valves to control the flow entering and exiting the pumping chamber. These valves are especially suitable for this pump because they are easy to mount on the face of the piston and can be conveniently manufactured for prototypes using chemical etching. Additionally, made from flexible materials, these valves minimize the moving mass, which enhances the pump's bandwidth, particularly in the 1 kHz range [293].

Fig. 123 presents a longitudinal section view of the ring stack actuator and piston assembly, with a detailed bill of materials available in Table 26.

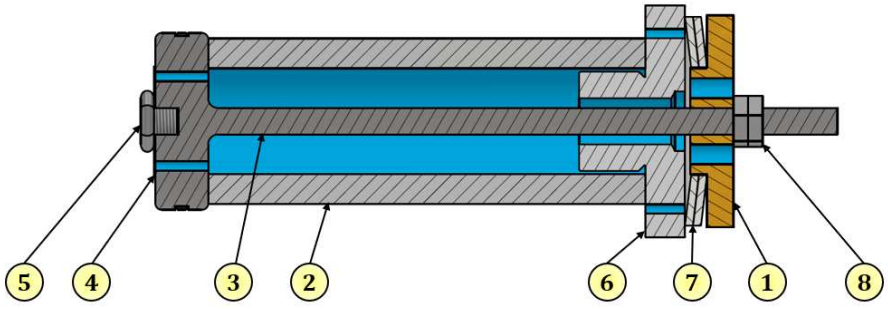

Fig. 123. Longitudinal section view of the ring stack actuator – piston assembly, with blue indicating the low-pressure fluid pathway.

Table 26. Bill of materials of the ring stack actuator – piston assembly.

Part Number	Item	Material
1	Spacer	Copper BS B32
2	Ring Stack Actuator	PIC151
3	Piston	Stainless Steel 440C
4	Inlet Reed Valve	Stainless Steel 440C
5	Valve Screw	Stainless Steel 440C
6	Piston Clamp	Stainless Steel 440C
7	Belleville Washers	Carbon Steel 51CrV4
8	Bolts	Stainless Steel 440C

Cooling the piezo stack is vital because reaching the Curie temperature causes the piezo ceramic to de-pole, resulting in a loss of force generation [294]. The recommended maximum operating temperature for the chosen stack is 85 °C [271].

In this design, the inlet reed valve is integrated into the piston, reducing chamber volume and allowing low-pressure flow through the center of the stack, which helps dissipate heat. The hydraulic oil is electrically insulating, enabling safe wet operation for thermal management.

Modelling the thermal dynamics of the pump is difficult due to unknown factors like heat transfer and dielectric losses. As a result, a worst-case scenario will be used to estimate runtime limits, assuming all input energy to the stack is converted to heat and that heat conduction is no better than in free air. Therefore:

$$T_{st} = T_0 + \Delta T(1 - e^{\frac{t}{\tau}}) \tag{67}$$

$$\Delta T = \frac{W_T}{k(T)A_{surf}}, \tag{68}$$

$$\tau = \frac{V_{st}\rho_{st}c_{st}}{k(T)A_{surf}}. \tag{69}$$

where, T_0 represents the initial temperature of the stack, while ΔT indicates the maximum temperature increase. The power of heat generation, W_T, is assumed to equal the total power in the stack, which has been calculated to be 600 W based on a capacitance of 1.2 μF, a driving voltage of 1 kV, and a driving frequency of 1 kHz. The overall heat transfer coefficient, $k(T)$ is assumed to be 30 W/m²K (Zheng et al., 1996), and A_{surf} refers to the surface area of the stack. The specific heat capacity of the stack, c_{st}, is 350 J/(kgK), while its density and volume are ρ_{st} and V_{st}, respectively [271].

Given that the upper limit for the stack temperature is 85 °C and the ambient temperature is 20 °C, the maximum operating time is calculated to be τ = 86.5 seconds. Since ancillary actuators in landing gear typically need to operate for around 10 s, this brief operating window is not a concern. However, this limit will be considered during testing.

Regarding the pumping chamber, it has been designed with a height of just 1 mm to maximize the displacement of both the inlet and outlet reed valves. Since the flow requirements for both the

inlet and outlet are the same, it was decided to make the valves and their mountings identical. Therefore, the pumping chamber is confined between the piston and the valve plate. The latter has a similar arrangement to the piston, including twelve orifices and an outlet reed valve positioned on its left end face with another valve screw.

Fig. 124(a) provides a longitudinal section view of the entire pump, showing the position of the 0.2 mm thick disc-style reed valves. Fig. 124(b) displays the pump components. Finally, Fig. 124(c) shows the prototype of the assembled piezopump tested at the University of Bath [271].

In terms of the flow path and overall pump architecture, as shown in Fig. 124a, oil enters the pump through the inlet end cap. It then passes through eight orifices in the spacer, entering the pump body and the hole in the ring stack. The piston, located on the left end of the stack, has its rod passing through the stack hole, clamping and preloading the stack with the help of a piston clamp, Belleville washers, and bolts. Featuring twelve orifices, the piston is equipped with an inlet reed valve fixed onto its left face using a valve screw. A similar arrangement is found on the valve plate, where twelve orifices are covered by an outlet reed valve positioned onto the left face of the valve plate using another valve screw. The extension and retraction of the stack govern the opening and closing of the inlet and outlet reed valves, allowing oil to either flow within the pump chamber (intake) or exit (delivery) based on internal pressure. Finally, the pressurized oil, coming from the outlet reed valve, exits the pump through the outlet end cap.

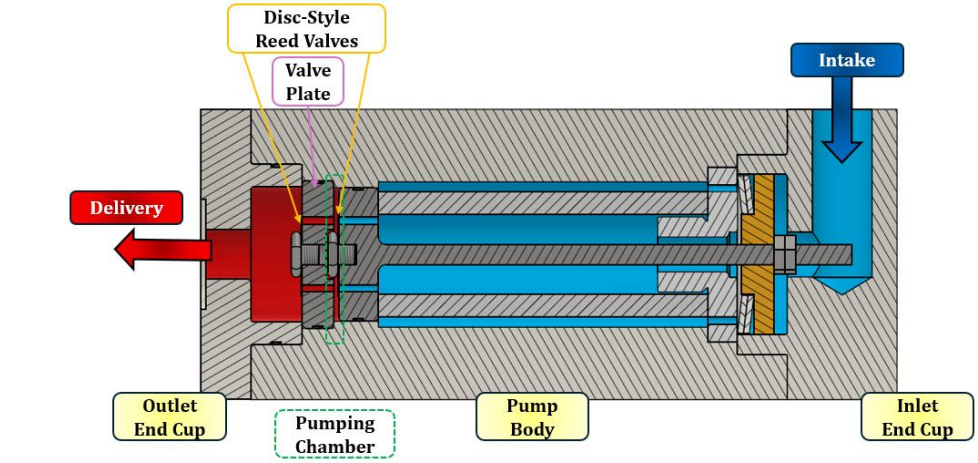

(**a**)

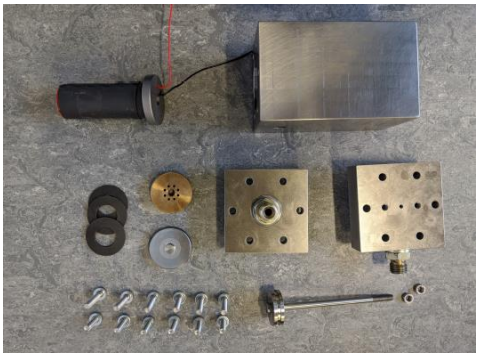

(**b**)

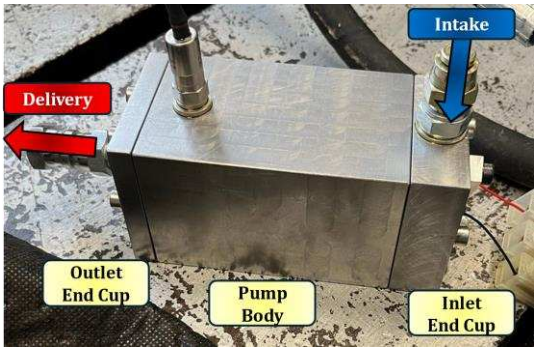

(**c**)

Fig. 124. Piezohydraulic pump developed at the University of Bath [271]: (**a**) Longitudinal section view of the entire pump; (**b**) Thick disc-style reed valve with corresponding valve screw; (**c**) Assembled pump prototype.

6.2 Numerical Model of the Single Cylinder Piezohydraulic Pump

The single cylinder piezohydraulic pump, previously illustrated in Fig. 124a, is modelled within the Simulink environment, as depicted in the graphical scheme shown in Fig. 125.

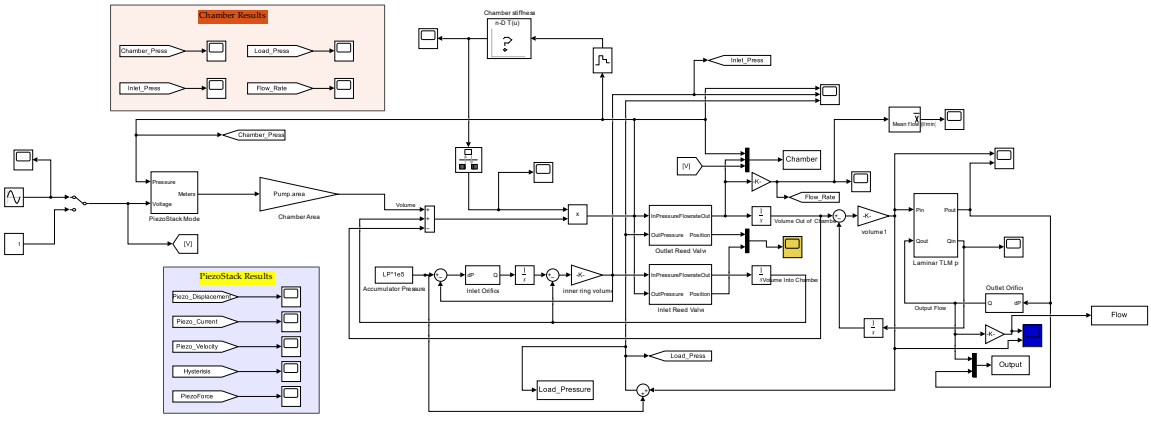

Fig. 125. Single cylinder piezohydraulic pump Simulink model.

The pump's output is treated as a small volume of 0.3 L, which supplies a hydraulic line with a diameter of 10 mm, equipped with a variable orifice at its end. The pump's inlet is represented as a constant pressure source that feeds into an orifice, the area of which corresponds to the flow path between the piston rod and the piston clamp.

6.2.1 Piezo Stack modelling

Hysteresis in PEAs is a well-known phenomenon and is simulated here using the Bouc-Wen model, which is widely used for its flexibility and capacity to represent various hysteretic behaviours. This model, as shown in Equation (70), uses parameters α, β, and δ, which can be adjusted to fit different hysteresis profiles, with x_V representing the input voltage and z_V the output voltage loss.

$$\dot{z}_V = \alpha\dot{x}_V - \beta|\dot{x}_V||z_V|^{n-1}z - \delta\dot{x}_V|z_V|^n, \tag{70}$$

A 10% voltage loss was assumed and the parameters set accordingly. The piston and piezostack assembly are represented as a mass-spring-damper system. A free-body diagram illustrating this setup is shown in Fig. 126.

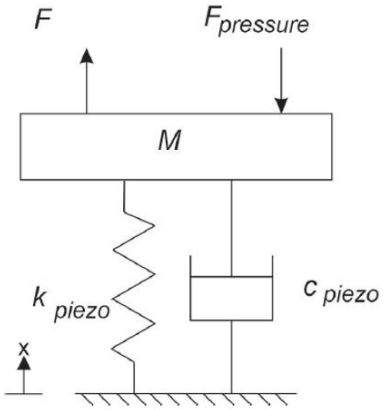

Fig. 126. Piston and piezostack force diagram.

where, M represents the total moving mass, composed of the piezo stack's effective mass (estimated at 40% of its actual mass, based on [295]), the mass of the piston, and the mass of the spacer that positions the Belleville washers. The system stiffness is calculated as a combination of the piezo stack's intrinsic stiffness:

$$k_{piezo} = \frac{F_{b,max}}{x_{max}}, \tag{71}$$

and the Belleville washer stiffness, which are combined in parallel. Taking into account the damping effects of the fluid and seals, the system is treated as critically damped, yielding an estimated coefficient , c_{piezo}.

The external forces acting on the system include, the force generated by the piezo stack (F) and the force resulting from the chamber pressure ($F_{pressure}$), given by:

$$F = K_{VF} V_{eff}, \tag{72}$$

$$F_{pressure} = (p_{ch} - p_{bias}) A_p. \tag{73}$$

where V_{eff} is the effective driving voltage; p_{ch} is the pressure in the piston chamber and p_{bias} is the pressure directly upstream of the inlet valve after passing through the stack rather than at the pump inlet port.

6.2.2 Pumping Chamber modelling

The chamber pressure can be calculated by first determining the total volume change in the pumping chamber. This is done by multiplying the displacement of the stack and piston assembly by the piston area, yielding the volume change due to piston movement. This is then combined with the volume change resulting from flow through the inlet (Q_{in}) and outlet (Q_{out}) valves to obtain the net chamber volume change, ΔV_{ch}:

$$\Delta V_{ch} = x A_p + \int Q_{in} - \int Q_{out}, \tag{74}$$

The chamber pressure is then given by:

$$p_{ch} = K_{pump} \Delta V_{ch}, \tag{75}$$

Equation (75) describes how the pressure change in the pumping chamber depends on the net change in oil volume entering the chamber, taking into account the pump stiffness. The overall pump stiffness (K_{pump}), is a combination of:

- Fluid stiffness (K_{fluid}): accounting for the compressibility of the oil within the chamber;
- Pump radial stiffness ($K_{p,ra}$): representing the resistance to deformation of the pump body in the radial direction;
- Pump axial stiffness ($K_{p,ax}$): representing the resistance to deformation in the axial direction of the pump.

Specifically:

$$K_{fluid} = \frac{B A_{ch}}{L}, \tag{76}$$

$$K_{p,ra} = \frac{4 E t_{wall}}{\pi D_{ch}^3 L}, \tag{77}$$

$$K_{p,ax} = \frac{E \pi D_{ch} t_{wall}}{L A_p^2}, \tag{78}$$

$$K_{pump} = \frac{1}{\frac{1}{K_{fluid}} + \frac{1}{K_{p,ra}} + \frac{1}{K_{p,ax}}}. \tag{79}$$

where:

- B is the bulk modulus of the working fluid, assumed to be 0.8 GPa to account for any air present in the hydraulic fluid;

- A_{ch} is the pumping chamber area;
- L is the height of the pumping chamber, set at 1 mm;
- E is the Young's modulus of the pumping chamber material, which is 207 GPa for 440C stainless steel;
- D_{ch} is the diameter of the pumping chamber, equal to the diameter of the piston;
- t_{wall} is the thickness of the chamber wall, assumed to be 15 mm.

6.2.3 Check Valve modelling

The pressure in the pumping chamber controls the opening of the passive disc reed valves. For simplicity, it is assumed that the inlet and outlet check valves are identical. These valves are modelled to account for effects such as valve and fluid inertia, valve bounce, and context-dependent opening times. A simplified approach is proposed, using a single-degree-of-freedom model with lumped mass and stiffness parameters, allowing the disc reed valve to be treated similarly to a poppet valve. Fig. 127 illustrates the passive poppet-type valve model [296].

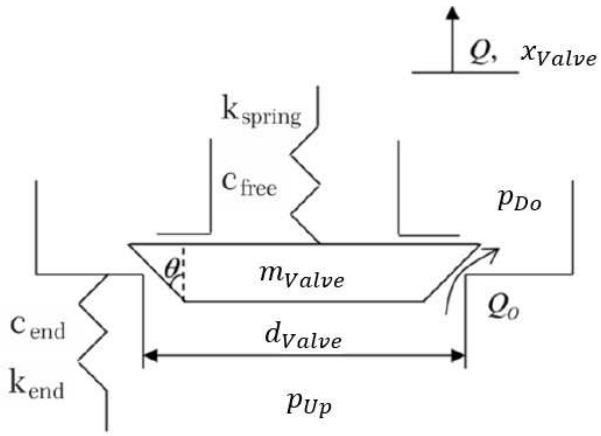

Fig. 127. Check valve model [296].

The valve has a mass (m_{Valve}) and is closed by a spring with linear stiffness (k_{spring}) and there is an associated damping (c_{free}):

$$c_{free} = 2\xi\sqrt{k_{spring}m_{Valve}}, \tag{80}$$

When the valve reaches the end stop, it experiences a high stiffness (k_{end}), and its damping (c_{end}) also changes, as described by Equation (80). The net force accelerating the valve mass (F_{Valve}) is influenced by spring and damper forces and the pressure difference across the valve face area. Depending on the position of the valve, the net force can take one of three forms:

$$Case\ 1 \rightarrow Valve\ Fully\ Open\ (x_{Valve} \geq x_{end})$$
$$F_{Valve} = A_{Valve}C_f(p_{Up} - p_{Do}) - c_{end}\dot{x}_{Valve} - k_{end}(x_{Valve} - x_{end}) - k_{spring}x_{Valve} - F_{pre} \quad (81)$$

$$Case\ 2 \rightarrow Valve\ Partially\ Open\ (0 < x_{Valve} < x_{end})$$
$$F_{Valve} = A_{Valve}C_f(p_{Up} - p_{Do}) - c_{free}\dot{x}_{Valve} - k_{spring}x_{Valve} - F_{pre} \quad (82)$$

$$Case\ 2 \rightarrow Valve\ Fully\ Closed\ (x_{Valve} \leq 0)$$
$$F_{Valve} = A_{Valve}C_f(p_{Up} - p_{Do}) - c_{end}\dot{x}_{Valve} - k_{end}x_{Valve} - k_{spring}x_{Valve} - F_{pre} \quad (83)$$

Here, A_{Valve} represents the valve face area, and C_f is the valve force coefficient set at 0.4; F_{pre} denotes the preload force on the valve. The pressures upstream (p_{Up}) and downstream (p_{Do}) of the valve vary depending on whether it is the inlet or outlet valve. By using this net force, the check valve's position can be determined through integration, as follows:

$$\ddot{x}_{Valve} = \frac{F_{Valve}}{m_{Valve} + m_{fluid}}, \quad (84)$$

where m_{fluid} is the "added mass" due to the fluid displaced as the valve moves. The flow through the valve is:

$$Q = Q_0 + A_{valve}\dot{x}_{Valve}, \quad (85)$$

where Q_0 is the flow rate through the valve orifice. This flow rate, Q_0, can be determined by integrating the pressure change resulting from fluid inertia:

$$(p_{Up} - p_{Do}) = \frac{\rho_{fluid}}{2}\left(\frac{Q_0}{C_d\pi A_{Valve}}\right)^2 + \frac{\rho_{fluid}l_{fluid}}{a_{Valve}}\frac{dQ_0}{dt}. \quad (86)$$

where ρ_{fluid} is the fluid density, taken as 850 kg/m³, and C_d represents the valve discharge coefficient, which depends on valve design and is set to 0.72. l_{fluid} is the characteristic length of the fluid, assumed to be the thickness of the valve (t_{Valve}), and a_{Valve} is the valve opening area. A minimum opening area of 1 mm² is set to account for leakage and ensure mathematical stability

6.2.4 Reed Valve modifications

The actual form of the valve is shown in Fig. 128.

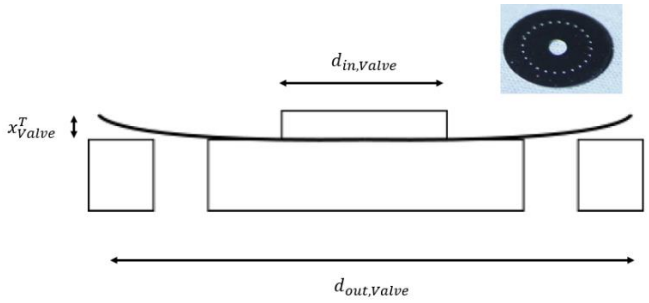

Fig. 128. Disc type reed valve cross section

The valve opening area (a_{Valve}) is calculated as:

$$a_{Valve} = \pi d_{Valve} x_{Valve}^{T}, \tag{87}$$

where d_{Valve} is the diameter of the annular region behind the valve, and x_{Valve}^{T} is the disc's tip displacement. The disc stiffness is derived using a simplified Timoshenko bending equation for a ring, assuming that all force acts at the annulus center when the valve is closed and that the disc's inner diameter equals the clamp piece's outer diameter. This allows for the calculation of tip displacement, as follows:

$$x_{Valve}^{T} = k_1 \frac{(p_{Up} - p_{Do}) d_{Valve}^2}{2 E_{Valve} t_{Valve}^3}, \tag{88}$$

Here, k_1 is a coefficient that depends on boundary conditions and the ratio of valve diameter to hole diameter, and E_{Valve} is the valve Young's modulus (207 GPa for HR302 stainless steel). Using the disc's displacement and the load force, a stiffness value can be determined. Assuming the disc deforms into a triangular cross-section, the effective mass of the valve is taken as one-third of the valve's mass, plus the mass of fluid displaced by the valve's movement:

$$m_{Valve} = \frac{1}{3} A_{Valve} (\rho_{Valve} t_{Valve} + \rho_{fluid} x_{Valve}^{T}), \tag{89}$$

where A_{Valve} is the valve face area, ρ_{Valve} is valve material density and ρ_{fluid} is the oil density.

The dimensions of the valve were found using an optimisation process as explained in [291]. This resulted in an inner diameter of $d_{in,Valve}$ = 6 mm, outer diameter of $d_{out,Valve}$ = 16 mm and thickness of t_{Valve} = 0.2 mm for both the inlet and the outlet reed valve.

6.3 Simulation Results of the Single Cylinder Piezohydraulic Pump

To address the high-frequency operation of the pump, output impedance is crucial. A simple load system model was developed, featuring a hydraulic volume matching the pump's output chamber (0.01 L) connected to a transmission line, as described by [297]. The transmission line, assumed to be 3 m long and 6 mm in diameter, accounts for significant wave effects at high frequencies. Its output connects to a variable area orifice, simulating a loading valve, allowing for the adjustment of pressure levels. The pump's inlet is kept at a constant 20 bar to prevent cavitation and maintain fluid stiffness.

A summary of the key parameters for this simulation can be found in Table 27.

Table 27. Key Simulations Parameters.

Parameter	Symbol	Value	Unit
Piezo Stack Stiffness	k_{piezo}	120	MN/m
Piezo Stack Damping	c_{piezo}	5.6	kNs/m
Piezo Stack Mass	M	0.138	Kg
Bulk Modulus	B	0.8	GPa
Fluid Density	ρ_{fluid}	850	kg/m^3
Pumping Chamber Young Modulus	E	207	GPa
Pumping Chamber Area	A_{ch}	560	mm^2
Pumping Chamber Height	L	1	Mm
Pumping Chamber Thickness Wall	t_{wall}	15	Mm
Valve Young Modulus	E_{Valve}	207	GPa
Valve Stiffness	k_{spring}	1.16	MN/m
Valve Damping	c_{free}	30.7	Ns/m
Valve Mass	m_{Valve}	0.53	G
Valve Discharge Coefficient	C_D	0.72	-
Valve Force Coefficient	C_f	0.4	-
Valve Inner Diameter	$d_{in,Valve}$	6	Mm
Valve Outer Diameter	$d_{out,Valve}$	16	Mm
Valve Thickness	t_{Valve}	0.2	Mm

Fig. 129 presents the simulation results of pressure, flow, and power outputs at different driving frequencies. The data shows that power output continues to rise up to a piezo stack driving frequency equal to 1500 Hz, indicating the pump's ability to produce higher power at increased frequencies. The maximum flow rate observed is 1.9 L/min under no-load conditions. The highest pressure difference recorded is 104 bar, occurring when there is no flow, which is expected.

The target output of 60 bar at a flow rate of 1 L/min is achieved at 1500 Hz, which is significantly higher than the 840 Hz predicted when compressibility effects were ignored. Additionally, at a lower frequency of 1200 Hz, the pump generates 100 W of output power at 48.5 bar and a flow rate of 1.2 L/min.

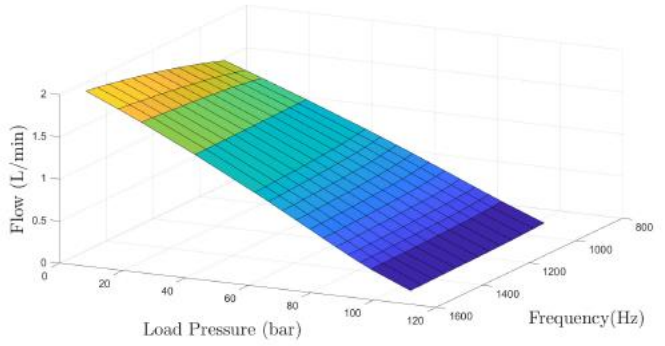

(**a**)

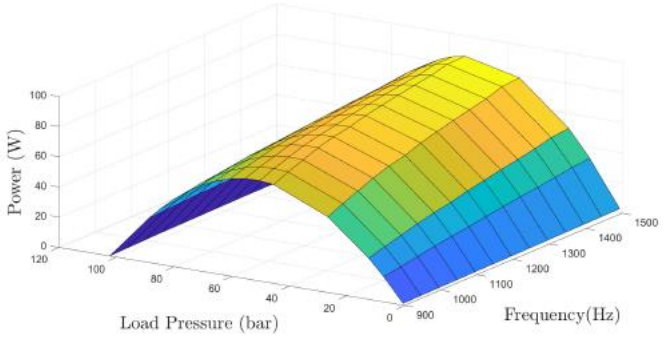

(**b**)

Fig. 129. Simulation results: (**a**) Pressure difference and Flow; (**b**) Power Output.

6.4 Test Rig of the Single Cylinder Piezohydraulic Pump

To assess the performance of the single cylinder piezohydraulic pump, a prototype was tested in a test rig shown in Fig. 130a with detailed components listed in Table 28. Fig. 130b provides a photo of the test setup.

Table 28. Test rig components.

Number	Component
1	Piezohydraulic Pump
2	Pressure Sensor – Temperature Sensor (Pumping Chamber)
3	Pressure Sensor (Pipe)
4	Pipe
5	Pressure Sensor (Up-Down Valve Side)
6	Direct Drive Servovalve
7	Pressure Relief Valve
8	Flow Sensor
9	Accumulator
10	Needle Valve

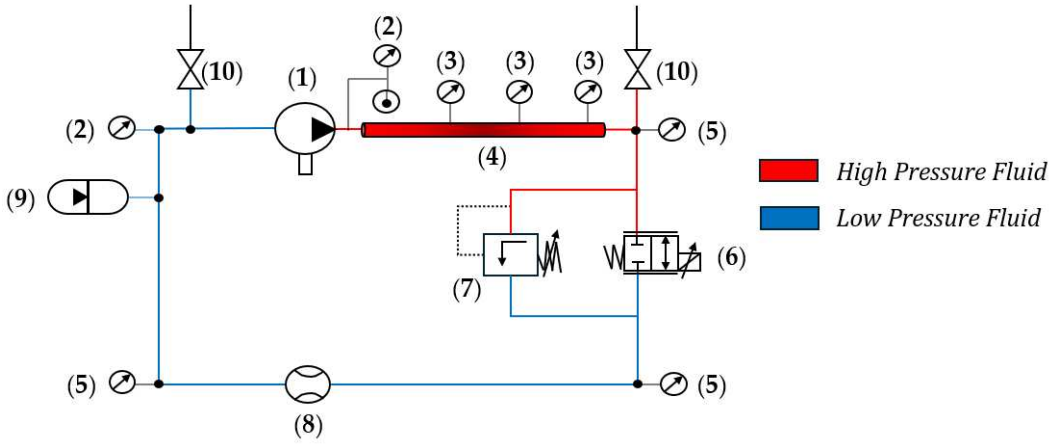

(**a**)

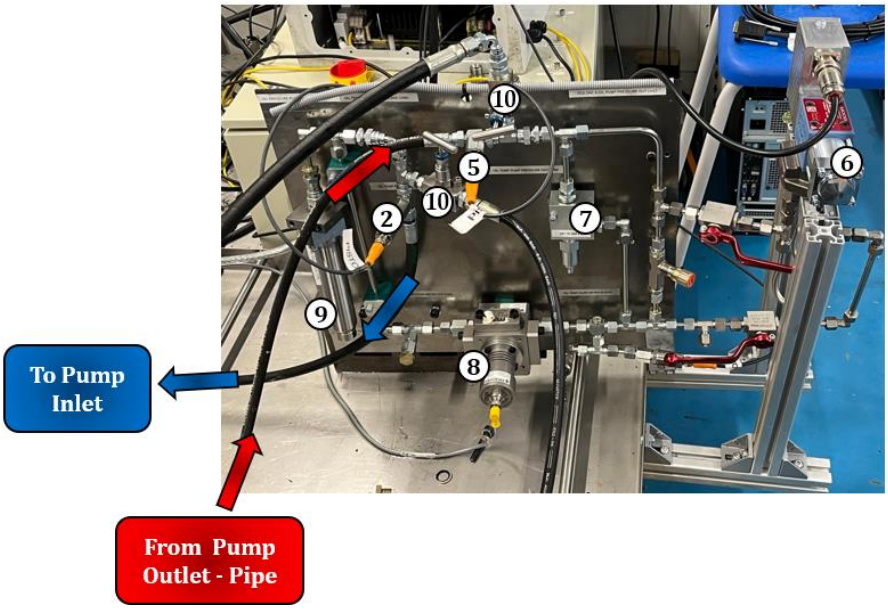

(**b**)

Fig. 130. Test rig for evaluating pump performance: (**a**) Schematic circuit; (**b**) Photograph of the setup.

In the test setup, oil from the pump (1) flowed through a 3-meter-long pipe with a 6 mm diameter (4). A direct drive servovalve at the pipe's end allowed for varying load pressures. To safeguard against potential over-pressure situations and damage, a pressure relief valve (7) set to open at 200 bar was installed. The oil then entered a small hydraulic volume equivalent to the output chamber of the pump, measuring 0.01 L (9). The pump maintained a constant inlet pressure of 20 bar to enhance oil stiffness and prevent cavitation.

The pressure and temperature in the pumping chamber are measured using an EFE PCM127 sensor (2), which combines a PT1000 temperature (2) probe with a thin film pressure transducer (2). This is connected to the pumping chamber via a small drilling so that the volume of the cylinder is

not increased excessively. The pressure difference across the Moog D633 load valve (6) is measured using Parker PTDVB250 sensors on either side of the valve (5).

The test circuit included both mean and instantaneous flow measurements to analyze the pump's high-frequency behaviour. Mean flow was measured with a Max Machinery P214 piston flow meter (8) (bandwidth of 100 Hz), while higher-frequency measurements were obtained using the three-transducer method, employing a PCB Piezotronics dynamic pressure sensor (3). These measurements were combined using two complementary filters, calibrated to cross over at 50 Hz, ensuring accuracy in both data sets.

Due to the high voltage (1 kV peak-to-peak) and frequencies (up to 1.4 kHz) required for testing, a bespoke power electronic converter was developed to drive the piezo stack at the high frequencies and voltages required. The electronics were designed to produce a sinusoidal voltage between 0 and 1 kV at frequencies ranging from 500 Hz to 1.4 kHz. The power supply was envisaged from a High-Voltage Direct Current bus. For testing, this was emulated by a 450 V lab power supply unit (PSU). High efficiency and high power density were achieved through a switched mode topology, utilising 1200 V SiC MOSFETs. The driver consisted of two stages. Firstly, an asynchronous boost converter increased the voltage from the lab power supply by a ratio of 2.25:1. Then, a PWM-controlled half-bridge generated the sinusoidal output waveform by tracking a referenced signal provided by a controller implemented in the Simulink Real-Time environment. This is shown schematically in Fig. 131.

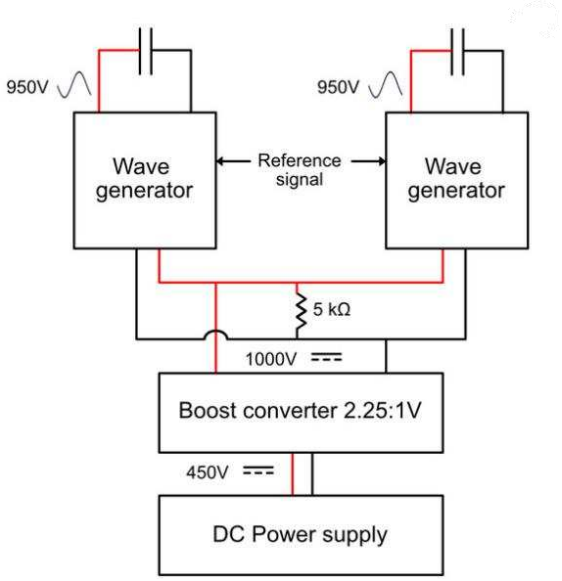

Fig. 131. Schematic of custom power electronics.

The power electronics were designed to be able to operate across a very wide range and follow arbitrary signals. This meant that in the case of user error or extreme edge cases, there could be stability issues. Therefore, a resistor was included at the output of the boost converter, but it is not expected to be needed outside the laboratory environment. Given the prototype construction, there

was significant free space within the electronics enclosures, so the boost converter and one wave generator were housed in the same enclosure. The assembled units can be seen in Fig. 132; the large passive components of the boost converter are visible in the upper unit, but the same PCB is used for both, with some components not populated in the lower unit.

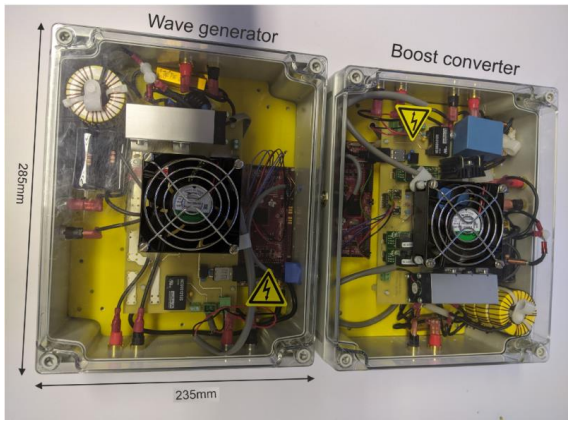

Fig. 132. Test rig power electronics.

6.5 Experimental Results of the Single Cylinder Piezohydraulic Pump

The pump prototype was tested following the same method as the simulation model, using a Moog D633-303B modulating valve (6) (direct drive servovalve) to control outlet load pressure. Measurements of pressure and flow were taken at frequencies ranging from 1000 Hz to 1400 Hz with a driving voltage of 950 V, as shown in Fig. 133.

The experimental results showed that both maximum flow and pressure were lower than predicted in simulations. This performance drop above 1250 Hz is attributed to limitations in the reed valves and the power electronics, which could only supply 950 V, leading to reduced power transfer to the piezo stack.

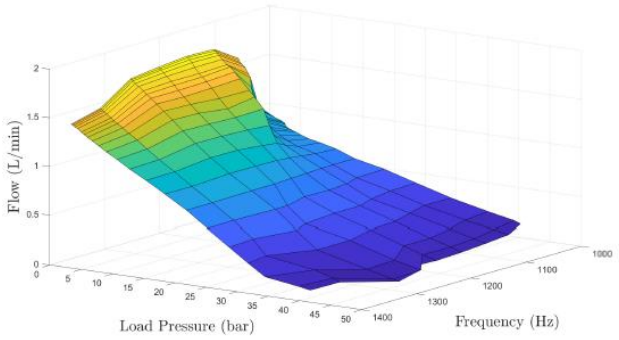

Fig. 133. Measured pressure and flow characteristics of the developed single cylinder piezohydraulic pump.

Additionally, the experimental results, as shown in Fig. 134 and Fig. 135, indicate that at a driving frequency of 1250 Hz and a mean load pressure difference of 15 bar, there is a significantly higher

positive flow compared to negative flow, with a positive peak of 4.3 L/min and an average flow rate of 1.05 L/min. The maximum chamber pressure recorded was 70 bar, which is notably higher than the average outlet pressure of 35 bar (comprising a 15 bar increase plus a 20 bar inlet pressure). This suggests a considerable pressure drop across the reed valve. This observation is further supported by the minimum pressure of 0 bar, which is significantly lower than the inlet pressure, indicating that cavitation may occur even with 20 bar of pressurization.

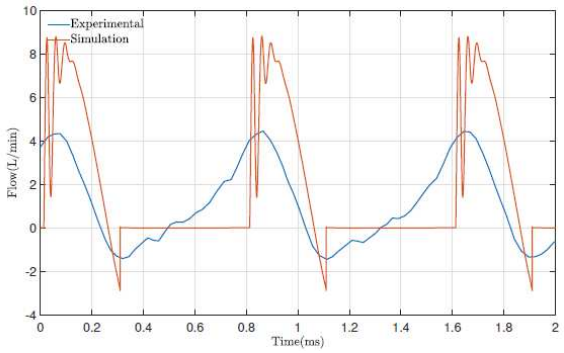

Fig. 134. Instantaneous flow leaving chamber at 1250 Hz driving frequency and mean load pressure difference of 15 bar.

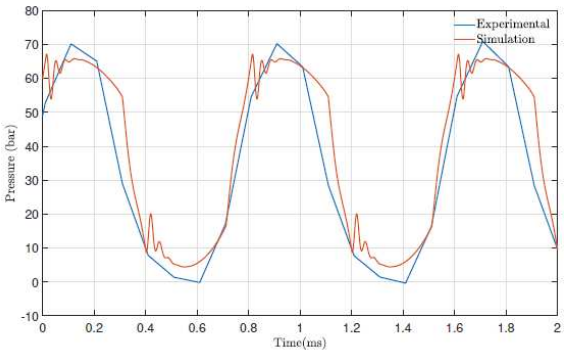

Fig. 135. Instantaneous chamber pressure at 1250 Hz driving frequency and mean load pressure difference of 15 bar.

The power delivered by the pump can be found by multiplying the differential pressure across the pump, by the measured flow. The mean output at a range of frequencies and output loads is shown in Fig. 136.

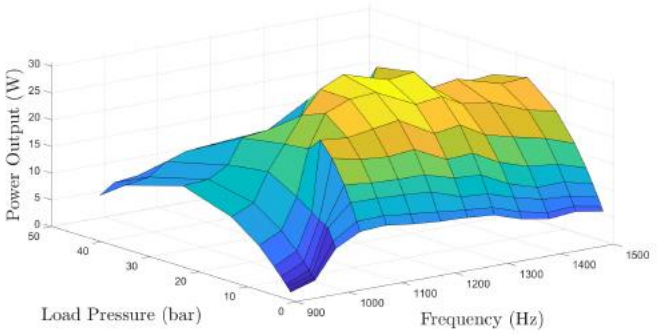

Fig. 136. Real Power Output.

These studies [271], [291] conducted by the research group of the University of Bath have achieved a significant breakthrough in piezopump output power, surpassing the target of 20 W with a demonstrated 30 W output, advancing piezohydraulic actuation for aerospace applications. Key innovations include the use of high-frequency passive reed valves and custom power electronics, both of which enhance performance while keeping the design compact. Although simulations overestimated power output, these studies offer a foundation for future improvements in multi-cylinder design.

6.6 Multi-Cylinder Piezohydraulic Pump Concept

Building on the results of the single cylinder (single pumping chamber) piezohydraulic pump previously tested, this part of the research focuses on enhancing performance by developing a multi-cylinder (multiple pumping chamber) piezohydraulic pump. Specifically, a two-cylinder piezohydraulic pump was created using the same design as the single cylinder version but incorporating two pumping units instead of one. A photo of the two-cylinder piezohydraulic pump is shown in Fig. 137.

Fig. 137. Two-cylinder piezohydraulic pump developed in collaboration with the University of Bath research group.

6.7 Modelling of a Multi-Cylinder Piezohydraulic Pump

A simple model can be used to show that a multi-cylinder pump (multiple pumping chamber) can deliver more flow than a single cylinder pump of the same total capacity. This is due to reduced flow ripple. In a single cylinder pump, the piezostack delivers the flow against high pressure peaks, which reduces its displacement and hence the average flow delivered.

If x_{max} is the free (i.e., zero load) extension of the stack caused by an applied voltage, F is the stack actuation force, and x is the actual stack extension under a combined electrical input and mechanical loading, the relationship between them is given by:

$$x = x_{max} - \frac{F}{k_{piezo}} \tag{90}$$

where k_{piezo} is the stiffness of the stack. The free displacement is proportional to the voltage, and if this is a sinusoid of angular frequency, ω, (offset to be unidirectional), the stack displacement during the delivery stroke at time, t, can be written as:

$$x = X_f(\sin(\omega t) + 1) - \frac{p_{cy}A_p}{k_{piezo}} \tag{91}$$

where X_f represents the peak free displacement, A_p the piston area, and p_{cy} the cylinder pressure. For a pump with z cylinders and equally spaced drive signal phasing, Equation (91) can be written for cylinder i as follows:

$$x = X_f(\sin\left(\omega t + \frac{2\pi i}{z}\right) + 1) - \frac{p_{cy}A_p}{k_{piezo}} \tag{92}$$

Neglecting compressibility, the delivered flow from each cylinder is:

$$\begin{aligned} Q_i &= A_p \frac{dx_i}{dt} && when\ \frac{dx_i}{dt} \geq 0 \\ Q_i &= 0 && when\ \frac{dx_i}{dt} < 0 \end{aligned} \tag{93}$$

and the total flow delivered by the multi-cylinder piezohydraulic pump is:

$$Q_{TOT} = \sum_{i=1}^{z} Q_i \tag{94}$$

Assuming ideal non-return valves and a zero pump outlet pressure, the individual cylinder pressures are also zero, and Equation (92) to Equation (94) give the pump flow shown in Fig.138. This is for a 3-cylinder pump sized to give a peak cylinder flow $X_f A_p \omega$ of 0.8 L/min.

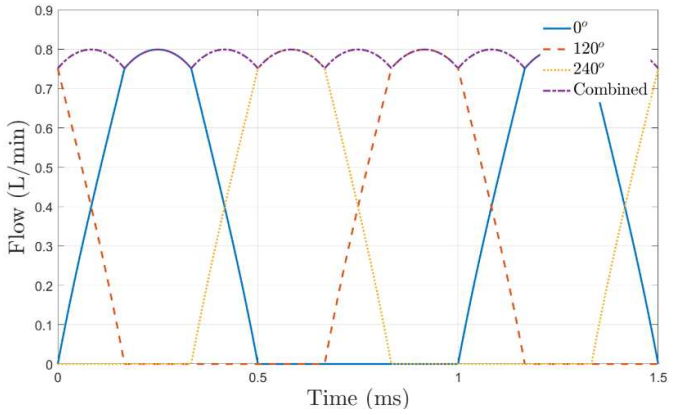

Fig. 138. Individual and summed flow from a three-cylinder piezopump model.

To perform useful work, the pump must operate against a non-zero outlet pressure. A common load is a restrictor characterised as a sharp-edged orifice where the pressure (p_{OUT}) is proportional by means of coefficient (k) to the square of the flow:

$$p_{OUT} = kQ_{TOT} \tag{95}$$

With the flow varying as shown in Fig. 138, the outlet pressure (p_{OUT}) can be described by a mean value and a ripple. The ripple amplitude is expected to decrease as the number of cylinders increases. During the delivery stroke, the stack displacement (as given by Equation (92)) will be zero as long as the cylinder pressure remains lower than the outlet pressure. In this case, the delivery non-return valve stays closed, allowing the cylinder pressure to build up accordingly:

$$p_{cy} = \frac{X_f k_{piezo}}{A_p}\left(\sin\left(\omega t + \frac{2\pi i}{z}\right) + 1\right) \qquad when\ \ p_{cy} < p_{OUT} \tag{96}$$

At other times, when the ideal non-return valve opens, the cylinder pressure equals the outlet pressure and Equation (92) becomes:

$$x_i = X_f(\sin\left(\omega t + \frac{2\pi i}{z}\right) + 1) - \frac{p_{OUT} A_p}{k_{piezo}} \tag{97}$$

Equations (93) through (97) make it possible to analyse how the number of cylinders in the pump affects the average flow output. Flow ripple, and therefore pressure ripple, impact the ability of the stacks to extend (Equation (97)) and displace fluid. Fig. 139 shows results for pumps with 1 to 5 cylinders, all designed to provide the same average flow at zero pressure and a maximum pressure of 50 bar at zero flow. The flow clearly increases with the number of cylinders up to three, especially at higher average outlet pressures. Adding more cylinders, from three to five, reduces ripple further, but the reduction with three cylinders is already small enough that it does not significantly affect the flow delivered.

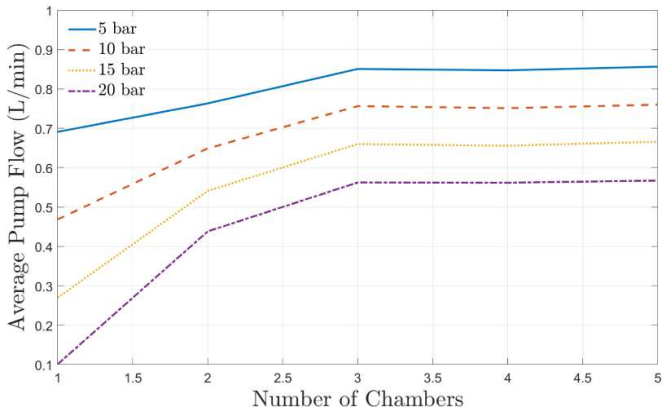

Fig. 139. Effect of number of cylinders on pump flow at different mean outlet pressures.

A simple way to represent the piezo stack electrically is as a capacitor with a parallel resistor. The capacitor's value can be taken from the manufacturer's specifications, with the resistor's value calculated to dissipate power equal to the expected mechanical power output. Fig. 140 shows the result of using this simple model for a three-cylinder pump using a 1.2 μF capacitance value, 505 W power dissipation, and stacks driven with a zero to 1 kV sine wave at 1 kHz.

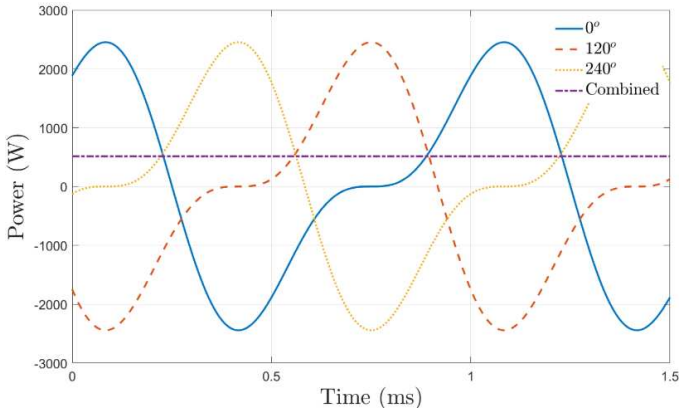

Fig. 140. Individual and summed electrical power for three piezo stacks.

The combined electrical power requirement is constant, compared to the high swings between input (positive) and returned (negative) power for the individual stacks. This makes the piezopump as a whole a significantly easier electrical load to drive. It also significantly reduces the size of the passive components needed in the power supply stage of the power electronics and, therefore, both the cost and volume.

6.8 Test rig of the Multi-Cylinder Piezohydraulic Pump

The test circuit replicated the setup used for the single cylinder prototype, with the addition of a second pumping cylinder in parallel. A schematic of this configuration is shown in Fig. 141, and the components are the same as those listed earlier in previous Table 28.

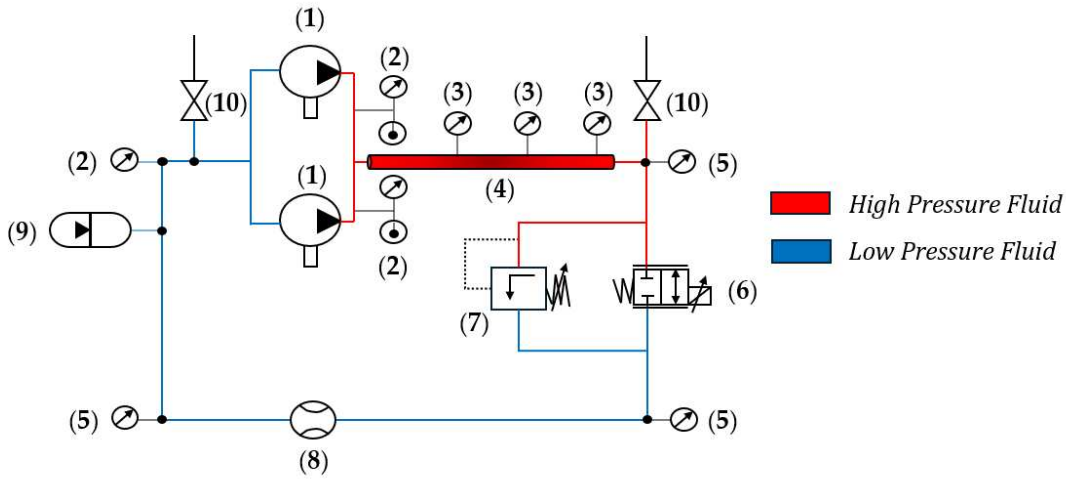

Fig. 141. Schematic of the two-cylinder piezohydrailic pump test rig with components listed in Table 28.

To confirm the effect of phasing on the pump performance, the two pump units were tested at 72°, 108°, 144°, and 180° out of phase. To protect the electronics, a peak voltage of 700 V was used in place of the stack's maximum voltage of 1000 V. This also gave a correspondingly lower current. At each phase shift, the load on the pump was varied by modulating the Moog D633 valve from fully open to fully closed in 18 geometrically spaced steps.

6.9 Experimental Results of the Multi-Cylinder Piezohydraulic Pump

As discussed above, all tests were conducted at 700 V, which is significantly lower than the voltage used in previous studies to evaluate the performance of the single cylinder piezohydraulic pump on the same test rig. Consequently, the hydraulic output is also lower for a single cylinder, as the reduced voltage results in a corresponding decrease in piston movement as shown in Fig. 142.

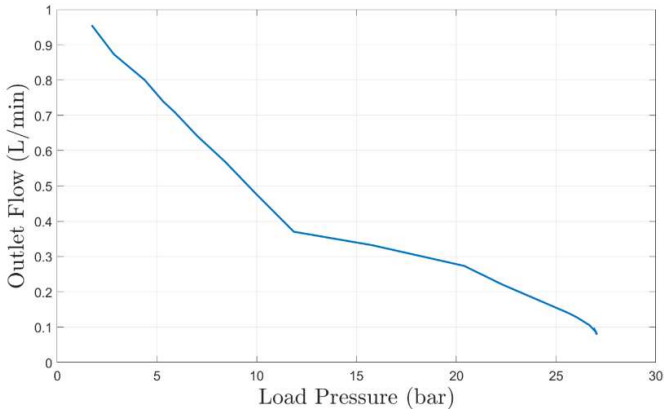

Fig. 142. Measured pressure–flow characteristics of a single cylinder unit at 700 V and 1250 Hz.

Fig. 142 is constructed from 18 experiments, with the load valve opening varied across them. The data set from one of these experiments can be seen in Fig. 143.

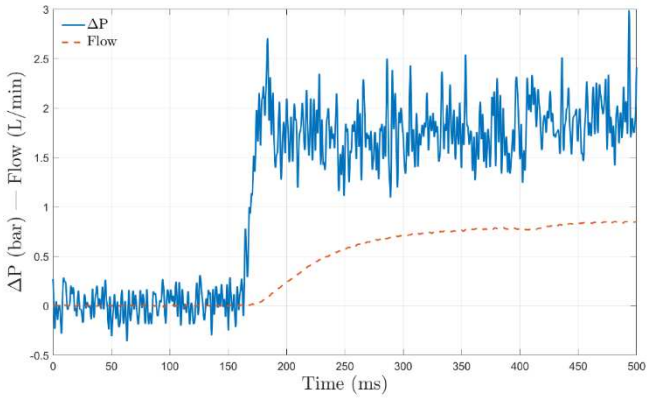

Fig. 143. Pressure difference and flow with load valve fully open, single cylinder.

When two cylinders are operated in tandem, there is a doubling of the output flow if they are operated in anti-phase, with the expected drop off in output as they move towards being in-phase. This is most notable between 144° and 72° as shown in Fig. 144.

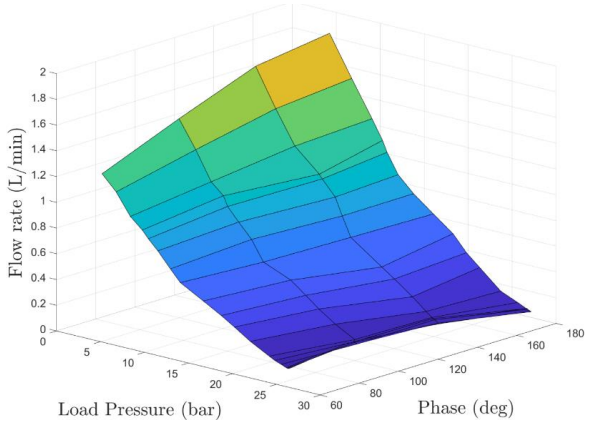

Fig. 144. Measured pressure–flow characteristic of the dual-unit piezopump at different phase shifts.

In the same way as for the single cylinder characteristics, the pressure–flow characteristics for each different phase shift are derived from 18 experiments. Fig. 145 shows the instantaneous pressure difference and flow in one of these experiments (for 180° phase shift).

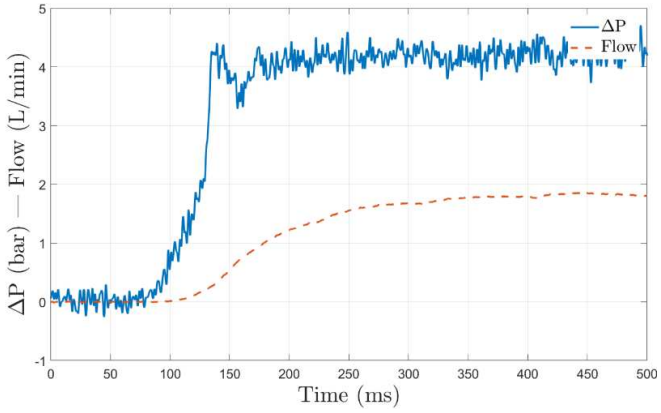

Fig. 145. Pressure difference and flow with load valve fully open and two cylinders in anti-phase.

The pressure difference at the load remains nearly constant due to the filtering effect of the fluid impedance and the compliance of the hose between the pump and pressure sensor, as well as the bandwidth limitations of the Parker PTDVB250 sensors. However, the pressure ripple at the pump outlet is effectively captured by the PCB Piezotronics sensors. Fig. 146 shows that when the cylinders operate in anti-phase, there is approximately a three-fold reduction in ripple.

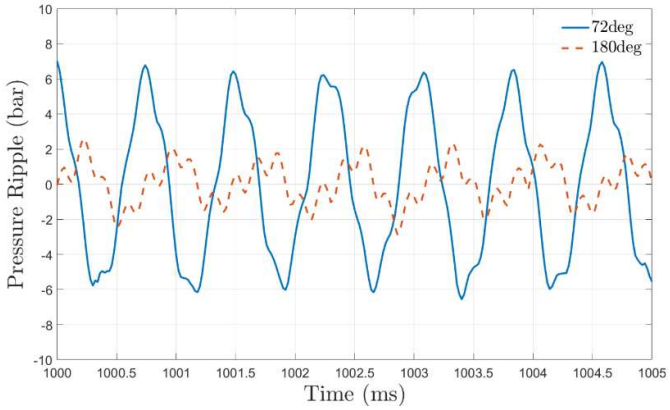

Fig. 146. Pressure ripple for the same valve opening at 72° and 180° phase.

The ability of multiple cylinders to be more effective and generate lower ripple is demonstrated in these data; however, this effect is not as strong as expected. Examining the pressure in each of the two pumping chambers, as shown in Fig. 147, offers a possible explanation.

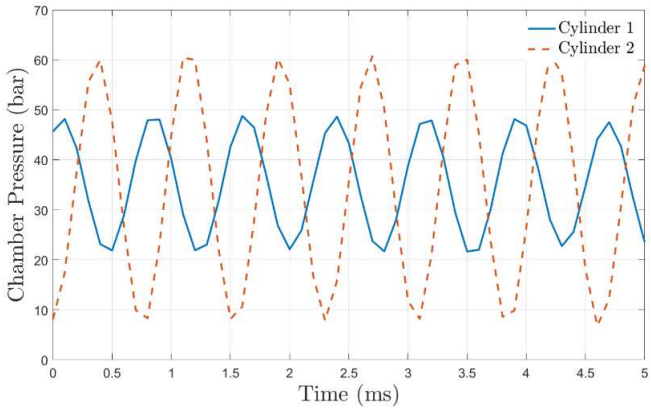

Fig. 147. Pressure of each pumping chamber.

Cylinder 1 only achieves around 65% of the pressure of cylinder 2, suggesting that, even though they are nominally identical, they are not in practice. Multi-layer PEAs, such as those used in the pumping cylinders, consist of stacked piezoelectric elements enclosed between electrodes. Existing research highlights that delamination during processing, attributed to causes such as insufficient adhesion between the electrodes and piezoelectric layers, may result in crack propagation [298]. This gives a possible explanation for the difference in the performance of the two pumping cylinders.

To investigate the potential presence of defects or the onset of fatigue damage in the two piezostack actuators, a non-destructive testing method was employed. Specifically, the impedance spectroscopy (IS) method, validated in prior research [299], [300], was utilised. If the stacks are performing as expected, they should both conform to the manufacturer's specifications and exhibit the same behaviour as one another.

Impedance spectroscopy was conducted using a Newtons4th Ltd. PSM3750 Frequency Response Analyzer. Each cylinder received a sinusoidal AC signal of 0.1 V at 100 frequency points spanning from 100 Hz to 1 MHz. This is a reasonably coarse grid of frequencies for the full identification of stack behaviour but sufficient to confirm a defect's presence.

Fig. 148 compares the impedance of the stacks, highlighting the likely presence of a defect in Stack 1.

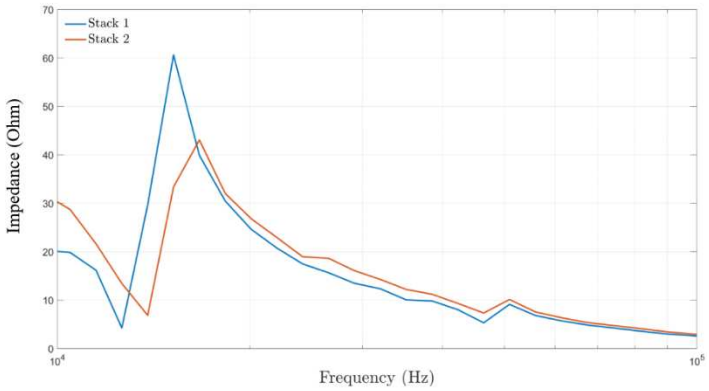

(**a**)

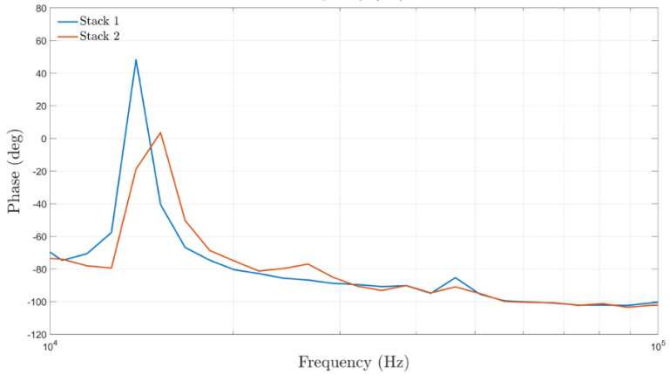

(**b**)

Fig. 148. Bode plot for the piezo stack of each pumping cylinder: (**a**) Impedance; (**b**) Phase Angle.

The shift in the resonant peak between the two cylinders is visible and amounts to 1.5 kHz, with the damaged stack having a lower peak and a higher frequency. It was found that the pre-load also affected the exact location of the resonant peak, but the frequency shift was observed at all different pre-load conditions.

Fig. 149 shows a clear increase in hydraulic power output as the pumping cylinders move closer to operating in anti-phase.

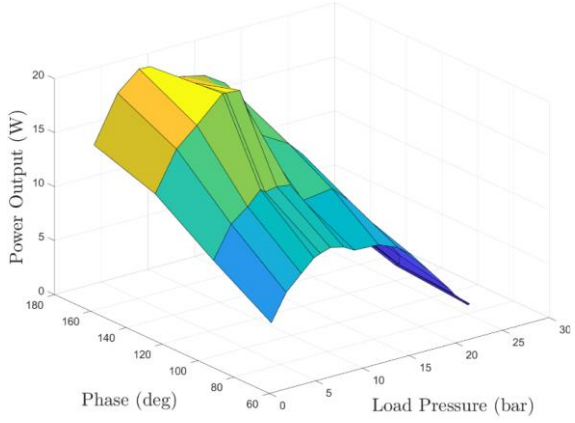

Fig. 149. Measured hydraulic power of two-cylinder piezohydraulic pump.

There is an anomaly at around 10 bar load pressure, where the 144° results show a steep improvement not seen in the other data sets. It is hypothesised that, given the difference in each cylinder's response, the addition of outputs may be improved when not in perfect anti-phase. Whilst it is believed the scale of the difference between the two piezo stacks' performance is due to damage to one of the stacks, the tolerance in the stack performance is also quite large, with the maximum displacement having tolerance of up to 30% [301]. This means that the possibility of small movements away from anti-phase, leading to improved performance, is likely to be true in general.

Although the two-cylinder piezohydraulic pump is not operating at its maximum efficiency, the test results still allow for an investigation of the power electronics behaviour when driving a multi-cylinder piezohydraulic pump. Analysis of the electrical input during the phase tests reveals a clear reduction in current ripple measured at the power supply, as shown in Fig. 150.

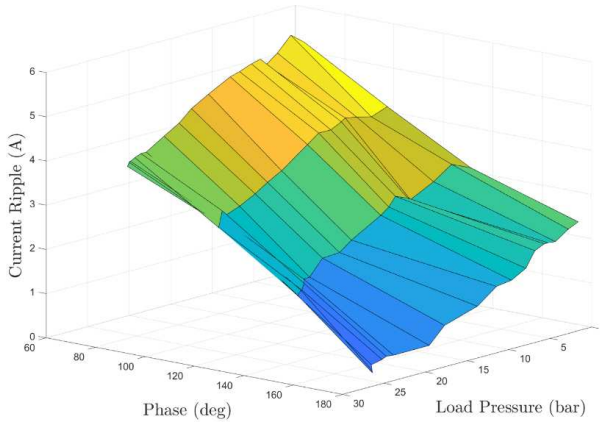

Fig. 150. Measured current ripple at power supply.

This reduction in current ripple has a knock-on effect on the stability of the voltage from the boost converter, as shown in Fig. 151, with a five-fold reduction in the voltage ripple in the condition plotted.

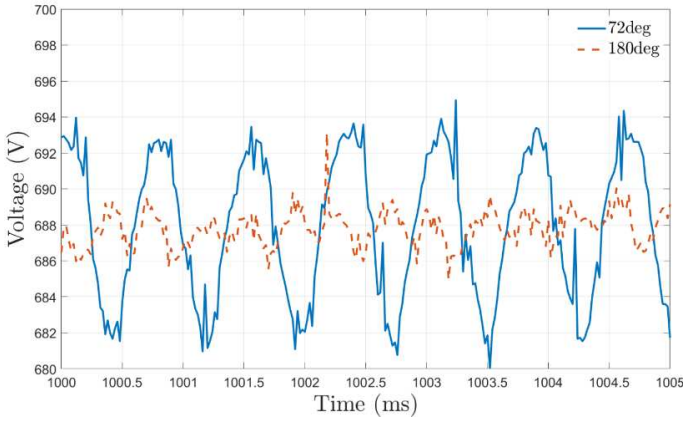

Fig. 151. Voltage at output of boost stage power electronics.

Unlike the hydraulic power results, there is a consistent improvement as the stack drive signals approach anti-phase. The pump's power factor also steadily increases as the cylinders move towards anti-phase, with a three-fold increase between 72° and 180°, as shown in Fig. 152.

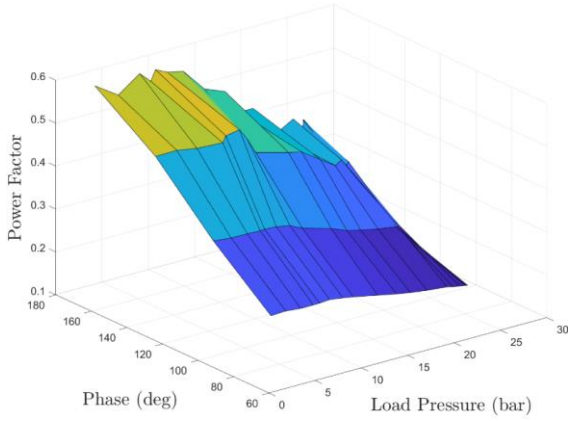

Fig. 152. Pump power factor at different phase shifts and loads.

6.10 Discussion

To increase power from piezopumps, it was necessary to increase the number of cylinders within each pump, as a practical limit exists on the size of a single stack. It was suggested that this approach would also improve pump performance beyond what a simple increase in capacity would predict. A basic simulation showed that multiple parallel-connected cylinders operating with equally spaced phasing led to increased flow output by reducing ripple. It was also demonstrated that this configuration improved electrical power quality, as the large current swings from each stack cancelled out across the overall pump.

These hydraulic and electrical improvements were validated experimentally using a two-cylinder piezohydraulic pump, which showed a significant advantage in hydraulic flow and power output over a single cylinder pump. However, differences in the behaviour of the two piezo stacks introduced some deviations from expected performance.

This work [51], conducted during the visiting Ph.D. period at the University of Bath (UK), demonstrated that a piezopump could deliver sufficient flow and pressure to drive a hydraulic actuator in the tens-of-watts power range. In the context of piezopumps, this represented a high-power output, and the benefits of a multi-cylinder design were clearly demonstrated at this power level, highlighting its potential for aerospace applications, such as landing gear actuation.

Future pump development will focus on testing a three-cylinder piezohydraulic pump and further refining the power electronics by optimizing them for a reduced operating range to ensure load stability.

7. PIEZOHYDRAULIC PUMP CAVITATION ANALYSIS

Despite the high performance demonstrated in Chapter 6, the single cylinder piezohydraulic pump design developed at the University of Bath—featuring a piezo stack driving a piston at high frequency and a pair of passive reed valves regulating flow in and out of the pumping chamber—has shown to be prone to cavitation, as indicated by the experimental results. Cavitation can lead to component damage, reduced efficiency, and noise generation.

In response to this, this part of the research project presents a numerical investigation using a CFD software (Ansys Fluent) to assess the potential for cavitation in this specific single cylinder piezohydraulic pump. The study focuses on simulating various oil flow scenarios through the pump with a fixed inlet pressure of 20 bar, while varying the opening of the inlet reed valve from its minimum (0.1 mm) to maximum (0.7 mm) values, and adjusting the pump chamber pressure.

The findings of this study were presented at important international [46] and national [47] conferences on fluid power.

7.1 Computational Fluid Dynamic (CFD) Analysis

7.1.1 Simplified Model for Cavitation Investigation

The experimental results of the single cylinder piezohydraulic pump developed at the University of Bath showed that at an operating frequency of 1250 Hz and a mean load pressure difference of 15 bar, the minimum chamber pressure dropped to approximately 0 bar [271]. This value was significantly lower than the inlet pressure of 20 bar, suggesting the potential occurrence of cavitation due to the high pressure drop across the inlet reed valve. Since cavitation within the piezohydraulic pump is difficult to confirm visually, its occurrence must be further studied through detailed CFD analysis.

The CFD analysis of the piezohydraulic pump began with the creation of a 3D model using Autodesk Inventor Professional, as shown in Fig. 153a.

To better understand the operating conditions that might lead to cavitation during the intake stage, particularly focusing on the different openings of the inlet reed valve, the 3D model was simplified into a 2D model through three key approximations:

1. Creating a Simplified 3D Domain: Two cutting planes were marked on the 3D model to create a simplified 3D domain, as shown in Fig. 153b. This domain includes the oil within the inner part of the ring stack, the twelve piston orifices, and part of the pumping chamber, as depicted in Fig. 153c. The oil between the ring stack actuator and the pump body was omitted because it is not influential in analysing cavitation.

2. Considering Geometry Axial Symmetry: Due to the axial symmetry of the pump's geometry, only a slice of this simplified 3D domain was examined. This slice contains the oil flowing into one of the twelve piston orifices, highlighted in green in Fig. 153c.
3. Focusing on the Mid-Plane Section: The analysis focused only on the mid-plane section of this slice to investigate potential cavitation scenarios, leading to the development of the 2D simplified model system of the piezohydraulic pump, illustrated in Fig. 153d.

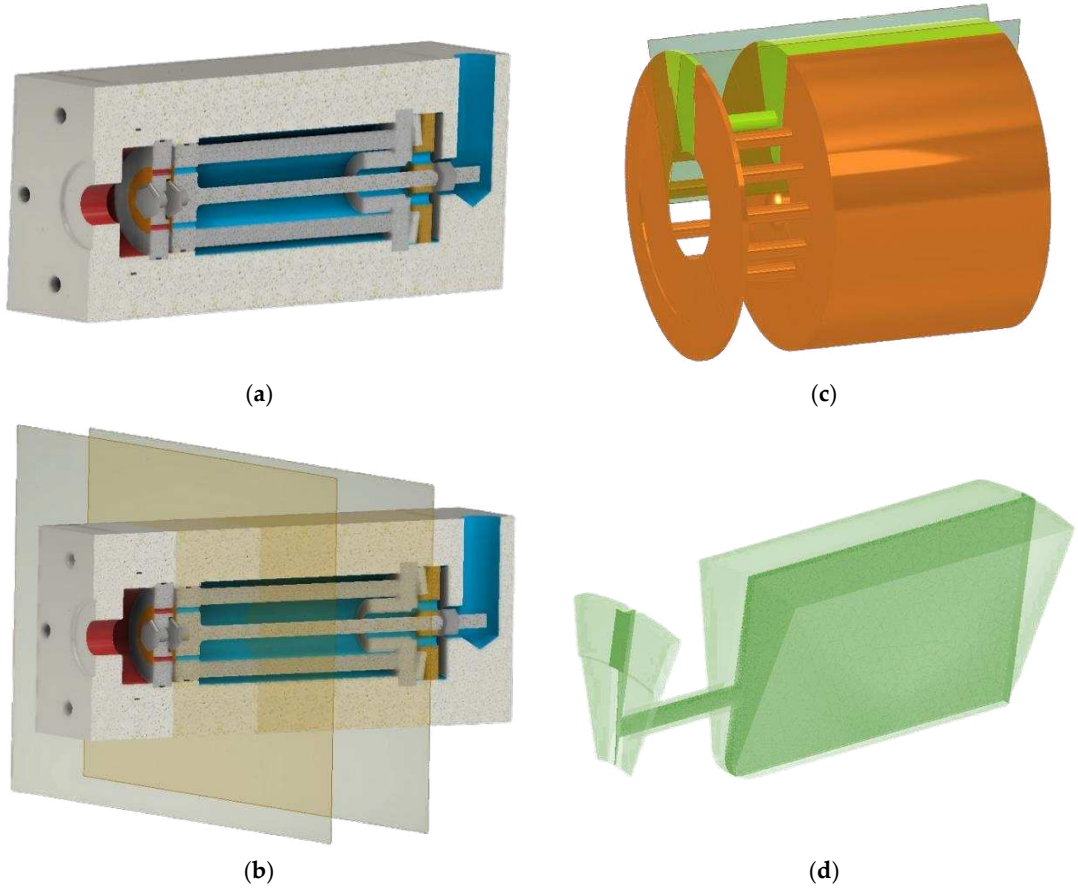

Fig. 153. Piezohydraulic pump developed at the University of Bath [271]: (**a**) 3D model created using Autodesk Inventor Professional; (**b**) Two cutting planes used to simplify the 3D domain; (**c**) Oil included in the simplified 3D domain, with the slice due to axial symmetry highlighted in green; (**d**) 2D model system resulting from the mid-plane section of the slice.

7.1.2 Computational Mesh

The 2D model system, based on previous considerations, was discretized using Cadence Fidelity Pointwise. Unstructured meshes, composed of triangular elements with explicit connectivity, were employed in this analysis for their flexibility and automation in the generation process [302]. The grid was created for all possible openings of the inlet reed valve, ranging from 0.1 mm (minimum value) to 0.7 mm (maximum value) in 0.1 mm increments.

For non-restricted parts of the pump, the mesh setup used fewer than 25 points, resulting in large interval sizes from 0.1 mm to 0.9 mm. In contrast, for the edges of the piston orifice and the inlet reed valve, more than 1,000 points were used, creating very small interval sizes from 0.0025 mm to 0.01 mm. This detailed approach aimed to identify pressure and velocity gradients and flow swirls to predict potential cavitation during the intake stage, when oil flows through the small passage uncovered by the inlet reed valve opening.

After discretizing all edges, the entire flow domain was meshed for the seven different cases corresponding to the seven different openings of the inlet reed valve. Fig. 154 provides images of three of the seven computational meshes of the 2D pump model system, specifically for inlet reed valve openings of 0.1 mm, 0.4 mm, and 0.7 mm. It is important to note that the seven computational meshes each uses fewer than 57,000 total cells, resulting in a relatively low computational cost for obtaining the CFD simulations.

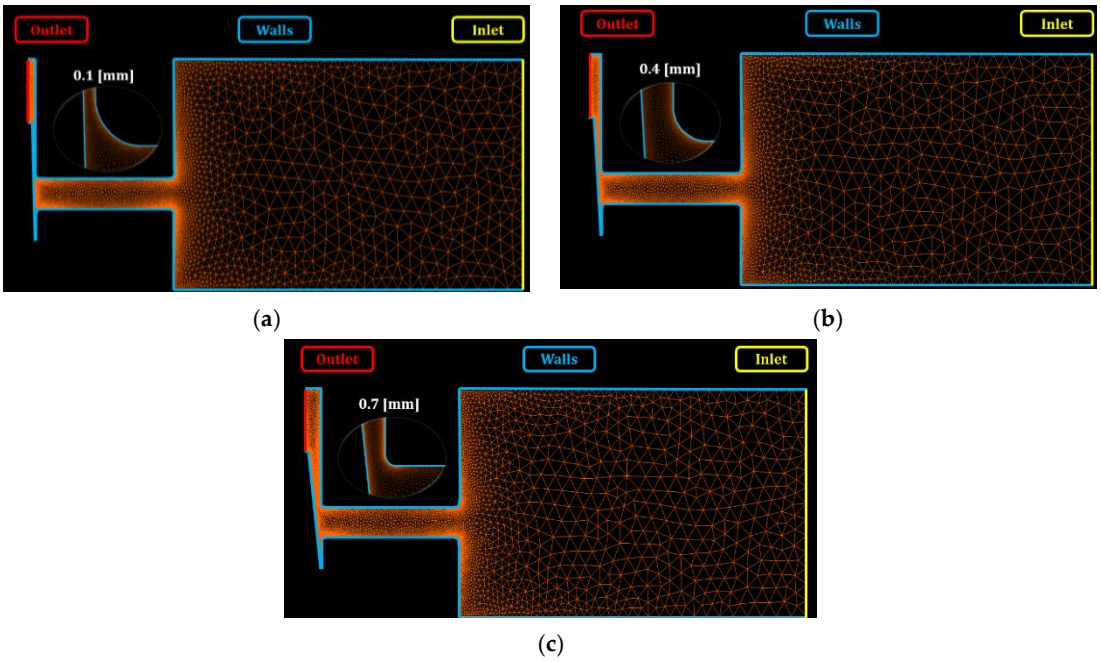

Fig. 154. Computational mesh of the 2D pump model system for three different openings of the inlet reed valve: (**a**) 0.1 mm; (**b**) 0.4 mm; (**c**) 0.7 mm.

Finally, Table 29 provides a detailed description of the boundary conditions set before exporting the seven computational grids.

Table 29. Boundary conditions.

Zone/Line	Boundary Condition	Description
Inlet	Pressure Inlet (p_{in})	Fixed Pressure at the pump inlet
Outlet	Pressure Outlet (p_{cham})	Pressure value set in the pumping chamber during intake stage
Walls	–	Lines in the 2D meshed model system defining the walls
Oil Zone	–	Area bounded by the inlet, outlet, and walls.

7.1.3 Governing Equations

The seven computational grids were imported into Ansys Fluent for CFD simulations.

For solving, the semi-implicit method for pressure-linked equations (SIMPLE) pressure-based segregated algorithm was selected. Among the available segregated algorithms in Ansys Fluent (including SIMPLE, SIMPLEC, PISO), the SIMPLE algorithm was chosen for this problem based on its suitability for the physics involved.

To predict cavitation, three main methods can be employed, namely the multiphase flow model, the homogeneous equilibrium model, and the interface tracking model [303], [304], [305]. In this study, since the main focus is on severe variation of density, the multiphase flow model is chosen. Specifically, the Schnerr and Sauer equations were used for simulating cavitation in a multiphase flow, as well documented in [306].

Vapour was treated as incompressible. Specifically, in the numerical model, vapour phase exists only when pressure values are below the vapour pressure, enabling vapour density to be assumed constant. The liquid oil was set with a density of 866 kg/m³ and a dynamic viscosity of 0.027 kg/(m·s), while the vapour oil was set with a density of 4 kg/m³ and a dynamic viscosity of $3 \cdot 10^6$ kg/(m·s).

In CFD programs, there are several turbulence models available, including the standard $k-\varepsilon$, RNG $k-\varepsilon$, realizable $k-\varepsilon$, and SST $k-\omega$ models [307]. The choice of turbulent model significantly affects the accuracy of simulation results. Studies have shown that the SST $k-\omega$ model provides reliable results with an error margin of around +/- 5% [308]. Therefore, in this study, the SST $k-\omega$ method was employed to predict turbulence.

The turbulence equations for k and ω, as well as the momentum equations, were solved initially using a first-order upwind discretization and then a second-order upwind discretization to stabilize the simulation. For pressure interpolation, the PRESTO! scheme, specifically designed for flows with steep pressure gradients, was selected [309]. Additionally, a first-order upwind scheme was employed for the discretization of the vapor transport equation.

Regarding the termination criterion, it was decided to stop the simulations when the mass flow rate maintained its third significant digit unchanged, rather than terminating iterations based on scaled residuals falling below a fixed value. This computational strategy ensured accurate prediction of potential cavitation within the pump chamber. Approximately 5,000 iterations (2,000 using first-order upwind discretization and 3,000 using second-order upwind discretization) were required to

fulfil the convergence criterion without encountering any convergence issues. Table 30 presents the scaled residuals recorded for a simulated inlet reed valve opening $v_{opn_{min}} = 0.1$ mm. Table 31 below summarizes all the conditions that were configured in Ansys Fluent for obtaining these simulations.

Table 30. Scaled residuals after 5,000 iterations (opening inlet reed valve condition $\mathrm{v_{opn_{min}}} = 0.1$ mm).

Equation	Scaled residual
Continuity	9.01 e^{-07}
x-Momentum	2.23 e^{-07}
y-Momentum	2.69 e^{-07}
k	2.16 e^{-08}
ω	5.77 e^{-08}
Vapour	0

Table 31. Setting employed for the simulations.

Equation	Multiphase (Mixture) Model
Solver	SIMPLE
Turbulence Model	SST k-ω
Cavitation Model	Schnerr and Sauer
Discretization of Pressure Equation	PRESTO!
Discretization of Volume Fraction	First order upwind
Discretization of Momen. and Turbulence	Second order upwind
Under-relaxation of Pressure	0.3
Under-relaxation of Volume Fraction	0.5
Under-relaxation of Momentum	0.7
Under-relaxation of Turbulence Quantities	0.8
Inlet Pressure (p_{in})	20 bar absolute
Chamber Pressure (p_{cham})	Variable
Density and Viscosity Liquid-Oil	866 kg/m^3; 0.027 kg/(m·s)
Density and Viscosity Vapour-Oil	4 kg/m^3; $3 \cdot 10^{-06}$ kg/(m·s)
Vapour Pressure	10 Pa
Bubble Number Density	Default
Termination Criterion	Convergence in Mass-Flow Rate (third digit)

7.2 CFD Simulation Results

In this 2D simplified analysis, simulations aimed to assess potential scenarios that could trigger cavitation by considering a fixed inlet pump pressure of p_{in} =20 bar. The simulations varied the openings of the inlet reed valve (v_{opn}) from 0.1 mm (minimum value) to 0.7 mm (maximum value) in increments of 0.1 mm. Additionally, different plausible values of the pumping chamber pressure (p_{cham}) during the intake stage, derived from experimental pump results, were considered.

Specifically, for each opening degree of the inlet reed valve, the simulations started by setting a very low pumping chamber pressure (0.5 bar) and increased it by 0.5 bar increments until a specific pumping pressure value no longer caused additional cavitation. Therefore, several steady-state scenarios regarding the intake stage were analysed. It is also important to note that these simulations were conducted with a relative pressure of 1.01 bar in mind.

Fig. 155 and Fig. 156 display the CFD simulation results depicting the velocity contour, pressure contour, and volume fraction of the vapour oil phase for an inlet reed valve opening v_{opn}= 0.4 mm and two different pumping chamber pressures, specifically p_{cham} = 2 bar and p_{cham} = 5 bar, respectively. Upon analysing Fig. 155 and Fig. 156, it becomes evident that the pumping chamber pressure significantly influences the velocity and pressure fields within the 2D oil domain for a fixed inlet reed valve opening. Specifically, the lower pumping chamber pressure (p_{cham} = 2 bar) caused a higher pressure drop across the inlet reed valve, resulting in a greater increase in average oil velocity near the restriction area, with a maximum computed value of 69.7 m/s. Consequently, local pressure values dropped below the vapour pressure, triggering vapour oil phase formation and subsequent cavitation. Additionally, it is important to note that both pumping chamber pressures considered (p_{cham} = 2 bar and p_{cham} = 5 bar) led to vapour oil phase formation and then cavitation; however, the higher pumping chamber pressure (p_{cham} = 5 bar) resulted in a reduced area of the vapour oil phase.

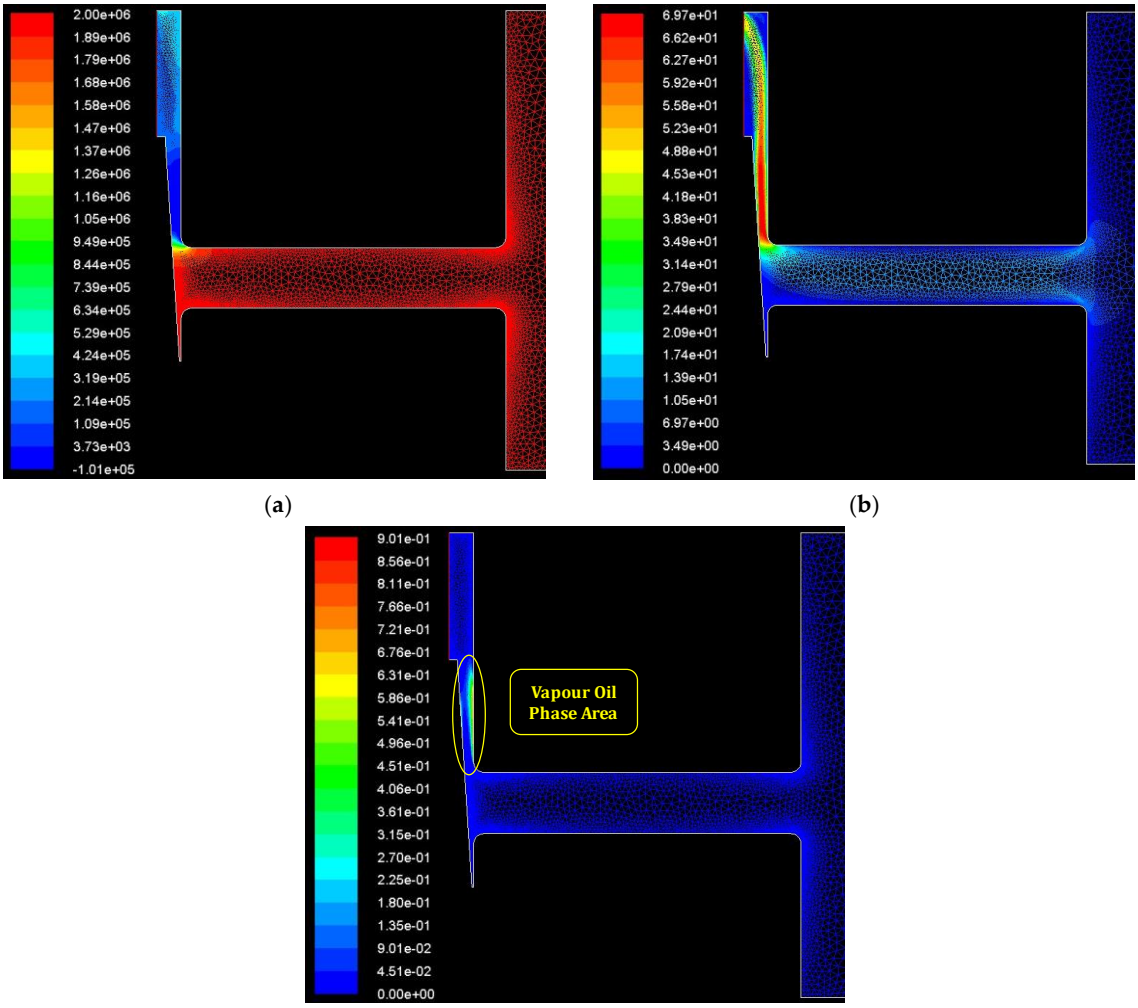

Fig. 155. CFD simulation results considering p_{in} = 20 bar, v_{opn} = 0.4 mm and p_{cham} = 2 bar: (**a**) Pressure Contour [Pa]; (**b**) Velocity Contour [m/s]; (**c**) Volume fraction of vapour oil phase [-].

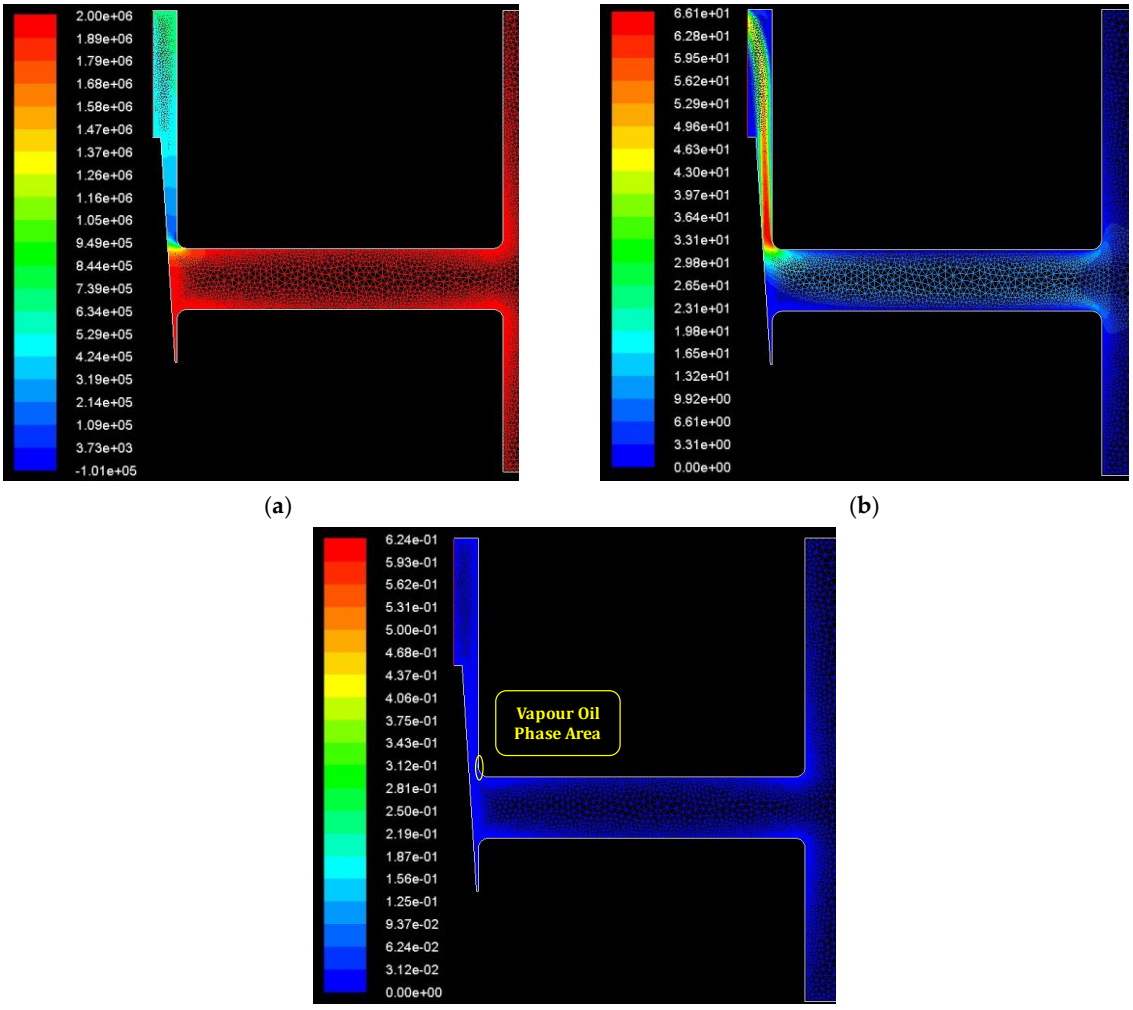

Fig. 156. CFD simulation results considering p_{in} =20 bar, v_{opn} = 0.4 mm and p_{cham} = 5 bar: (**a**) Pressure Contour [Pa]; (**b**) Velocity Contour [m/s]; (**c**) Volume fraction of vapour oil phase [-].

To analyse the effect of varying both the inlet reed valve opening v_{opn} and chamber pressure p_{cham}, Fig. 157 and Fig. 158 illustrates that as the opening of the inlet reed valve increases and the chamber pressure decreases, both the area of the vapour oil phase and the volume fraction of vapour oil also increase. This trend potentially leads to higher occurrences of cavitation because the decreasing chamber pressure, combined with an increased inlet reed valve opening, causes an increase in average velocity near the restricted area, leading to lower local pressure values and triggering cavitation, as shown in Fig. 159.

The semi-logarithmic plots in Fig. 157b and 158b provide a better understanding of the extremely low values of the vapor oil phase area and volume vapor oil fraction that can be achieved for specific input conditions (v_{opn} and p_{cham}).

Additionally, Fig. 157, 158, and 159 show that despite the minimum value of pumping chamber pressure considered (p_{cham} = 0.5 bar), very low openings of the inlet reed valve (v_{opn} = 0.1 mm and

v_{opn} = 0.2 mm), do not trigger vapor phase formation since the maximum average oil velocity near the restricted area in both cases is lower than 60 m/s, which can be considered a threshold value for triggering cavitation.

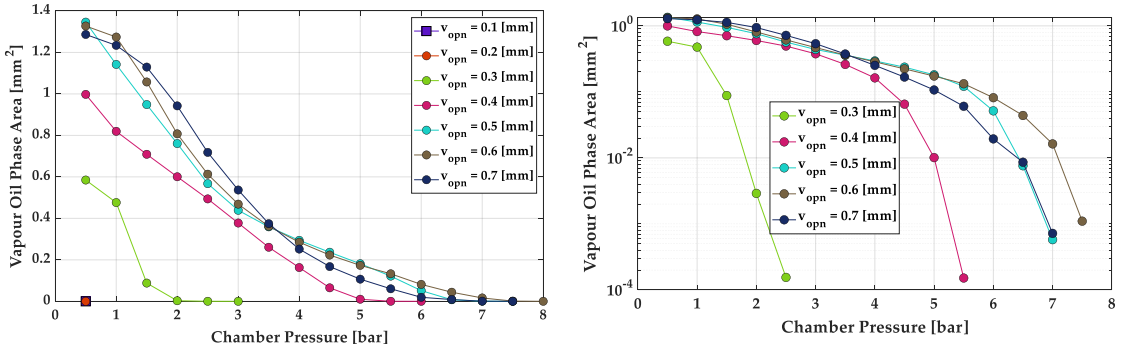

(**a**) (**b**)

Fig. 157. Vapour oil phase area mm² with p_{in} = 20 bar, varying v_{opn} from 0.1 mm to 0.7 mm (increments of 0.1 mm) and p_{cham} (increment of 0.5 bar starting from 0.5 bar): (**a**) Normal Plot; (**b**) Semi-logarithmic Plot.

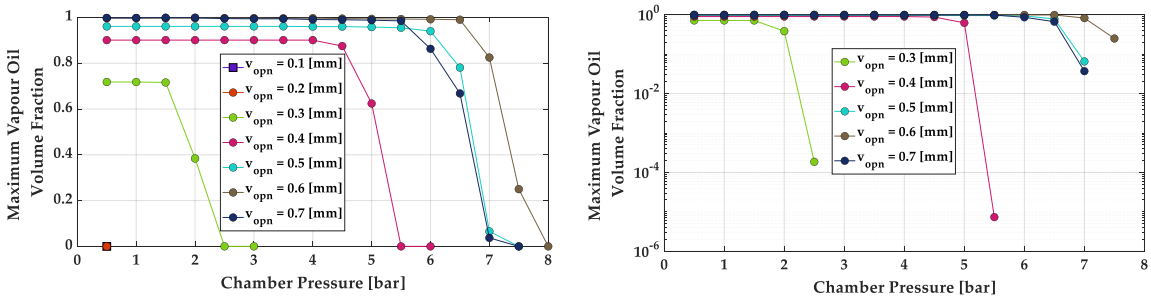

(**a**) (**b**)

Fig. 158. Vapour oil volume fraction with p_{in} = 20 bar, varying v_{opn} from 0.1 mm to 0.7 mm (increments of 0.1 mm) and p_{cham} (increment of 0.5 bar starting from 0.5 bar): (**a**) Normal Plot; (**b**) Semi-logarithmic Plot.

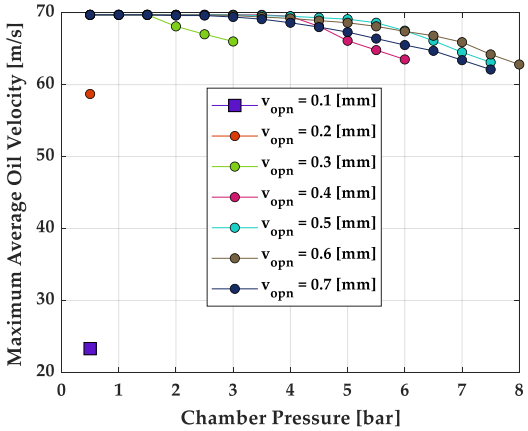

Fig. 159. Maximum average oil velocity near the restricted area m/s with p_{in} = 20 bar, varying v_{opn} from 0.1 mm to 0.7 mm (increments of 0.1 mm) and p_{cham} (increment of 0.5 bar starting from 0.5 bar).

Finally, Fig. 160 presents a heatmap illustrating all potential cavitation scenarios. As previously explained, these scenarios are explored by maintaining a fixed inlet pressure of p_{in} =20 bar while varying both the opening degree of the inlet reed valve (v_{opn}) and the pumping chamber pressure (p_{cham}). The graph analysis reveals that larger openings of the inlet reed valve result in higher average oil flow velocity near the restricted area. This increased velocity leads to greater pressure drops, which can potentially trigger cavitation.

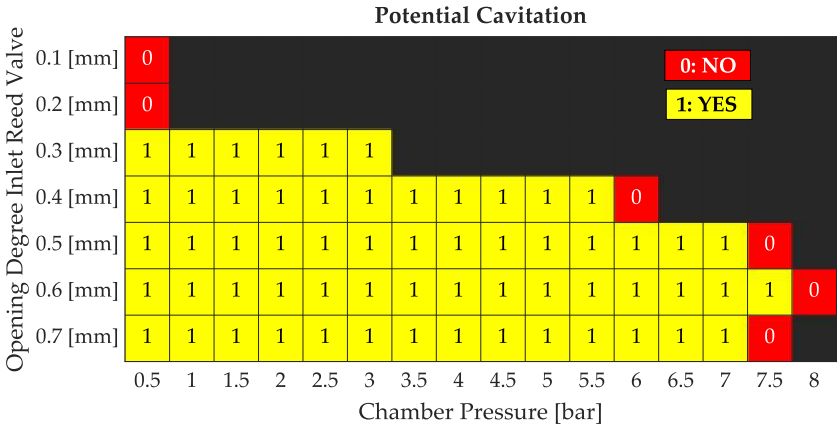

Fig. 160. Possible cavitation scenarios considering p_{in} = 20 bar and varying v_{opn} from 0.1 mm to 0.7 mm (increments of 0.1 mm) and p_{cham} (increment of 0.5 bar starting from 0.5 bar).

In conclusion, it is important to note that, to validate our CFD analysis, these simulations should also be conducted using the simplified 3D domain rather than a mid-plane section of a slice of this 3D simplified domain in order to better capture the three-dimensional nature of the fluid flow. The mid-plane section (2D domain) was used solely to assess potential cavitation scenarios.

The next step of this research work will be to compare the mean flow rate obtained from experimental tests (over a complete cycle) with the flow rate derived from the mean values of the 3D simplified model, which will be discretized and simulated again using Ansys Fluent. This comparison will account once again for all possible inlet reed valve openings and different pumping chamber pressures to evaluate various steady-state scenarios during the intake stage.

7.3 Discussion

These latter studies [46], [47] within this research project initiated an investigation into the cavitation potential in the piezohydraulic pump developed at the University of Bath (UK), utilizing CFD simulations in Ansys Fluent. These simulations were performed with a fixed inlet pressure of p_{in} = 20bar while varying the inlet reed valve openings (v_{opn}) from 0.1 mm to 0.7 mm in 0.1 mm increments. Different values of pumping chamber pressure (p_{cham}) during the intake stage were also examined. For each inlet valve opening, simulations started at a low chamber pressure (0.5 bar) and increased it by 0.5 bar increments until reaching a threshold where additional cavitation was no longer observed.

The CFD results showed that as the valve opening increased and chamber pressure decreased, the vapor oil phase area and vapor volume fraction also increased, leading to higher cavitation risk due to elevated oil velocity near the restricted area.

Future developments will aim to validate the CFD model by comparing its flow characteristics with experimental data from pump testing.

8. CONCLUSION AND FUTURE DEVELOPMENTS

This PhD research focused on using PEAs to create advanced systems for servovalves and pumps. The goal was to solve long-standing problems in traditional designs and open up new possibilities for fluid power applications.

A detailed numerical model of an aircraft fuel system revealed that conventional servovalves consume a lot of power, highlighting the need for more efficient designs of these critical control components, which are extensively used in various industrial and aeronautical applications. To address this, a novel direct-drive servovalve architecture was developed, replacing conventional LFMs with APAs. Different schemes using one or two APAs were proposed. The simplest setup, where a single APA pushes and pulls the spool within its bushing sleeve, was simulated realizing a Simulink model. Compared to conventional servovalves, this innovative design offers advantages such as a simpler structure, faster response, lighter weight, and improved dynamic performance. However, it also has limitations, including the low shear force of APAs and their relatively high cost. Even so, the potential for cost reduction through large-scale production makes this solution promising for industrial use.

The research also explored digital hydraulic technology, introducing HFSVs in 2/2 and 4/2 configurations. These valves, powered by ring stack actuators and controlled via PWM technique, were modelled using well-established equations in Simulink environment. Compared to conventional spool valves, including proportional and servovalves, the proposed HFSVs offer several advantages, such as lower power consumption due to their poppet design, faster response times, and the ability to handle high flow rates with minimal pressure drops. These features make them a promising solution for integrating digital hydraulics into industrial and aerospace applications while enhancing the energy efficiency of hydraulic systems. Nonetheless, challenges persist, including the large size of the PEA and the requirement for a high-performance amplifier to ensure effective operation.

Significant advancements were also made in the development of piezohydraulic pumps, particularly with the multi-cylinder design, which showed clear advantages over the single cylinder configuration. A ring stack actuator was again selected as the driving power source for fluid delivery. The prototype, built and tested at the University of Bath, revealed that when the cylinders operated in anti-phase, notable improvements were achieved in reducing pressure and current ripple, optimizing the driving signal voltage, and increasing the output flow rate. This multi-cylinder piezohydraulic pump represents a milestone in piezoelectric pump technology, delivering power output in the ten-watt range and making it suitable for aerospace applications such as landing gear actuation. However, a critical challenge identified was the risk of cavitation due to the high-pressure drop across the inlet reed valve, despite a pressurization of 20 bar.

Looking ahead, future work will focus on several key areas. First, the innovative valve designs developed during this research will be tested at the Polytechnic University of Bari to validate the promising numerical results achieved. Additionally, further efforts will be directed toward testing a three-cylinder piezohydraulic pump to assess its performance. Work will also focus on optimizing the power electronics of the multi-cylinder piezohydraulic pump to improve load stability and overall performance, especially within a restricted operating range. Lastly, a more comprehensive CFD analysis will be conducted on Ansys Fluent to better understand the cavitation effects in these innovative pumps.

By addressing these challenges and building on the progress made, the next steps will be crucial for advancing the practical application and commercialization of piezoelectric-based systems, ultimately enabling their widespread use in industries such as aerospace and robotics, and advancing high-performance fluid power technologies.

REFERENCES

[1] P. Tamburrano, F. Sciatti, A. R. Plummer, E. Distaso, P. De Palma, and R. Amirante, "A review of novel architectures of servovalves driven by piezoelectric actuators," *Energies (Basel)*, vol. 14, no. 16, p. 4858, 2021.

[2] F. Sciatti, P. Tamburrano, E. Distaso, and R. Amirante, "Digital hydraulic valves: Advancements in research," *Heliyon*, 2024.

[3] "International Civil Aviation Organization Industry High Level Group (2019), Aviation Benefits Report 2019. https://www.icao.int/sustainability/Documents/AVIATION-BENEFITS-2019-web.pdf. Accessed July 30, 20224."

[4] D. S. Lee *et al.*, "The contribution of global aviation to anthropogenic climate forcing for 2000 to 2018," *Atmos Environ*, vol. 244, p. 117834, 2021.

[5] H. J. Undertaking, "Hydrogen powered aviation: A fact-based study of hydrogen technology, economics, and climate impact by 2050," 2020.

[6] K. Oesingmann, W. Grimme, and J. Scheelhaase, "Hydrogen in aviation: A simulation of demand, price dynamics, and CO2 emission reduction potentials," *Int J Hydrogen Energy*, vol. 64, pp. 633–642, 2024.

[7] S. Gössling and A. Humpe, "The global scale, distribution and growth of aviation: Implications for climate change," *Global Environmental Change*, vol. 65, p. 102194, 2020.

[8] D. S. Lee *et al.*, "Aviation and global climate change in the 21st century," *Atmos Environ*, vol. 43, no. 22–23, pp. 3520–3537, 2009.

[9] J. Kotcher, E. Maibach, and W.-T. Choi, "Fossil fuels are harming our brains: identifying key messages about the health effects of air pollution from fossil fuels," *BMC Public Health*, vol. 19, pp. 1–12, 2019.

[10] J. Rohacs, U. Kale, and D. Rohacs, "Radically new solutions for reducing the energy use by future aircraft and their operations," *Energy*, vol. 239, p. 122420, 2022.

[11] L. W. Mays, "A very brief history of hydraulic technology during antiquity," in *Environmental Fluid Mechanics*, 2008, pp. 471–484. doi: 10.1007/s10652-008-9095-2.

[12] M. Papoutsidakis, A. Chatzopoulos, D. Papachristos, and C. Drosos, "Hydraulics and Pneumatics: Operational Characteristics and Control for Modern Industry Applications," *Int J Comput Appl*, vol. 178, no. 25, pp. 31–40, Jun. 2019, doi: 10.5120/ijca2019919049.

[13] J. Mokyr *et al.*, "Knowledge, Technology, and Economic Growth During the Industrial Revolution," 2000.

[14] M. G. El-Din and M. Rabi, *Fluid Power Engineering*, First edition. New York: McGraw-Hill Education, 2009. [Online]. Available: https://www.accessengineeringlibrary.com/content/book/9780071622462

[15] Moog, "Proportional and Servo Valve Technology," 2003.

[16] T. Hunt and N. Vaughan, "The Hydraulic Handbook," *Elsevier*, 1996.

[17] P. Tamburrano, A. R. Plummer, E. Distaso, and R. Amirante, "A review of direct drive proportional electrohydraulic spool valves: Industrial state-of-the-art and research advancements," *Journal of Dynamic Systems, Measurement and Control, Transactions of the ASME*, vol. 141, no. 2, Feb. 2019, doi: 10.1115/1.4041063.

[18] R. Amirante, P. G. Moscatelli, and L. A. Catalano, "Evaluation of the flow forces on a direct (single stage) proportional valve by means of a computational fluid dynamic analysis," *Energy Convers Manag*, vol. 48, no. 3, pp. 942–953, 2007.

[19] B. Jin, Y. Zhu, W. Li, D. Zhang, L. Zhang, and F. Chen, "A differential control method for the proportional directional valve," *Journal of Zhejiang University SCIENCE C*, vol. 15, pp. 892–902, 2014.

[20] R. Amirante, A. Innone, and L. A. Catalano, "Boosted PWM open loop control of hydraulic proportional valves," *Energy Convers Manag*, vol. 49, no. 8, pp. 2225–2236, 2008.

[21] P. Tamburrano, A. R. Plummer, E. Distaso, and R. Amirante, "A review of electro-hydraulic servovalve research and development," *International Journal of Fluid Power*, vol. 20, no. 1, pp. 53–98, 2019, doi: 10.13052/ijfp1439-9776.2013.

[22] A. Plummer, "Electrohydraulic servovalves – past, present, and future.," in *Proc 10th International Fluid Power Conference*, 2016.

[23] Irwin E. Treager, *Aircraft Gas Turbine Engine Technology* . 1995.

[24] B. Wang, H. Ji, and Z. Ye, "Simulation on Fuel Metering Unit Used for TurboShaft Engine Model," *International Journal of Energy and Power Engineering*, vol. 13, no. 1, pp. 1–7, 2019.

[25] D. Li, J. Hang, Y. Li, and S. Dong, "Fuel Flowrate Control for Aeroengine and Fuel Thermal Management for Airborne System of Aircraft—An Overview," *Applied Sciences*, vol. 12, no. 1, p. 279, 2021.

[26] R. Amirante, L. Andrea Catalano, and P. Tamburrano, "The importance of a full 3D fluid dynamic analysis to evaluate the flow forces in a hydraulic directional proportional valve," *Eng Comput (Swansea)*, vol. 31, no. 5, pp. 898–922, 2014.

[27] X. Sun, S. Liu, J. Bao, J. Li, and Z. Liu, "A performance prediction method for a high-precision servo valve supported by digital twin assembly-commissioning," *Machines*, vol. 10, no. 1, p. 11, 2021.

[28] B. Gao, W. Zhang, L. Zheng, and H. Zhao, "Research on High-Precision Position Control of Valve-Controlled Cylinders Based on Variable Structure Control," *Machines*, vol. 11, no. 6, p. 623, 2023.

[29] H. Heinken, S. Ulrich, R. Bruns, and S. Schneider, "High-response electrorheological servo valve," *J Intell Mater Syst Struct*, vol. 31, no. 2, pp. 297–307, 2020.

[30] E. A. Sideris and H. C. De Lange, "Pumps operated by solid-state electromechanical smart material actuators-A review," *Sens Actuators A Phys*, vol. 307, p. 111915, 2020.

[31] V. K. A. Shankar, S. Umashankar, S. Paramasivam, and N. Hanigovszki, "A comprehensive review on energy efficiency enhancement initiatives in centrifugal pumping system," *Appl Energy*, vol. 181, pp. 495–513, 2016.

[32] D. J. Laser and J. G. Santiago, "A review of micropumps," *Journal of micromechanics and microengineering*, vol. 14, no. 6, p. R35, 2004.

[33] P. Woias, "Micropumps—past, progress and future prospects," *Sens Actuators B Chem*, vol. 105, no. 1, pp. 28–38, 2005.

[34] N.-C. Tsai and C.-Y. Sue, "Review of MEMS-based drug delivery and dosing systems," *Sens Actuators A Phys*, vol. 134, no. 2, pp. 555–564, 2007.

[35] F. Amirouche, Y. Zhou, and T. Johnson, "Current micropump technologies and their biomedical applications," *Microsystem technologies*, vol. 15, pp. 647–666, 2009.

[36] H. Li, J. Liu, K. Li, and Y. Liu, "A review of recent studies on piezoelectric pumps and their applications," *Mech Syst Signal Process*, vol. 151, p. 107393, 2021.

[37] P. Tamburrano, A. R. Plummer, P. Elliott, P. de Palma, E. Distaso, and R. Amirante, "Internal leakage in the main stage of servovalves: An analytical and CFD analysis," in *AIP Conference Proceedings*, American Institute of Physics Inc., Dec. 2019. doi: 10.1063/1.5138879.

[38] P. Tamburrano *et al.*, "2D CFD analysis of servovalve main stage internal leakage," in *ASME/BATH 2019 Symposium on Fluid Power and Motion Control, FPMC 2019*, American Society of Mechanical Engineers (ASME), 2020. doi: 10.1115/FPMC2019-1705.

[39] R. Scheidl, M. Linjama, and S. Schmidt, "Is the future of fluid power digital?," *Proceedings of the Institution of Mechanical Engineers, Part I: Journal of Systems and Control Engineering*, vol. 226, no. 6, pp. 721–723, 2012.

[40] M. S. A. Laamanen and M. Vilenius, "Is it time for digital hydraulics," in *The eighth Scandinavian international conference on fluid power*, 2003.

[41] P. Achten, M. Linjama, R. Scheidl, and S. Schmidt, "Discussion: Is the future of fluid power digital?," *Proceedings of the Institution of Mechanical Engineers, Part I: Journal of Systems and Control Engineering*, vol. 226, no. 6, pp. 724–727, 2012.

[42] F. Sciatti, P. Tamburrano, P. De Palma, E. Distaso, and R. Amirante, "Detailed simulations of an aircraft fuel system by means of Simulink," in *Journal of Physics: Conference Series*, IOP Publishing, 2022, p. 012033.

[43] F. Sciatti, P. Tamburrano, E. Distaso, and R. Amirante, "Modelling of the Entire Aircraft Fuel System Through Simulink for Accurate Performance Evaluation," in *Fluid Power Systems Technology*, American Society of Mechanical Engineers, 2023, p. V001T01A050.

[44] F. Sciatti, P. Tamburrano, E. Distaso, and R. Amirante, "Digital Hydraulic Technology: Applications, Challenges, and Future Direction," in *Journal of Physics: Conference Series*, IOP Publishing, 2023, p. 012053.

[45] F. Sciatti, P. Tamburrano, A. R. Plummer, E. Distaso, P. De Palma, and R. Amirante, "Numerical Simulations of a High Frequency Switching 4/2 ON/OFF Valve for Pulse Modulation Switching Digital Circuits".

[46] F. Sciatti *et al.*, "Numerical Analysis of a High-Power Piezoelectric Pump using Computational Fluid Dynamics (CFD) Simulations," in *GFPS 2024*, 2024.

[47] F. Sciatti *et al.*, "Investigation of Cavitation Phenomena in a 'High-Power' Piezohydraulic Pump: A Computational Fluid Dynamics (CFD) Approach," in *ATI 2024*, 2022.

[48] P. Tamburrano, E. Distaso, A. R. Plummer, F. Sciatti, P. De Palma, and R. Amirante, "Direct drive servovalves actuated by amplified piezo-stacks: Assessment through a detailed numerical analysis," *Actuators*, vol. 10, no. 7, Jul. 2021, doi: 10.3390/act10070156.

[49] P. Tamburrano, P. De Palma, A. R. Plummer, E. Distaso, F. Sciatti, and R. Amirante, "Simulation of a high frequency on/off valve actuated by a piezo-ring stack for digital hydraulics," 2021.

[50] P. Tamburrano, F. Sciatti, E. Distaso, and R. Amirante, "Comprehensive Numerical Analysis of a Four-Way Two-Position (4/2) High-Frequency Switching Digital Hydraulic Valve Driven by a Ring Stack Actuator," *Energies (Basel)*, vol. 16, no. 21, p. 7355, 2023.

[51] N. Sell, F. Sciatti, A. Plummer, and T. Love, "Design and testing of a multi-cylinder piezo pump for hydraulic actuation," *Energies (Basel)*, 2024.

[52] Federal Aviation Administration (FAA), "https://www.faa.gov/."

[53] E.-S. Ahmed, "Aircraft propulsion and gas turbine engines," 2008, *CRC Press, Taylor & Francis Group, US*.

[54] R. Langton, C. Clark, M. Hewitt, and L. Richards, *Aircraft fuel systems*. John Wiley & Sons, 2009.

[55] R. Royce, *The jet engine*. John Wiley & Sons, 2015.

[56] N. Morioka and H. Oyori, "More electric architecture for engine and aircraft fuel system," SAE Technical Paper, 2013.

[57] Y. Wang, D. Fan, C. Zhang, K. Peng, and D. Shi, "Design and analysis of the variable pressure-drop fuel metering device," in *2017 36th Chinese Control Conference (CCC)*, IEEE, 2017, pp. 6434–6439.

[58] W. Liwen and Z. Lu, "Internal fault diagnosis of aircraft engine fuel metering unit based on artificial immune algorithm".

[59] G. Carrese, T. Krepec, and C. H. To, "Simulation, testing and optimization of a new low cost electronic fuel control unit for small gas turbine engines," *SAE transactions*, pp. 199–207, 1990.

[60] Z. Wen, T. Zhizhong, L. I. Songjing, L. I. Hongzhou, and L. Zhang, "Thermodynamic characteristic study of a high-temperature flow-rate control valve for fuel supply of scramjet engines," *Chinese Journal of Aeronautics*, vol. 25, no. 4, pp. 559–565, 2012.

[61] M. Montazeri-Gh and S. Jafari, "Evolutionary optimization for gain tuning of jet engine min-max fuel controller," *J Propuls Power*, vol. 27, no. 5, pp. 1015–1023, 2011.

[62] B. Wang, H. Zhao, and Z. Ye, "A co-modeling method based on component features for mechatronic devices in aero-engines," *International Journal of Turbo & Jet-engines*, vol. 34, no. 3, pp. 255–267, 2017.

[63] H. Balakrishnan, J.-P. Clarke, E. M. Feron, R. J. Hansman, and H. Jimenez, "Challenges in aerospace decision and control: Air transportation systems," *Advances in control system technology for aerospace applications*, pp. 109–136, 2016.

[64] S. S. Karpenko, E. Y. Zybin, and V. V Kosyanchuk, "Nonparametric method for failures detection and localization in the actuating subsystem of aircraft control system," in *IOP Conference Series: Materials Science and Engineering*, IOP Publishing, 2018, p. 012010.

[65] B. Wang, H. Zhao, L. Yu, and Z. Ye, "Study of temperature effect on servovalve-controlled fuel metering unit," *J Eng Gas Turbine Power*, vol. 137, no. 6, 2015.

[66] S. M. Agh, J. Pirkandi, M. Mahmoodi, and M. Jahromi, "Development of a novel rotary flow control valve with an electronic actuator and a pressure compensator valve for a gas turbine engine fuel control system," *Flow Measurement and Instrumentation*, vol. 74, p. 101759, 2020.

[67] H. Jie, L. I. Yunhua, and Y. Liman, "A novel low pressure-difference fluctuation electro-hydraulic large flowrate control valve for fuel flowrate control of aeroengine afterburner system," *Chinese Journal of Aeronautics*, vol. 35, no. 11, pp. 363–376, 2022.

[68] N. R. Council, *Aviation fuels with improved fire safety: a proceedings*. National Academies Press, 1997.

[69] F. Claeyssen *et al.*, "New actuators for aircraft, space and military applications," in *Proceedings of the 12th International Conference on New Actuators*, 2010, pp. 324–330.

[70] X. Zhou *et al.*, "Review on piezoelectric actuators: materials, classifications, applications, and recent trends," *Frontiers of Mechanical Engineering*, vol. 19, no. 1, p. 6, 2024.

[71] M. Zupan, M. F. Ashby, and N. A. Fleck, "Actuator classification and selection—the development of a database," *Adv Eng Mater*, vol. 4, no. 12, pp. 933–940, 2002.

[72] D. T. Branson, F. C. Wang, D. N. Johnston, D. G. Tilley, C. R. Bowen, and P. S. Keogh, "Piezoelectrically actuated hydraulic valve design for high bandwidth and flow performance," *Proceedings of the Institution of Mechanical Engineers, Part I: Journal of Systems and Control Engineering*, vol. 225, no. 3, pp. 345–359, 2011.

[73] A. Bosotti, R. Paparella, and F. Puricelli, "PI piezo lifetime test report," 2005.

[74] R. Mbarki, N. Baccam, K. Dayal, and P. Sharma, "Piezoelectricity above the Curie temperature? Combining flexoelectricity and functional grading to enable high-temperature electromechanical coupling," *Appl Phys Lett*, vol. 104, no. 12, 2014.

[75] H. Li, Y. Xu, M. Shao, L. Guo, and D. An, "Analysis for hysteresis of piezoelectric actuator based on microscopic mechanism," in *Iop conference series: Materials science and engineering*, IOP Publishing, 2018, p. 012031.

[76] Y. Ishikiriyama and T. Morita, "Improvement of self-sensing piezoelectric actuator control using permittivity change detection," *Journal of Advanced Mechanical Design, Systems, and Manufacturing*, vol. 4, no. 1, pp. 143–149, 2010.

[77] Y. Ma, J. Mao, and Z. Zhang, "On generalized dynamic Preisach operator with application to hysteresis nonlinear systems," *IEEE Transactions on Control Systems Technology*, vol. 19, no. 6, pp. 1527–1533, 2010.

[78] M.-L. Zhou, Y. Tian, W. Gao, and Z. Yang, "High precise control method for a new type of piezoelectric electro-hydraulic servo valve," *Journal of Central South University of Technology*, vol. 14, no. 6, pp. 832–837, 2007.

[79] Y. K. Yong, "Preloading piezoelectric stack actuators in high-speed nanopositioning systems," *Front Mech Eng*, vol. 2, p. 8, 2016.

[80] S. YOKOTA, K. HIRAMOTO, and K. AKUTSU, "An ultra fast-acting electro-hydraulic digital valve and high-speed electro-hydraulic servo valves using multilayered PZT elements," in *Proceedings of the JFPS International Symposium on Fluid Power*, The Japan Fluid Power System Society, 1993, pp. 121–130.

[81] M. Zhou, W. Gao, Z. Yang, and Y. Tian, "High precise fuzzy control for piezoelectric direct drive electro-hydraulic servo valve," *Journal of Advanced Mechanical Design, Systems, and Manufacturing*, vol. 6, no. 7, pp. 1154–1167, 2012.

[82] G. Changbin and J. Zongxia, "A piezoelectric direct-drive servo valve with a novel multi-body contacting spool-driving mechanism: Design, modelling and experiment," *Proc Inst Mech Eng C J Mech Eng Sci*, vol. 228, no. 1, pp. 169–185, 2014.

[83] Y. B. Bang, K. I. Lee, C. S. Joo, and J. W. Hur, "Two-stage electrohydraulic servovalve using stack-type piezoelectric elements," *Proc Inst Mech Eng C J Mech Eng Sci*, vol. 218, no. 1, pp. 53–65, 2004.

[84] Y.-B. Bang, C.-S. Joo, K.-I. Lee, J.-W. Hur, and W.-K. Lim, "Development of a two-stage high speed electrohydraulic servovalve systems using stack-type piezoelectric elements," in *Proceedings 2003 IEEE/ASME International Conference on Advanced Intelligent Mechatronics (AIM 2003)*, IEEE, 2003, pp. 131–136.

[85] M. Reichert, "Development of high-response piezo-servovalves for improved performance of electrohydraulic cylinder drives," 2010.

[86] T. Jungblut, H. Atzrodt, T. Drögemüller, and S. Herold, "Transient simulation of a hybrid test rig for broadband loading," in *7th EUROMECH Solid Mechanic Conference (ESMC 2009), Lisbon, Portugal*, 2009.

[87] F. Claeyssen, R. Le Letty, F. Barillot, and O. Sosnicki, "Amplified piezoelectric actuators: Static & dynamic applications," *Ferroelectrics*, vol. 351, no. 1, pp. 3–14, 2007.

[88] J. E. Lindler and E. H. Anderson, "Piezoelectric direct drive servovalve," in *Smart structures and materials 2002: industrial and commercial applications of smart structures technologies*, SPIE, 2002, pp. 488–496.

[89] H. Zeng, R.-B. Yuan, C. Sun, and Z. Zhang, "Study on performance of laminated piezoelectric pneumatic servo valve," *Procedia Eng*, vol. 31, pp. 1140–1148, 2012.

[90] J. Jeon, Q.-H. Nguyen, Y.-M. Han, and S.-B. Choi, "Design and evaluation of a direct drive valve actuated by piezostack actuator," *Advances in Mechanical Engineering*, vol. 5, p. 986812, 2013.

[91] C. Han, Y.-H. Hwang, and S.-B. Choi, "Tracking control of a spool displacement in a direct piezoactuator-driven servo valve system," *Front Mater*, vol. 4, p. 9, 2017.

[92] S. Karunanidhi and M. Singaperumal, "Mathematical modelling and experimental characterization of a high dynamic servo valve integrated with piezoelectric actuator," *Proceedings of the Institution of Mechanical Engineers, Part I: Journal of Systems and Control Engineering*, vol. 224, no. 4, pp. 419–435, 2010.

[93] X. CHEN, Y. Z. H. U, Q. G. A. O, and B. Niyomwungeri, "Simulation research for fluid-solid interaction performance of a piezoelectric bimorph actuator applied in servo valves," in *2019 IEEE 8th International Conference on Fluid Power and Mechatronics (FPM)*, 2019, pp. 236–242. doi: 10.1109/FPM45753.2019.9035768.

[94] Z. Lihui, E. Shiju, Z. Xilin, and G. Chunfu, "Development of hydroelectric servo-valve based on piezoelectric elements," in *2010 International Conference on Mechanic Automation and Control Engineering*, IEEE, 2010, pp. 3330–3333.

[95] G.-M. Cheng, P. Li, and Z.-G. Yang, "Double-nozzle piezoelectric servovalve," *Guangxue Jingmi Gongcheng(Optics and Precision Engineering)*, vol. 13, no. 3, pp. 276–828, 2005.

[96] S. F. Rezeka, A. Khalil, and A. Abdellatif, "Parametric study of electro-hydraulic servo valve using a piezo-electric actuator," *International Review of Mechanical Engineering*, vol. 5, no. 5, pp. 961–967, 2011.

[97] A. Milecki and D. Rybarczyk, "Investigations of applications of smart materials and methods in fluid valves and drives," *Journal of Machine Engineering*, vol. 19, no. 4, pp. 122–134, 2019.

[98] D. K. Sangiah, A. R. Plummer, C. R. Bowen, and P. Guerrier, "Modelling and experimental validation of a novel piezohydraulic servovalve," in *Dynamic Systems and Control Conference*, 2011, pp. 343–350.

[99] D. K. Sangiah, A. R. Plummer, C. R. Bowen, and P. Guerrier, "A novel piezohydraulic aerospace servovalve. Part 1: design and modelling," *Proceedings of the Institution of Mechanical Engineers, Part I: Journal of Systems and Control Engineering*, vol. 227, no. 4, pp. 371–389, 2013.

[100] D.-J. Kim, J.-D. Yu, and Y.-H. Byun, "Piezoelectric ring bender for characterization of shear waves in compacted sandy soils," *Sensors*, vol. 21, no. 4, p. 1226, 2021.

[101] M. J. F. Bertin, A. R. Plummer, C. R. Bowen, and D. N. Johnston, "An investigation of piezoelectric ring benders and their potential for actuating servo valves," in *Fluid Power Systems Technology*, American Society of Mechanical Engineers, 2014, p. V001T01A034.

[102] P. Tamburrano, R. Amirante, E. Distaso, and A. R. Plummer, "Full simulation of a piezoelectric double nozzle flapper pilot valve coupled with a main stage spool valve," *Energy Procedia*, vol. 148, pp. 487–494, 2018.

[103] L. J. Persson, A. R. Plummer, C. R. Bowen, and I. Brooks, "Design and modelling of a novel servovalve actuated by a piezoelectric ring bender," in *Fluid Power Systems Technology*, American Society of Mechanical Engineers, 2015, p. V001T01A043.

[104] L. Persson, A. Plummer, C. Bowen, and I. Brooks, "A lightweight, low leakage piezoelectric servovalve," in *Recent Advances in Aerospace Actuation Systems and Components 2016*, 2016.

[105] F. Stefanski, B. Minorowicz, J. Persson, A. Plummer, and C. Bowen, "Non-linear control of a hydraulic piezo-valve using a generalised Prandtl–Ishlinskii hysteresis model," *Mech Syst Signal Process*, vol. 82, pp. 412–431, 2017.

[106] P. Tamburrano, A. R. Plummer, P. De Palma, E. Distaso, and R. Amirante, "A novel servovalve pilot stage actuated by a piezo-electric ring bender: A numerical and experimental analysis," *Energies (Basel)*, vol. 13, no. 3, 2020, doi: 10.3390/en13030671.

[107] P. Tamburrano, A. R. Plummer, P. De Palma, E. Distaso, and R. Amirante, "A novel servovalve pilot stage actuated by a piezoelectric ring bender (Part II): Design model and full simulation," *Energies (Basel)*, vol. 13, no. 9, May 2020, doi: 10.3390/en13092267.

[108] P. Tamburrano, R. Amirante, E. Distaso, and A. R. Plummer, "A novel piezoelectric double-flapper servovalve pilot stage: Operating principle and performance prediction," in *Fluid Power Systems Technology*, American Society of Mechanical Engineers, 2018, p. V001T01A032.

[109] M. Linjama, J. Grönholm, and M. Paloniitty, "Switching control of a water hydraulic cylinder with slow parallel-connected on/off valves," in *Workshop on Digital Fluid Power*, 2019.

[110] R. Rituraj and R. Scheidl, "Advancements in the Control Strategy for Digital Hydraulically Driven Knee Exoskeleton," in *Fluid Power Systems Technology*, American Society of Mechanical Engineers, 2022, p. V001T01A006.

[111] M. Pan, N. Johnston, A. Plummer, S. Kudzma, and A. Hillis, "Theoretical and experimental studies of a switched inertance hydraulic system," *Proceedings of the Institution of Mechanical Engineers, Part I: Journal of Systems and Control Engineering*, vol. 228, no. 1, pp. 12–25, 2014.

[112] R. Leifeld, M. Vukovic, and H. Murrenhoff, "STEAM–the best of both worlds," in *Proceedings of the 7th workshop on digital fluid power, Linz, Austria*, 2015.

[113] D. B. Roemer, C. Norgaard, M. M. Bech, and P. Johansen, "Valve and Manifold Considerations for Efficient Digital Hydraulic Machines," in *Proceedings of the Eighth Workshop on Digital Fluid Power, Tampere, Finland*, 2016, pp. 24–25.

[114] T. Noritsugu, "Development of PWM mode electro-pneumatic servomechanism. I: Speed control of a pneumatic cylinder," *The Journal of fluid control*, vol. 17, no. 1, pp. 65–80, 1986.

[115] T. Noritsugu, "Development of PWN mode electro-pneumatic servomechanism. II: Position control of a pneumatic cylinder," *The Journal of fluid control*, vol. 17, no. 2, pp. 7–31, 1987.

[116] K. Ahn and S. Yokota, "Intelligent switching control of pneumatic actuator using on/off solenoid valves," *Mechatronics*, vol. 15, no. 6, pp. 683–702, 2005.

[117] Vemet forward, "https://www.valmet.com/media/articles/up-andrunning/ newtechnology/FPDigHydr/."

[118] K. Merrill, M. Holland, M. Batdorff, and J. Lumkes Jr, "Comparative study of digital hydraulics and digital electronics," *International journal of fluid power*, vol. 11, no. 3, pp. 45–51, 2010.

[119] R. Scheidl, H. Kogler, and B. Winkler, "HYDRAULIC SWITCHING CONTROL-OBJECTIVES, CONCEPTS, CHALLENGES AND POTENTIAL APPLICATIONS.," *Hidraulica*, no. 1, 2013.

[120] M. Huova and A. Plöckinger, "Improving resolution of digital hydraulic valve system by utilizing fast switching valves," 2010.

[121] Q. Zhang, X. Kong, B. Yu, K. Ba, Z. Jin, and Y. Kang, "Review and development trend of digital hydraulic technology," Jan. 01, 2020, *MDPI AG*. doi: 10.3390/app10020579.

[122] M. Linjama, "DIGITAL FLUID POWER-STATE OF THE ART," 2011.

[123] H. Yang, "Progress and Trend of Construction Machinery Intelligence," in *Construction Machinery Technology and Management*, Beijing, China, 2017, pp. 19–21.

[124] J. V. Poncelet, *Cours de mécanique appliquée aux machines*. Gauthier-Villars, 1874.

[125] C. Fink, "Über gebräuchliche Modifikationen des Wattschen Regulators," *VDI Zeitschrift*, vol. 9, no. 4, pp. 271–280, 1865.

[126] J. Farcot, *Le servo-moteur ou asservi.* J. Baudry, 1873.

[127] F. Wang, L. Gu, and Y. Chen, "A continuously variable hydraulic pressure converter based on high-speed on–off valves," *Mechatronics*, vol. 21, no. 8, pp. 1298–1308, 2011.

[128] Q. Gao, "Nonlinear adaptive control with asymmetric pressure difference compensation of a hydraulic pressure servo system using two high speed on/off valves," *Machines*, vol. 10, no. 1, p. 66, 2022.

[129] F. Wang, L. Gu, and Y. Chen, "A hydraulic pressure-boost system based on high-speed on–off valves," *IEEE/ASME transactions on mechatronics*, vol. 18, no. 2, pp. 733–743, 2012.

[130] R. L. Ballard, "System for Minimizing Skidding," US Patent No 3528708, 1968

[131] F. Meßner and R. Scheidl, "Development and experimental results of a small fast switching valve derived from fuel injection technology," in *Proceedings of the eighth workshop on digital fluid power*, 2016, pp. 9–25.

[132] H. Wang, Z. Chen, J. Huang, L. Quan, and B. Zhao, "Development of high-speed on–off valves and their applications," *Chinese Journal of Mechanical Engineering*, vol. 35, no. 1, p. 67, 2022.

[133] A. Laamanen, L. Siivonen, M. Linjama, and M. Vilenius, "Digital flow control unit-an alternative for a proportional valve," *Power Transmission and Motion Control, PTMC2004*, pp. 297–308, 2004.

[134] M. Heikkilä and M. Linjama, "Displacement control of a mobile crane using a digital hydraulic power management system," *Mechatronics*, vol. 23, no. 4, pp. 452–461, 2013.

[135] M. Linjama, M. Huova, M. Pietola, J. Juhala, and K. Huhtala, "Hydraulic hybrid actuator: theoretical aspects and solution alternatives," in *The Fourteenth Scandinavian International Conference on Fluid Power*, 2015, p. 11.

[136] M. Linjama, K. T. Koskinen, and M. Vilenius, "Accurate trajectory tracking control of water hydraulic cylinder with non-ideal on/off valves," *International Journal of Fluid Power*, vol. 4, no. 1, pp. 7–16, 2003.

[137] I. Schepers, D. Weiler, and J. Weber, "Comparison and evaluation of digital control methods for on/off valves," in *Proceedings of the Fifth Workshop on Digital Fluid Power*, 2012, pp. 103–122.

[138] I. Schepers, D. Weiler, and J. Weber, "Optimized pulse modulation: A novel idea of a digital control method for on/off valves," in *Dynamic Systems and Control Conference*, 2011, pp. 363–366.

[139] I. Schepers, D. Schmitz, D. Weiler, O. Cochoy, and U. Neumann, "A novel model for optimized development and application of switching valves in closed loop control," *International Journal of Fluid Power*, vol. 12, no. 3, pp. 31–40, 2011.

[140] M. Pan, N. Johnston, and A. Hillis, "Active control of pressure pulsation in a switched inertance hydraulic system," *Proceedings of the Institution of Mechanical Engineers, Part I: Journal of Systems and Control Engineering*, vol. 227, no. 7, pp. 610–620, 2013.

[141] N. Akkurt, T. Shedd, A. A. Memon, M. R. Ali, and M. Bouye, "Analysis of the forced convection via the turbulence transport of the hybrid mixture in three-dimensional L-shaped channel," *Case Studies in Thermal Engineering*, vol. 41, p. 102558, 2023.

[142] Q. Gao, J. Wang, Y. Zhu, J. Wang, and J. Wang, "Research Status and Prospects of Control Strategies for High Speed On/Off Valves," *Processes*, vol. 11, no. 1, p. 160, 2023.

[143] Q. Gao, Y. Zhu, C. Wu, and Y. Jiang, "Identification of critical moving characteristics in high speed on/off valve based on time derivative of the coil current," *Proceedings of the Institution of Mechanical Engineers, Part I: Journal of Systems and Control Engineering*, vol. 235, no. 7, pp. 1084–1099, 2021.

[144] Q. Gao, Y. Zhu, and Y. Wang, "Rapid flow measurement for high speed on/off valve based on coil current derivative," *Journal of Mechanical Science and Technology*, vol. 36, no. 6, pp. 2957–2967, 2022.

[145] J. ZHAO, C. ZHANG, Z. ZHAO, Z. WANG, and J. YAO, "Static and dynamic characteristics of high-speed on-off digital valves," *China Mechanical Engineering*, vol. 29, no. 02, p. 145, 2018.

[146] L. I. Pai-xia, Z. Xiao-jun, and L. I. U. Ke-ming, "Response Characteristics of High-speed On-off Valve with Double Voltage Driving," *CHINESE HYDRAULICS & PNEUMATICS*, no. 07, p. 59, 2018.

[147] I.-Y. Lee, "Switching response improvement of a high speed on/off solenoid valve by using a 3 power source type valve driving circuit," in *2006 IEEE International Conference on Industrial Technology*, IEEE, 2006, pp. 1823–1828.

[148] J. Zhao, M. Wang, Z. Wang, L. Grekhov, T. Qiu, and X. Ma, "Different boost voltage effects on the dynamic response and energy losses of high-speed solenoid valves," *Appl Therm Eng*, vol. 123, pp. 1494–1503, 2017.

[149] J. Zhao, P. Yue, L. Grekhov, and X. Ma, "Hold current effects on the power losses of high-speed solenoid valve for common-rail injector," *Appl Therm Eng*, vol. 128, pp. 1579–1587, 2018.

[150] Q. Zhong, B. Zhang, H. C. Hong, and H. Y. Yang, "Three power sources excitation control strategy of high speed on/off valve based on current feedback," *J. Zhejiang Univ*, vol. 52, pp. 8–15, 2018.

[151] Q. Zhong *et al.*, "Performance analysis of high speed on/off valve by multi-voltages compound excitation," *J. Mech. Eng*, vol. 57, pp. 191–201, 2021.

[152] Q. Zhong *et al.*, "Analysis of dynamic characteristics and power losses of high speed on/off valve with pre-existing control algorithm," *Energies (Basel)*, vol. 14, no. 16, p. 4901, 2021.

[153] G. A. O. Qiang, Z. H. U. Yuchuan, L. U. O. Zhang, and C. Xiaoming, "Analysis and optimization on compound PWM control strategy of high-speed on/off valve," 北京航空航天大学学报, vol. 45, no. 6, pp. 1129–1136, 2019.

[154] Q. Gao, Y. Zhu, Z. Luo, and N. Bruno, "Investigation on adaptive pulse width modulation control for high speed on/off valve," *Journal of Mechanical Science and Technology*, vol. 34, pp. 1711–1722, 2020.

[155] Q. Zhong, B. Zhang, H.-Y. Yang, J.-E. Ma, and R.-F. Fung, "Performance analysis of a high-speed on/off valve based on an intelligent pulse-width modulation control," *Advances in Mechanical Engineering*, vol. 9, no. 11, p. 1687814017733247, 2017.

[156] B. Zhang *et al.*, "Self-correcting PWM control for dynamic performance preservation in high speed on/off valve," *Mechatronics*, vol. 55, pp. 141–150, 2018.

[157] Q. Gao, "Investigation on the transient impact characteristics of fast switching valve during excitation stage," *Journal of Low Frequency Noise, Vibration and Active Control*, vol. 41, no. 4, pp. 1322–1338, 2022.

[158] I. Flugge-Lotz and C. Taylor, "Synthesis of a nonlinear control system," *IRE transactions on automatic control*, vol. 1, no. 1, pp. 3–9, 1956.

[159] A. Laamanen, M. Linjama, and M. Vilenius, "Characteristics of a digital flow control unit with PCM control," in *7th Triennial International Symposium on Fluid Control, Measurement and Visualization, Sorrento, Italy, August 25-28.2003*, Optimage Ltd., Edinburgh, UK, EH10 5PJ, 2003, p. 16.

[160] M. Linjama, "On the numerical solution of steady-state equations of digital hydraulic valve-actuator system," in *Proceedings of the Eight Workshop on Digital Fluid Power*, 2016, pp. 141–155.

[161] M. Linjama, M. Huova, and M. Karvonen, "Modelling of flow characteristics of on/off valves," in *The 5th Workshop on Digital Fluid Power*, 2012.

[162] L. Rong, W. Xuanyin, T. Guoliang, and D. Fan, "Theoretical and experimental study on hydraulic servo position control system with generalization pulse code modulation control," in *Conference on Fluid Power Transmission and Control*, Citeseer, 2001, pp. 3–5.

[163] V. H. Donkov, T. Andersen, M. Linjama, and M. Ebbesen, "Digital hydraulic technology for linear actuation: A state of the art review," *International Journal of Fluid Power*, pp. 263–304, 2020.

[164] A. Laamanen, M. Linjama, and M. Vilenius, "Pressure peak phenomenon in digital hydraulic systems-a theoretical study," in *Bath Workshop on Power Transmission and Motion Control (PTMC 2005), 7-9 September 2005*, 2005, pp. 91–104.

[165] A. Laamanen, M. Linjama, and M. Vilenius, "On the pressure peak minimization in digital hydraulics," 2007.

[166] J. S. Lee, K. B. Lee, and C. G. Lee, "An experimental study on the control of pressure transients using an orifice," *International journal of pressure vessels and piping*, vol. 78, no. 5, pp. 337–341, 2001.

[167] H. Tanaka, "Electro-hydraulic PCM control," *The Journal of fluid control*, vol. 18, no. 1, pp. 34–46, 1988.

[168] A. Laamanen, M. Nurmia, M. Linjama, K. T. Koskinen, and M. Vilenius, "Two different control methods for digital flow control unit," in *The Eight Scandinavian International Conference on Fluid Power, Proceedings of the Conference, May 7-9, 2003, Tampere, Finland, SICFP´03*, Tampere University of Technology, 2003, pp. 887–898.

[169] M. Linjama and M. Vilenius, "Digital hydraulic control of a mobile machine joint actuator mockup," *Power Transmission and Motion Control: PTMC*, 2004.

[170] A. Laamanen, M. Linjama, and M. Vilenius, "The effect of coding method on pressure peaks in digital hydraulic system," in *Proceedings of the 4th FPNI-PhD Symposium, Sarasota 2006, June 13-17, 2006, Sarasota, FL, USA*, 2006, pp. 285–295.

[171] M. Linjama, "Fundamentals of digital microhydraulic," in *Proceedings of the 8th International Fluid Power Conference, Dresden, March 26-28, 2012*, Technische Universität Dresden, Institute of Fluid Power, 2012, pp. 385–396.

[172] M. Paloniitty and M. Linjama, "High-linear digital hydraulic valve control by an equal coded valve system and novel switching schemes," *Proceedings of the Institution of Mechanical Engineers, Part I: Journal of Systems and Control Engineering*, vol. 232, no. 3, pp. 258–269, 2018.

[173] W. Li, J. Han, and L. Ren, "New Control Theory and Method of the Digital Hydraulic Cylinder," *Ji Xie She Ji Yu Yan Jiu(Machine Design and Research)*, vol. 29, no. 1, pp. 91–93, 2013.

[174] R. Scheidl, B. Winkler, H. Kogler, P. Ladner, R. Haas, and E. Lukachev, "Digital fluid technologies for the steel industry," *BHM Berg-und Hüttenmännische Monatshefte*, 2016.

[175] H. Hesse and H. Moller, "Modulated Pulse Duration Control of Solenoid Valve," *Olhydraulik und Pneumatik*, pp. 11–16, 1972.

[176] Y. M. El-Ibiary, P. R. Ukrainetz, and N. PN, "Design and Assessment of A New Solenoid-operated Ball Valve for Digital Application," in *Proceedings of 34 th National Conference on Fluid Power, Philadelphia*, 1978, pp. 31–35.

[177] K. Ichiryu, "Recent Trends of Hydraulic Technology," *Journal of Japan Society of Mechanical Engineers*, pp. 78–790, 1984.

[178] H. Luo, Y. Yang, and L. Xu, "The PWM Electrohydraulic Control System Using Computer," in *42th National Conference on Fluid Power*, Chicago, 1987.

[179] G. A. Parker and I. Yuksel, "A Novel Electro-Hydraulic Switching Valve," in *B.H.R.A*, 1981.

[180] P. Cui, R. T. Burton, and P. R. Ukrainetz, "Development of a high speed on/off valve," *SAE transactions*, pp. 312–316, 1991.

[181] J. Yu, X. Han, and Y. Zhang, "Application of high speed digital control solenoid valves in the electronic control of diesel engines," *Journal of Beijing Institute of Technology*, vol. 14, no. 1, pp. 91–95, 1994.

[182] X. Kong and S. Li, "Dynamic performance of high speed solenoid valve with parallel coils," *Chinese Journal of Mechanical Engineering*, vol. 27, no. 4, pp. 816–821, 2014.

[183] H. C. Tu, M. B. Rannow, J. D. van de Ven, M. Wang, P. Y. Li, and T. R. Chase, "High speed rotary pulse width modulated on/off valve," in *ASME International Mechanical Engineering Congress and Exposition*, 2007, pp. 89–102.

[184] L. Gu *et al.*, "Development of a large flow-rate high speed on/off valve for underwater hydraulic ejection system," in *2013 OCEANS-San Diego*, IEEE, 2013, pp. 1–5.

[185] J. Zhang, M. Yang, and B. Xu, "Design and experimental research of a miniature digital hydraulic valve," *Micromachines (Basel)*, vol. 9, no. 6, p. 283, 2018.

[186] M. Yang, J. Zhang, and B. Xu, "Experimental study and simulation analysis on electromagnetic characteristics and dynamic response of a new miniature digital valve," *Advances in Materials Science and Engineering*, vol. 2018, pp. 1–8, 2018.

[187] M. Yang, J. Zhang, B. Xu, and W. Wang, "Study on electromagnetic force of the new micro digital valve," *Microsystem Technologies*, vol. 25, pp. 2399–2409, 2019.

[188] L. Sui, X. Xiong, and G. Shi, "Piezoelectric actuator design and application on active vibration control," *Phys Procedia*, vol. 25, pp. 1388–1396, 2012.

[189] S. YOKOTA and K. AKUTU, "A fast-acting electro-hydraulic digital transducer: A poppet-type on-off valve using a multilayered piezoelectric device," *JSME international journal. Ser. 2, Fluids engineering, heat transfer, power, combustion, thermophysical properties*, vol. 34, no. 4, pp. 489–495, 1991.

[190] H. Yamada, G. Wennmacher, T. Muto, and Y. Suematsu, "Development of a high-speed on/off digital valve for hydraulic control systems using a multilayered PZT actuator," *International Journal of Fluid Power*, vol. 1, no. 2, pp. 5–10, 2000.

[191] X. Ouyang, H. Yang, H. Jiang, and B. Xu, "Simulation of the piezoelectric high-speed on/off valve," *Chinese Science Bulletin*, vol. 53, no. 17, pp. 2706–2711, 2008.

[192] Y. Zeng, D. Wang, B. Zi, and Q. Zeng, "Dynamic characteristics of priority control system for high-speed on–off digital valve," *Advances in Mechanical Engineering*, vol. 7, no. 4, p. 1687814015582098, 2015.

[193] S. Wang, B. Zhang, Q. Zhong, and H. Yang, "Study on control performance of pilot high-speed switching valve," *Advances in Mechanical Engineering*, vol. 9, no. 7, p. 1687814017708908, 2017.

[194] Q. Gao, Y. Zhu, C. Wu, and Y. Jiang, "Development of a novel two-stage proportional valve with a pilot digital flow distribution," *Frontiers of Mechanical Engineering*, vol. 16, pp. 420–434, 2021.

[195] H. Kogler and R. Scheidl, "Two basic concepts of hydraulic switching converters," in *Proceedings of the First Workshop on Digital Fluid Power, DFP08, Tampere, Finland*, 2008, pp. 113–128.

[196] M. Pan and A. Plummer, "Digital switched hydraulics," *Frontiers of Mechanical Engineering*, vol. 13, no. 2, pp. 225–231, 2018.

[197] C. Yuan, M. Pan, and A. Plummer, "A review of switched inertance hydraulic converter technology," *J Dyn Syst Meas Control*, vol. 142, no. 5, p. 050801, 2020.

[198] S. Nordås, M. K. Ebbesen, and T. O. Andersen, "Analysis of requirements for valve accuracy and repeatability in high efficiency digital displacement motors," in *Fluid Power Systems Technology*, American Society of Mechanical Engineers, 2018, p. V001T01A055.

[199] K. Zhu, L. Gu, Y. Chen, and W. Li, "High speed on/off valve control hydraulic propeller," *Chinese journal of mechanical engineering*, vol. 25, no. 3, pp. 463–473, 2012.

[200] M. B. Rannow and P. Y. Li, "Soft switching approach to reducing transition losses in an on/off hydraulic valve," in *Dynamic Systems and Control Conference*, 2009, pp. 613–620.

[201] F. Rickenberg, "Valve," Patent No. 1757059, 1930

[202] J. L. Bower, "Digital fluid control system," Sep. 12, 1961, *Google Patents*.

[203] R. Murphy and J. Weil, "Hydraulic Control System. ," US Patent No. 3038449., 1962

[204] T. K. Virvalo, "Cylinder speed synchronization," *Hydraulics & Pneumatics*, vol. 31, no. 12, pp. 55–57, 1978.

[205] M. Linjama, K. T. KOSKINEN, and M. Vilenius, "Pseudo-proportional position control of water hydraulic cylinder using on/off valves," in *Proceedings of the JFPS International Symposium on Fluid Power*, The Japan Fluid Power System Society, 2002, pp. 155–160.

[206] A. Laamanen, M. Linjama, J. Tammisto, K. T. Koskinen, and M. Vilenius, "Velocity control of water hydraulic motor," in *Proceedings of the JFPS International Symposium on Fluid Power*, The Japan Fluid Power System Society, 2002, pp. 167–172.

[207] M. Linjama and M. Vilenius, "Improved digital hydraulic tracking control of water hydraulic cylinder drive," *International journal of fluid power*, vol. 6, no. 1, pp. 29–39, 2005.

[208] M. Linjama, M. Huova, and M. Vilenius, "Online minimization of power losses in distributed digital hydraulic valve system," in *Proceedings of the 6th International Fluid Power Conference Dresden, Fluid Power in Motion, 6iFK, April 1.-2.2008, Dresden*, 2008, pp. 157–171.

[209] M. Huova, M. Karvonen, V. Ahola, M. Linjama, and M. Vilenius, "Energy efficient control of multiactuator digital hydraulic mobile machine," in *7th International Fluid Power Conference (7th IFK), 22-24 March 2010, Aachen, Germany*, 2010, pp. 1–12.

[210] M. Paloniitty, M. Linjama, and K. Huhtala, "Concept of digital microhydraulic valve system utilising lamination technology," in *International Fluid Power Conference*, Hp-Fördervereinigung Fluidtechnik Ev, 2014, pp. 303–313.

[211] M. Paloniitty, M. Linjama, and K. Huhtala, "Equal coded digital hydraulic valve system–improving tracking control with pulse frequency modulation," *Procedia Eng*, vol. 106, pp. 83–91, 2015.

[212] M. Linjama, M. Paloniitty, L. Tiainen, and K. Huhtala, "Mechatronic design of digital hydraulic micro valve package," *Procedia Eng*, vol. 106, pp. 97–107, 2015.

[213] M. Ketonen and M. Linjama, "High flowrate digital hydraulic valve system," in *Proc. of The Ninth Workshop on Digital Fluid Power, Aalborg, Denmark*, 2017.

[214] Q. Gao, Y. Zhu, and J. Liu, "Dynamics modelling and control of a novel fuel metering valve actuated by two binary-coded digital valve arrays," *Machines*, vol. 10, no. 1, p. 55, 2022.

[215] M. Linjama and M. Vilenius, "Energy-efficient motion control of a digital hydraulic joint actuator," in *Proceedings of the JFPS International Symposium on Fluid Power*, The Japan Fluid Power System Society, 2005, pp. 640–645.

[216] M. Huova and A. Laamanen, "Control of three-chamber cylinder with digital valve system," in *Proceedings of The Second Workshop on Digital Fluid Power 12-13 November 2009, Linz, Austria*, 2009, pp. 94–105.

[217] K. Heybroek and E. Norlin, "Hydraulic multi-chamber cylinders in construction machinery," in *Hydraulikdagarna, Linköping, Sweden, 16-17 March 2015 Hydraulic*, 2015, pp. 1–8.

[218] R. Hu, L. He, D. Hu, Y. Hou, and G. Cheng, "Recent studies on the application of piezoelectric pump in different fields," *Microsystem Technologies*, pp. 1–20, 2023.

[219] H. K. Ma, R. H. Chen, N. S. Yu, and Y. H. Hsu, "A miniature circular pump with a piezoelectric bimorph and a disposable chamber for biomedical applications," *Sens Actuators A Phys*, vol. 251, pp. 108–118, 2016.

[220] T. Peng, Z. Yang, and J. Kan, "Investigation on piezo-pump used in water-cooling-system for computer CPU Chip," *J. Refrig*, vol. 30, no. 3, pp. 30–34, 2009.

[221] R. R. Gidde, P. M. Pawar, and V. P. Dhamgaye, "Fully coupled modeling and design of a piezoelectric actuation based valveless micropump for drug delivery application," *Microsystem Technologies*, vol. 26, no. 2, pp. 633–645, 2020.

[222] X. Wu, L. He, Y. Hou, X. Tian, and X. Zhao, "Advances in passive check valve piezoelectric pumps," *Sens Actuators A Phys*, vol. 323, p. 112647, 2021.

[223] J. Zhang, Y. Wang, and J. Huang, "Equivalent circuit modeling for a valveless piezoelectric pump," *Sensors*, vol. 18, no. 9, p. 2881, 2018.

[224] A. Olsson, O. Larsson, J. Holm, L. Lundbladh, O. Öhman, and G. Stemme, "Valve-less diffuser micropumps fabricated using thermoplastic replication," *Sens Actuators A Phys*, vol. 64, no. 1, pp. 63–68, 1998.

[225] 张建辉, **黎毅力**, and **夏**齐霄, "Analysis of the pump volume flow rate and tube property of the piezoelectric valveless pump with Y-shape tubes," *Journal of Mechanical Engineering*, vol. 43, no. 11, pp. 136–141, 2007.

[226] Q. Yan, Y. Yin, W. Sun, and J. Fu, "Advances in valveless piezoelectric pumps," *Applied Sciences*, vol. 11, no. 15, p. 7061, 2021.

[227] O. Akiyoshi, "Flow direction of piezoelectric pump with nozzle/diffuser-elements," *Chin. J. Mech. Eng*, vol. 17, pp. 107–109, 2004.

[228] J. H. Zhang, Y. Li, and J. Liu, "Simulation and experiment of valveless piezoelectric pump with Y-shape tubes," *Optics and Precision Engineering*, vol. 16, no. 4, pp. 669–675, 2008.

[229] J. Zhang, X. Leng, and C. Zhao, "A spiral-tube-type valveless piezoelectric pump with gyroscopic effect," *Chinese science bulletin*, vol. 59, pp. 1885–1889, 2014.

[230] C. J. Morris and F. K. Forster, "Low-order modeling of resonance for fixed-valve micropumps based on first principles," *Journal of Microelectromechanical Systems*, vol. 12, no. 3, pp. 325–334, 2003.

[231] Q. Xia, J. Zhang, and H. Li, "Valve-less piezoelectric pump with unsymmetrical slope chamber bottom," *Optics and Precision Engineering*, vol. 14, no. 4, pp. 641–647, 2006.

[232] J. Ji, J. Zhang, Q. Xia, S. Wang, J. Huang, and C. Zhao, "Theoretical analysis and experimental verification on valve-less piezoelectric pump with hemisphere-segment bluff-body," *Chinese Journal of Mechanical Engineering*, vol. 27, no. 3, pp. 595–605, 2014.

[233] J. Cai, J. Huang, F. J. Hu, and J. H. Zhang, "Research on valve-less piezoelectric pump with parallel connection conical spiral cavity," *J. Vib. Meas. Diagn*, vol. 33, pp. 29–32, 2013.

[234] R. F. Pires, S. L. Vatanabe, A. R. de Oliveira, P. H. Nakasone, and E. C. N. Silva, "Water cooling system using a piezoelectrically actuated flow pump for a medical headlight system," in *Industrial and Commercial Applications of Smart Structures Technologies 2007*, SPIE, 2007, pp. 203–213.

[235] Q. Bao *et al.*, "A novel PZT pump with built-in compliant structures," *Sensors*, vol. 19, no. 6, p. 1301, 2019.

[236] E. Stemme and G. Stemme, "A valveless diffuser/nozzle-based fluid pump," *Sens Actuators A Phys*, vol. 39, no. 2, pp. 159–167, 1993.

[237] A. Olsson, P. Enoksson, G. Stemme, and E. Stemme, "Micromachined flat-walled valveless diffuser pumps," *Journal of microelectromechanical systems*, vol. 6, no. 2, pp. 161–166, 1997.

[238] N.-T. Nguyen and X. Huang, "Miniature valveless pumps based on printed circuit board technique," *Sens Actuators A Phys*, vol. 88, no. 2, pp. 104–111, 2001.

[239] I. Izzo, D. Accoto, A. Menciassi, L. Schmitt, and P. Dario, "Modeling and experimental validation of a piezoelectric micropump with novel no-moving-part valves," *Sens Actuators A Phys*, vol. 133, no. 1, pp. 128–140, 2007.

[240] J. Huang, J. Zhang, X. Xun, and S. Wang, "Theory and experimental verification on valveless piezoelectric pump with multistage Y-shape treelike bifurcate tubes," *Chinese Journal of Mechanical Engineering*, vol. 26, no. 3, pp. 462–468, 2013.

[241] J. Zhang, Q. Xia, Y. Huang, X. Leng, J. Huang, and C. Zhao, "Theory and experimental verification of valveless piezoelectric pump with rotatable unsymmetrical slopes," *Sci China Technol Sci*, vol. 54, pp. 3070–3077, 2011.

[242] D. Zhao, L.-P. He, W. Li, Y. Huang, and G.-M. Cheng, "Experimental analysis of a valve-less piezoelectric micropump with crescent-shaped structure," *Journal of Micromechanics and Microengineering*, vol. 29, no. 10, p. 105004, 2019.

[243] L. He, D. Zhao, W. Li, Q. Xu, and G. Cheng, "Performance analysis of valveless piezoelectric pump with dome composite structures," *Review of Scientific Instruments*, vol. 90, no. 6, 2019.

[244] C. R. de Lima, S. L. Vatanabe, A. Choi, P. H. Nakasone, R. F. Pires, and E. C. N. Silva, "A biomimetic piezoelectric pump: Computational and experimental characterization," *Sens Actuators A Phys*, vol. 152, no. 1, pp. 110–118, 2009.

[245] X. Hu, J. Zhang, Y. Huang, Q. Xia, W. Huang, and C. Zhao, "Principle and experimental verification of caudal-fin-type piezoelectric-stack pump with variable-cross-section oscillating vibrator," *Chinese Journal of Mechanical Engineering*, vol. 25, no. 1, pp. 128–136, 2012.

[246] M. C. Carrozza, N. Croce, B. Magnani, and P. Dario, "A piezoelectric-driven stereolithography-fabricated micropump," *Journal of Micromechanics and Microengineering*, vol. 5, no. 2, p. 177, 1995.

[247] K. Junwu, Y. Zhigang, P. Taijiang, C. Guangming, and W. Boda, "Design and test of a high-performance piezoelectric micropump for drug delivery," *Sens Actuators A Phys*, vol. 121, no. 1, pp. 156–161, 2005.

[248] G.-H. Feng and E. S. Kim, "Micropump based on PZT unimorph and one-way parylene valves," *Journal of micromechanics and microengineering*, vol. 14, no. 4, p. 429, 2004.

[249] Y. Luo, M. Lu, and T. Cui, "A polymer-based bidirectional micropump driven by a PZT bimorph," *Microsystem technologies*, vol. 17, pp. 403–409, 2011.

[250] T.-Q. Truong and N.-T. Nguyen, "A polymeric piezoelectric micropump based on lamination technology," *Journal of Micromechanics and Microengineering*, vol. 14, no. 4, p. 632, 2004.

[251] T. Peng *et al.*, "A high-flow, self-filling piezoelectric pump driven by hybrid connected multiple chambers with umbrella-shaped valves," *Sens Actuators B Chem*, vol. 301, p. 126961, 2019.

[252] S. Nayak and R. Muralidhara, "Experimental performance evaluation on piezo-hydraulic pump using flexurally amplified piezoelectric actuators," *Mater Today Proc*, vol. 92, pp. 84–91, 2023.

[253] P. N. Anh, J.-S. Bae, and J.-H. Hwang, "Computational fluid dynamic analysis of flow rate performance of a small piezoelectric-hydraulic pump," *Applied Sciences*, vol. 11, no. 11, p. 4888, 2021.

[254] X. Zhao, D. Zhao, and Q. Guo, "A theoretical and experimental study of a piezoelectric pump with two elastic chambers," *Sensors*, vol. 20, no. 20, p. 5867, 2020.

[255] J. Zhang, Q. Xia, D. Lai, O. Akiyoshi, and Z. Hong, "Discovery and analysis on cavitation in piezoelectric pumps.," *Chinese Journal of Mechanical Engineering(English Edition)*, vol. 17, no. 4, pp. 591–594, 2004.

[256] K. Opitz, O. Schade, and E. Schlücker, "Cavitation in reciprocating positive displacement pumps," in *Proceedings of the 27th international pump users symposium*, Turbomachinery Laboratory, Texas A&M University, 2011.

[257] Y. Ye, J. Chen, Q. S. Pan, and Z. H. Feng, "Suppressing the generation of cavitation by increasing the number of inlet check valves in piezoelectric pumps," *Sens Actuators A Phys*, vol. 293, pp. 56–61, 2019.

[258] X. He, X. Deng, S. Yang, Y. Bi, and Q. Jiang, "Numerical analysis of cavitation flow in vortex-valve piezoelectric micropump," *Drain. Irrig. Mach*, vol. 27, pp. 352–356, 2009.

[259] B. Pečar *et al.*, "Micropump operation at various driving signals: numerical simulation and experimental verification," *Microsystem Technologies*, vol. 21, pp. 1379–1384, 2015.

[260] T. Dolžan, B. Pečar, M. Možek, D. Resnik, and D. Vrtačnik, "Self-priming bubble tolerant microcylinder pump," *Sens Actuators A Phys*, vol. 233, pp. 548–556, 2015.

[261] A. Ullmann, "The piezoelectric valve-less pump—performance enhancement analysis," *Sens Actuators A Phys*, vol. 69, no. 1, pp. 97–105, 1998.

[262] Y. Li, V. T. Le, N. S. Goo, T. H. Kim, and C. S. Lee, "High actuation force of piezoelectric hybrid actuator with multiple piezoelectric pump design," *J Intell Mater Syst Struct*, vol. 28, no. 18, pp. 2557–2571, 2017.

[263] D. G. Lee, S. W. Or, and G. P. Carman, "Design of a piezoelectric-hydraulic pump with active valves," *J Intell Mater Syst Struct*, vol. 15, no. 2, pp. 107–115, 2004.

[264] T. Lemke *et al.*, "A high performance bidirectional micropump utilizing advanced low voltage piezo multilayer actuator technology for a novel artificial sphincter system," in *4th European Conference of the International Federation for Medical and Biological Engineering: ECIFMBE 2008 23–27 November 2008 Antwerp, Belgium*, Springer, 2009, pp. 1517–1520.

[265] P.-H. Cazorla *et al.*, "Piezoelectric micro-pump with PZT thin film for low consumption microfluidic devices," *Procedia Eng*, vol. 87, pp. 488–491, 2014.

[266] T. X. Dinh, S. Sugiyama, and P. H. Pham, "Fluidic device with pumping and sensing functions for precise flow control," *Sens Actuators B Chem*, vol. 150, no. 2, pp. 819–824, 2010.

[267] Z. Zhang, J. Kan, G. Cheng, H. Wang, and Y. Jiang, "A piezoelectric micropump with an integrated sensor based on space-division multiplexing," *Sens Actuators A Phys*, vol. 203, pp. 29–36, 2013.

[268] S. Chen, S. Wang, X. Xie, Z. Zhang, Y. Jiang, and G. Cheng, "Practical research on computer chip water cooling system with combined piezoelectric pump unit," *Opt. Precis. Eng.*, vol. 26, no. 05, pp. 1140–1147, 2018.

[269] T. Ma, S. Sun, B. Li, and J. Chu, "Piezoelectric peristaltic micropump integrated on a microfluidic chip," *Sens Actuators A Phys*, vol. 292, pp. 90–96, 2019.

[270] W. J. Spencer, W. T. Corbett, L. R. Dominguez, and B. D. Shafer, "An electronically controlled piezoelectric insulin pump and valves," *IEEE Trans Sonics Ultrason*, vol. 25, no. 3, pp. 153–156, 1978.

[271] N. Sell *et al.*, "Design and testing of a high power piezo pump for hydraulic actuation," *J Intell Mater Syst Struct*, 2023.

[272] J.-H. Hwang, J.-S. Bae, Y.-H. Hwang, and J.-Y. Kwon, "Pressurization characteristics of a piezoelectric-hydraulic pump for UAV brake systems," *International Journal of Aeronautical and Space Sciences*, vol. 19, pp. 776–784, 2018.

[273] G.-W. Kim and K. W. Wang, "Enhanced control performance of a piezoelectric—hydraulic pump actuator for automotive transmission shift control," *Proceedings of the Institution of Mechanical Engineers, Part D: Journal of Automobile Engineering*, vol. 224, no. 2, pp. 161–174, 2010.

[274] J. Y. Hwang *et al.*, "Periodic fuel supply to a micro-DMFC using a piezoelectric linear actuator," *Journal of Micromechanics and Microengineering*, vol. 20, no. 8, p. 085023, 2010.

[275] T. Zhang and Q.-M. Wang, "Valveless piezoelectric micropump for fuel delivery in direct methanol fuel cell (DMFC) devices," *J Power Sources*, vol. 140, no. 1, pp. 72–80, 2005.

[276] W. J. Thayer, "Transfer functions for Moog servovalves," *Moog technical bulletin*, vol. 103, pp. 1–11, 1965.

[277] I. N. C. Moog, "Type 30 Nozzle-Flapper Flow Control Servovalves," 2014, *Catalog*.

[278] Y. Yuan, Z. Zhao, and T. Zhang, "A mimicking technique of back pressure in the hardware-in-the-loop simulation of a fuel control unit," *Simulation*, vol. 96, no. 4, pp. 375–385, 2020.

[279] T. W. Wild, *Aircraft powerplants*. McGraw-Hill Education, 2018.

[280] Noliac Website, "http://www.noliac.com/products/actuators/ring-stacks/show/nac2125-hxx/."

[281] Noliac, "http://www.noliac.com/fileadmin/user_upload/images/Tutorials/Publications/Noliac_publications/Actuator_2010_Design_of_Lightweight__Temperature_Stable_and_Highly_Dynamic_Amplified_Piezoelectric_Actuators.pdf."

[282] https://www.dura-bondbearing.com/wp-content/uploads/2018/06/valve-seat-tech-guide.pdf, "Engine Parts Technical Supplements ."

[283] Inc. The MathWorks, "Matlab & Simulink. SimscapeTM User's Guide R2023a."

[284] Y. L. Fan, Y. Lei, J. W. Zhang, J. Wang, and Z. Li, "Flow Force of Pressure Independent Control Valve with Different Valve Core Structural," in *Journal of Physics: Conference Series*, IOP Publishing, 2020, p. 12149.

[285] R. Li *et al.*, "Review of the Research on and Optimization of the Flow Force of Hydraulic Spool Valves," *Processes*, vol. 11, no. 7, p. 2183, 2023.

[286] N. D. Manring and R. C. Fales, *Hydraulic control systems*. John Wiley & Sons, 2019.

[287] J. D. Stringer, *Hydraulic systems analysis: an introduction*. Macmillan International Higher Education, 1976.

[288] T.-G. Zsurzsan, C. Mangeot, M. A. E. Andersen, Z. Zhang, and N. A. Andersen, "Piezoelectric stack actuator parameter extraction with hysteresis compensation," in *2014 16th European Conference on Power Electronics and Applications*, IEEE, 2014, pp. 1–7.

[289] P. Tamburrano, A. R. Plummer, P. De Palma, E. Distaso, and R. Amirante, "A novel servovalve pilot stage actuated by a piezo-electric ring bender: A numerical and experimental analysis," *Energies (Basel)*, vol. 13, no. 3, p. 671, 2020.

[290] A. Henke, M. A. Kümmel, and J. Wallaschek, "A piezoelectrically driven wire feeding system for high performance wedge-wedge-bonding machines," *Mechatronics*, vol. 9, no. 7, pp. 757–767, 1999.

[291] N. Sell, A. Plummer, N. Johnston, and J. du Bois, "Simulating a high frequency piezo pump with disc reed valves," in *Scandinavian International Conference on Fluid Power*, 2021, pp. 274–282.

[292] "https://www.piceramic.com/en/products/piezoceramic-actuators/stack-actuators/p-010xxh-p-025xxh-pica-thru-ring-actuators-102800. Accessed on February 2024."

[293] J. Huang, Y.-C. Zhu, W.-D. Shi, and J.-H. Zhang, "Theory and experimental verification on cymbal-shaped slotted valve piezoelectric pump," *Chinese Journal of Mechanical Engineering*, vol. 31, no. 1, pp. 1–8, 2018.

[294] Q. Liao, P. Huang, Z. An, D. Li, H. Huang, and C. Zhang, "Origin of thermal depolarization in piezoelectric ceramics," *Scr Mater*, vol. 115, pp. 14–18, 2016.

[295] J. G. Fox and J. Mahanty, "The effective mass of an oscillating spring," *Am J Phys*, vol. 38, no. 1, pp. 98–100, 1970.

[296] D. N. Johnston, "Numerical modelling of reciprocating pumps with self-acting valves," *Proceedings of the institution of mechanical engineers, Part I: Journal of systems and control engineering*, vol. 205, no. 2, pp. 87–96, 1991.

[297] N. Johnston, M. Pan, and S. Kudzma, "An enhanced transmission line method for modelling laminar flow of liquid in pipelines," *Proceedings of the Institution of Mechanical Engineers, Part I: Journal of Systems and Control Engineering*, vol. 228, no. 4, pp. 193–206, 2014.

[298] T. V. K. Vo, T. M. Lubecki, W. T. Chow, A. Gupta, and K. H. H. Li, "Large-scale piezoelectric-based systems for more electric aircraft applications," *Micromachines (Basel)*, vol. 12, no. 2, p. 140, 2021.

[299] C. R. Bowen, M. Lopez-Prieto, S. Mahon, and F. Lowrie, "Impedance spectroscopy of piezoelectric actuators," *Scr Mater*, vol. 42, no. 8, pp. 813–818, 2000.

[300] C. R. Bowen, S. Mahon, and M. L. Prieto, "Non-destructive evaluation of multi-layer actuators," *Ferroelectrics*, vol. 241, no. 1, pp. 199–206, 2000.

[301] Available online. (Accessed on 8 April 2024), "LTD., P.I. PiezoWalk Actuators."

[302] A. Loseille, "Unstructured mesh generation and adaptation," in *Handbook of Numerical Analysis*, vol. 18, Elsevier, 2017, pp. 263–302.

[303] C. Vanhille, "Numerical simulations of stable cavitation bubble generation and primary Bjerknes forces in a three-dimensional nonlinear phased array focused ultrasound field," *Ultrason Sonochem*, vol. 63, p. 104972, 2020.

[304] S. Som, *Development and validation of spray models for investigating diesel engine combustion and emissions*. University of Illinois at Chicago, 2009.

[305] M. Yusvika, A. R. Prabowo, D. D. D. P. Tjahjana, and J. M. Sohn, "Cavitation prediction of ship propeller based on temperature and fluid properties of water," *J Mar Sci Eng*, vol. 8, no. 6, p. 465, 2020.

[306] M. Nezamirad, A. Yazdi, S. Amirahmadian, N. Sabetpour, and A. Hamedi, "Utilization of Schnerr-Sauer cavitation model for simulation of cavitation inception and super cavitation," *International Journal of Aerospace and Mechanical Engineering*, vol. 16, no. 3, pp. 31–35, 2022.

[307] L. Davidson, “Fluid mechanics, turbulent flow and turbulence modeling,” 2015, *Citeseer*.

[308] E. Pal, I. Kumar, J. B. Joshi, and N. K. Maheshwari, “CFD simulations of shell-side flow in a shell-and-tube type heat exchanger with and without baffles,” *Chem Eng Sci*, vol. 143, pp. 314–340, 2016.

[309] J. Xiao *et al.*, “Assessment of different CFD modeling and solving approaches for a supersonic steam ejector simulation,” *Atmosphere (Basel)*, vol. 13, no. 1, p. 144, 2022.